Order Reconstruction and Solution Landscapes for Liquid Crystalline Systems

James Dalby

Department of Mathematics and Statistics

University of Strathclyde

A Thesis presented for the degree of
Doctor of Philosophy

June 2023

Declaration

This thesis is the result of the author's original research. It has been composed by the author and has not been previously submitted for examination which has led to the award of a degree.

Chapter 3 and Chapter 4 contain material posted to arXiv, reference [1]. The analytical results contained therein are a result of the author's own original research in collaboration with the article's co-authors; Yucen Han, Apala Majumdar and Lidia Mrad.

Chapter 5 contains material published in an article, reference [2]. The analytical results contained therein are a result of the author's own original research in collaboration with the article's co-authors; Patrick. E. Farrell, Apala Majumdar and Jingmin Xia.

Chapter 7 contains material published in a letter, reference [3]. The work in Chapter 7 is based on the research carried out in collaboration with the letter's co-authors; Yucen Han, Apala Majumdar, Benjamin M.G.D Carter and Thomas Machon.

Signed:

Date:

Acknowledgements

I would like to thank my supervisor Apala Majumdar for her continuous support, expertise and encouragement, I could not have chosen a better supervisor to work with. Looking back at my older work during the writing of this thesis, I cannot quite believe the improvements I have made over the last three years from her guidance and feedback. Despite completing almost all of my PhD virtually, I have had the privilege to be involved in three collaborations thanks to the opportunities Apala has given me.

I would also like to thank my many other collaborators - Jingmin Xia and Patrick Farrell, with whom I have my first co-authored paper published with, I first met them both in December 2019 at a conference in Providence (at what turned out to be one of the few in-person events I would attend) and I was pleasantly surprised when I got the chance to work with them both a few months later; Lidia Mrad, who I also met at the same conference and went on to have many useful scientific discussions with during our work on nematodynamics; and finally, Thomas Machon and Benjamin Carter, who generously hosted me at Bristol during our work together. I would like to give special thanks to my collaborator and friend Yucen Han, for her truly endless help, at times she has been a second supervisor to me.

A big thanks to my good friends Alex, Cameron and Matt for always getting online. Their friendly jibes was just the encouragement I needed to finish my PhD. Further thanks to Alex and Matt for regularly hosting me in London, as well as allowing me to visit other friends, this proved to be a useful stopover when travelling from Cornwall to conferences (which was less than ideal).

And of course, thank you to my parents for their encouragement and support throughout my life. Also, as per his request, thank you to my brother Matthew for proof reading some of my work since my grammar is so poor.

Abstract

Liquid crystals are the surprisingly less well known fourth phase of matter, sitting between the familiar solid and liquid phases. These materials combine fluidity with orientational and/or positional order, yielding surprising and desirable properties relevant for use in tailor-made applications. In this thesis, we place an emphasis on the study of order reconstruction (OR) solutions. These OR solutions describe polydomain structures i.e., multiple sub-domains separated by domain walls. We study OR solutions within the Landau-de Gennes continuum theory for liquid crystals in a reduced, one-dimensional setting relevant for microfluidic problems. OR solutions in nematic liquid crystals are well known, but we demonstrate the existence of OR solutions in the physical settings of ferronematics, and both passive and active nematodynamics, demonstrating the universality of such solutions. This work involves studying coupled systems of non-linear ordinary differential equations, and utilising techniques from the calculus of variations, partial differential equation theory, and asymptotic analysis, to gain insight. We also place significant emphasis on studying solution landscapes i.e., how all critical points (stable and unstable) of an energy functional connect to one another, and this is implemented through advanced numerical methods. In our final chapter, this sheds light on a competition between uniaxiality and biaxiality in cholesteric liquid crystals, and a way to potentially observe biaxiality experimentally.

Contents

Chapter 1

Introduction

1.1 What are liquid crystals?

In one sentence: *liquid crystals are examples of partially ordered materials that are intermediate between the solid and liquid phases of matter.*

To understand what this means, it is useful to recap the conventional solid and liquid phases, which we are all most familiar with. In a crystalline solid, the molecules are fixed in a rigid lattice structure which cannot move, making the structure highly ordered, whilst in an isotropic liquid, the molecules are free to move at random and are highly disordered. Liquid crystals then, can be thought of as a hybrid of the solid and liquid phases, adopting features from each. In a liquid crystal, the molecules are not held in a fixed lattice and as such, can flow. They do however maintain a degree of positional and/or orientational ordering in at least one-dimension (see Figure 1.1). Here, positional order means molecules arrange in some kind of ordered lattice structure, while orientational order means that the molecules tend to align in the same direction, in an averaged sense.

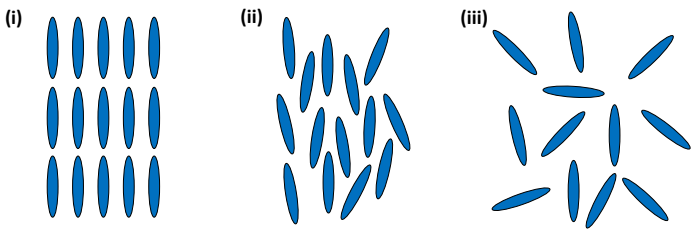

Figure 1.1: Sketch of ellipsoidal shaped molecules (blue shapes) in: (i) a solid crystalline phase, (ii) an example liquid crystal phase and (iii) an isotropic liquid phase.

Typically, this order manifests in the molecules aligning along certain locally preferred directions throughout the material. This is not as restrictive as a fixed lattice, nor as free as a liquid. It is this combination of fluidity and order that gives liquid crystals unique physical properties, and makes them such a rich and interesting set of materials.

A primary cause of this order is the shape of the underlying molecules in the material. Typical shapes for liquid crystal molecules are rod or disc/plate shaped molecules [4], and more recently banana or pizza-slice-shaped molecules have received attention [5]. It is their shape and order that makes liquid crystal materials anisotropic, that is, they have a directional dependent response to external stimuli, such as light, and electric and magnetic fields. The response to light for instance, gives liquid crystals distinct optical properties since they are birefringent. In Figure 1.2, some beautiful examples of the images that can be generated through polarised optical microscopy can be seen. The response to electric and magnetic fields can be used to dictate, stabilise, or switch the state of the liquid crystal. This control can then be exploited for tailor-made applications.

Since liquid crystals sit between the solid and liquid phase, one may ask how do we achieve a liquid crystalline phase? Just as we can induce a phase transition

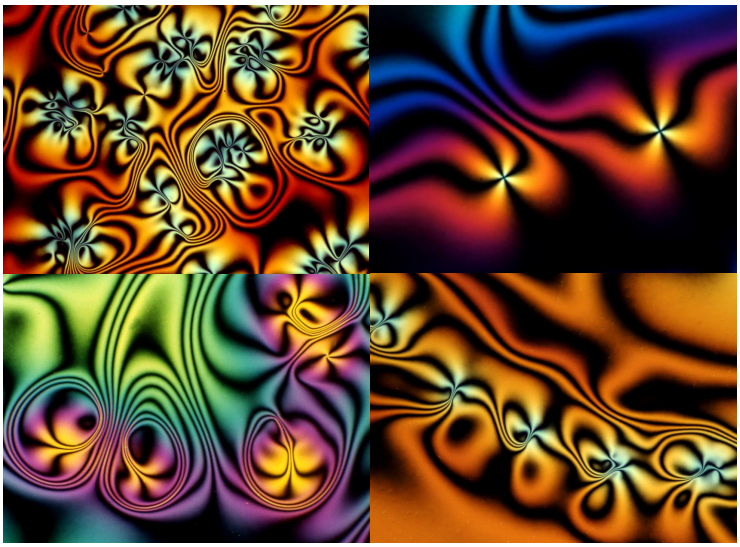

Figure 1.2: Polarising microscope textures of thin liquid crystalline films. Courtesy: Oleg Lavrentovich, Liquid Crystal Institute, Kent State University, National Science Foundation, *www.nsf.gov*.

(i.e. a change in state) by cooling a liquid to a solid, for certain materials, we can cool (heat) a liquid (solid) to a liquid crystal. Liquid crystals were first discovered in 1888 by Friedrich Reinitzer by doing such a procedure (reported in [6]). Reinitzer was heating a sample of cholesteryl benzoate when he seemingly observed two melting points, one from a solid to a cloudy liquid at $145^{o}C$, and from this cloudy state to a clear liquid (now known as the *clearing point*) at $178.5^{o}C$ [7]. Moreover, the procedure was reversible. This cloudy state was the newly discovered liquid crystal phase, however, the term "liquid crystal" was not proposed until 1900 by physicist Otto Lehmann. Lehmann drove progress in the years that followed and notably completed the first polarised optical microscopy experiments [7]. This was followed by the work of the chemist Daniel Vorländer, who proved that the characteristics of a liquid crystal were due to the rigid linear structure of their molecules [8]. Another important discovery came in 1922, when Georges Friedel [7, 9] was able to classify liquid crystals into three categories: the

nematic, cholesteric, and smectic phases.

1.2 Classification of liquid crystals

We now know liquid crystals can be divided into two main classes, the first being those which undergo phase transitions due to changes in temperature, termed *thermotropic* liquid crystals [10]. The second class of liquid crystals are those which undergo phase transitions due to a change in their concentration in a solvent, termed *lyotropic* liquid crystals [10]. It is thermotropic liquid crystals that we study in this thesis. Within these classes, liquid crystals experience different phases as they transition between the liquid and solid states, termed *mesophases*, which can be distinguished by the type of ordering present. Examples include, the nematic, cholesteric and smectic phases identified by Friedel, which we now touch on.

1.2.1 Nematic liquid crystals

The simplest, and most common liquid crystal phase, is the nematic phase, where the constituent molecules are typically cylinder/ellipsoidal or cuboid shaped [11]. The shape of the molecules result in nematic liquid crystals (NLCs) having long range orientational order with preferred directions of average molecular alignment. However, they have no positional order (i.e., they can translate freely in space while being aligned on average [12]). Moreover, nematic molecules have head to tail symmetry since the top and bottom of the molecules are indistinguishable. This information is modelled by a director $\mathbf{n}$, a unit vector pointing in the preferred direction of average molecular alignment (see Figure 1.3 for a depiction of the nematic phase and director $\mathbf{n}$). Due to the head to tail symmetry of the molecules, $\mathbf{n}$ and $-\mathbf{n}$ are physically equivalent. As such, it can be better to think of the

director as a line field, rather than a vector field [13].

Nematics (and liquid crystals in general) can be divided into two broad categories, *uniaxial* and *biaxial*. We say a nematic phase is uniaxial if there is one preferred direction of alignment, such that all directions perpendicular to this direction are physically equivalent. Generally, an uniaxial nematic phase is composed of cylindrical or rod shaped molecules which have rotational symmetry about their long axis. We say a nematic phase is biaxial if it has two locally preferred directions of molecular alignment, and consequently two directors. Biaxial nematic phases typically occur for cuboid shaped molecules which have no axis of rotational symmetry but three axes of reflective symmetry [11].

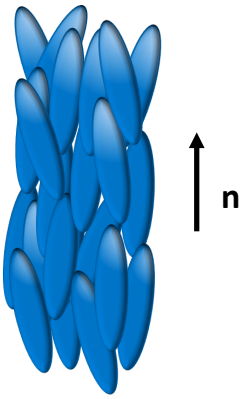

Figure 1.3: A schematic of the nematic phase and its associated director **n**. **n** could be drawn in the opposite direction (the same comment applies to Figure 1.4 and Figure 1.5).

1.2.2 Cholesteric liquid crystals

Another liquid crystal phase is the cholesteric phase, which can be formed by the addition of a chiral dopant to a NLC [14]. This causes the nematic molecules to be chiral (i.e., their mirror images are not superimposable) and form a helical structure. The local director rotates a full 360° as we move through the helix,

and the distance over which this occurs, is labelled as the pitch p_0 of the cholesteric. Figure 1.4 shows the equilibrium structure of the phase. Unsurprisingly, cholesterics are also referred to as chiral nematics [15].

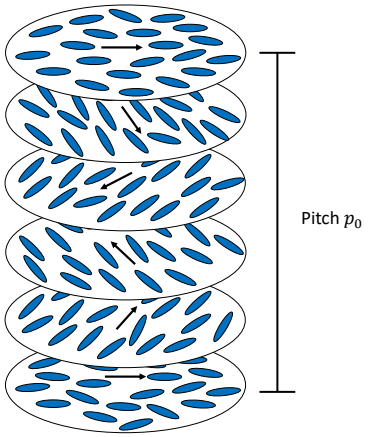

Figure 1.4: A schematic of the cholesteric phase. The black arrows represent the local director $\mathbf{n}$, while p_0 is the pitch, the distance over which a 2π rotation of the director is completed.

1.2.3 Smectic liquid crystals

Smectics are examples of layered liquid crystals wherein there is nematic ordering within the layers and positional ordering in one direction (i.e., the direction orthogonal to the layers). The layers are independent of one another in that they are free to slide over each other. There are two common smectic phases known as the smectic A and smectic C phases [16]. In the smectic A phase, the director is parallel to the layer normal, while in the smectic C phase, the director may orient itself at an angle to the layer normal (see Figure 1.5).

1.2.4 Defects

A recurring and distinguishing feature in liquid crystals is *defects*. Defects correspond to points, lines, or surfaces in the sample where the orientation of the

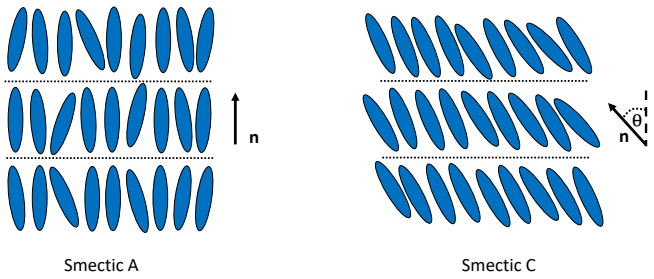

Figure 1.5: A schematic of the smectic A and C phases. In the smectic A phase, the director **n** is parallel to the layer normal. In the smectic C phase, the director is at an angle θ to the layer normal (marked by a dashed line).

molecules can no longer be defined by a director [13, 17]. This is a result of rapid changes in the director profile which can be caused by geometric frustration from the confining geometry, applied external fields, or a phase transition. Examples of defects due to confinement can be seen in Figure 1.2 at the points where black streaks meet. Defects can exist in one-, two-, and three-dimensions, and their classifications are different in each dimension. A point defect in two-dimensions can be given an associated charge k. This can be calculated by travelling along a closed loop around the defect and simultaneously measuring the multiple k of 2π, the director rotates by along this loop [18]. The charge can take the values $k = \pm\frac{1}{2}, \pm 1, \pm\frac{3}{2}, ...$, where a $+$ $(-)$ means the director rotates clockwise (anti-clockwise) around the defect. Examples of the director field for such defects are shown in Figure 1.6, while two ± 1 defects can be seen in the top right image of Figure 1.2. Defects can also take the form of lines known as disclinations (characterised by a rotational displacement of the structure, making it a defect in orientational order) or dislocations (a linear displacement in the structure of the material, making it a defect in positional order) [18]. A charge can also be assigned to a disclination in the same way as for point defects, by considering a closed path around the disclination. In three-dimensions, defects can take the

form of surfaces, such as domain walls. Domain walls and disclinations are the most relevant defects for the problems studied in this thesis.

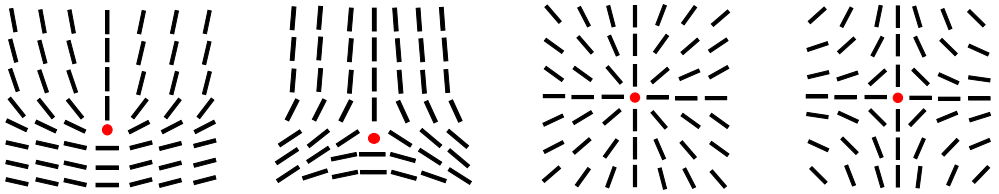

Figure 1.6: Schematics of the director field (drawn as line fields) around some point defects (drawn as dots) in two-dimensions.

1.3 Liquid crystals and their uses

1.3.1 Applications of liquid crystals

Before diving into the mathematical content of this thesis, we summarise just a few of the many interesting applications liquid crystals have, in order to motivate the reader as to why we should study these materials. Applications include metamaterials, biomaterials, drug technologies, various sensor devices (including sensors for medical and biological purposes), and applications in nanotechnologies, to name but a few [19]. In this section, we focus on three examples. We start with an application that someone with little knowledge of liquid crystals maybe aware of, and then move on to those that people outside of the field may never have heard of.

Liquid crystal displays

A commercially successful application of liquid crystals is in the multi billion dollar liquid crystal display (LCD) industry [19, 20]. LCDs appear in our everyday lives

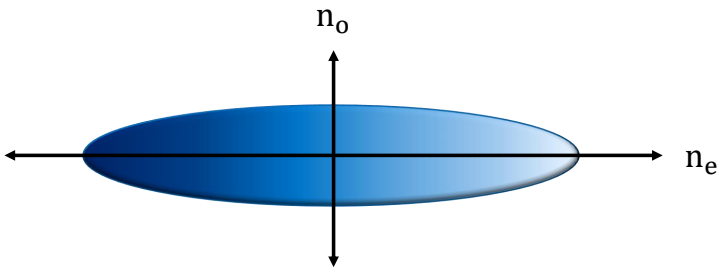

Figure 1.7: Directions in which light experiences the ordinary $\mathbf{n}_o$, and extraordinary $\mathbf{n}_e$, refractive index for an ellipsoidal shaped molecule.

in the form of TV, laptop and phone displays, for example. Liquid crystals are the working material of choice due to their birefringence. Considering a typical ellipsoidal shaped nematic molecule, it has a single optical axis defined by the director. Polarised light propagating along this optical axis experiences an extraordinary refractive index $\mathbf{n}_e$ only, however, light incident from any other direction also experiences an ordinary refractive index $\mathbf{n}_o$, governed by the short axis of the molecule (see Figure 1.7). Referring back to Figure 1.2, the dark lines correspond to regions where the average molecular orientation is parallel to one of the polarisers. In these regions, polarised light propagates on average along the long axis of the molecules and hence, experiences one refractive index leaving its polorisation unaffected and the region dark, since the two polarisers are not aligned. Conversely, the coloured regions correspond to polarised light which does not propagate along the long axis and therefore, splits into two mutually orthogonal rays (termed ordinary and extraordinary rays). After exiting the liquid crystal, these rays are out of phase, but are recombined when they pass through the second polariser giving rise to different colours.

With an understanding of birefringence, we now explain how a twisted nematic device (TND) works and how this can exploited for displays. TNDs do not

appear in modern high resolution displays, instead, what are known as thin film transistors are used. However, they still utilise the same basic principle of the TND (as do many other devices). TNDs consist of liquid crystal material (typically a nematic or cholesteric) sandwiched between two glass plates, which are further placed between two polarisers set at 90^o to each other. The glass plates are given a surface treatment such that the molecules prefer to align along a certain direction on the top and bottom plate. These directions are typically orthogonal to one another so that in the absence of any electric field, the molecules naturally twist between the glass plates. In this twisted state, incident polarised light will experience different optical axes. This changes its orientation allowing it to pass through the second polariser, giving us a transparent state. When an electric field is applied, the dielectric response of the liquid crystal molecules causes them to align with the direction of the field. Hence, by applying the electric field in the vertical direction, the molecules align parallel to the vertical field. In this aligned state, incident polarised light only sees the long axis of the molecules, its orientation is therefore unaffected and with the polarisers being at 90^o to one another, we get a dark state. These transparent and dark states are the basic ingredients required in LCDs. A diagram of the TND setup is shown in Figure 1.8.

The aligned state with the electric field on, immediately relaxes back into the twisted state when the field is turned off and is, therefore, unstable. The requirement of constant power to maintain the alignment is not desirable, and is why there is significant interest in so called bistable or multistable systems i.e., systems that have two or more stable states without any external input. By system, we mean a liquid crystal confined to a geometry and possibly subject to some boundary effects and/or external field, for example. Consequently, multistable systems only require power to switch between stable states. A commercially successful

example is the Zenithal Bistable Device [21], while experimental realisation of a planar bistable nematic device is achievable in shallow square wells filled with NLC [22]. It is worth noting, both of these bistable systems were only discovered in the mid 2000s, making multistable systems in applications a relatively new and unexploited area. It is for this reason, large parts of this thesis are devoted to the study of solution landscapes which have multiple stable states.

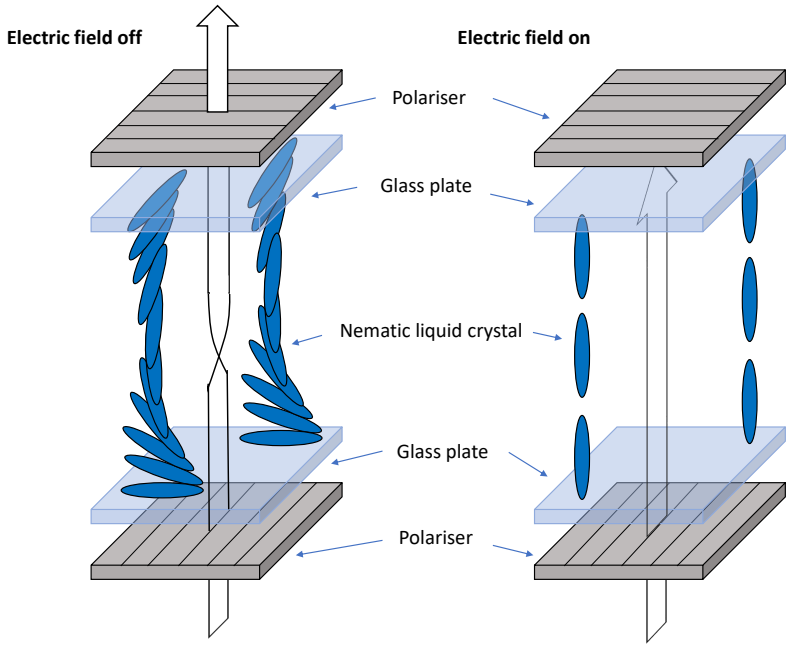

Figure 1.8: A schematic representation of a twisted nematic device.

A related, but less well-known application, is that of variable or switchable contact lenses. Such devices use liquid crystal contact lenses that can change focal power by applying a small electric field across the device [23]. These devices use the same basic principle as the twisted nematic device described previously. By using an applied electric field, the orientation of the liquid crystal molecules in the lens can be changed, which in turn changes the focal power (see Figure 1.9 (a)).

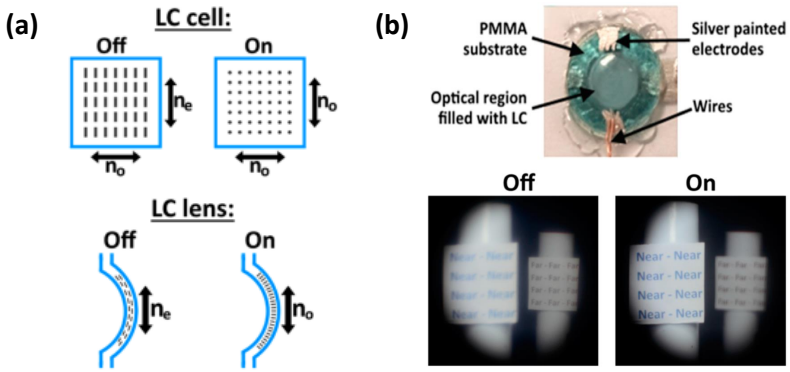

Figure 1.9: (a) A schematic representation of how different director orientations (controlled by an electric field being on or off) in a device, and a lens, effect the refractive index. (b) An example liquid crystal contact lens, and the images seen through this lens when an electric field is on or off. These images are from [23].

This means these contacts can effectively switch between different lenses and therefore, be used for both short and long distance viewing (see Figure 1.9 (b)). Everyone's ability to focus on nearby objects diminishes with age, and with an ageing population this is an issue which will only become more prominent [23]. These switchable devices, therefore, offer an effective solution to a very relevant problem in today's society.

Liquid crystals in biology

Given that liquid crystals have fluidity and order simultaneously, it may not be surprising to learn that the membrane of every cell in our bodies is in a liquid crystal phase [19]. A solid phase would be too rigid and impermeable, while an isotropic liquid would not be able to separate the cell from its surroundings [19]. A liquid crystal phase, on the other hand, provides the required structure and freedom our cells need. Even DNA forms liquid crystal phases [24]. Needless to

say, the relevance of liquid crystals in biology, and by extension, biotechnology does not end here. For example, liquid crystals have tremendous potential for use in biological sensors. Recall that the reorientation of the molecules in a liquid crystal has a dramatic impact on its optical properties, and that they are sensitive to their chemical and physical environment. Therefore, if we add a liquid crystal with a specific alignment to an aqueous phase, and a biomolecular binding event is present, the director profile may reorient altering the optical properties observed through polarised optical microscopy, hence allowing us to detect these events. This process can also be applied to the detection of bacteria and viruses [25]. Liquid crystals are also being investigated for use in drug delivery technologies [26]. Here, lyotropic liquid crystals are placed inside thin nanometer sized shells (of amphiphilic block co-polymer) which can then be heavily loaded with drugs for oral delivery. Crucially, the drugs are protected in the particle core from chemical degradation on its journey to the site of release. This protective layer also means the release rate is much slower when compared to conventional drugs, which combined with the high load capacity, make these particles interesting possibilities for cancer treatment [19]. Biological applications of liquid crystals also extend to active matter systems, which we introduce in Section 1.3.2.

Thwarting counterfeiting

One final application which is less well-known, but nonetheless interesting and extremely important, is the use of liquid crystals to spot counterfeit items. To do this, what are known as cholesteric spherical reflectors (CSRs) are used [27–30]. These are essentially shells made of cholesteric liquid crystal, which can be created by coating a drop of water in cholesteric through a clever microfluidic setup (see [27, 29] for details). These shells can be used in the prevention of

counterfeiting due to their optical properties when illuminated. In particular, CSRs reflect different wavelengths of light depending on the direction light is shined from and where it meets the shell. Combining these shells at random, which have different thicknesses, orientations and pitches of the cholesteric helix, means every arrangement is unique [27]. Hence, there is an effectively infinite set of optical responses depending on how we illuminate the CRSs. In Figure 1.10, examples of the incredibly diverse optical patterns that can be generated are shown.

The underlying principle in identifying if an item is genuine, is a "challenge" (i.e. some kind of test) and a "response" (the result of the test). Refering back to our CSRs, how we illuminate the CSRs can be used as the challenge, and the response the optical pattern we observe. So by requiring a specific optical pattern as the response, an item can be validated. This can be practically implemented by coating a given item with a layer of CSRs. This is a unique, uncloneable (even the producer cannot repeat a given arrangement), and tamper-proof label, which can be used for identification [28, 30]. Applications of CSRs do not end here though. Without going into details, CSRs can be used in supply chain track and trace, supporting autonomous robots and augmented reality [30], search and rescue [28], and even disease testing.

1.3.2 Generalisations of liquid crystals

We now describe some examples of how liquid crystals can be utilised in different physical settings. The scenarios discussed are those that we cover in this thesis.

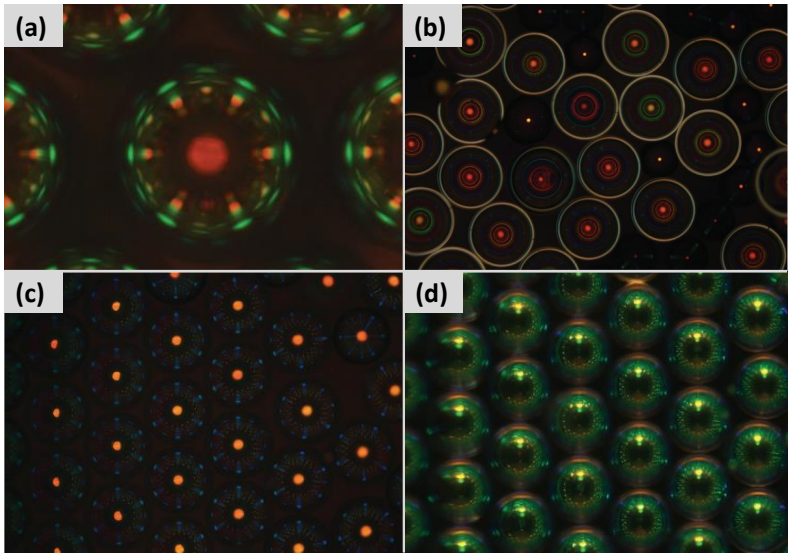

Figure 1.10: Reflection polarising microscopy images of CSRs. (a) A close up of the optical patterns generated by these shells reflecting light. (b) The thickness of the shells is always asymmetric, so by shining light through the thinnest part of the shells circular patterns can be generated. (c) and (d) highlight how changing the angle of incident light from above the shells (i.e, 90° to the plane the shells lie in) in (c), to 45° in (d), drastically changes the observed optical pattern. These images are from [28] with permission from Wiley (this article is available under the Creative Commons CC-BY-NC-ND license and permits non-commercial use of the work as published, without adaptation or alteration provided the work is fully attributed).

.

Ferronematics

Applications of NLCs typically utilise their response to external electric fields as opposed to magnetic fields, since their response to magnetic fields is much weaker (perhaps seven orders of magnitude smaller) than their dielectric response [12]. Ferronematics seek to rectify this problem, and thus extend applications of nematics to devices which exploit magnetic fields. First proposed by Brochard and de Gennes in the 1970s [31], ferronematics are a class of composite nematics with magnetic properties which can be composed of a dilute suspension of magnetic nanoparticles (MNPs) in a nematic host. Brochard and de Gennes suggested that such a colloidal suspension could induce a spontaneous magnetisation without any external magnetic fields, and substantially enhance the magnetic response of the material. The first experimental realisations of such ferronematics came quickly by Rault, Cladis and Burger [32], however, this system did not display spontaneous magnetisation in the absence of an external magnetic field. Since then, notable theoretical contributions have come from [33] and [34] , but only recently in [35], were the crucial factors for a stable ferronematic suspension with spontaneous magnetisation identified (the use of nanometre sized magnetic platelets being the key). In terms of applications, ferronematics have tremendous potential, for metamaterials, topological materials, and nano-systems [36].

Nematodynamics

Dynamic scenarios, where a NLC is able to continuously move or flow as a result of external agents, are referred to as nematodynamics. In these dynamic settings, there is an intrinsic coupling between the fluid motion and orientational order of the nematic phase. This coupling gives rise to non-Newtonian properties and stresses, as well as unusual mechanical and rheological properties [37], all of which

present new possibilities for applications. Nematodynamics are most relevant to microfluidic problems, that is, fluid flow confined to thin planar cells or channels. Applications of microfluidics and nematodynamics include optofluidic devices and guided micro-cargo transport through microfluidic networks [38, 39].

Active matter

Flow-induced deformations of nematic textures in confinement are ubiquitous, both in passive systems where the hydrodynamics are driven by external agents, and also in active matter systems. Active matter refers to systems composed of self-driven units, each capable of taking in and dissipating energy to create systemic movement [40]. The interaction of active particles with each other and with the medium they live in, gives rise to highly correlated collective motion and mechanical stress. Active particles are self-propelled and the direction of their motion can be determined by their own anisotropy, rather than an external field. Consequently, these active systems exhibit a wealth of unusual non-equilibrium properties, such as, order-disorder transitions, turbulence, and pattern formation on mesoscopic scales [41]. Examples of active systems that can exhibit liquid crystalline order include, the cytoskeleton of living cells [42] (in fact, active stresses have been found to be important in animal cell division [43]), bacterial suspensions [44], and even schools of fish and flocks of birds [41], all of which are of interest from a modelling perspective.

More on cholesterics

Due to their chirality, cholesterics display rich structural features and defects, particularly in confinement, since it is often incompatible with the twisted ground state of the cholesteric [45]. For a given geometry, with specified boundary conditions, there is a huge variety of metastable states [46], including, knotted disclin-

ation lines [47], solitons (e.g. domain walls) [48], point defect constellations [49], skyrmion lattices (i.e., two-dimensional solitons) [50], as well as complex patterns in shells [51], cylinders [52] and tori [53]. A classical example of cholesterics in confinement is a Grandjean-Cano wedge, where a lattice of dislocation lines are observed [54]. An interesting side note is that there are parallels between these defect structures in cholesterics, in particular skyrmions, and other condensed matter systems such as chiral ferromagnets, Bose–Einstein condensates and the Quantum Hall effect [52]. Cholesterics have subsequently received greater interest, in part due to the relative experimental ease with which these defects can be realised. As such, cholesterics can serve as a model system to investigate such defect structures in condensed matter systems [50]. A universal or even partially complete understanding of how and why these complex structures form, has so far proved elusive. If understood, this richness would surely have great potential for applications. In Chapter 7, we make a first attempt at such an understanding.

1.4 Mathematics and liquid crystals

Reading the first three sections of this Introduction, one may be confused as to where mathematics fits into the study of liquid crystals. Studying liquid crystals from a chemistry, physics or engineering perspective, may seem clear, but why mathematics? The strength of mathematics lies in its ability to model systems from a macroscopic scale to nano-scale (i.e., length scales visible to the eye, or visible with the use of a microscope). This is achieved by modelling liquid crystals as a continuum, that is, considering the behaviour of a system as a continuous mass, rather than focusing on the behaviour of individual particles. Mathematics then fits into the bigger picture of the study of liquid crystals in two ways: (i) experimentalists (e.g chemists, physicists, engineers) observe a

phenomena but do not fully understand why it occurs, mathematical modelling and techniques can be employed to try and understand why, (ii) mathematicians model a previously unexplored system and use mathematics to gain insight and make predictions about the behaviour of this system, this can then be used to inform experiment designs and tell experimentalists what to expect. The mathematical toolbox employed in this endeavour is almost endless, and includes but is not limited to, the calculus of variations, partial and ordinary differential equations, bifurcation analysis, dynamical system theory, topology, stochastic methods, numerical analysis, and numerical methods/algorithms. Interest in machine learning for liquid crystals is even emerging. Mathematics for liquid crystals, therefore, provides the opportunity to make a difference in real world applications, whilst also being a fantastic playground for mathematical techniques.

In this section, we introduce some of the mathematical ideas and frameworks which are tremendously powerful for modelling liquid crystal systems on a continuum scale. We focus on the modelling of NLCs here, as this provides the foundations which can then be built upon to model other liquid crystal phases/materials. The modelling of liquid crystals is a challenging mathematical question, this is in part due to the different types of behaviour we may like to capture. Unsurprisingly then, there are several different modelling approaches which have their advantages and disadvantages. To understand any of these models, we first explain the notion of a scalar order parameter.

1.4.1 The director and scalar order parameter

There are two basic ingredients which describe a liquid crystal: (i) a director, and (ii) a scalar order parameter. We have already introduced the director $\mathbf{n}$, a unit vector which describes the preferred direction of average molecular orientation.

As such, we can consider $\mathbf{n} \in \mathbb{S}^2$, where $\mathbb{S}^2$ is the unit sphere. Furthermore, this director can vary in both space and time i.e. $\mathbf{n}(\mathbf{x}, t)$ at a point in space $\mathbf{x}$, at time t. We then use a *scalar order parameter* (denoted by s) to measure the amount of orientational order about the director. This can be defined as a weighted average of the angles θ_m between the long axis of the molecules and the director

$$s = \frac{1}{2} \int_{\mathcal{B}} \left(3\cos^2 \theta_m - 1\right) f(\theta_m) \, \mathrm{d}A, \tag{1.4.1}$$

where $f(\theta_m)$ is the probability density function governing the probability of finding a molecule with angle θ_m, at a point $\mathbf{x}$, in some ball $\mathcal{B}$ [11]. There are three stand out values for the scalar order parameter. First, when $\theta_m = 0$, so that molecules align perfectly with the director and $s = 1$ (since $\int_{\mathcal{B}} f(\theta_m) \, \mathrm{d}A = 1$). Conversely, in an isotropic phase when particles are orientated randomly and consequently resemble a uniform distribution, $f(\theta_m)$ must be a constant, in fact $f(\theta_m) = \frac{1}{4\pi}$. Integrating (1.4.1) in this case, we find $s = 0$. Finally, when molecules are perpendicular to the director ($\theta_m = \frac{\pi}{2}$) we find $s = -\frac{1}{2}$. Most liquid crystals exhibit an order parameter in the range $0.3 < s < 0.8$ [55], making a negative order parameter as hypothetical as a perfectly ordered state. However, recently in [55], a liquid crystal with a negative order parameter was experimentally realised in the form of elastomeric shells (in non-technical terms, these are in essence liquid crystal balloons). The molecules all lie in the plane of the shell, but within that plane they are disordered and this gives rise to the negative order parameter.

1.4.2 Continuum theories

With the director and scalar order parameter defined, we thus begin to discuss models for NLCs. The three main continuum theories utilised are, the Oseen-Frank theory, the Ericksen theory, and the Landau-de Gennes theory (LdG).

These theories can be identified by the types of behaviour they can model.

The Oseen-Frank theory introduced by Oseen [56], and later developed by Frank [57], is the simplest of the three which models the director, at every point in space as a unit vector field, but assumes a fixed scalar order parameter. This means it can only account for uniaxial phases and limits its ability to capture defects where the director is discontinuous [17]. For an uniaxial nematic liquid crystal, confined to some domain Ω (Ω can be a one-, two-, or three-dimensional domain), the Oseen-Frank energy is

$$F_{OF}(\mathbf{n}) = \int_\Omega K_{11}(\nabla \cdot \mathbf{n})^2 + K_{22}(\mathbf{n} \cdot \nabla \times \mathbf{n})^2 + K_{33}(\mathbf{n} \times \nabla \times \mathbf{n})^2 + (K_{22} + K_{24})\nabla \cdot [(\mathbf{n} \cdot \nabla)\mathbf{n} - (\nabla \cdot \mathbf{n}))\mathbf{n}] \ \mathrm{d}\Omega, \quad (1.4.2)$$

where K_{11}, K_{22}, K_{33} and K_{24} are the Frank elastic constants. The terms with coefficients K_{11}, K_{22} and K_{33}, represent what are known as *splay*, *twist* and *bend* deformations respectively (see Figure 1.11 for a depiction of each) [12]. The term with coefficient $K_{22}+K_{24}$, is termed the saddle splay term and can be expressed as a surface integral using the divergence theorem, while in one-dimension this term is identically zero. These elastic constants can be of the same order of magnitude, so it is not uncommon to use what is called a one-constant approximation and take $K_{11} = K_{22} = K_{33}$, and $K_{24} = 0$ [12].

The Ericksen continuum theory introduced by Jerald Ericksen [58], is more general than the Oseen-Frank theory. As well as having a director $\mathbf{n}$ (modelled as a unit vector), it allows for a variable scalar order parameter s, meaning it can capture defects, but it is still limited to uniaxial nematics. Defects are captured by letting s vanish in regions where the director can no longer be defined, this effectively regularises these problematic regions, and defects are consequently modelled as

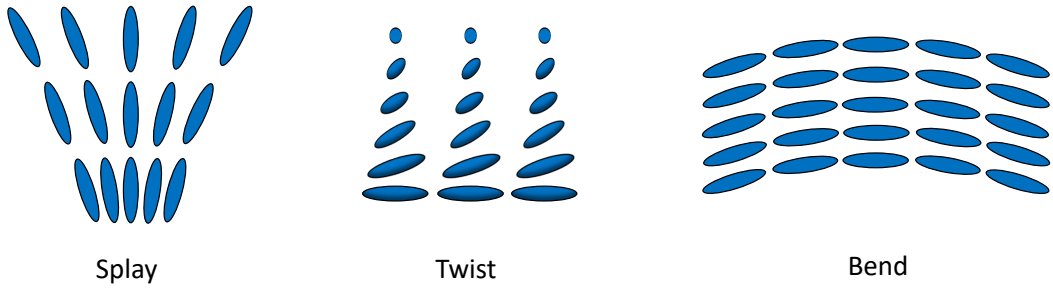

Figure 1.11: A schematic representation of the splay, twist, and bend deformations.

locally isotropic regions (although no change in temperature is involved) [17]. Using the one-constant approximation, the simplest form of the Ericksen energy is

$$F_E(s, \mathbf{n}) = \int_\Omega K_E |\nabla s|^2 + s^2 |\nabla \mathbf{n}|^2 + W(s) \, \mathrm{d}\Omega, \tag{1.4.3}$$

where K_E is an elastic constant and $W(s)$ is a temperature dependent or thermotropic bulk potential (we elaborate on such a potential in Section 1.5.2).

The LdG theory, is the most general of the three since it can capture both uniaxiality and biaxiality, as well as defects. It is for these reasons that we work with the LdG theory in this thesis, which we explain in detail in the next section.

1.5 The Landau-de Gennes theory

1.5.1 The Q-tensor

In the LdG framework, all the information about the state of a liquid crystal is captured by a symmetric traceless 3×3 matrix $\mathbf{Q}$ (equivalently called the

Q-tensor, or **Q**-tensor order parameter) [14]. Specifically,

$$\mathbf{Q} = \begin{pmatrix} Q_{11} & Q_{12} & Q_{13} \\ Q_{12} & Q_{22} & Q_{23} \\ Q_{13} & Q_{23} & -Q_{11} - Q_{22} \end{pmatrix}. \tag{1.5.1}$$

Hence, we say $\mathbf{Q} \in S_0 := \{\mathbf{Q} \in \mathbb{M}^{3\times 3} : Q_{ij} = Q_{ji}, Q_{ii} = 0\}$ (where $\mathbb{M}^{3\times 3}$ denotes the space of all 3×3 matrices).

Following the description in [13, 59], we outline where such an order parameter comes from. Similar to Section 1.4.1, we start by defining a probability density function $\rho(\mathbf{x}, \mathbf{p})$, which gives the probability that a molecule in $\mathcal{B}(\mathbf{x}, \delta)$ (i.e., a ball radius $\delta > 0$, centre $\mathbf{x}$) has orientation $\mathbf{p} \in \mathbb{S}^2$. Here, $\mathbf{p}$ models the long axis of the molecule and we consider $\mathbf{p}$ and $-\mathbf{p}$ to be equivalent, hence $\rho(\mathbf{x}, \mathbf{p}) = \rho(\mathbf{x}, -\mathbf{p})$. Furthermore, since ρ is a probability density function, it must satisfy

$$\rho(\mathbf{x}, \mathbf{p}) \geq 0, \text{ and } \int_{\mathbb{S}^2} \rho(\mathbf{x}, \mathbf{p}) \, \mathrm{d}\mathbf{p} = 1. \tag{1.5.2}$$

Here $\mathrm{d}\mathbf{p}$ denotes the area element on $\mathbb{S}^2$. Looking at the moments of ρ, we see

$$\int_{\mathbb{S}^2} \mathbf{p}\, \rho(\mathbf{x}, \mathbf{p}) \, \mathrm{d}\mathbf{p} = -\int_{\mathbb{S}^2} \mathbf{p}\, \rho(\mathbf{x}, -\mathbf{p}) \, \mathrm{d}\mathbf{p} = 0, \tag{1.5.3}$$

i.e., the first moment is zero, while the second moment is

$$\mathbf{M}(\mathbf{x}) = \int_{\mathbb{S}^2} \mathbf{p} \otimes \mathbf{p}\, \rho(\mathbf{x}, \mathbf{p}) \, \mathrm{d}\mathbf{p}. \tag{1.5.4}$$

Note, $\mathbf{p} \otimes \mathbf{p}$ is a matrix defined by the vector tensor product $(\mathbf{p} \otimes \mathbf{p})_{ij} = p_i p_j$ for $i, j = 1, 2, 3$. If we consider an isotropic arrangement of particles, ρ must be a constant and therefore, $\rho = \frac{1}{4\pi}$. Since $\mathbf{p} \in \mathbb{S}^2$ can be written as $\mathbf{p} = (\sin\theta\cos\phi, \sin\theta\sin\phi, \cos\theta)$, we see $\mathbf{M}(\mathbf{x}) = \frac{1}{3}\mathbf{I}_3$ (where $\mathbf{I}_3$ is the 3×3 identity

matrix) in the isotropic case. The **Q**-tensor is then defined as

$$\mathbf{Q}(\mathbf{x}) = \mathbf{M}(\mathbf{x}) - \frac{1}{3}\mathbf{I}_3, \tag{1.5.5}$$

so that it measures the deviation of $\mathbf{M}(\mathbf{x})$ from its isotropic value. Clearly $\mathbf{Q} = \mathbf{Q}^T$ and tr$\mathbf{Q} = 0$.

Q has five degrees of freedom, and this is sufficient to capture biaxiality, as we now explain. First, recall a biaxial liquid crystal has two directors, hence, we require two scalar order parameters to describe the associated orientational order. Since **Q** is a symmetric 3×3 matrix, it has an orthonormal set of eigenvectors, furthermore, **Q** can be expressed in terms of these eigenvectors $\mathbf{n}_i$ and associated eigenvalues λ_i (by the spectral decomposition theorem) as

$$\mathbf{Q} = \lambda_1 \mathbf{n}_1 \otimes \mathbf{n}_1 + \lambda_2 \mathbf{n}_2 \otimes \mathbf{n}_2 + \lambda_3 \mathbf{n}_3 \otimes \mathbf{n}_3. \tag{1.5.6}$$

Similarly, $\mathbf{I}_3$ can be expressed as $\mathbf{I}_3 = \sum_{i=1}^{3} \mathbf{n_i} \otimes \mathbf{n}_i$. Combining this with the constraint $\lambda_1 + \lambda_2 + \lambda_3 = 0$ (since **Q** is traceless), we see

$$\mathbf{Q} = (2\lambda_1 + \lambda_2)(\mathbf{n}_1 \otimes \mathbf{n}_1) + (2\lambda_2 + \lambda_1)(\mathbf{n}_2 \otimes \mathbf{n}_2) - (\lambda_1 + \lambda_2)\mathbf{I}_3.$$

Hence, setting

$$s = \lambda_1 - \lambda_3 = 2\lambda_1 + \lambda_2, \tag{1.5.7a}$$

$$r = \lambda_2 - \lambda_3 = \lambda_1 + 2\lambda_2, \tag{1.5.7b}$$

we have

$$\mathbf{Q} = s\left(\mathbf{n}_1 \otimes \mathbf{n}_1 - \frac{1}{3}\mathbf{I}_3\right) + r\left(\mathbf{n}_2 \otimes \mathbf{n}_2 - \frac{1}{3}\mathbf{I}_3\right). \tag{1.5.8}$$

The **Q**-tensor in (1.5.8) is *biaxial* and it describes a biaxial state since we have two order parameters, s and r, associated to the directors $\mathbf{n}_1$ and $\mathbf{n}_2$ (which are eigenvectors of **Q**), respectively. From (1.5.7), a biaxial state corresponds to **Q**

having three distinct eigenvalues. If we have a pair of equal non-zero eigenvalues, $\mathbf{Q}$ is *uniaxial*. For example, if $\lambda_2 = \lambda_3$, $\mathbf{Q}$ can be written as

$$\mathbf{Q} = s\left(\mathbf{n}_1 \otimes \mathbf{n}_1 - \frac{1}{3}\mathbf{I}_3\right) \tag{1.5.9}$$

(analogous forms follows if $\lambda_1 = \lambda_3$ or $\lambda_1 = \lambda_2$). Such a $\mathbf{Q}$-tensor is uniaxial, since we have one director $\mathbf{n}_1$, an eigenvector corresponding to a non-degenerate eigenvalue, and one order parameter s. Finally, if all three eigenvalues are equal, so that $s = r = 0$, $\mathbf{Q} = \mathbf{0}$ and is therefore *isotropic* [60].

Remark 1.5.1.

1. Similar to the Ericksen theory, defects can be captured by the order parameter $\mathbf{Q}$ vanishing in regions where the director can no longer be defined i.e., $\mathbf{Q} = \mathbf{0}$, so that the region is isotropic. Defects can also be discontinuities in the eigenvectors, or regions where the number of distinct eigenvalues change.
2. Changing the sign of an eigenvector in (1.5.8) and (1.5.9), does not change $\mathbf{Q}$. As such, the physical equivalence of $\mathbf{n}_i$ and $-\mathbf{n}_i$ is captured. We therefore regard the director as a line field when extracted from the $\mathbf{Q}$-tensor in this thesis.

1.5.2 Modelling a liquid crystal system

The $\mathbf{Q}$-tensor order parameter is the main ingredient of the LdG continuum theory. In static situations, to describe a liquid crystal system it is necessary to define a total free energy (as seen in Section 1.4.2), which captures the energetic behaviour of that system. There are two key components to any such free energy, an elastic energy density f_e, which penalises spatial inhomogenaities or material distortions, and a bulk energy density f_b, which accounts for bulk effects arising from the liquid crystal material. Considering a liquid crystal sample contained in a domain

Ω, the total free energy is

$$F_{LG}[\mathbf{Q}] = \int_{\Omega} f_e(\mathbf{Q}) + f_b(\mathbf{Q}) \, \mathrm{d}\Omega. \tag{1.5.10}$$

These two contributions are sufficient for the problems considered in this thesis. However, additional effects due to external electric fields, external magnetic fields, or surface energies at the boundary $\partial\Omega$, can be incorporated [11].

The thermotropic bulk energy

The thermotropic bulk potential f_b, is a function of $\mathbf{Q}$ which determines the state the liquid crystal would prefer to be in, the choices being, the isotropic, uniaxial, or biaxial state. Intuitively, at high temperatures, f_b should be minimised by an isotropic state ($\mathbf{Q} = \mathbf{0}$), while at low temperatures, it should be minimised by a uniaxial or biaxial state. Isotropic and uniaxial states can be accounted for with the following standard fourth order bulk energy density [11, 61] (see Section 2.1.1 for an explanation as to why):

$$f_b(\mathbf{Q}) = \frac{A}{2}\mathrm{tr}\mathbf{Q}^2 - \frac{B}{3}\mathrm{tr}\mathbf{Q}^3 + \frac{C}{4}(\mathrm{tr}\mathbf{Q}^2)^2, \quad \text{where} \tag{1.5.11a}$$

$$\mathrm{tr}\mathbf{Q}^2 = Q_{ij}Q_{ij} = |\mathbf{Q}|^2, \text{ and } \mathrm{tr}\mathbf{Q}^3 = \mathbf{Q}_{\alpha\beta}\mathbf{Q}_{\beta\gamma}\mathbf{Q}_{\gamma\alpha}. \tag{1.5.11b}$$

Here, $B, C > 0$ are material dependent bulk constants independent of temperature, while A depends linearly on temperature and is given by

$$A = \alpha(T - T^*),$$

where $\alpha > 0$ is a material dependent constant, T is the absolute temperature of the system, and T^* is a characteristic liquid crystal temperature [14, 60]. In (1.5.11b), the Einstein summation convention is used, and Q_{ij} denotes the i, j^{th} component of $\mathbf{Q}$. We work with the bulk potential (1.5.11a) in this thesis, which can account

for first-order nematic-isotropic phase transitions. For an understanding of where (1.5.11a) comes from, we refer the reader to section 4.2 of [13]. Some background results/properties concerning f_b are discussed in Section 2.1.1.

The elastic energy

It would be energetically favourable for $\mathbf{Q}$ to be spatially constant, so to penalise material distortions, any elastic energy density should depend on the spatial derivatives of $\mathbf{Q}$. Using the Einstein summation convention, the most general elastic energy density can be written as,

$$f_e(\mathbf{Q}) = \frac{L_1}{2}Q_{ij,k}Q_{ij,k} + \frac{L_2}{2}Q_{ij,j}Q_{ik,k} + \frac{L_3}{2}Q_{ik,j}Q_{ij,k} + \frac{L_4}{2}\epsilon_{ijk}Q_{il}Q_{jl,k} + \frac{L_5}{2}Q_{lk}Q_{ij,l}Q_{ij,k}, \quad (1.5.12)$$

where $Q_{ij,k} = \frac{\partial Q_{ij}}{\partial x_k}$, $\epsilon_{i,j,k}$ is the Levi-Civita symbol, and $i, j, k = 1, 2, 3$ [62]. Here, the L_i are elastic constants which depend on the liquid crystal material and can be related to the Frank elastic constants as in [11]. A first simplification of the energy density (1.5.12), is

$$f_e(\mathbf{Q}) = \frac{L_1}{2}|\nabla\mathbf{Q}|^2 + \frac{L_2}{2}(\nabla\cdot\mathbf{Q})^2, \quad (1.5.13)$$

where the first term is an isotropic contribution, while the second term accounts for anisotropy (see [63] for a study with this elastic energy density). For a nematic liquid crystal, it is common to use a one constant approximation [64–66], which in the LdG formalism, means taking $L_1 = K$ and $L_i = 0$, for $i = 2, \ldots, 5$. In the one constant approximation then, the energy density (1.5.12) reduces significantly to

$$f_e(\mathbf{Q}) = \frac{K}{2}|\nabla\mathbf{Q}|^2, \quad (1.5.14)$$

i.e., the familiar Dirichlet energy density. In (1.5.13) and (1.5.14), we have used the matrix norm in (1.5.11b). We use the one constant approximation in every chapter except Chapter 7, where we model cholesteric liquid crystals. As mentioned previously, cholesterics are chiral, and to account for this we must include the term corresponding to L_4 in (1.5.12).

Boundary conditions

Since we consider liquid crystals in confinement, we need to specify the director properties on the domain boundaries. This is done by imposing boundary conditions on $\mathbf{Q}$, of which there are two types, strong and weak anchoring. Strong, or infinite anchoring, is implemented by imposing Dirichlet boundary conditions

$$\mathbf{Q} = \mathbf{Q}_b, \text{ on } \partial\Omega. \tag{1.5.15}$$

Considering a square geometry for example, where $\partial\Omega$ is the edges of the square, if the imposed boundary conditions are the same on all sides, we label these as *homogeneous* boundary conditions. If our boundary conditions are not the same on all four sides and therefore conflicting, we call them *inhomogeneous*. If our boundary condition is such that the director is normal or orthogonal to the side of the square, we call these *homeotropic* boundary conditions [17]. Conversely, if the director is required to align parallel to the side of the square, this is labelled as *planar* boundary conditions [11]. Strong anchoring is appropriate for modelling situations where the boundaries of a geometry have been treated to strongly favour a certain direction of molecular alignment.

Weak anchoring is more physically realistic than infinite anchoring, and is suitable for situations where the orientation of the director at the boundary is less strongly prescribed. This is imposed by a surface energy, which enforces a preferred director

profile by penalising deviations from this preferred direction. For example, the most appropriate surface energy is the Rapini-Popoular or Durand-Nobili surface anchoring energy. The latter can be expressed as follows [67]

$$\int_{\partial\Omega} W \mathrm{tr}(\mathbf{Q}-\mathbf{Q}_b)^2 \, \mathrm{d}A. \tag{1.5.16}$$

Here, W is the anchoring strength (which can take different values along the boundary) and $\mathbf{Q}_b$ is the preferred value of the $\mathbf{Q}$-tensor on the boundary. This surface energy is particularly useful since in the $W \to \infty$ limit, weak anchoring solutions converge to the strong anchoring solutions [68].

The variational approach

With a free energy and boundary conditions in hand, the final ingredient is an appropriate admissible space. We can then derive the Euler-Lagrange equations associated with our free energy and solve them subject to appropriately defined boundary conditions, within our admissible space. Solutions of the Euler-Lagrange equations are critical points of the free energy and describe the equilibrium configurations of the liquid crystal system being considered. In general, the physically observable equilibria are modelled as local or global minimisers of our free energy. We follow this approach throughout much of this thesis, so to make these ideas clear, we consider a standard example in Section 2.1.3.

1.6 Thesis outline

This thesis is organised as follows:

- In Chapter 2, we review relevant mathematical results and concepts required to study the problems in this thesis.
- In Chapter 3, we consider NLCs in a channel geometry. The focus of our

study is on investigating the connection between the imposed Dirichlet boundary conditions on the nematic director and properties of solutions, which we address by employing a **Q**- and associated (s, θ)-formulation (s being the scalar order parameter and θ the director angle). In particular, we study the compatibility of OR solutions with these boundary conditions and show we have a unique solution in the (s, θ)-framework, for all boundary conditions that do not permit OR solutions. We then study the limit of small channel widths, where we can explicitly compute solutions and verify our results surrounding OR solutions. Finally, we conduct numerical experiments to support our theoretical results.

- In Chapter 4, we study OR solutions in the Beris-Edwards framework for nematodynamics, for both passive and active nematic flows in a channel. We show that OR solutions exist for passive flows with constant velocity and pressure, and the results from Chapter 3 can be applied to this case. With this insight, we then compute asymptotic expansions for OR-type solutions for (i) passive flows with non-constant velocity and pressure, and (ii) active flows, which shed light into the internal structure of domain walls. The asymptotics are complemented by extensive numerical studies that demonstrate the ubiquity of OR-type structures in these scenarios.

- In Chapter 5, we study a model system for ferronematics with nematic and magnetic order (first proposed in [69, 70]), within a channel geometry. The system is characterised by a tensor-valued nematic order parameter **Q** and a vector-valued magnetisation **M**, and the observable states are modelled as stable critical points of an appropriately defined free energy which includes a nemato-magnetic coupling term, characterised by a parameter c. We (i) derive L_∞ bounds for **Q** and **M**; (ii) prove a uniqueness result in specified

parameter regimes; (iii) analyse order reconstruction solutions, possessing domain walls, and their stabilities as a function of channel width and c; and (iv) supplement these analytical results with supporting numerics.

- In Chapter 6, we build upon the initial numerical study in Chapter 5, by employing the high-index optimisation-based shrinking dimer method (HiOSD) [71], to explore solution landscapes for the ferronematic problem considered. Solution landscapes show how all critical points (stable and unstable) connect to one another, and hence, show us possible pathways for switching between stable states in multistable systems. Therefore, the insight gained here is potentially relevant for the creation of switchable ferronematic devices. We pay particular attention to OR solutions and identify their importance to the solution landscapes considered.

- In Chapter 7, we turn our attention away from the reduced modelling approach and OR solutions, and consider a one-dimensional model for cholesteric liquid crystals which utilises all five degrees of freedom of the $\mathbf{Q}$-tensor. We begin by performing asymptotic analysis for a standard model for cholesteric liquid crystals. Using this limiting insight, and the HiOSD method, we probe the solution landscape for this cholesteric system where we identify a competition between uniaxial and biaxial pathways, between different stable states. Cholesterics exhibit great morphological richness of static metastable states and understanding the transitions between such states is key for the development of switchable devices.

- In Chapter 8, a summary of the main themes in this thesis is presented, as well as some questions to address in future work.

Chapter 2

Literature review

2.1 Background results

2.1.1 Homogeneous solutions

We begin by looking at critical points of the bulk energy f_b, which are solutions of a homogeneous, or spatially constant problem in the absence of boundary conditions. Such solutions can be crucial in understanding the behaviour of the full inhomogenoeous problem, as we shall see in Chapter 5. We first reproduce a well known result following the proof in [60].

Proposition 2.1.1. *The critical points of the bulk energy density, f_b in* (1.5.11a)*, are given by either isotropic or uniaxial* $\mathbf{Q}$*-tensors of the form*

$$\mathbf{Q} = s\left(\mathbf{n}\otimes\mathbf{n} - \frac{1}{3}\mathbf{I}_3\right), \tag{2.1.1}$$

where s is a scalar order parameter and $\boldsymbol{n}$ is one of the eigenvectors of $\mathbf{Q}$*.*

Proof. Recall, $\mathbf{Q}$ can be written as

$$\mathbf{Q} = \lambda_1 \mathbf{n}_1 \otimes \mathbf{n}_1 + \lambda_2 \mathbf{n}_2 \otimes \mathbf{n}_2 + \lambda_3 \mathbf{n}_3 \otimes \mathbf{n}_3,$$

where $\{\mathbf{n}_1, \mathbf{n}_2, \mathbf{n}_3\}$ are orthonormal eigenvectors with corresponding eigenvalues $\{\lambda_1, \lambda_2, \lambda_3\}$. As a consequence of the orthogonality, powers of the matrix $\mathbf{Q}$ are of the form $\mathbf{Q}^n = \sum_{i=1}^3 \lambda_i^n (\mathbf{n}_i \otimes \mathbf{n}_i)^n$, so that $\mathrm{tr}\mathbf{Q}^n = \sum_{i=1}^3 \lambda_i^n$. From this, we see the bulk energy density depends only on the eigenvalues of $\mathbf{Q}$. As a result, the stationary points of f_b, are given by the stationary points of the function $f : \mathbb{R}^3 \to \mathbb{R}$ defined by

$$f(\lambda_1, \lambda_2, \lambda_3) = \frac{A}{2} \sum_{i=1}^3 \lambda_i^2 - \frac{B}{3} \sum_{i=1}^3 \lambda_i^3 + \frac{C}{4} \left(\sum_{i=1}^3 \lambda_i^2 \right)^2 - 2\delta \sum_{i=1}^3 \lambda_i, \tag{2.1.2}$$

where we have introduced a Lagrangian multiplier δ, in the last term to account for the tracelessness of $\mathbf{Q}$. Differentiating (2.1.2) with respect to each of the eigenvalues, and setting the result equal to zero, yields the following system of equations

$$\frac{\partial f}{\partial \lambda_i} = 0 \iff A\lambda_i - B\lambda_i^2 + C \left(\sum_{k=1}^2 \lambda_k^2 \right) \lambda_i = 2\delta, \quad \text{for} \quad i = 1, 2, 3. \tag{2.1.3}$$

Taking the difference of any two of the equations in (2.1.3) means we can rewrite the system as

$$(\lambda_i - \lambda_j) \left[A - B(\lambda_i + \lambda_j) + C \sum_{k=1}^3 \lambda_k^2 \right] = 0, \quad 1 \leqslant i < j \leqslant 3. \tag{2.1.4}$$

Now, let $\{\lambda_i\}$ be a solution of the system (2.1.3) with three distinct eigenvalues. Considering (2.1.4) for the pairs (λ_1, λ_2) and (λ_1, λ_3), produces the equations

$$A - B(\lambda_1 + \lambda_2) + C \sum_{k=1}^3 \lambda_k^2 = 0, \tag{2.1.5}$$

$$A - B(\lambda_1 + \lambda_3) + C \sum_{k=1}^3 \lambda_k^2 = 0. \tag{2.1.6}$$

Subtracting the two equations above yields

$$-B(\lambda_2 - \lambda_3) = 0, \tag{2.1.7}$$

which contradicts the hypothesis that $\lambda_2 \neq \lambda_3$. We therefore conclude that a stationary point of f_b must have at least two equal eigenvalues, corresponding to either an uniaxial, or isotropic state. Returning to (1.5.7), we see that one of s or r must be zero, or $s = r$, giving the form (2.1.1) for $\mathbf{Q}$. □

As a result of Proposition 2.1.1, it suffices to consider uniaxial $\mathbf{Q}$-tensors of the form (2.1.1) when computing the critical points of f_b. Calculating $\mathrm{tr}\mathbf{Q}^2$ and $\mathrm{tr}\mathbf{Q}^3$ for such a $\mathbf{Q}$, we find

$$f_b(s) = \frac{A}{3}s^2 - \frac{2B}{27}s^3 + \frac{C}{9}s^4. \tag{2.1.8}$$

The stationary points are the roots of the following equation

$$\frac{\mathrm{d}f_b}{\mathrm{d}s} = \frac{2}{9}s(3A - Bs + 2Cs^2) = 0, \tag{2.1.9}$$

which yields three critical points

$$s = 0, \quad \text{and} \quad s_\pm = \frac{B \pm \sqrt{B^2 - 24AC}}{4C}. \tag{2.1.10}$$

We see $f_b(0) = 0$, and

$$f_b(s_\pm) = \frac{s_\pm^2}{54}(9A - Bs_\pm),$$

so that $f_B(s_-) > f_B(s_+)$. Hence, the global bulk energy minimiser is either the isotropic state $\mathbf{Q} = \mathbf{0}$ corresponding to $s = 0$, or the ordered nematic state

$$\mathbf{Q} = s_+ \left(\mathbf{n} \otimes \mathbf{n} - \frac{1}{3}\mathbf{I}_3\right),$$

where $\mathbf{n}$ is the eigenvector with a non-degenerate eigenvalue. The stability of these

critical points can be further checked by computing $\frac{\mathrm{d}^2 f_b}{\mathrm{d}s^2}$ (see [11, 60] for details). It follows that for our purposes, it is sufficient to work with low temperatures below T^*, so that $A < 0$, and the uniaxial nematic state with $s = s_+$, is globally stable.

2.1.2 Biaxiality

From the discussion in the previous subsection, we see critical points of (1.5.10) with biaxiality, are a result of the elastic energy density f_e, and its competition with f_b. Biaxiality is often found in the vicinity of defects, as we shall see in Chapter 7. In fact, we can measure biaxiality with what is called the biaxiality parameter β. For $\mathbf{Q} \in S_0 \setminus \{\mathbf{0}\}$, β is defined as [65, 72]

$$\beta = 1 - 6\frac{(\mathrm{tr}\mathbf{Q}^3)^2}{(\mathrm{tr}\mathbf{Q}^2)^3}. \tag{2.1.11}$$

From Lemma 1 in [65], it is known that $\beta \in [0, 1]$, $\beta = 0$ corresponds to a uniaxial $\mathbf{Q}$-tensor, and any non-zero value of β means $\mathbf{Q}$ is biaxial. When $\beta = 1$, our $\mathbf{Q}$-tensor is labelled as maximally biaxial and a quick calculations shows this occurs if and only if one of the eigenvalues of $\mathbf{Q}$ is zero, so that the two remaining eigenvalues are equal in magnitude and opposite in sign. Furthermore, the following inequality holds,

$$\frac{-|\mathbf{Q}|^3}{\sqrt{6}}\left(1 - \frac{\beta}{2}\right) \leqslant \mathrm{tr}\mathbf{Q}^3 \leqslant \frac{|\mathbf{Q}|^3}{\sqrt{6}}\left(1 - \frac{\beta}{2}\right). \tag{2.1.12}$$

2.1.3 Existence and properties of solutions

We now return to our variational approach outlined in Section 1.5.2, for finding equilibrium configurations of a liquid crystal system. Combining the elastic energy density (1.5.14) and the bulk energy density (1.5.11a), our total free energy for

a NLC in the absence of surface effects, on a domain Ω (Ω can be one-, two or three-dimensional), is

$$F_{LG}(\mathbf{Q}) = \int_\Omega \frac{K}{2}|\nabla \mathbf{Q}|^2 + \frac{A}{2}\mathrm{tr}\mathbf{Q}^2 - \frac{B}{3}\mathrm{tr}\mathbf{Q}^3 + \frac{C}{4}(\mathrm{tr}\mathbf{Q}^2)^2 \, \mathrm{d}\Omega. \tag{2.1.13}$$

Following [22, 68, 73], we enforce uniaxial Dirichlet boundary conditions,

$$\mathbf{Q} = \mathbf{Q}_b := s_+ \left(\mathbf{n}_b \otimes \mathbf{n}_b - \frac{1}{3}\mathbf{I}_3 \right) \text{ on } \partial\Omega, \tag{2.1.14}$$

where $\mathbf{n}_b \in C^\infty(\mathbb{S}^2)$, and s_+ is the global minimiser of the bulk potential at low temperatures, discussed in Section 2.1.1. Moving onto our admissible space, we require critical points of (2.1.13) to belong to

$$\mathcal{A}_n := \{\mathbf{Q} \in W^{1,2}(\Omega; S_0) : \mathbf{Q} = \mathbf{Q}_b \text{ on } \partial\Omega\}. \tag{2.1.15}$$

Here, $W^{1,2}$ denotes the Sobolev space of square-integrable $\mathbf{Q}$-tensors with square-integrable first derivatives, which is a common choice for many variational problems. More precisely,

$$W^{1,2}(\Omega; S_0) = \left\{ \mathbf{Q} \in S_0 : \int_\Omega |\mathbf{Q}|^2 + |\nabla \mathbf{Q}|^2 \, \mathrm{d}\Omega < \infty \right\}. \tag{2.1.16}$$

The first question we would like to answer, is whether there exists a minimiser of the energy (2.1.13), in the admissible space $\mathcal{A}_n$. This can be done by an application of the direct method in the calculus of variations [74]. There are three components to this process: (i) we require our admissible space to be non-empty, (ii) are energy must be weakly lower semi-continuous, that is,

$$\lim_{n\to\infty} F_{LG}(\mathbf{Q}_n) \geq F_{LG}(\mathbf{Q}), \tag{2.1.17}$$

whenever $\mathbf{Q}_n \rightharpoonup \mathbf{Q}$ weakly in $W^{1,2}$, and (iii) are energy must be coercive i.e.,

$$\frac{K}{2}|\nabla \mathbf{Q}|^2 + \frac{A}{2}\mathrm{tr}\mathbf{Q}^2 - \frac{B}{3}\mathrm{tr}\mathbf{Q}^3 + \frac{C}{4}(\mathrm{tr}\mathbf{Q}^2)^2 \geq \gamma_1|\nabla \mathbf{Q}|^2 + \gamma_2 \tag{2.1.18}$$

$$\implies F_{LG}(\mathbf{Q}) \geq \gamma_3 ||\nabla \mathbf{Q}||_{L^2(\Omega)} + \gamma_4 \text{ for } \gamma_1, \gamma_3 > 0 \text{ and } \gamma_2, \gamma_4 \in \mathbb{R}, \quad (2.1.19)$$

for all $\mathbf{Q} \in \mathcal{A}_n$, ensuring that our energy is bounded from below and $F_{LG}(\mathbf{Q}) \to \infty$ as $||\nabla \mathbf{Q}||_{L^2(\Omega)} \to \infty$. Our boundary condition belongs to our admissible space (since it is smooth and bounded) ensuring it is non-empty. The energy (2.1.13) is quadratic and thus convex in the gradient of $\mathbf{Q}$, hence by [74] (Chapter 8, Theorem 1), it is weakly lower semi-continuous. To satisfy the definition of coercivity, we only need f_b to be bounded from below, but this is immediate since the bulk potential f_b is a quartic polynomial in $|\mathbf{Q}|$, which has well defined minima. Hence, there exists at least one minimiser of (2.1.13), in the admissible space $\mathcal{A}_n$.

This minimiser, and in fact any critical point of (2.1.13), is a solution of the associated Euler-Lagrange equations

$$K \triangle Q_{ij} = AQ_{ij} - B\left(Q_{ip}Q_{pj} - \frac{1}{3}\text{tr}\mathbf{Q}^2\delta_{ij}\right) + C(\text{tr}\mathbf{Q}^2)Q_{ij} \quad i,j = 1,2,3. \quad (2.1.20)$$

This is established using arguments in elliptic regularity. For example, in Proposition 13 of [65], such arguments are used to prove any solution of the system (2.1.20) is (real) analytic in Ω, giving us the required smoothness for our next proposition.

The maximum principle

Another useful tool when studying a liquid crystal problem, which we will call upon multiple times in this thesis, is a L^∞ bound for the norm of critical points of the LdG free energy. Such bounds can be obtained by a maximum principle argument. We now present the well known bounds for a conventional nematic as derived in [60, 65].

Proposition 2.1.2. *Let $\Omega \subset \mathbb{R}^3$ be a bounded and simply-connected open set with*

smooth boundary. Let $\mathbf{Q}$ *be a global minimiser of the energy* (2.1.13)*, in the space* $\mathcal{A}_n$*, then*

$$||\mathbf{Q}||_{L^\infty(\Omega)} = \operatorname*{ess\ sup}_{\mathbf{x}\in\Omega} |\mathbf{Q}(\mathbf{x})| \leqslant \sqrt{\frac{2}{3}} s_+, \tag{2.1.21}$$

where s_+ *is defined in* (2.1.10)*.*

Proof. We prove the statement by contradiction. Assume that there exists a point $\mathbf{x}^* \in \bar{\Omega}$, where $|\mathbf{Q}|$ attains its maximum and this is such that $|\mathbf{Q}(\mathbf{x}^*)| > \sqrt{\frac{2}{3}} s_+$. On $\partial\Omega$, $|\mathbf{Q}| = \sqrt{\frac{2}{3}} s_+$ (due to our boundary condition (2.1.14)), so $\mathbf{x}^* \in \Omega$. Since the function $|\mathbf{Q}|^2 : \bar{\Omega} \to \mathbb{R}$ must also attain its maximum at $\mathbf{x}^* \in \Omega$, we have that

$$\triangle \left(\frac{1}{2} |\mathbf{Q}|^2 \right) (\mathbf{x}^*) \leqslant 0. \tag{2.1.22}$$

Multiplying both sides of (2.1.20) by Q_{ij}, and using the tracelesness of $\mathbf{Q}$, we obtain

$$K \triangle Q_{ij} Q_{ij} = A \mathrm{tr}\mathbf{Q}^2 - B \mathrm{tr}\mathbf{Q}^3 + C(\mathrm{tr}\mathbf{Q}^2)^2. \tag{2.1.23}$$

Since $\triangle \left(\frac{1}{2} |\mathbf{Q}|^2 \right) = (\triangle Q_{ij}) Q_{ij} + |\nabla \mathbf{Q}|^2$, and using (2.1.23), we find

$$\begin{aligned} K \triangle \left(\frac{1}{2} |\mathbf{Q}|^2 \right) &= A \mathrm{tr}\mathbf{Q}^2 - B \mathrm{tr}\mathbf{Q}^3 + C(\mathrm{tr}\mathbf{Q}^2)^2 + K |\nabla \mathbf{Q}|^2 \\ &\geq A|\mathbf{Q}|^2 - \frac{B}{\sqrt{6}} |\mathbf{Q}|^3 + C|\mathbf{Q}|^4 + K|\nabla \mathbf{Q}|^2 \\ &:= f(|\mathbf{Q}|) + K|\nabla \mathbf{Q}|^2. \end{aligned} \tag{2.1.24}$$

In the inequality we have used (2.1.12) with $\beta = 0$, which yields $\mathrm{tr}\mathbf{Q}^3 \leqslant \frac{|\mathbf{Q}|^3}{\sqrt{6}}$. A direct calculation shows $f\left(\sqrt{\frac{2}{3}} s_+\right) = 0$, and it is clear $f(0) = 0$ is a repeated root. Since f is a quartic polynomial with a positive coefficient for $|\mathbf{Q}|^4$, it follows that $\sqrt{\frac{2}{3}} s_+ > 0$ is the largest positive root of $f(|\mathbf{Q}|)$, and

$$f(|\mathbf{Q}|) > 0 \text{ for } |\mathbf{Q}| > \sqrt{\frac{2}{3}} s_+.$$

Applying this inequality to (2.1.24), we see

$$\triangle\left(\frac{1}{2}|\mathbf{Q}|^2\right)(\mathbf{x}) > 0 \tag{2.1.25}$$

for all interior points $\mathbf{x} \in \Omega$, where $|\mathbf{Q}(x)| > \sqrt{\frac{2}{3}}s_+$. This includes $\mathbf{x}^*$, which contradicts (2.1.22). □

2.2 The reduced modelling approach

For thin three-dimensional systems, where the height is much smaller than the cross section (see Figure 2.1 for instance), it can be sufficient to model the problem as being two-dimensional rather than three-dimensional. For example, for the bistable nematic device found in [22], the height of the square wells are less that half the cross section of the square, and consequently, molecules are primarily in the plane of the square cross section. Furthermore, similar observations have been made in [75], where the authors consider an fd-virus system suspended in shallow rectangular wells. Measuring the director at different well heights, the profile is invariant across the height of the channel and they find planar alignment in the cross section of the wells. In such situations, we do not need to capture the system behaviour in all three-dimensions and a two-dimensional description is sufficient.

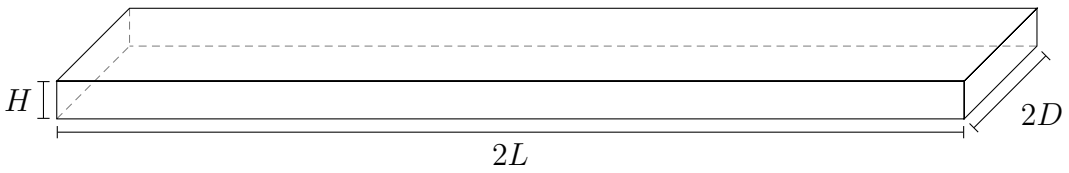

Figure 2.1: Long thin/shallow channel geometry. Here, the length $2L$, is much larger than the width $2D$, so that $D \ll L$, while the height H, is $H \ll D$.

In fact, the reduction from a three- to a two-dimensional model, can be justified rigorously with the use of Γ-convergence techniques. In [76], Theorem 5.1, the authors use such methods to show that when the height of our geometry is sufficiently small, we can indeed model the system as being two-dimensional rather than three-dimensional (also see Theorem 2.1 in [77]). The authors consider a film of nematic liquid crystals in the limit of vanishing film thickness. They impose planar surface anchoring conditions on the top and bottom surfaces of the film, and uniaxial Dirichlet boundary conditions on the lateral boundary of the film. As the height of the domain tends to zero, they find minimisers of the three-dimensional energy converge to minimisers of a two-dimensional energy (the Γ-limit), so that it suffices to study the variational problem on the cross section of the domain. That is [77], as $H \to 0$, minimisers of

$$F_{3D}(\mathbf{Q}_f) = \int_0^H \int_\Omega \frac{K}{2}\left(|\nabla_{x,y}\mathbf{Q}_f|^2 + |\nabla_z \mathbf{Q}_f|^2\right) + f_b(\mathbf{Q}_f)\ \mathrm{d}V + \int_{\Omega\times\{0,H\}} f_s(\mathbf{Q}_f, \mathbf{v})\ \mathrm{d}S$$

(Ω is a two-dimensional domain, $\mathbf{v} \in \mathbb{S}^2$ is normal to the surface of the film and for clarity, $\mathbf{Q}_f$ denotes the full 3×3 tensor (1.5.1)) converge to minimisers of

$$F_{2D}(\mathbf{Q}_f) = \int_\Omega \frac{K}{2}|\nabla_{x,y}\mathbf{Q}_f|^2 + f_b(\mathbf{Q}_f)\ \mathrm{d}A.$$

Here, f_s is a surface anchoring energy that favours planar boundary conditions on the top and bottom surfaces, more specifically ([76] equation (16))

$$f_s(\mathbf{Q}_f, \mathbf{v}) = \alpha[(\mathbf{Q}_f\mathbf{v}\cdot\mathbf{v}) - \beta]^2 + \gamma|(\mathbf{I}_3 - \mathbf{v}\otimes\mathbf{v})\mathbf{Q}_f\mathbf{v}|^2, \tag{2.2.1}$$

where α, β and γ are explicitly computable constants.

It follows that minimising the surface energy (2.2.1), requires one of the eigenvectors of the $\mathbf{Q}_f$-tensor to be $\mathbf{v}$ (i.e. normal to the surface of the film) with associated eigenvalue β [76]. Taking the z-direction to be normal to the surface

of the film, $\mathbf{v} = (0, 0, 1)$ must be an eigenvector of $\mathbf{Q}_f$. Considering $\mathbf{Q}_f\mathbf{v} = \beta\mathbf{v}$, we see $Q_{13} = Q_{23} = 0$. Hence, we have three degrees of freedom instead of five. For convenience, we can then redefine the components of $\mathbf{Q}_f$ as,

$$\mathbf{Q}_f = \begin{pmatrix} Q_{11} - q_3 & Q_{12} & 0 \\ Q_{12} & -Q_{11} - q_3 & 0 \\ 0 & 0 & 2q_3 \end{pmatrix}. \tag{2.2.2}$$

It also follows from $\mathbf{Q}_f\mathbf{v} = \beta\mathbf{v}$, that $2q_3 = \beta$. Hence, we can express the full $\mathbf{Q}_f$-tensor (2.2.2) as the sum of

$$\begin{pmatrix} & & 0 \\ & \mathbf{Q} & 0 \\ & & 0 \\ 0 & 0 & 0 \end{pmatrix},$$

where

$$\mathbf{Q} = \begin{pmatrix} Q_{11} & Q_{12} \\ Q_{12} & -Q_{11} \end{pmatrix}, \tag{2.2.3}$$

and $\frac{3}{2}\beta\left(\mathbf{v}\otimes\mathbf{v} - \frac{1}{3}\mathbf{I}_3\right)$, yielding only two degrees of freedom, Q_{11} and Q_{12}. Therefore, it is sufficient to work with (2.2.3) which is known as the reduced LdG $\mathbf{Q}$-tensor.

The reduced tensor (2.2.3) is a symmetric traceless 2×2 matrix, i.e., $\mathbf{Q} \in S_0 := \{\mathbf{Q} \in \mathbb{M}^{2\times 2} : Q_{ij} = Q_{ji}, Q_{ii} = 0\}$ (where $\mathbb{M}^{2\times 2}$ is the space of all 2×2 matrices). The reduced LdG $\mathbf{Q}$-tensor can therefore be written in terms of its positive eigenvalue λ_1, and orthonormal eigenvectors $\mathbf{n}$ and $\mathbf{m}$ (by the spectral decomposition theorem) as

$$\mathbf{Q} = \lambda_1\left(\mathbf{n}\otimes\mathbf{n} - \mathbf{m}\otimes\mathbf{m}\right). \tag{2.2.4}$$

We take the director to be the eigenvector of $\mathbf{Q}$ which has a positive eigenvalue (i.e.

$\mathbf{n}$) and using the spectral decomposition theorem again, we can rewrite (2.2.4) as

$$\mathbf{Q} = s\left(\mathbf{n}\otimes\mathbf{n} - \frac{1}{2}\mathbf{I}_2\right), \tag{2.2.5}$$

where $s = 2\lambda_1$ is interpreted as the scalar order parameter and $\mathbf{I}_2$ is the 2×2 identity matrix.

In the reduced case, the LdG free energy (2.1.13), reduces to the Ginzburg-Landau energy [78]

$$F(\mathbf{Q}) = \int_\Omega \frac{K}{2}|\nabla\mathbf{Q}|^2 + \frac{|\mathbf{Q}|^2}{2}\left(A + \frac{C}{2}|\mathbf{Q}|^2\right)\,\mathrm{d}\Omega. \tag{2.2.6}$$

For the $\mathbf{Q}$-tensor (2.2.5), $\mathrm{tr}(\mathbf{Q}^3) = 0$, so the constant B does not appear in f_b (1.5.11a). Hence, the second term in (2.2.6) is simply the bulk energy density for this reduced problem. The reduced Euler-Lagrange equations associated with (2.2.6), are

$$K\triangle Q_{11} = AQ_{11} + 2CQ_{11}(Q_{11}^2 + Q_{12}^2), \tag{2.2.7a}$$

$$K\triangle Q_{12} = AQ_{12} + 2CQ_{12}(Q_{11}^2 + Q_{12}^2). \tag{2.2.7b}$$

We have shown above that the reduced $\mathbf{Q}$-tensor (2.2.3), maps to the full $\mathbf{Q}_f$-tensor (2.2.2). For the special temperature $A = -\frac{B^2}{3C}$, $q_3 = -\frac{B}{6C}$ is a constant [79] and the corresponding full $\mathbf{Q}_f$-tensor (2.2.2) is an exact solution of the full Euler-Lagrange equations (2.1.20) (subject to appropriately defined boundary conditions) and hence analytic, from the discussion in Section 2.1.3. Consequently, the reduced $\mathbf{Q}$-tensor (2.2.3) is analytic, ensuring solutions of the system (2.2.7) are analytic.

When used in this thesis (specifically, chapters 3, 4, 5 and 6)), the reduced $\mathbf{Q}$-tensor (2.1.1) is appropriate as we model long shallow channel geometries, which are relevant for microfluidic problems (see Figure 2.1). The shallowness of the

channel means we can first reduce the problem to a two-dimensional one, captured by (2.2.3). Then, since $L \gg D$ is considered to be effectively infinite, structural properties should be uniform along the length of the channel, so we need only consider the behaviour across the width. Hence, we can employ (2.2.3) as a function of one variable only. We do not give rigorous proofs of this dimension reduction in this thesis, given that our work is in the spirit of formal mathematical modelling. Finally, we note that the reduced modelling approach (2.2.3), has been successfully employed in [68, 77, 79, 80].

Remark 2.2.1. A quick remark on Γ-convergence is as follows and is based on the discussion at the start of [81]. At its most basic level, Γ-convergence is designed to express the convergence of minimisation problems as some parameter approaches zero. For example, consider the following minimisation problem

$$m_\epsilon = \min\{F_\epsilon(\mathbf{Q}_\epsilon) : \mathbf{Q}_\epsilon \in \mathcal{A}_\epsilon\}, \tag{2.2.8}$$

for some dimensionless parameter ϵ and admissible space $\mathcal{A}_\epsilon$. In the $\epsilon \to 0$ limit, it turns out to be more convenient to study the asymptotic behaviour not through the study of properties of the solution $\mathbf{Q}_\epsilon$, but instead, a limit energy F_0, such that as $\epsilon \to 0$, solutions of the problem

$$m_0 = \min\{F_0(\mathbf{Q}_0) : \mathbf{Q}_0 \in \mathcal{A}_0\}, \tag{2.2.9}$$

are a good approximation to the problem (2.2.8). By good approximation, we mean $m_\epsilon \to m_0$ and $\mathbf{Q}_\epsilon \to \mathbf{Q}_0$ as $\epsilon \to 0$. The notion of convergence here is a choice made by the user. In this thesis we will consider sequences converging in L^1, i.e.,

$$\int_\Omega |\mathbf{Q}_\epsilon - \mathbf{Q}_0| \, \mathrm{d}\Omega \to 0 \text{ as } \epsilon \to 0.$$

In this instance, F_0 is termed the Γ-limit of F_ϵ. The existence of such a Γ-limit

requires two properties to hold:

1. For every $\mathbf{Q} \in \mathcal{A}_0$, and for every $\mathbf{Q}_\epsilon \to \mathbf{Q}$, we have

$$F_0(\mathbf{Q}) \leq \liminf_{\epsilon \to 0} F_\epsilon(\mathbf{Q}_\epsilon).$$

2. For every $\mathbf{Q} \in \mathcal{A}_0$, we can find a sequence $\bar{\mathbf{Q}}_\epsilon \to \mathbf{Q}$ such that

$$F_0(\mathbf{Q}) \geq \limsup_{\epsilon \to 0} F_\epsilon(\bar{\mathbf{Q}}_\epsilon).$$

These conditions mean that the energies F_ϵ are equi-coercive. From these two conditions, the *fundamental theorem of* Γ*-convergence* is obtained.

Theorem 2.2.2. *Let $(\mathcal{A}, d)$ be a metric space, let F_ϵ be a equi-coercive sequence of functions on $\mathcal{A}$, and let $F_0 = \Gamma\text{-}\lim_{\epsilon \to 0} F_\epsilon$, then the following limit exists*

$$\min_{\mathcal{A}} F_0 = \lim_{\epsilon \to 0} \inf_{\mathcal{A}} F_\epsilon. \tag{2.2.10}$$

Moreover, if $\mathbf{Q}_\epsilon$ is a precompact sequence such that $\lim_{\epsilon \to 0} F_\epsilon(\mathbf{Q}_\epsilon) = \lim_{\epsilon \to 0} \inf_{\mathcal{A}} F_\epsilon$, then every limit of a subsequence of $\mathbf{Q}_\epsilon$ is a minimum point for F_0 [81].

This understanding is sufficient for our purposes, as a rigorous and complete understanding of Γ-convergence is not the focus of this thesis, rather, we want to utilise existing results from this area of mathematics to gain insight into our liquid crystal problems.

2.3 Order reconstruction solutions

A key theme throughout this thesis is that of *order reconstruction* (OR) and OR-type solutions. These solutions model liquid crystal polydomains i.e., liquid

crystal sub-domains separated by domain walls or singular lines/surfaces. We defer the precise mathematical description of OR and OR-type solutions to the relevant chapters, for now, we point out the key feature of such solutions is that in our reduced description (2.2.3), $\mathbf{Q} = \mathbf{0}$, or equivalently, $s = 0$ somewhere, and these singularities represent domain walls separating possibly distinct liquid crystal sub-domains. In Figure 2.2, examples of ferronematic polydomains can be seen. Here, the thick lines are the domain walls which separate liquid crystal sub-domains.

We are interested in OR and OR-type solutions for two reasons: (i) because of their ability to describe experimentally observed phenomena, and (ii) the potential applications of the polydomain structures they describe. For example, OR and OR-type solutions are relevant for modelling chevron or zigzag patterns and disclinations observed in pressure-driven flows [18, 82] (see Figure 2.3). These disclinations can be used in the architecture of micro-wires, or as soft rails for the transport of colloidal particles or droplets in microfluidic channels [18]. OR-type solutions are also useful for modelling situations in smectics and active nematics. For example, when a cell filled with a smectic A liquid crystal is cooled to the smectic C phase, a similar chevron/zigzag texture is observed and has been the impetus of considerable experimental and theoretical interest [83–85]. While in active nematics, aligned fibers confined in a cylindrical cell can be controlled to display a laminar flow and parallel lanes of defect cores [86], which can be well described by OR-type solutions. More generally, polydomain structures (captured by OR and OR-type solutions) would have distinct optical and/or mechanical properties if experimentally realised, making them of clear physical interest for applications.

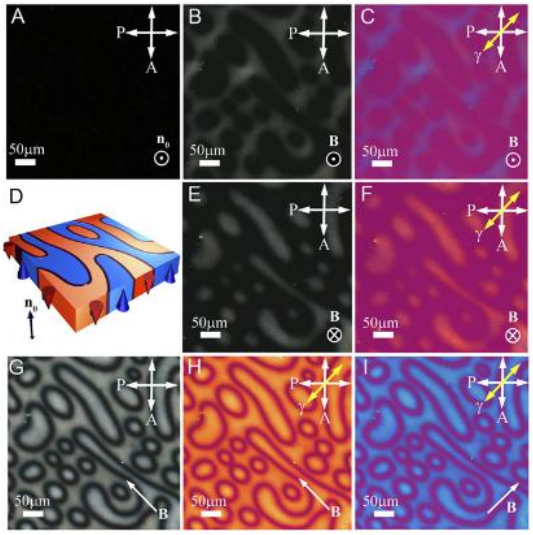

Figure 2.2: Ferronematic polydomains under different orientations of an applied magnetic field **B**, viewed via polarised optical microscopy with (colour images) and without (black and white images) a phase retardation plate. (D) shows a schematic of the domain walls. Image from [36] with permission from the Proceedings of the National Academy of Sciences.

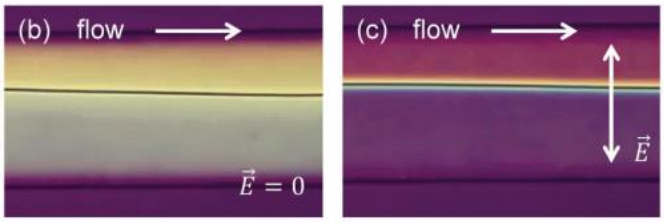

Figure 2.3: Disclination lines found in passive nematic flows confined to a narrow channel, with (b) and without (c) an applied electric field. Reproduced from Ref. [18] with permission from the Royal Society of Chemistry.

Mathematically, OR solutions have been studied extensively in purely nematic systems, see [64, 66, 87] for studies in one, two and three spatial dimensions respectively. In one-dimension, OR solutions simply partition the interval under consideration into sub-intervals with constant director profiles, separated by domain walls. In two-dimensions, and on square domains, the observed OR solution is referred to as the *well order reconstruction solution* (WORS), since it possess an uniaxial defect cross along the diagonals of the square. In three-dimensions, and on a cuboidal domain with a square cross section, the z-invariant WORS is reported. We build on the existing work in two ways: (i) we investigate the compatibility of OR with different physical settings, namely, ferronematics, and passive and active nematodynamics; and (ii) we investigate the compatibility of OR solutions with the imposed boundary conditions on the nematic director. The connection between OR solutions and the boundary conditions, and the related uniqueness result, are some of the main achievements of this work.

Before moving on, we stress that although we consider one-dimensional mathematical problems, the physical setting is still three-dimensional. Because of the nature of the geometry being considered, and the modelling assumptions we make, the profiles found across the width of the channel can be extrapolated along the

length and height of the channel. This means nodal points with $\mathbf{Q} = \mathbf{0}$ translate to disclinations or singular surfaces (labelled as domain walls) in the physical channel. This is why our one-dimensional OR solutions model such phenomena.

Chapter 3

Confined nematics in a channel geometry

This chapter is derived in part from Dalby, Han, Majumdar and Mrad (2022) [1].

3.1 The problem

In this chapter, we consider a one-dimensional problem for conventional nematics relevant for long thin microfluidic channels. We model this situation by a reduced Landau-de Gennes (LdG) **Q**-tensor as seen in Section 2.2. A similar one-dimensional setup relevant for modelling nematic liquid crystals confined between two parallel plates, has been studied rigorously in [64]. Here, the author proves the existence of a unique energy minimiser for sufficiently small cell widths, and that this minimiser is an order reconstruction (OR) solution. Furthermore, this OR solution loses stability for sufficiently large cells via a pitchfork bifurcation. These facts were previously known numerically from the work in [88]. In both [64, 88], they consider Dirichlet boundary conditions such that the director is mutu-

ally orthogonal on either side of the cell. The novelty and key difference between our study and [64, 88], is that we investigate the impact of different Dirichlet boundary conditions on the nematic director, i.e., different director orientations at the boundary. Specifically, the aim is to study the effects that these different boundary conditions have on the existence, regularity and uniqueness of solutions. In particular, we study OR solutions (introduced in Section 3.1.2) describing nematic polydomains in connection to these questions. We do this by employing both a **Q**- and associated (s, θ)-formulation (introduced in Section 3.1.2) where appropriate.

In Section 3.2, we prove a series of results which culminate in an interesting uniqueness result, that is, we show we have a unique solution in the (s, θ)-formalism provided an OR solution does not exist. While in the **Q**-formalism, we prove OR is in fact only possible for mutually orthogonal boundary conditions on the nematic director. In Section 3.3, we perform an in-depth asymptotic analysis in the limit of small channel widths where we can explicitly compute solutions and hence, directly verify results in Section 3.2. Finally, in Section 3.4, we numerically compute solutions of the **Q**-Euler-Lagrange equations to highlight the impact of boundary conditions on solution profiles and give numerical support to our theoretical results.

3.1.1 Model framework

As discussed in Section 2.2, we consider nematic liquid crystals (NLCs) sandwiched inside a three-dimensional channel, $\tilde{\Omega} = \{(x, y, z) \in \mathbb{R}^3 : -L \leq x \leq L, -D \leq y \leq D, 0 \leq z \leq H\}$ where L, D, and H are the half-length, half-width and height of the channel, respectively, and we assume that $L \gg D$ (see Figure 2.1). We further assume planar surface anchoring conditions (as in (2.2.1)) on the top and bottom

channel surfaces at $z = 0$ and $z = H$, which effectively means that the NLC molecules lie in the xy-plane on these surfaces, without a specified direction. Such boundary conditions are used in experiments, see for example the planar bistable nematic device in [22] and the experiments on fd-viruses in [75]. We impose z-invariant Dirichlet conditions on $y = \pm D$ and periodic conditions on $x = \pm L$, compatible with the planar conditions on $z = 0, H$. Given the planar surface anchoring conditions on the top and bottom surfaces and that the well height is small, we assume that the system is invariant in the z-direction. Furthermore, since $L \gg D$ (is considered to be effectively infinite), it is reasonable from a modelling perspective to assume the system is invariant in x, so that structural properties vary in the y direction only. This leaves us with an effective one-dimensional problem, for $y \in [-D, D]$.

Given the above modelling assumptions regarding z-invariance, we assume the physically relevant nematic states are described by a reduced LdG nematic order parameter, as explained in Section 2.2. Recall, $\mathbf{Q}$ given in (2.2.5), is a symmetric traceless 2×2 matrix, i.e., $\mathbf{Q} \in S_0 := \{\mathbf{Q} \in \mathbb{M}^{2\times 2} : Q_{ij} = Q_{ji}, Q_{ii} = 0\}$ and

$$\mathbf{Q} = s\left(\mathbf{n} \otimes \mathbf{n} - \frac{1}{2}\mathbf{I}_2\right), \tag{3.1.1}$$

where s is the scalar order parameter and $\mathbf{n}$ is the nematic director (a unit vector describing the average direction of orientational ordering in the xy-plane, which corresponds to the eigenvector of $\mathbf{Q}$ with a positive eigenvalue). Moreover, s can be interpreted as a measure of the degree of orientational order about $\mathbf{n}$, so that the nodal sets of s (i.e., where $s = 0$) define nematic defects in the xy-plane. We take $\mathbf{n}$ to be

$$\mathbf{n} = (\cos(\theta), \sin(\theta)), \tag{3.1.2}$$

where θ denotes the angle between $\mathbf{n}$ and the x-axis. One can then readily verify

using (3.1.1), (2.2.3) and (3.1.2), that the two independent components of $\mathbf{Q}$ can be expressed as

$$Q_{11} = \frac{s}{2}\cos(2\theta), \quad Q_{12} = \frac{s}{2}\sin(2\theta). \tag{3.1.3}$$

It follows from (3.1.3) and basic trigonometric identities that s and θ can be extracted from Q_{11} and Q_{12} by

$$s = 2\sqrt{Q_{11}^2 + Q_{12}^2} \quad \text{and} \quad \theta = \frac{1}{2}\tan^{-1}\left(\frac{Q_{12}}{Q_{11}}\right). \tag{3.1.4}$$

We will work with the $\mathbf{Q}$- and (s,θ)-formulations at different points in this chapter, so these relations will be useful when comparing the two formulations.

We model physically realistic configurations as local or global minimisers of the LdG energy functional, which is given as (see Section 1.5.2 and Section 2.2)

$$\tilde{F}(\mathbf{Q}) = \int_{-D}^{D} \frac{K}{2}|\nabla\mathbf{Q}|^2 + f_b(\mathbf{Q})\ \mathrm{d}y, \tag{3.1.5}$$

where $f_b(\mathbf{Q})$ is the bulk energy density accounting for bulk effects, $|\nabla\mathbf{Q}|^2 = \Sigma_{i,j=1}^{2} Q'_{ij}Q'_{ij}$ is the elastic energy density (here and hereafter in this chapter, $'$ will denote differentiation with respect to y) accounting for spatial inhomogeneities, and $K > 0$ is a material dependent elastic constant. The bulk energy density can be expressed as in Section 2.2 (2.2.6), namely

$$f_b(\mathbf{Q}) = \frac{A}{2}\mathrm{tr}(\mathbf{Q}^2) + \frac{C}{4}(\mathrm{tr}(\mathbf{Q}^2))^2. \tag{3.1.6}$$

The variable A is a material and temperature dependent constant, while $C > 0$ is a material dependent constant. We work with low temperatures for which $A < 0$, so that the nematic phase is preferred. In terms of s, (3.1.6) becomes

$$f_b(s) = \frac{A}{4}s^2 + \frac{C}{16}s^4.$$

Critical points of this bulk potential are solutions of the algebraic equation

$$\frac{\mathrm{d}f_b(s)}{\mathrm{d}s} = \frac{s}{2}\left(\frac{C}{2}s^2 + A\right) = 0,$$

of which there are three: $s = 0$ and $s_\pm = \pm\sqrt{\frac{-2A}{C}}$. $s_\pm$ gives the lowest bulk energy value and therefore, the bulk energy minimisers are given by reduced $\mathbf{Q}$-tensors of the form (3.1.1), with

$$s = s_\pm := \pm\sqrt{\frac{-2A}{C}}, \tag{3.1.7}$$

and $\mathbf{n} \in \mathbb{S}^2$ arbitrary.

Using the definitions of Q_{11} and Q_{12} in (3.1.3), we rewrite (3.1.5) in terms of s and θ as follows,

$$\tilde{F}(s,\theta) = \int_{-D}^{D} K\left(\frac{(s')^2}{4} + s^2(\theta')^2\right) + \frac{s^2}{4}\left(\frac{C}{4}s^2 + A\right)\,\mathrm{d}y. \tag{3.1.8}$$

To reduce the number of model parameters, we now non-dimensionalise the problem. To do this, we rescale the variables as

$$y = D\bar{y}, \quad s = \sqrt{\frac{-2A}{C}}\bar{s}, \quad \mathbf{Q} = \sqrt{\frac{-2A}{C}}\bar{\mathbf{Q}}, \tag{3.1.9}$$

and substituting (the rescalings for y and s) into the free energy (3.1.8), we have

$$\tilde{F}(s,\theta) = D\int_{-1}^{1} \frac{K}{D^2}\left(\frac{-2A}{C}\right)\left(\frac{(\bar{s}')^2}{4} + \bar{s}^2(\theta')^2\right) - \frac{A^2}{2C}\bar{s}^2 + \frac{A^2}{4C}\bar{s}^4\,\mathrm{d}\bar{y}.$$

Multiplying the above energy by $\frac{CD}{-2AK}$, yields the dimensionless free energy

$$\bar{F}(\bar{s},\theta) := \frac{CD}{-2AK}\tilde{F}(s,\theta) = \int_{-1}^{1} \frac{(\bar{s}')^2}{4} + \bar{s}^2(\theta')^2 + \frac{\epsilon\bar{s}^2}{4}\left(\frac{\bar{s}^2}{2} - 1\right)\,\mathrm{d}\bar{y}, \tag{3.1.10}$$

where ϵ is a dimensionless parameter, given as [68]

$$\epsilon = \frac{|A|D^2}{K}. \tag{3.1.11}$$

ϵ is a scaled elastic constant, which is material, temperature, and geometry

dependent. Importantly, ϵ is proportional to the physical channel width squared. Our effective domain is now $\Omega = [-1, 1]$. Note, the relationships in (3.1.3) and (3.1.4) are unchanged after rescaling. Henceforth, we drop the bars from the rescaled variables and all quantities are dimensionless unless stated otherwise.

3.1.2 The (s, θ)-formulation: governing equations, boundary conditions, and order reconstruction solutions

The Euler-Lagrange equations of the functional (3.1.10) are:

$$s'' = 4s(\theta')^2 + \epsilon s(s^2 - 1), \tag{3.1.12a}$$

$$2(s'\theta') + s\theta'' = (s^2\theta')' = 0 \implies s^2\theta' = W, \tag{3.1.12b}$$

where W is a constant of integration to be determined. We impose the following Dirichlet boundary conditions:

$$s(-1) = s(1) = 1, \tag{3.1.13a}$$

$$\theta(-1) = 0, \quad \theta(1) = \theta_1 \in \left(0, \frac{\pi}{2}\right]. \tag{3.1.13b}$$

That is, we require the nematic ordering to equal the bulk energy minimising value s_+, on the bounding plates. In contrast, we enforce conflicting Dirichlet boundary conditions on θ by allowing θ_1 to vary in $\left(0, \frac{\pi}{2}\right]$. This necessarily means the director rotates across the channel. An illustration of these boundary conditions can be found in Figure 3.1. A potential issue follows from (3.1.4): the range of θ when extracted from $\mathbf{Q}$, is $(-\frac{\pi}{4}, \frac{\pi}{4})$, but our boundary conditions extend to $\frac{\pi}{2}$. However, we circumvent this issue by using the function $\text{atan2}(y, x) \in (-\pi, \pi]$, which returns the angle between the line connecting the point (x, y) to the origin

and the positive x axis. Henceforth, we define

$$\theta := \frac{1}{2}\text{atan2}(Q_{12}, Q_{11}) = \begin{cases} \frac{1}{2}\tan^{-1}\left(\frac{Q_{12}}{Q_{11}}\right) & \text{if } Q_{11} > 0 \\ \frac{1}{2}\tan^{-1}\left(\frac{Q_{12}}{Q_{11}}\right) + \frac{\pi}{2} & \text{if } Q_{11} < 0 \text{ and } Q_{12} \geq 0 \\ \frac{1}{2}\tan^{-1}\left(\frac{Q_{12}}{Q_{11}}\right) - \frac{\pi}{2} & \text{if } Q_{11} < 0 \text{ and } Q_{12} < 0 \\ +\frac{\pi}{4} & \text{if } Q_{11} = 0 \text{ and } Q_{12} > 0 \\ -\frac{\pi}{4} & \text{if } Q_{11} = 0 \text{ and } Q_{12} < 0 \\ \text{undefined} & \text{if } Q_{11} = 0 \text{ and } Q_{12} = 0. \end{cases} \tag{3.1.14}$$

We update (3.1.4) to the following

$$s = 2\sqrt{Q_{11}^2 + Q_{12}^2} \quad \text{and} \quad \theta = \frac{1}{2}\text{atan2}\left(Q_{12}, Q_{11}\right). \tag{3.1.15}$$

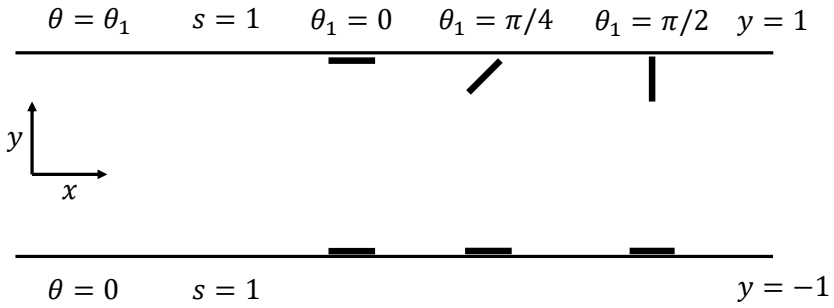

Figure 3.1: Boundary conditions for s and θ and some example director boundary conditions.

Remark 3.1.1. Imposing the boundary conditions (3.1.13a), in (3.1.12b), we see

$$W := \theta'(-1) = \theta'(1). \tag{3.1.16}$$

We further note that W in (3.1.12b) cannot change sign as it is a fixed constant of integration. It is clear $s^2 \geq 0$ in Ω. We then note, $\theta(-1) = 0$ and $\theta_1 > 0$ implies $\theta'(y) > 0$ for some $y \in \Omega$, for θ to satisfy the boundary condition at $y = 1$.

Hence, $W \geq 0$ and $\theta' \geq 0$ for all $y \in [-1, 1]$, since W is a fixed constant. As θ is a non-decreasing function, it must satisfy

$$0 \leq \theta \leq \theta_1, \ \forall y \in [-1, 1] \text{ and } \forall \theta_1 \in \left(0, \frac{\pi}{2}\right]. \tag{3.1.17}$$

In this (s, θ)-formulation, we focus on solutions when $W \neq 0$, so that (3.1.12) can be written as

$$s'' = \frac{4W^2}{s^3} + \epsilon s(s^2 - 1), \tag{3.1.18a}$$

$$s^2\theta' = W. \tag{3.1.18b}$$

Since the right hand side of (3.1.18a) is a polynomial in s (where $s \neq 0$), any classical C^2 (i.e., twice continuously differentiable) solutions will actually be smooth, and hence, so will solutions θ to (3.1.18b). Moreover, a solution s, must be non-negative. In what follows, we study solutions with $W \neq 0$ in the (s, θ)-formulation and consider smooth, classical solutions of (3.1.12), subject to the boundary conditions in (3.1.13).

The governing equations (3.1.12) change when $W = 0$. Taking $W = 0$, the system (3.1.12) becomes

$$s'' = \epsilon s(s^2 - 1), \tag{3.1.19a}$$

$$s^2\theta' = 0. \tag{3.1.19b}$$

Therefore, we can in principle take θ to be constant anywhere $s \neq 0$, and then simply enforce $s = 0$ at any points where θ (necessarily) jumps to satisfy its conflicting Dirichlet boundary conditions. Hence, θ is essentially some translated and rescaled Heaviside function. Such profiles will satisfy the system of equations (3.1.19), almost everywhere away from any jump discontinuities in θ (where its

derivative is infinite).

Remark 3.1.2. We interpret OR solutions as solutions of (3.1.12) and (3.2.20) (introduced in Section 3.2.1) with polydomain structures. Specifically, OR solutions describe polydomains with distinct constant nematic director profiles on different sub-domains, and these sub-domains are separated by singular lines or singular surfaces, referred to as domain walls, to account for jumps in the nematic director across sub-domain boundaries. In the (s, θ)-formulation and our one-dimensional framework, OR solutions correspond to a partition of the domain $\Omega = [-1, 1]$ into sub-domains, $\Omega = \sum_{j=1}^{n} \Omega_j$, where each Ω_j is a sub-domain. The sub-domains correspond to intervals with constant θ (recall that θ is the orientation of $\mathbf{n}$), and the domain wall is described by a point with $s = 0$, to regularise the jump in θ between sub-domains. In three-dimensions, the sub-domains correspond to three-dimensional cuboidal regions and the domain walls are singular surfaces in θ.

OR solutions can be related to the constant W in (3.1.12b). If $W = 0$, we either have $s = 0$ or θ=constant almost everywhere, compatible with the definition of an OR solution. Conversely, an OR solution, by definition, has $W = 0$ since they have piecewise constant θ-profiles. In other words, OR solutions exist if and only if $W = 0$. If $W \neq 0$, then OR solutions are necessarily disallowed because a non-zero value of W implies that $s \neq 0$ on Ω. Hence, the system (3.1.18) yields non-OR solutions, while (3.1.19) can yield OR solutions. Moreover, from the discussion following (3.1.19), OR solutions are in principle compatible with any θ_1 in the (s, θ)-formulation, something we will see is untrue in the $\mathbf{Q}$-formulation.

The (s, θ)-formulation is essentially an Ericksen continuum model, since it models the nematic state via a variable scalar order parameter and the director angle

θ. Hence, this (s, θ)-framework contains a subset of all the possible solutions in the **Q**-framework (introduced in Section 3.2.1). Consequently, we will see the (s, θ)-framework can yield different predictions to the **Q**-framework. In general, both formulations have pros and cons (which we explore in this chapter), and using both can be valuable in gaining a deeper understanding of the problem.

3.2 Properties of solutions

In this section, we prove results regarding properties of solutions in both the (s, θ)- and **Q**-formulation. First, we prove a maximum principle for solutions of the system (3.1.12). To get the upper bound, we follow methods parallel to those in Proposition 2.1.2, but additional work is needed to prove the positivity of s.

Theorem 3.2.1. *(Maximum Principle) Let s and θ be solutions of* (3.1.12a) *and* (3.1.12b)*, where s is at least C^2 and θ is at least C^1, then*

$$0 < s \leq 1 \quad \forall y \in [-1, 1]. \tag{3.2.1}$$

Proof. Let (s, θ) denote a solution pair of (3.1.12a) and (3.1.12b), such that s is at least C^2 and assume for contradiction that s has a local minimum at $\hat{y}$, such that $s(\hat{y}) \leq 0$. This implies $W = 0$ using (3.1.12b). If $W = 0$, then we must have $s = 0$ or constant θ, at every point in Ω. This solution is determined by the ordinary differential equation:

$$s'' = \epsilon s(s^2 - 1), \tag{3.2.2}$$

which can be integrated to obtain the scalar order parameter. Doing this, we find

$$s' = \pm\sqrt{\left(\epsilon\left(\frac{s^4}{2} - s^2\right) + J\right)}. \tag{3.2.3}$$

Evaluating at $s = 1$, we see $J \geq \frac{\epsilon}{2}$. At the minimum, $s'(\hat{y}) = 0$, hence

$$s^2(\hat{y}) = 1 \pm \sqrt{1 - \frac{2J}{\epsilon}}, \tag{3.2.4}$$

which requires $J \leq \frac{\epsilon}{2}$. Combining these inequalities yields $J = \frac{\epsilon}{2}$. We then have

$$s' = \pm\sqrt{\frac{\epsilon}{2}(s^2 - 1)^2}. \tag{3.2.5}$$

Fixing the sign in the above to be either positive or negative, we have a first order ordinary differential equation subject to the boundary condition $s(-1) = 1$, or $s(1) = 1$. In any case, $s \equiv 1$ is a solution, hence, by the Picard-Lindelöf Theorem, this is the unique solution. Clearly this is positive everywhere, which contradicts our assumption $s(\hat{y}) \leq 0$.

We prove that $s \leq 1$ by a direct application of the maximum principle. Assume that there exists a point $y^* \in [-1, 1]$ where s attains its maximum, and $s(y^*) > 1$ so that $y^* \in (-1, 1)$. The function s^2 must also attain its maximum at the point $y^* \in (-1, 1)$, so

$$\left(s^2\right)''(y^*) \leq 0.$$

Next, note that $(s^2)'' = 2(s')^2 + 2ss''$. We now multiply (3.1.12a) by s, and substitute for $s''s$ in the resulting expression to obtain

$$\frac{1}{2}\left(s^2\right)'' = (s')^2 + 4s^2(\theta')^2 + \epsilon s^2(s^2 - 1). \tag{3.2.6}$$

Using $s(y^*) > 1$, (3.2.6) implies that $(s^2)''(y^*) > 0$, which is a contradiction. Hence, we conclude that $s \leq 1$ for all $y \in [-1, 1]$. □

Theorem 3.2.2. *Any non-constant and non-OR solution, s, of the Euler-Lagrange equations* (3.1.12)*, has a single critical point which is necessarily a non-zero global minimum at some $y^* \in (-1, 1)$.*

Proof. For clarity, we denote a specific solution of (3.1.12a) and (3.1.12b), by (s_{sol}, θ_{sol}) in this proof. Recall that for non-OR solutions, we necessarily have $W \neq 0$ and $s \neq 0$ everywhere. In this case, the system (3.1.12) can be written as (3.1.18) and we consider smooth solutions s_{sol}.

The symmetric Dirichlet boundary conditions for s, imply that a non-constant solution has $s'_{sol}(y^*) = 0$, for some $y^* \in (-1, 1)$, where s' is defined as,

$$s' = \pm\sqrt{\left(-4W^2 s^{-2} + \epsilon\left(\frac{s^4}{2} - s^2\right) + J\right)}. \tag{3.2.7}$$

Here, J is a constant of integration and $J = 4W^2 + \frac{\epsilon}{2} + s'(1)^2$, hence we must have

$$J \geq 4W^2 + \frac{\epsilon}{2}. \tag{3.2.8}$$

Since s' is defined in terms of s and not y, solutions of $s' = 0$ give us the extrema of a solution s_{sol} (i.e., maxima or minima), rather than the location of the critical points on the y-axis. The condition $s' = 0$, is equivalent to

$$J = 4W^2 s^{-2} - \epsilon\left(\frac{s^4}{2} - s^2\right). \tag{3.2.9}$$

If $\epsilon = 0$, we can only have one extremum, namely $s = \sqrt{\frac{4W^2}{A}}$, which in view of the boundary conditions and maximum principle, must be a minimum. For $\epsilon > 0$, solving (3.2.9) is equivalent to computing the roots of $f(s) = 0$ where

$$f(s) := s^6 - 2s^4 + \frac{2J}{\epsilon}s^2 - \frac{8W^2}{\epsilon}. \tag{3.2.10}$$

Firstly, note that f has a root for $s \in (0, 1]$, since $f(0) = \frac{-8W^2}{\epsilon} < 0$ and $f(1) = -1 + \frac{2J}{\epsilon} - \frac{8W^2}{\epsilon} \geq 0$, by (3.2.8). Differentiating (3.2.10), we obtain

$$\frac{\mathrm{d}f}{\mathrm{d}s}(s) = 6s^5 - 8s^3 + \frac{4J}{\epsilon}s,$$

so that the critical points of f are given by

$$s = 0,\ \tilde{s}_{\pm} = \sqrt{\frac{8 \pm \sqrt{64 - \frac{96J}{\epsilon}}}{12}}, \tag{3.2.11}$$

provided that $J \leq \frac{2}{3}\epsilon$. There are now three cases to consider.

Case 1: If $J > \frac{2}{3}\epsilon$, $f(s)$ has one critical point at $s = 0$, which is a negative global minimum. Hence, f has one root in the range, $s \in (0, 1]$.

Case 2: If $J = \frac{2}{3}\epsilon$, the two critical points $\tilde{s}_{\pm}$ coincide. The point $s = 0$ is still a minimum of $f(s)$ and the coefficient of s^6 is positive (so $f \to \infty$ as $s \to \infty$), so we deduce that $\tilde{s}_{\pm}$ is a stationary point of inflection (this can be checked via direct computation). So again, f has one root for $s \in (0, 1]$.

Case 3: Finally, if $J < \frac{2}{3}\epsilon$, $\tilde{s}_{\pm}$ are distinct critical points of f. The point, $s = 0$, is still a minimum of $f(s)$ and the coefficient of s^6 is positive, so that there are two possibilities: (a) $\tilde{s}_{\pm}$ are distinct saddle points, and since f is increasing for $s > 0$, we see f has a single root for $s \in (0, 1]$, or (b) $\tilde{s}_{-}$ is a local maximum and $\tilde{s}_{+}$ is a local minimum of $f(s)$. In the latter case, $s = 0$ is still a global minimum for $f(s)$, because $f(\tilde{s}_{+}) > f(0)$. Using this information, we can produce a sketch of $f(s)$ (shown in Figure 3.2), and there are five cases to consider for the number of roots of f.

In cases (i) and (v) of Figure 3.2, f has only one root for $s \in (0, 1]$. Next, in order for the derivative s'_{sol} to be real, the term under the square root in (3.2.7), has to be non-negative. This requires that $f(s) \geq 0$ for all $s \in [c, 1]$, for some $c > 0$. Applying this argument to cases (ii) and (iii) in Figure 3.2 by omitting regions with $f(s) < 0$, we deduce that f has a single root for $s \in (0, 1]$.

For case (iv), we have two distinct roots in an interval such that $f(s) \geq 0$, one

of which is $\tilde{s}_+$, and the other root is labelled as s_1. Recalling that $\tilde{s}_+$ is also a solution of $f'(s) = 0$, we deduce that $\tilde{s}_+$ is a repeated root of f. Then, f can be factorised as:

$$\begin{aligned} f(s) &= (s - \tilde{s}_+)^2(s + \tilde{s}_+)^2(s - s_1)(s + s_1) \\ &= s^6 - (2\tilde{s}_+^2 + s_1^2)s^4 + (\tilde{s}_+^4 + 2s_1^2\tilde{s}_+^2)s^2 - s_1^2\tilde{s}_+^4. \end{aligned} \tag{3.2.12}$$

Comparing the coefficient of s^4 and s^0 in (3.2.10), with (3.2.12), we have $s_1^2 = 2(1 - \tilde{s}_+^2)$ and $s_1^2 = \frac{8W^2}{\epsilon\tilde{s}_+^4}$, which implies

$$4W^2 + \epsilon\tilde{s}_+^4(\tilde{s}_+^2 - 1) = 0. \tag{3.2.13}$$

Comparing (3.1.18a) with (3.2.13), we deduce that, $s''(\tilde{s}_+) = 0$. Differentiating (3.1.18a) again, we can solve the resulting equation subject to $s''(y^+) = s'(y^+) = 0$ and $s(y^+) = \tilde{s}_+$, for some $y^+ \in \Omega$. By the uniqueness theory for Cauchy problems, this implies that $s_{sol} \equiv \tilde{s}_+$, which is inadmissible and this case is excluded.

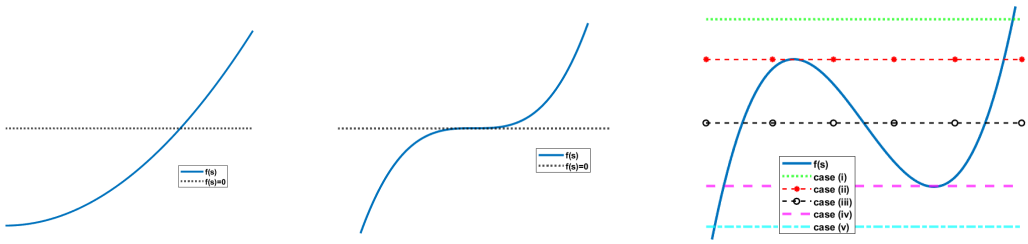

Case 1 Case 2 Case 3 (b)

Figure 3.2: The horizontal lines represent $f(s) = 0$.

In cases 1, 2 and 3 we have demonstrated that s_{sol} has a unique positive critical value, which must be the minimum value. The unique minimum value is attained at a unique interior point (if there were two interior minima at say y^* and y^{**}, a non-constant solution would exhibit a local maximum between the two minima,

which is excluded by a unique critical value for s_{sol}). This completes the proof. □

In the next theorem, we prove that we have a unique solution to (3.1.12) whenever $W \neq 0$, i.e., whenever an OR solution does not exist.

Theorem 3.2.3. *For $W \neq 0$, the system* (3.1.12)*, subject to the boundary conditions* (3.1.13)*, has a unique solution for a fixed ϵ and θ_1.*

Proof. Recall, for $W \neq 0$, the system (3.1.12) can be written as

$$s'' = \frac{4W^2}{s^3} + \epsilon s(s^2 - 1), \tag{3.2.14a}$$

$$s^2\theta' = W. \tag{3.2.14b}$$

Throughout this proof we take $W > 0$, so that $s \neq 0$ and consider smooth solutions.

In the first step, we show that (3.2.14) has a unique solution for fixed W, ϵ and θ_1. Assume for contradiction that $(\tilde{s}_1, \tilde{\theta}_1)$ and $(\tilde{s}_2, \tilde{\theta}_2)$ are distinct solutions pairs of (3.2.14), which satisfy (3.1.13). As such, they must have distinct derivatives at $y = -1$ (otherwise they would satisfy the same Cauchy problem). Suppose with out loss of generality

$$\tilde{s}_1'(-1) < \tilde{s}_2'(-1) \leq 0. \tag{3.2.15}$$

Since $\tilde{s}_1(1) = \tilde{s}_2(1) = 1$, there exists $y_0 = \min\{y > -1 : \tilde{s}_1(y_0) = \tilde{s}_2(y_0) := s_0\}$. Therefore, $\tilde{s}_1 < \tilde{s}_2$ for all $y \in (-1, y_0)$. Further, since $\tilde{s}_1$ and $\tilde{s}_2$ have one non-zero global minimum (Theorem 3.2.2), there are four possibilities for the location of y_0: (i) case I: $y_0 = 1$; (ii) case II: $y_0 < \min\{\alpha, \beta\}$ where $\tilde{s}_1$ attains its unique minimum at $y = \alpha$ and $\tilde{s}_2$ attains its unique minimum at $y = \beta$; (iii) case III: $\alpha \leq y_0 \leq \beta$, or $\beta \leq y_0 \leq \alpha$; and (iv) case IV: $y_0 > \max\{\alpha, \beta\}$. In case I, $\tilde{s}_1 < \tilde{s}_2$ implies $\tilde{\theta}_1' > \tilde{\theta}_2'$ for all $y \in (-1, 1)$, since both solution pairs satisfy (3.2.14b).

Hence, $\tilde{\theta}_1(y) - \tilde{\theta}_2(y)$ is increasing, and cannot vanish at $y = 1$, contradicting the boundary condition at $y = 1$.

For case II, we have

$$\tilde{s}_2'(y_0) \leq \tilde{s}_1'(y_0) < 0$$

so that

$$(\tilde{s}_2'(-1))^2 - (\tilde{s}_2'(y_0))^2 < (\tilde{s}_1'(-1))^2 - (\tilde{s}_1'(y_0))^2.$$

Using (3.2.7), this is equivalent to

$$\begin{aligned} -4W^2 - \frac{\epsilon}{2} + J_2 - \left(-\frac{4W^2}{s_0^2} + \epsilon s_0^2 \left(\frac{s_0^2}{2} - 1 \right) + J_2 \right) < \\ -4W^2 - \frac{\epsilon}{2} + J_1 - \left(-\frac{4W^2}{s_0^2} + \epsilon s_0^2 \left(\frac{s_0^2}{2} - 1 \right) + J_1 \right), \end{aligned}$$

where J_1 and J_2 are constants of integration associated with $\tilde{s}_1$ and $\tilde{s}_2$ respectively, and may not be equal. However, the left and right hand sides are in fact equal, yielding the desired contradiction, hence $\tilde{s}_1 = \tilde{s}_2$. Letting $\tilde{s}_1 = \tilde{s}_2 := s$ and integrating $\tilde{\theta}_1' = W/s^2$, it follows that $\tilde{\theta}_1$ is unique and is given by

$$\tilde{\theta}_1(y) = \theta_1 - \int_y^1 \frac{W}{s^2(u)} \, \mathrm{d}u, \text{ where } W = \theta_1 \left(\int_{-1}^1 \frac{1}{s^2} \, \mathrm{d}y \right)^{-1}. \tag{3.2.16}$$

The preceding arguments show that $\tilde{\theta}_1 = \tilde{\theta}_2$ too.

For Cases III and IV, there must exist another point of intersection, $y = y_1 \in (\max\{\alpha, \beta\}, 1]$, such that

$$(\tilde{s}_1 - \tilde{s}_2)(y_1) = 0; \text{ and } 0 < \tilde{s}_1'(y_1) \leq \tilde{s}_2'(y_1).$$

In this case, we can use

$$(\tilde{s}_2'(-1))^2 - (\tilde{s}_2'(y_1))^2 < (\tilde{s}_1'(-1))^2 - (\tilde{s}_1'(y_1))^2$$

to get the desired contradiction, hence $\tilde{s}_1 = \tilde{s}_2$. Repeating the above arguments, we find (3.2.16) and $\tilde{\theta}_1 = \tilde{\theta}_2$. We therefore conclude that for fixed W, ϵ and θ_1, the solution of (3.1.12) is unique.

Next, we show the constant W, is unique for fixed ϵ and θ_1. We assume that there exist two distinct solution pairs, $(\tilde{s}_1, \tilde{\theta}_1)$ and $(\tilde{s}_2, \tilde{\theta}_2)$, which by the first part of the proof, are the unique solutions of

$$\tilde{s}_1'' = \frac{4W_1^2}{\tilde{s}_1^3} + \epsilon\tilde{s}_1(\tilde{s}_1^2 - 1), \quad \tilde{s}_2'' = \frac{4W_2^2}{\tilde{s}_2^3} + \epsilon\tilde{s}_2(\tilde{s}_2^2 - 1)$$

and

$$\tilde{s}_1^2\tilde{\theta}_1' = W_1, \quad \tilde{s}_2^2\tilde{\theta}_2' = W_2,$$

respectively, subject to (3.1.13), for the same value of θ_1. Let $0 < W_1 \leq W_2$. Using a change of variable $u_k = 1 - \tilde{s}_k \in [0, 1)$, for $k = 1, 2$ so that $u_k(-1) = u_k(1) = 0$, we can use the method of sub- and super-solutions. First, the equation for u_k is

$$-u_k'' = \frac{4W_k)^2}{(1-u_k)^3} + \epsilon(1-u_k)(u_k - 2)u_k := g_{W_k}(u_k), \tag{3.2.17}$$

Then u_2 is a super-solution of (3.2.17) with $k = 1$, since

$$-u_2'' = g_{W_2}(u_2) \geq g_{W_1}(u_2),$$

while $u_0 \equiv 0$ is a sub-solution ($g_{W_1}(0) \geq 0$). By the maximum principle $0 < u_2$. Hence, by [74], there exists a solution u_*, of $-u_*'' = g_{W_1}(u_*)$ with $u_*(-1) = u_*(1) = 0$, such that $0 \leq u_* \leq u_2$. However, we have proved uniqueness for a fixed W, so $u_* = u_1$ and therefore

$$u_1 \leq u_2 \implies \tilde{s}_2 \leq \tilde{s}_1.$$

This implies

$$\tilde{\theta}_1' = \frac{W_1}{\tilde{s}_1^2} \leq \frac{W_2}{\tilde{s}_2^2} = \tilde{\theta}_2' \quad \forall y \in [-1,1]. \tag{3.2.18}$$

Since $\tilde{\theta}_2(1) = \theta_1$, if $\tilde{\theta}_1' < \tilde{\theta}_2'$ anywhere, then $\tilde{\theta}_1(1) = \theta_1$ does not hold, hence we must have equality i.e., $\tilde{\theta}_1' = \tilde{\theta}_2'$. It therefore follows that $W_1\tilde{s}_2^2 = W_2\tilde{s}_1^2$, but the boundary conditions necessitate that $W_1 = W_2 := W$ and hence, $\tilde{s}_1 = \tilde{s}_2 := s$. Repeating arguments above, we obtain (3.2.16) so that $\tilde{\theta}_1 = \tilde{\theta}_2$ and this completes the proof. □

Theorem 3.2.4. *For $W \neq 0$, the unique solution, (s, θ) of (3.1.12), has the following symmetry properties:*

$$s(y) = s(-y) \text{ and } \theta(y) = -\theta(-y) \quad \forall y \in [-1,1].$$

Then s has a unique non-zero minimum at $y = \frac{1}{2}$.

Proof. It can be readily checked that for $W \neq 0$, the system of equations (3.1.12) admits a solution pair, (s, θ) such that s is even, and θ is odd for $y \in [-1, 1]$, compatible with the boundary conditions. Combining this observation with Theorem 3.2.2 and Theorem 3.2.3, the conclusion of the theorem follows. □

3.2.1 The Q-formulation

In our next results, we utilise the **Q**-formulation where we can study solutions with $\mathbf{Q} = \mathbf{0}$ or equivalently $s = 0$, without running into issues with the regularity of solutions. To this end, we now introduce the relevant quantities needed.

First, applying the scalings for y and $\mathbf{Q}$ in (3.1.9), to (3.1.5), we find the dimensionless free energy can be written in terms of the components of $\mathbf{Q}$ as follows:

$$F(\mathbf{Q}) = \int_{-1}^{1} (Q_{11}')^2 + (Q_{12}')^2 + \epsilon(Q_{11}^2 + Q_{12}^2)(2(Q_{11}^2 + Q_{12}^2) - 1)\, \mathrm{d}y. \tag{3.2.19}$$

The Euler-Lagrange equations of the functional (3.2.19) are:

$$Q_{11}'' = \epsilon Q_{11}(4(Q_{11}^2 + Q_{12}^2) - 1), \tag{3.2.20a}$$

$$Q_{12}'' = \epsilon Q_{12}(4(Q_{11}^2 + Q_{12}^2) - 1). \tag{3.2.20b}$$

Regarding boundary conditions, applying the Dirichlet conditions in (3.1.13) to (3.1.3), the boundary conditions are given in terms of Q_{11} and Q_{12} as:

$$Q_{11}(-1) = \frac{1}{2},\ Q_{11}(1) = \frac{1}{2}\cos(2\theta_1), \tag{3.2.21a}$$

$$Q_{12}(-1) = 0,\ Q_{12}(1) = \frac{1}{2}\sin(2\theta_1). \tag{3.2.21b}$$

We take our admissible space to be

$$\mathcal{A}_{\mathbf{Q}} := \left\{ \mathbf{Q} \in W^{1,2}(\Omega; S_0) :\ \mathbf{Q} \text{ satisfies the boundary conditions (3.2.21)} \right\}. \tag{3.2.22}$$

Remark 3.2.5. OR solutions can also be defined in the **Q**-formulation, although their signature is less obvious. OR solutions have $\mathbf{Q} = \mathbf{0}$ somewhere (i.e., a non-empty nodal set) and this implies we have a domain wall. An advantage of the **Q**-formulation, is that the governing equations and regularity of solutions, do not change between OR and non-OR solution, unlike the (s, θ)-formulation. Moreover, all solutions of (3.2.20) are analytic and we prove this in Theorem 3.2.8, but first, we draw a connection between the **Q**- and (s, θ)-formulations for $W > 0$.

Theorem 3.2.6. *The constant W, in* (3.1.16)*, is related to* **Q** *through the following equation*

$$2(Q_{12}'Q_{11} - Q_{11}'Q_{12})(y) = W \quad \forall y \in [-1, 1]. \tag{3.2.23}$$

Furthermore, for $W > 0$, so that $|\mathbf{Q}| = \sqrt{tr(\mathbf{Q}^2)} \neq 0$ and OR solutions are disallowed, if $\tilde{\mathbf{Q}}$ is a (classical) solution to the **Q***-Euler-Lagrange equations* (3.2.20)*,*

then $(\tilde{s}, \tilde{\theta})$ *given by* (3.1.15) *with* $\tilde{\theta} \geq 0$ *for all* $y \in \Omega$*, is a (classical) solution to the* (s, θ)*-Euler-Lagrange equations* (3.1.12)*. Similarly, for* $W > 0$*, so that* $s \neq 0$ *and OR solutions are disallowed, if* $(\tilde{s}, \tilde{\theta})$ *is a (classical) solution to the* (s, θ)*-Euler-Lagrange equations* (3.1.12)*, then* $\tilde{\mathbf{Q}}$ *given by* (3.1.3)*, is a (classical) solution to the* $\mathbf{Q}$*-Euler-Lagrange equations* (3.2.20)*. Hence, for a fixed* ϵ *and fixed* θ_1 *such that* $W > 0$ *only in* (3.2.23)*, we have a unique solution in the* $\mathbf{Q}$*-formulation.*

Proof. In this proof, we consider all solutions to be classical. Let $(\tilde{Q}_{11}, \tilde{Q}_{12})$ be a solution of the $\tilde{\mathbf{Q}}$-Euler-Lagrange equations (3.2.20), such that $|\mathbf{Q}| \neq 0$. Using (3.1.15) we can construct the corresponding $(\tilde{s}, \tilde{\theta})$-profiles (note, for θ given by (3.1.15), θ' is continuous away from $Q_{11} = Q_{12} = 0$) and check that they satisfy the (s, θ)-Euler-Lagrange equations (3.1.12). Note, we must require that $\tilde{\theta}$ given by (3.1.15) is non-negative in view of (3.1.17). First, calculating the required derivatives we have

$$\tilde{s}' = \frac{2(\tilde{Q}_{11}\tilde{Q}'_{11} + \tilde{Q}_{12}\tilde{Q}'_{12})}{\sqrt{\tilde{Q}_{11}^2 + \tilde{Q}_{12}^2}}, \tag{3.2.24}$$

$$\tilde{s}'' = -\frac{2(\tilde{Q}_{11}\tilde{Q}'_{11} + \tilde{Q}_{12}\tilde{Q}'_{12})^2}{\left(\tilde{Q}_{11}^2 + \tilde{Q}_{12}^2\right)^{\frac{3}{2}}} + \frac{2((\tilde{Q}'_{11})^2 + \tilde{Q}_{11}\tilde{Q}''_{11} + \tilde{Q}_{12}\tilde{Q}''_{12} + (\tilde{Q}'_{12})^2)}{\sqrt{\tilde{Q}_{11}^2 + \tilde{Q}_{12}^2}}, \tag{3.2.25}$$

$$\tilde{\theta}' = \frac{1}{2}\left(\frac{\tilde{Q}'_{12}\tilde{Q}_{11} - \tilde{Q}'_{11}\tilde{Q}_{12}}{\tilde{Q}_{11}^2 + \tilde{Q}_{12}^2}\right). \tag{3.2.26}$$

Therefore,

$$(\tilde{s}^2\tilde{\theta}')' = 2(\tilde{Q}''_{12}\tilde{Q}_{11} + \tilde{Q}'_{12}\tilde{Q}'_{11} - \tilde{Q}'_{11}\tilde{Q}'_{12} - \tilde{Q}''_{11}\tilde{Q}_{12}) = 0$$

$$\implies \tilde{s}^2\tilde{\theta}' = 2(\tilde{Q}'_{12}\tilde{Q}_{11} - \tilde{Q}'_{11}\tilde{Q}_{12}) = W, \tag{3.2.27}$$

where W is as in (3.1.16). Hence, $(\tilde{s}, \tilde{\theta})$ given by (3.1.15) (where $\tilde{\mathbf{Q}}$ satisfies (3.2.20)) satisfy (3.1.12b). Note, $|\mathbf{Q}| = \sqrt{2(Q_{11}^2 + Q_{12}^2)}$, hence if $W > 0$, we see

from (3.2.23), that $|\mathbf{Q}| \neq 0$. Moving on, we have

$$\begin{aligned}\tilde{s}'' - 4\tilde{s}\left(\tilde{\theta}'\right)^2 - \epsilon\tilde{s}(\tilde{s}^2-1) = &-\frac{2(\tilde{Q}_{11}\tilde{Q}'_{11}+\tilde{Q}_{12}\tilde{Q}'_{12})^2}{\left(\tilde{Q}_{11}^2+\tilde{Q}_{12}^2\right)^{\frac{3}{2}}}\\ &+\frac{2((\tilde{Q}'_{11})^2+\tilde{Q}_{11}\tilde{Q}''_{11}+\tilde{Q}_{12}\tilde{Q}''_{12}+(\tilde{Q}'_{12})^2)}{\sqrt{\tilde{Q}_{11}^2+\tilde{Q}_{12}^2}}\\ &-\frac{2(\tilde{Q}_{11}\tilde{Q}'_{12}-\tilde{Q}_{12}\tilde{Q}'_{11})^2}{(\tilde{Q}_{11}^2+\tilde{Q}_{12}^2)^{\frac{3}{2}}} - 2\epsilon\sqrt{\tilde{Q}_{11}^2+\tilde{Q}_{12}^2}(4(\tilde{Q}_{11}^2+\tilde{Q}_{12}^2)-1).\end{aligned}$$

Pulling out a factor of $(\tilde{Q}_{11}^2+\tilde{Q}_{12}^2)^{-\frac{3}{2}}$, expanding and simplifying, we have

$$2\tilde{Q}_{11}^2\tilde{Q}''_{11}+2\tilde{Q}_{11}^2\tilde{Q}_{12}\tilde{Q}''_{12}+2\tilde{Q}_{12}^2\tilde{Q}_{11}\tilde{Q}''_{11}+2\tilde{Q}_{12}^3\tilde{Q}''_{12}-2\epsilon(\tilde{Q}_{11}^2+\tilde{Q}_{12}^2)^2(4(\tilde{Q}_{11}^2+\tilde{Q}_{12}^2)-1).$$

Using the Euler–Lagrange equations (3.2.20), this can be rewritten as

$$2\epsilon(\tilde{Q}_{11}^4+2\tilde{Q}_{11}^2\tilde{Q}_{12}^2+\tilde{Q}_{12}^4)(4(\tilde{Q}_{11}^2+\tilde{Q}_{12}^2)-1)-2\epsilon(\tilde{Q}_{11}^2+\tilde{Q}_{12}^2)^2(4(\tilde{Q}_{11}^2+\tilde{Q}_{12}^2)-1),$$

which is equal to zero, hence $(\tilde{s},\tilde{\theta})$ given by (3.1.15) (where $\tilde{\mathbf{Q}}$ satisfies (3.2.20)) satisfy (3.1.12a).

Let $(\tilde{s},\tilde{\theta})$ be solutions of the (s,θ)-Euler-Lagrange equations (3.1.12), such that $W > 0$. Constructing the corresponding $\tilde{\mathbf{Q}}$-profile using (3.1.3), we check if this satisfies the $\mathbf{Q}$-Euler-Lagrange equations (3.2.20). The required derivatives are

$$\begin{aligned}\tilde{Q}''_{11} &= \frac{\tilde{s}''}{2}\cos(2\tilde{\theta}) - 2\tilde{s}'\tilde{\theta}'\sin(2\tilde{\theta}) - \tilde{s}\tilde{\theta}''\sin(2\tilde{\theta}) - 2\tilde{s}(\tilde{\theta}')^2\cos(2\tilde{\theta}),\\ \tilde{Q}''_{12} &= \frac{\tilde{s}''}{2}\sin(2\tilde{\theta}) + 2\tilde{s}'\tilde{\theta}'\cos(2\tilde{\theta}) + \tilde{s}\tilde{\theta}''\cos(2\tilde{\theta}) - 2\tilde{s}(\tilde{\theta}')^2\sin(2\tilde{\theta}),\end{aligned}$$

from which (3.2.20a) and (3.2.20b) become

$$\frac{\tilde{s}''}{2}\cos(2\tilde{\theta}) - 2\tilde{s}'\tilde{\theta}'\sin(2\tilde{\theta}) - \tilde{s}\tilde{\theta}''\sin(2\tilde{\theta}) - 2\tilde{s}(\tilde{\theta}')^2\cos(2\tilde{\theta}) = \frac{\epsilon\tilde{s}}{2}\cos(2\tilde{\theta})(\tilde{s}^2-1), \tag{3.2.28}$$

$$\frac{\tilde{s}''}{2}\sin(2\tilde{\theta}) + 2\tilde{s}'\tilde{\theta}'\cos(2\tilde{\theta}) + \tilde{s}\tilde{\theta}''\cos(2\tilde{\theta}) - 2\tilde{s}(\tilde{\theta}')^2\sin(2\tilde{\theta}) = \frac{\epsilon\tilde{s}}{2}\sin(2\tilde{\theta})(\tilde{s}^2-1), \tag{3.2.29}$$

respectively. Multiplying (3.2.28) by $2\cos(2\tilde{\theta})$, (3.2.29) by $2\sin(2\tilde{\theta})$ and adding the results yields (3.1.12a), while multiplying (3.2.28) by $\sin(2\tilde{\theta})$, (3.2.29) by $-\cos(2\tilde{\theta})$ and adding the result yields (3.1.12b). Hence, $\tilde{\mathbf{Q}}$ given by (3.1.3) (where $(\tilde{s},\tilde{\theta})$ satisfy (3.1.12)), satisfy (3.2.20).

Finally, Theorem 3.2.3 implies we must also have a unique solution to (3.2.20) if $W > 0$ only in (3.2.23). From (3.1.3), any $\mathbf{Q}$ can be expressed in terms of (s,θ), hence, if there were two solutions to (3.2.20) with $W > 0$, they must have different (s,θ)-profiles, contradicting the uniqueness. □

Remark 3.2.7. Theorem 3.2.8 tells us we have a unique solution in the $\mathbf{Q}$-formulation, provided solutions with $W \leq 0$ do not exist for a given ϵ and θ_1. It follows, that we can in principle have non-uniqueness when OR solutions exist, which necessarily have $W = 0$, but also via the emergence of solutions with $W < 0$, and these need not be OR solutions (we verify this numerically in Section 3.4). This is different to the (s,θ)-formulation, where in Theorem 3.2.3, we proved uniqueness provided OR solutions do not exist. The probable reason for this, is that in the (s,θ)-formulation the director is orientable (i.e., the director is a vector and not a line field), since for non-OR solutions W is a fixed positive constant ensuring θ must be positive and increasing. However, in the $\mathbf{Q}$-formulation, W can be negative in (3.2.23), in which case solutions in the $\mathbf{Q}$-formulation cannot be solutions in the (s,θ)-formulation which necessarily have $W \geq 0$ for θ_1 positive.

Theorem 3.2.8. *For all $\epsilon \geq 0$, there exists a minimiser of the energy* (3.2.19)*, in the admissible space* (3.2.22)*. Moreover, all solutions of the system* (3.2.20) *are analytic. OR solutions as defined in Remark 3.2.5 are only compatible with*

the boundary condition $\theta_1 = \frac{\pi}{2}$.

Proof. The existence of an energy minimiser for (3.2.19) in $\mathcal{A}_{\mathbf{Q}}$, is immediate from the direct methods in the calculus of variations, for all ϵ and ω, and the minimiser is a classical solution of the associated Euler-Lagrange equations (3.2.20), for all ϵ and θ_1. In fact, using arguments in elliptic regularity, one can show that all solutions of the system (3.2.20) are analytic [65] (recall the discussion in Section 2.2).

Recall an OR solution necessarily has $W = 0$ by definition. Applying this to (3.2.23),

$$Q'_{12}Q_{11} - Q'_{11}Q_{12} = 0 \quad \forall y \in [-1, 1]. \tag{3.2.30}$$

Evaluating at $y = -1$, we see $Q'_{12}(-1) = 0$. Differentiating (3.2.30), we have $Q''_{12}Q_{11} - Q''_{11}Q_{12} = 0$, which evaluated at $y = -1$ yields, $Q''_{12}(-1) = 0$. We can keep repeating this process of differentiation and evaluation at $y = -1$ to deduce $Q^{(n)}_{12}(-1) = 0$, for all integers $n \geq 0$. Since Q_{12} is analytic, it follows $Q_{12} = 0$ on Ω. For this to be compatible with the boundary conditions $Q_{12}(1) = \frac{1}{2}\sin(2\theta_1)$, it follows $\theta_1 = \frac{\pi}{2}$. □

Properties of the OR solution-branch have been studied in detail, in a one-dimensional setting, in the **Q**-framework [64]. Using the arguments in [64], one can prove that for $\theta_1 = \frac{\pi}{2}$, OR solutions exist for all $\epsilon \geq 0$ and an OR solution is the unique energy minimiser for sufficiently small ϵ, hence they are globally stable as $\epsilon \to 0$, but lose stability as ϵ increases. In particular, non-OR solutions emerge as ϵ increases for $\theta_1 = \frac{\pi}{2}$, which are stable, and these non-OR solutions do not have polydomain structures.

3.3 The limiting problem

In this section, we rigorously study the $\epsilon \to 0$ limit, which is physically relevant for nano-scale geometries (also see [79]). We compute the exact solutions of both (3.1.12) and (3.2.20), i.e. the (s, θ)- and $\mathbf{Q}$-formulations respectively, and show that they are in fact equivalent. We also directly verify the properties of solutions presented in Theorem 3.2.2, Theorem 3.2.4, and Theorem 3.2.8.

3.3.1 The (s, θ)-formulation

In the $\epsilon \to 0$ limit, equations (3.1.12a) and (3.1.12b) reduce to

$$s'' - 4s(\theta')^2 = 0, \tag{3.3.1a}$$

$$s^2\theta' = W. \tag{3.3.1b}$$

We again solve this system subject to the boundary conditions (3.1.13).

First, consider the case $W = 0$, so that one of s or θ' is zero at every point in Ω. (3.3.1a) reduces to the Laplace equation and we find

$$s = ay + b, \text{ for } a, b \in \mathbb{R}. \tag{3.3.2}$$

Since $W = 0$, $s(y^*) = 0$ at some interior point y^*, where θ has a discontinuous jump to satisfy its conflicting boundary conditions. The linear profile (3.3.2), cannot satisfy both boundary conditions and be zero somewhere, hence s must be defined piecewise. In principle, we could define s to be asymmetric, but for simplicity, we assume a symmetric solution with one zero, i.e.

$$s(y) = \begin{cases} -y & \text{for } y \in [-1, 0], \\ y & \text{for } y \in [0, 1]. \end{cases} \tag{3.3.3}$$

It follows that

$$\theta(y) = \begin{cases} 0 \text{ for } y \in [-1, 0) \\ \\ \theta_1 \text{ for } y \in (0, 1]. \end{cases} \tag{3.3.4}$$

Remark 3.3.1. This limiting computation, explicitly highlights how in the (s, θ)-formulation, OR solutions can be compatible with any value of θ_1. In contrast, Theorem 3.2.8 tells us OR solutions are compatible with $\theta_1 = \frac{\pi}{2}$ only, in the **Q**-formalism. This demonstrates why both formulations are required to gain a complete picture.

We now explicitly compute the unique solution of the system (3.3.1) for $W \neq 0$, and verify the conclusions of Theorem 3.2.2 and Theorem 3.2.4.

Proposition 3.3.2. *For $W > 0$, the solutions to the limiting equations* (3.3.1a) *and* (3.3.1b)*, are*

$$s(y) = \sqrt{\left(\frac{1 - \cos(2\theta_1)}{2}\right) y^2 + \frac{\sin^2(2\theta_1)}{2(1 - \cos(2\theta_1))}}, \tag{3.3.5a}$$

$$\theta(y) = \frac{1}{2}\tan^{-1}\left(\frac{(1 - \cos(2\theta_1))y}{\sin(2\theta_1)}\right) + \frac{1}{2}\tan^{-1}\left(\frac{1 - \cos(2\theta_1)}{\sin(2\theta_1)}\right), \tag{3.3.5b}$$

where $y \in [-1, 1]$. Moreover, s is symmetric and has a single non-zero minimum given by

$$s_{min} = s\,(0) = \frac{\sin(2\theta_1)}{\sqrt{2(1 - \cos(2\theta_1))}}. \tag{3.3.6}$$

Proof. Taking $W > 0$ and substituting for θ' using (3.3.1b) in (3.3.1a), we have

$$s'' - 4W^2 s^{-3} = 0. \tag{3.3.7}$$

The above equation is well defined and the solution s must be smooth. Let $s' = u$, so that

$$s'' = u' = \frac{\mathrm{d}u}{\mathrm{d}s}\frac{\mathrm{d}s}{\mathrm{d}y} = \frac{\mathrm{d}u}{\mathrm{d}s}u$$

and (3.3.7) becomes

$$\frac{\mathrm{d}u}{\mathrm{d}s}u = 4W^2 s^{-3}.$$

Thus is separable and integrating we obtain

$$s' = \pm\sqrt{J^2 - 4W^2 s^{-2}}. \tag{3.3.8}$$

Setting (3.3.8) equal to zero, we have two extrema

$$s = \pm\sqrt{\frac{4W^2}{J^2}}. \tag{3.3.9}$$

Since $W \neq 0$, s cannot be negative and the negative root above can be ruled out, hence s has a single minimum. The expression (3.3.8) is also separable, so integrating again we have

$$\begin{aligned} \pm(y+E) &= \int (J^2 - 4W^2 s^{-2})^{-\frac{1}{2}}\, \mathrm{d}s \\ &= \frac{2W}{J^2}\sqrt{\left(\frac{J}{2W}\right)^2 s^2 - 1}, \end{aligned} \tag{3.3.10}$$

hence,

$$s = \pm\sqrt{J^2(y+E)^2 + \frac{4W^2}{J^2}}, \tag{3.3.11}$$

for some constant E. Since $W \neq 0$, s cannot be negative anywhere and we can ignore the negative solution. Imposing the boundary conditions,

$$s(-1) = \sqrt{J^2(E-1)^2 + \frac{4W^2}{J^2}} = 1 \implies J^2E^2 + \frac{4W^2}{J^2} + J^2 - 2EJ^2 = 1, \tag{3.3.12}$$

and

$$s(1) = \sqrt{J^2(1+E)^2 + \frac{4W^2}{J^2}} = 1 \implies J^2E^2 + \frac{4W^2}{J^2} + J^2 + 2EJ^2 = 1.$$

Therefore,

$$4EJ^2 = 0 \implies E = 0.$$

Returning to (3.3.12), this yields

$$J_{\pm}^2 = \frac{1 \pm \sqrt{1 - 16W^2}}{2}. \tag{3.3.13}$$

Taking $E = 0$ in (3.3.11), we see that s attains its minimum in (3.3.9) at $y = 0$. Therefore,

$$s(y) = \sqrt{J_{\pm}^2 y^2 + \frac{4W^2}{J_{\pm}^2}}, \tag{3.3.14}$$

and s is symmetric about $y = 0$.

We can now use s, to solve for θ in (3.3.1b). Integrating we have

$$\begin{aligned} \theta + G &= \int \frac{W J_{\pm}^2}{J_{\pm}^4 y^2 + 4W^2} \, \mathrm{d}y \\ &= \frac{1}{2} \tan^{-1}\left(\frac{J_{\pm}^2 y}{2W}\right), \end{aligned}$$

(for G a constant of integration) so that

$$\theta(y) = \frac{1}{2} \tan^{-1}\left(\frac{J_{\pm}^2 y}{2W}\right) - G. \tag{3.3.15}$$

Imposing the boundary conditions,

$$\theta(-1) = \frac{1}{2} \tan^{-1}\left(-\frac{J_{\pm}^2}{2W}\right) - G = 0 \implies G = \frac{1}{2} \tan^{-1}\left(-\frac{J_{\pm}^2}{2W}\right) \tag{3.3.16}$$

and

$$\theta(1) = \frac{1}{2}\left(\tan^{-1}\left(\frac{J_{\pm}^2}{2W}\right) - \tan^{-1}\left(-\frac{J_{\pm}^2}{2W}\right)\right) = \tan^{-1}\left(\frac{J_{\pm}^2}{2W}\right) = \theta_1,$$

where in the second equality we have used the fact that $\tan^{-1}$ is odd. Solving for W,

$$\begin{aligned} \tan^{-1}\left(\frac{J_{\pm}^2}{2W}\right) = \theta_1 &\implies 4W \tan(\theta_1) = 1 \pm \sqrt{1 - 16W^2} \\ &\implies 8W(2W(\tan^2(\theta_1) + 1)) - \tan(\theta_1)) = 0 \end{aligned}$$

$$\implies W = 0 \quad \text{or} \quad W = \frac{\tan(\theta_1)}{2(\tan^2(\theta_1)+1)} = \frac{1}{4}\sin(2\theta_1). \tag{3.3.17}$$

We therefore need the second value of W in (3.3.17) and combining this with (3.3.13), it follows $J_{\pm}^2 = \frac{1\pm\cos(2\theta_1)}{2}$. The choice of the positive or negative root for $J_{\pm}^2$, depends on the boundary condition θ_1. Taking $y = 1$, we have

$$\begin{aligned} \theta(1) = \tan^{-1}\left(\frac{J_{\pm}^2}{2\sin(2\theta_1)}\right) &= \theta_1 \\ \implies \tan(\theta_1) &= \frac{1 \pm 1\cos(2\theta_1)}{\sin(2\theta_1)} \\ \implies 2\sin^2(\theta_1) - 1 &= \pm\cos(2\theta_1), \end{aligned} \tag{3.3.18}$$

and this only holds for the negative root, therefore,

$$J^2 = \frac{1-\cos(2\theta_1)}{2}. \tag{3.3.19}$$

Combing the definitions of J (3.3.19), W (3.3.17) and G (3.3.16), in (3.3.14) and (3.3.15), yields the required solutions. Finally, recalling (3.3.9), and again utilising the definitions of J (3.3.19) and W (3.3.17), we see the minimum value of s is determined by (3.3.6).

□

Remark 3.3.3. We note that as $\theta_1 \to \frac{\pi}{2}$ and hence $W \to 0$, (3.3.5a) reduces to (3.3.3), and for (3.3.5b), we have

$$\lim_{\theta_1 \to \frac{\pi}{2}} \theta = \begin{cases} 0 \text{ for } y \in [-1, 0) \\ \frac{\pi}{2} \text{ for } y \in (0, 1], \end{cases}$$

which agrees with (3.3.4) when $\theta_1 = \frac{\pi}{2}$.

3.3.2 The Q-formulation

Let us now consider the limiting problem for the **Q**-formulation. From the maximum principle, $||\mathbf{Q}||_{L^\infty}$ is bounded independently of ϵ, so in the $\epsilon \to 0$ limit, (3.2.20a) and (3.2.20b) reduce to

$$Q''_{11} = 0, \quad Q''_{12} = 0, \tag{3.3.20}$$

subject to the boundary conditions (3.2.21). These are just the Laplace equations for Q_{11} and Q_{12}, which admit the following unique solutions,

$$Q_{11,0}(y) = \frac{1}{4}(1 - (\cos(2\theta_1))y + \cos(2\theta_1) + 1), \tag{3.3.21a}$$

$$Q_{12,0}(y) = \frac{1}{4}\sin(2\theta_1)(y+1). \tag{3.3.21b}$$

Substituting (3.3.21a) and (3.3.21b), into (3.1.15), we get the following expressions for s and θ:

$$s_0 = \sqrt{\frac{1}{2}(1-\cos(2\theta_1))y^2 + \frac{1}{2}(1+\cos(2\theta_1)}, \tag{3.3.22a}$$

$$\theta_0 = \frac{1}{2}\text{atan2}\left(\sin(2\theta_1)(y+1), (\cos(2\theta_1)-1)y + \cos(2\theta_1) + 1\right). \tag{3.3.22b}$$

From Proposition 3.1 in [89], we know the limiting profiles (3.3.21a) and (3.3.21b) are good approximations to solutions of (3.2.20) for small ϵ. In fact, for a solution $\mathbf{Q}_\epsilon$ of (3.2.20), we have the following error bounds as $\epsilon \to 0$

$$||Q_{1i,\epsilon} - Q_{1i,0}||_{L^\infty} \leq P\epsilon, \tag{3.3.23}$$

where $P > 0$ is a constant independent of ϵ. However, no such result is known for the (s, θ) formulation and the limiting profiles (3.3.5a) and (3.3.5b). Next, we prove (3.3.22a) and (3.3.22b), are equivalent to (3.3.5a) and (3.3.5b) respectively, for $W > 0$ (hence verifying Theorem 3.2.6 when $\epsilon = 0$). Combined with the

accuracy of the limiting **Q**-solution, this suggests (3.3.5a) and (3.3.5b), are good approximations to solutions of the system (3.1.18) for small ϵ.

Proposition 3.3.4. *For $W > 0$, the s-solution profiles* (3.3.5a) *and* (3.3.22a)*, and the θ-solution profiles* (3.3.5b) *and* (3.3.22b)*, are equivalent.*

Proof. Agreement of the solution profiles from the (s, θ)- and **Q**-formulations, can be checked via direct computation. Agreement of the s-profiles (3.3.5a) and (3.3.22a), is immediate after noticing

$$\frac{\sin^2(2\theta_1)}{2(1-\cos(2\theta_1))} = \frac{1-\cos^2(2\theta_1)}{2(1-\cos(2\theta_1))} = \frac{(1-\cos(2\theta_1))(1+\cos(2\theta_1))}{2(1-\cos(2\theta_1))}.$$

We now move onto the θ-profiles. Using the identity

$$\tan^{-1}(x)+\tan^{-1}(y) = \begin{cases} \tan^{-1}\left(\frac{x+y}{1-xy}\right), & \text{for } xy<1 \\ \tan^{-1}\left(\frac{x+y}{1-xy}\right)+\pi, & \text{for } x>0,\ y>0,\ xy>1 \\ \tan^{-1}\left(\frac{x+y}{1-xy}\right)-\pi, & \text{for } x<0,\ y<0,\ xy>1, \end{cases}$$

with $x = \frac{(1-\cos(2\theta_1))y}{\sin(2\theta_1)}$ and $y = \frac{1-\cos(2\theta_1)}{\sin(2\theta_1)}$, (3.3.5b) becomes

$$\theta = \begin{cases} \frac{1}{2}\tan^{-1}\left(\frac{\sin(2\theta_1)(y+1)}{(\cos(2\theta_1)-1)y+\cos(2\theta_1)+1}\right), & \text{for } xy<1 \\ \frac{1}{2}\tan^{-1}\left(\frac{\sin(2\theta_1)(y+1)}{(\cos(2\theta_1)-1)y+\cos(2\theta_1)+1}\right)+\frac{\pi}{2}, & \text{for } x>0,\ y>0,\ xy>1 \\ \frac{1}{2}\tan^{-1}\left(\frac{\sin(2\theta_1)(y+1)}{(\cos(2\theta_1)-1)y+\cos(2\theta_1)+1}\right)-\frac{\pi}{2}, & \text{for } x<0,\ y<0,\ xy>1. \end{cases}$$

If $(\cos(2\theta_1)-1)y+\cos(2\theta_1)+1=0$ and $\sin(2\theta_1)(y+1)>0$ the above expression is undefined, hence we set $\theta = \frac{\pi}{4}$ in this case. Similarly, if $(\cos(2\theta_1)-1)y+\cos(2\theta_1)+1=0$ and $\sin(2\theta_1)(y+1)<0$, we set $\theta = -\frac{\pi}{4}$. If $(\cos(2\theta_1)-1)y+\cos(2\theta_1)+1=0$ and $\sin(2\theta_1)(y+1)=0$ an angle cannot be defined. Finally, looking at the

argument of $\tan^{-1}$ above, we can redefine this as follows

$$\theta = \begin{cases} \frac{1}{2}\tan^{-1}\left(\frac{\sin(2\theta_1)(y+1)}{(\cos(2\theta_1)-1)y+\cos(2\theta_1)+1}\right), & \text{for } (\cos(2\theta_1)-1)y+\cos(2\theta_1)+1>0 \\ \frac{1}{2}\tan^{-1}\left(\frac{\sin(2\theta_1)(y+1)}{(\cos(2\theta_1)-1)y+\cos(2\theta_1)+1}\right)+\frac{\pi}{2}, & \text{for } (\cos(2\theta_1)-1)y+\cos(2\theta_1)+1<0, \\ & \sin(2\theta_1)(y+1)>0 \\ \frac{1}{2}\tan^{-1}\left(\frac{\sin(2\theta_1)(y+1)}{(\cos(2\theta_1)-1)y+\cos(2\theta_1)+1}\right)-\frac{\pi}{2}, & \text{for } (\cos(2\theta_1)-1)y+\cos(2\theta_1)+1<0, \\ & \sin(2\theta_1)(y+1)<0. \end{cases}$$

Combined, this is just the definition of $\frac{1}{2}\text{atan2}(\sin(2\theta_1)(y+1), (\cos(2\theta_1)-1)y+\cos(2\theta_1)+1)$ with the case $\theta_1 = \frac{\pi}{2}$ and hence, $W = 0$ omitted, as required.

□

Using (3.3.22a), we again verify the symmetry of s-solutions (Theorem 3.2.2, Theorem 3.2.4), but we can additionally deal with solution profiles with $s = 0$ somewhere in Ω, and hence confirm OR solutions are compatibly with $\theta_1 = \frac{\pi}{2}$ only (Theorem 3.2.8).

Proposition 3.3.5. *Any solution s_0, to the limiting problem* (3.3.20) *is symmetric. Furthermore, any nontrivial solution s_0, for $\theta_1 \neq \frac{\pi}{2}$, has exactly one critical point at $y = 0$, which is a non-zero local minimum. For $\theta_1 = \frac{\pi}{2}$, s_0 has one minimum at $y = 0$, such that $s_0(0) = 0$.*

Proof. First consider the case $\theta_1 \neq \frac{\pi}{2}$. In this case it is sufficient to show that s_0 has one critical point and this occurs at $y = 0$. Differentiating (3.3.22a) and setting the result equal to zero, we have

$$s_0'(y) = \frac{(1-\cos(2\theta_1))y}{2\sqrt{\frac{1}{2}(1-\cos(2\theta_1))y^2+\frac{1}{2}(1+\cos(2\theta_1))}} = 0$$

$$\implies y = 0.$$

Hence, the solution to the limiting profile is symmetric and has one critical point at $y = 0$. Furthermore, by the maximum principle this must be a minimum.

Now let $\theta_1 = \frac{\pi}{2}$. From (3.3.22a), we see the solution is given by

$$s_0(y) = \begin{cases} -y & \text{for } y \in [-1, 0] \\ y & \text{for } y \in [0, 1], \end{cases}$$

which has a minimum value of 0 at $y = 0$, and this is the only point at which this occurs. Furthermore, the solution is symmetric.

To show $s_0(0) = 0$ when $\theta_1 = \frac{\pi}{2}$ only, first suppose $s_0(y) = 0$ for some $y \in [-1, 1]$. Then (3.3.22a) implies

$$\begin{aligned} &(1 - \cos(2\theta_1))y^2 + 1 + \cos(2\theta_1) = 0 \\ \implies\ &y^2 = \frac{-(1 + \cos(2\theta_1))}{1 - \cos(2\theta_1)} \leqslant 0, \end{aligned} \tag{3.3.24}$$

which is a contradiction unless $\theta_1 = \frac{\pi}{2}$. Therefore, $y = 0$ in this case and we conclude $s_0 \neq 0$ for $\theta_1 \neq \frac{\pi}{2}$ and $y \neq 0$. □

For completeness, and to elucidate the regularity of solution profiles, we include some example limiting profiles (3.3.22) along with plots in Figure 3.3. We point out that all the limiting profiles in Figure 3.3, agree with Proposition 3.3.2 and Proposition 3.3.5. We also see that as θ_1, decreases $s_0 \to 1$ everywhere, while θ_0 becomes more linear and tends to the constant solution $\theta_0 = 0$, as $\theta_1 \to 0$.

$$s_0(y) = \begin{cases} -y & y \in [-1, 0] \\ y & y \in [0, 1], \end{cases} \qquad \theta_0(y) = \begin{cases} 0 & y \in [-1, 0) \\ \frac{\pi}{2} & y \in (0, 1] \end{cases} \text{ for } \theta_1 = \frac{\pi}{2}. \tag{3.3.25}$$

Remark 3.3.6. From Remark 3.3.3, we see in the $\theta_1 \to \frac{\pi}{2}$ limit, (3.3.5a) and

(3.3.5b) agree with (3.3.22a) and (3.3.22b) when $\theta_1 = \frac{\pi}{2}$.

$$s_0(y) = \sqrt{\left(\frac{2+\sqrt{2}}{4}\right) y^2 + \frac{2-\sqrt{2}}{4}},$$
$$\theta_0(y) = \frac{1}{2}\text{atan2}\left(\frac{\sqrt{2}}{2}y, \frac{2-\sqrt{2}}{2} - \left(\frac{2+\sqrt{2}}{2}\right) y\right) \text{ for } \theta_1 = \frac{3\pi}{8}, \quad (3.3.26)$$

$$s_0(y) = \sqrt{\frac{1}{2}(y^2+1)}, \quad \theta_0(y) = \frac{1}{2}\text{atan2}\left(y, 1-y\right) \text{ for } \theta_1 = \frac{\pi}{4}, \quad (3.3.27)$$

$$s_0(y) = \sqrt{\left(\frac{2-\sqrt{2}}{4}\right) y^2 + \frac{2+\sqrt{2}}{4}},$$
$$\theta_0(y) = \frac{1}{2}\text{atan2}\left(\frac{\sqrt{2}}{2}y, \frac{2+\sqrt{2}}{2} + \left(\frac{\sqrt{2}-1}{2}\right) y\right) \text{ for } \theta_1 = \frac{\pi}{8}. \quad (3.3.28)$$

3.4 Numerics

In this section, we numerically explore solutions for different boundary conditions θ_1, and different values of ϵ. We solve the **Q**-Euler-Lagrange equations (3.2.20), subject to the boundary conditions (3.2.21), by gradient flow methods. This is implemented in MATLAB [90] (unless stated otherwise, all numerics are produced in MATLAB in this thesis). We do not attempt to solve the (s, θ)-Euler-Lagrange equations (3.1.12), due to the issue of division by zero and because the equations are highly non-linear.

To find solutions of (3.2.20), we solve the following gradient flow equations [68]:

$$\frac{\partial Q_{11}}{\partial t} = Q_{11}'' + \epsilon Q_{11}(1 - 4(Q_{11}^2 + Q_{12}^2)), \quad (3.4.1a)$$
$$\frac{\partial Q_{12}}{\partial t} = Q_{12}'' + \epsilon Q_{12}(1 - 4(Q_{11}^2 + Q_{12}^2)). \quad (3.4.1b)$$

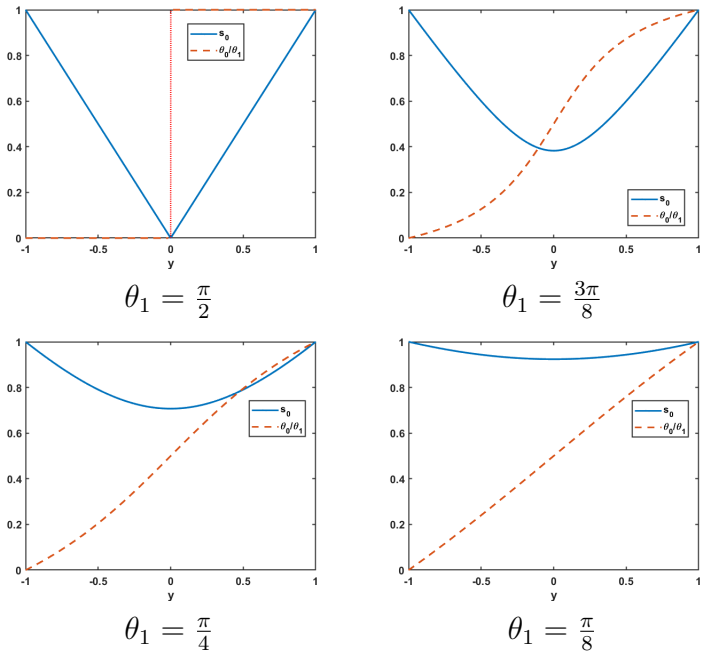

Figure 3.3: Example limiting profiles. Here, we plot (3.3.22a) and (3.3.22b) for the stated values of θ_1. The θ/θ_1 profile is discontinuous at $y = 0$, which is represented with a doted line (the same is true for subsequent plots).

The principle here, is that for long enough times solutions of the gradient flow equations evolve to minimisers (or critical points) of the free energy (3.2.19), i.e., they are steady solutions which satisfy $\frac{\partial Q_{1i}}{\partial t} = 0$, so that $\mathbf{Q}$ is a solution of (3.2.20). We solve (3.4.1) using finite difference methods in the spatial direction, by partitioning the domain $[-1, 1]$ into a uniform mesh with mesh size $1/50$, and use Euler's method in the time direction. Unless stated otherwise, we use the limiting profiles (3.3.21) as our initial conditions for computing solutions for all values of ϵ and θ_1. We deem the solution to have converged, when the norm of the gradient has fallen below 10^{-6} i.e.,

$$\left\| \begin{pmatrix} Q_{11}'' + \epsilon Q_{11}(1 - 4(Q_{11}^2 + Q_{12}^2)) \\ Q_{12}'' + \epsilon Q_{12}(1 - 4(Q_{11}^2 + Q_{12}^2)) \end{pmatrix} \right\|_{L^2} < 10^{-6}. \tag{3.4.2}$$

3.4.1 Accuracy of the limiting profiles

We begin by comparing the limiting profiles (3.3.22a) and (3.3.22b), to the numerical solution for small values of ϵ and different boundary conditions θ_1, to assess how good of an approximation they are. In this and later sections, we first solve the **Q**-Euler-Lagrange equations (3.2.20), and then simply extract the (s, θ)-profiles using (3.1.15).

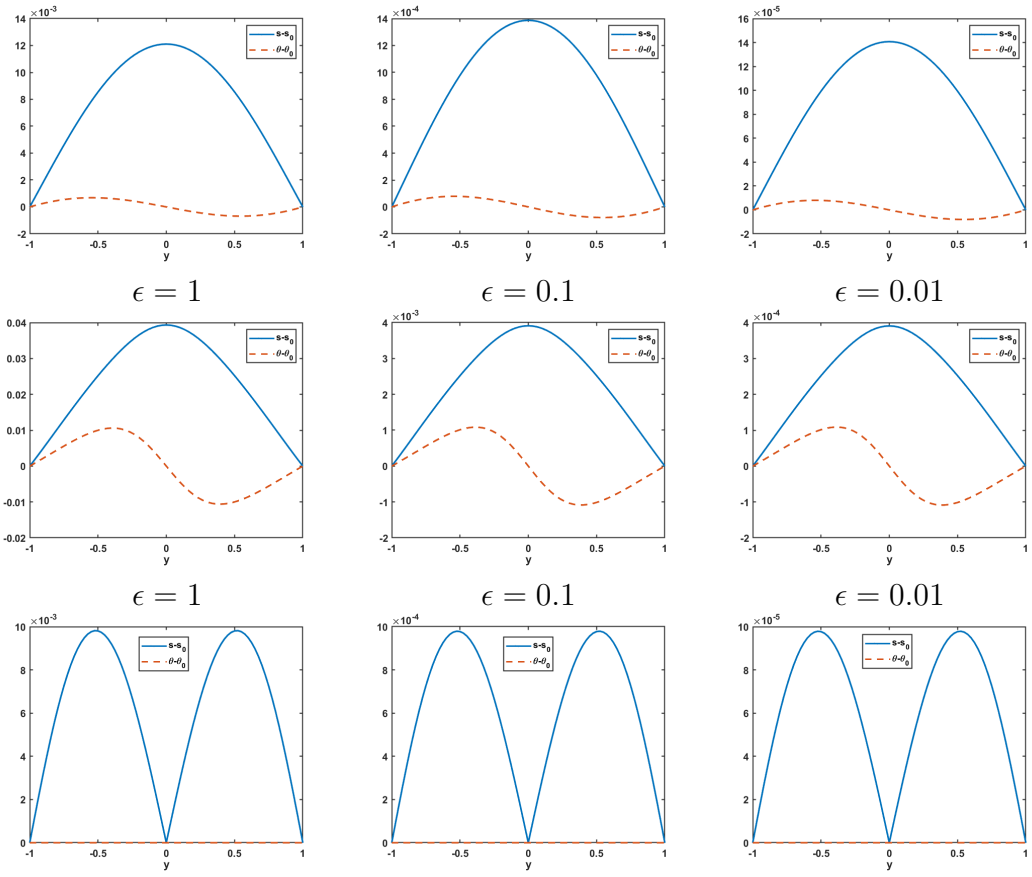

Figure 3.4: Error between the numerical solution to (3.2.20) (denoted by (s, θ)) and the limiting profiles (3.3.22a) and (3.3.22b), for different values of ϵ, when $\theta_1 = \frac{\pi}{8}$ (first row), $\theta_1 = \frac{\pi}{3}$ (second row), and $\theta_1 = \frac{\pi}{2}$ (third row).

In Figure 3.4, we plot the error (i.e., the difference) between the numerical solution

and the limiting profiles (3.3.22a) and (3.3.22b), for $\theta_1 = \frac{\pi}{8}, \frac{\pi}{3}, \frac{\pi}{2}$, each with $\epsilon = 0.01,\ 0.1,\ 1$. For all values of θ_1 and ϵ considered, the error is small for both s and θ (it does not exceed 0.04), and it decreases as ϵ decreases, so that we have excellent agreement for $\epsilon = 0.01$ and all choices of θ_1. In fact, we have perfect agreement between the θ-profiles (away from the discontinuity at $y = 0.5$ and this point has been omitted) when $\theta_1 = \frac{\pi}{2}$, for all values of ϵ considered.

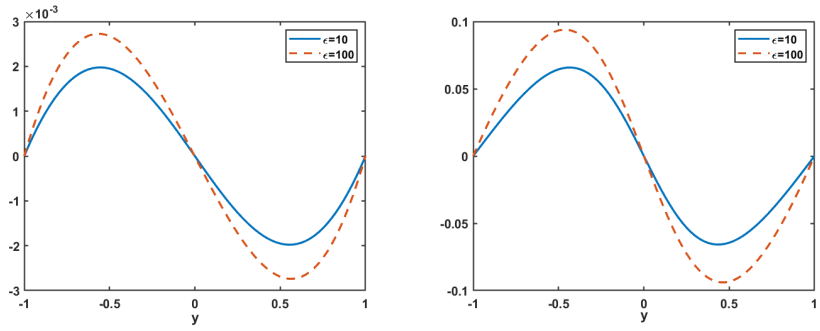

$\theta_1 = \frac{\pi}{8}$ $\theta_1 = \frac{\pi}{3}$

Figure 3.5: Error between the numerical solution to (3.2.20) and the limiting profiles (3.3.22b) (i.e. $\theta - \theta_0$), for large values of ϵ, when $\theta_1 = \frac{\pi}{8}$ and $\theta_1 = \frac{\pi}{3}$.

In Figure 3.4, the error in our limiting θ-profiles is always smaller than the error in our limiting s-profiles. This suggest they may still be good approximations for large values of ϵ. To this end, we look at the accuracy of the limiting θ-profiles for $\epsilon = 10, 100$, when $\theta_1 = \frac{\pi}{8}$ and $\theta_1 = \frac{\pi}{3}$ (see Figure 3.5). The limiting profile (3.3.22b), is still an excellent approximation to the numerical solution for $\theta_1 = \frac{\pi}{8}$, since the maximum error is of the order 10^{-3}. However, when $\theta_1 = \frac{\pi}{3}$, (3.3.22b) is no longer a good approximation, as the maximum error is almost 0.1. This suggests, not only does ϵ dictate the accuracy of our limiting profiles, but θ_1 does too. In Figure 3.6, we plot the error between the θ-profiles for $\epsilon = 0.1$ and four values of θ_1. As we increase θ_1 in $(0, \frac{\pi}{2})$, the maximum error increases. A possible explanation for this is, for larger values of θ_1 there is necessarily greater distortion

of the θ-profile, which is less well approximated by (3.3.22b).

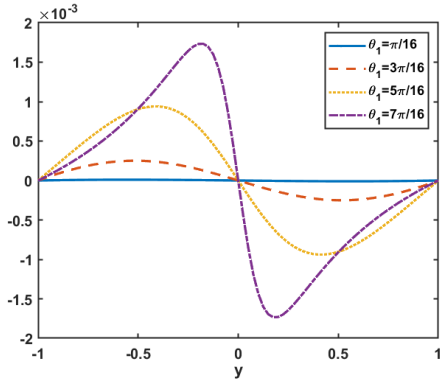

Figure 3.6: Error between the numerical solution and the limiting profile (3.3.22b) (i.e. $\theta - \theta_0$), for $\epsilon = 0.1$ and different values of θ_1.

3.4.2 Uniqueness in the (s, θ)-formulation

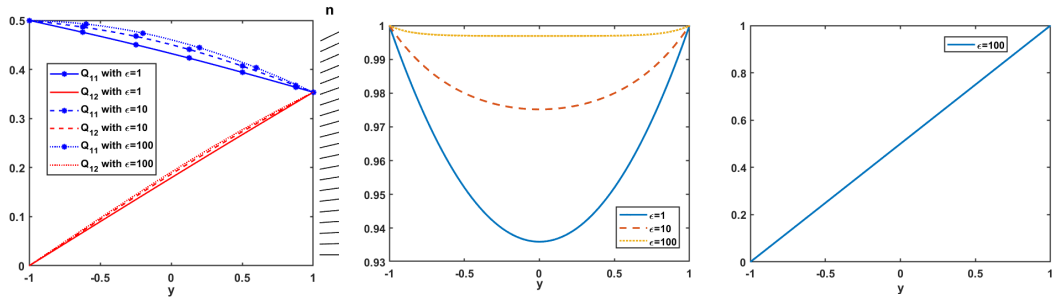

(a) (b) (c)

Figure 3.7: (a) plot of $\mathbf{Q}$ and (b) plot of s, for $\epsilon = 1, 10, 100$, and (c) plot of θ/θ_1 for $\epsilon = 100$ (the plots for $\epsilon = 1, 10$ look visually identical and are therefore omitted), all for $\theta_1 = \frac{\pi}{8}$. In (a), $\mathbf{n}$ is plotted for $\epsilon = 100$.

In this section, we study the effects of ϵ and θ_1 on the unique profile in the (s, θ)-formulation. From Theorem 3.2.6, this corresponds to the solution of (3.2.20) in the $\mathbf{Q}$-formulation with positive W. In this and the next section, the value of W is computed by numerically approximating (3.2.23). In Figure 3.7, Figure 3.8 and Figure 3.9, we plot the only numerical solution with $W > 0$ for $\theta_1 = \frac{\pi}{8}, \frac{\pi}{4}, \frac{3\pi}{8}$

respectively, when $\epsilon = 1, 10, 100$. We include the $\mathbf{n}$-profiles for $\epsilon = 100$ only in these cases, as there are minimal differences in rotation for the values of ϵ considered.

Looking at the $\mathbf{Q}$-profiles first (i.e., Figure 3.7 (a), Figure 3.8 (a), and Figure 3.9 (a)), we see that as ϵ increases, the Q_{11}- and Q_{12}-profiles deviate from their linear limiting profiles given in (3.3.21). Moreover, these deviations become more pronounced as θ_1 increases. For example, when $\theta_1 = \frac{\pi}{8}$, there is minimal difference between the solutions for $\epsilon = 1$ and $\epsilon = 100$, but there is a more substantial difference between the solutions for $\epsilon = 1$ and $\epsilon = 100$, when $\theta_1 = \frac{3\pi}{8}$. We note that, the directors corresponding to $\theta_1 = \frac{\pi}{8}$, $\theta_1 = \frac{\pi}{4}$ and $\theta_1 = \frac{3\pi}{8}$, in Figure 3.7 (a), Figure 3.8 (a) and Figure 3.9 (a) respectively, all rotate smoothly throughout the domain and are not polydomains, since none of the solutions $\mathbf{Q}$, are OR solutions. This is consistent with Theorem 3.2.8.

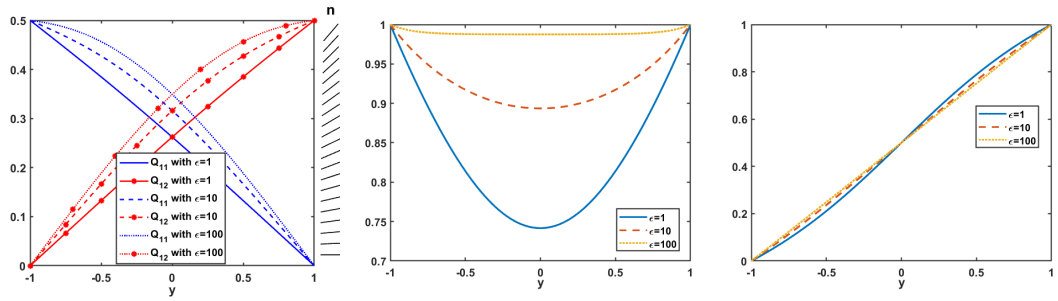

(a) (b) (c)

Figure 3.8: (a) plot of $\mathbf{Q}$, (b) plot of s, and (c) plot of θ/θ_1, for $\epsilon = 1, 10, 100$ and $\theta_1 = \frac{\pi}{4}$. In (a), $\mathbf{n}$ is plotted for $\epsilon = 100$.

Moving onto the associated (s, θ)-profiles, the results in Figure 3.7, Figure 3.8 and Figure 3.9, demonstrate that as θ_1 decreases (i.e, $\theta_1 \to 0$): (i) the θ-profiles become more linear and will eventually approach $\theta \equiv 0$, and (ii) $s \to 1$ everywhere. Comparing the θ/θ_1-profiles for the aforementioned figures, (i) is clear, and (ii)

can be spotted after noting that the single global minimum of s at $y = 0$ (as predicted in Theorem 4.2.3), increases as θ_1 decreases, for a fixed ϵ. We made these remarks in Section 3.3 too, but the results in this section, show these trends also hold true for numerical solutions of the Euler-Lagrange equations (3.2.20), for non-zero values of ϵ. On physical grounds these trends are perhaps not surprising. As we decrease θ_1 to zero, θ will become closer to a constant since $\theta(0) = 0$. Hence, the distortion of the director will decrease, and consequently, we would expect the order about the director to increase, therefore s should approach one. From Figure 3.7, Figure 3.8, and Figure 3.9, we also see that increasing ϵ has an analogous effect to decreasing θ_1, that is, as we increase ϵ, θ approaches a linear profile, whilst $s \to 1$.

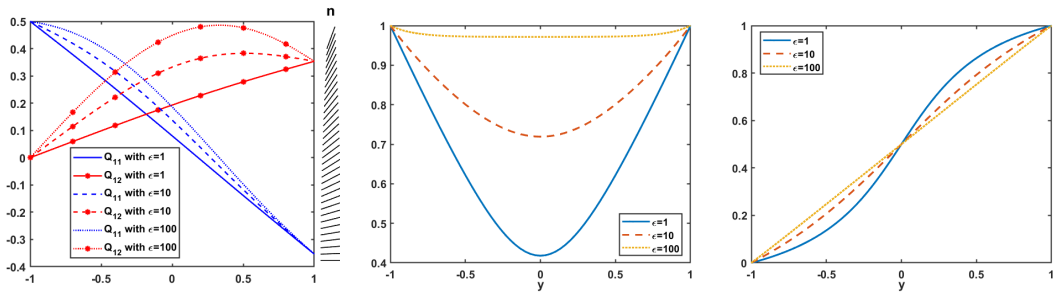

(a) (b) (c)

Figure 3.9: (a) plot of $\mathbf{Q}$, (b) plot of s, and (c) plot of θ/θ_1, for $\epsilon = 1, 10, 100$ and $\theta_1 = \frac{3\pi}{8}$. In (a), $\mathbf{n}$ is plotted for $\epsilon = 100$.

3.4.3 Non-uniqueness in the Q-formulation

We now explore the non-uniqueness that is permitted in the $\mathbf{Q}$-framework when $W \leq 0$ is allowed i.e., additional solutions of (3.2.20) with $W \leq 0$. We first focus in the case $\theta_1 = \frac{\pi}{2}$, as this is the special case that permits OR solutions. For $\epsilon < 12$ (approximately) and $\theta_1 = \frac{\pi}{2}$, we find only one critical point, indicating it is unique. This critical point is an OR solution since: (i) we have a domain

wall at $y = 0$ where $\mathbf{Q} = \mathbf{0}$, and (ii) extracting the corresponding (s, θ)-profiles, $s = 0$ at $y = 0$, while θ is piecewise constant away from $y = 0$, where it is has a discontinuous jump to satisfy its conflicting Dirichlet boundary conditions (see Figure 3.10). Moreover, we plot the director $\mathbf{n}$ and it is a polydomain ($\mathbf{n}$ denotes the director in all other plots too). For larger values of ϵ, this is no longer the case. In Figure 3.11, for $\epsilon = 1$ and $\epsilon = 30$, when $\theta_1 = \frac{\pi}{2}$, we find multiple solutions and hence, non-uniqueness. There are two solutions with non-zero non-constant Q_{12}, and as such, the director rotates smoothly over our domain and is not a polydomain i.e. they are not OR solutions. Both of these solutions can be distinguished by the sign of Q_{12} and hence the rotation of $\mathbf{n}$. These non-OR solutions are found by completing 100 simulations of our numerical scheme with random initial conditions (the entries of Q_{11} and Q_{12} are generated from a uniform distribution on $[-0.5, 0.5]$). We also find an OR solution (using (3.3.21) as our initial condition) and no other solutions. These conclusions are consistent with the results in [64].

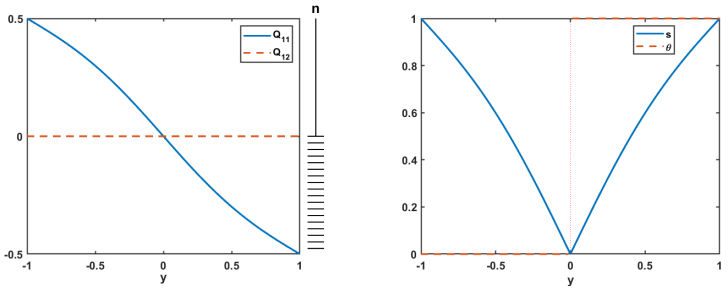

Figure 3.10: The only $\mathbf{Q}$-solution, and associated $(s, \theta/\theta_1)$-profiles for $\epsilon = 10$ and $\theta_1 = \frac{\pi}{2}$.

We briefly comment on the the (s, θ)-profiles in Figure 3.12, associated with the non-OR profiles in Figure 3.11 (the same comments as above apply to the OR solution). The profile associated to Non-OR 1, will be a solution of the (s, θ)-Euler-Lagrange equations (3.1.12), from Theorem 3.2.6. Both s and θ are smooth,

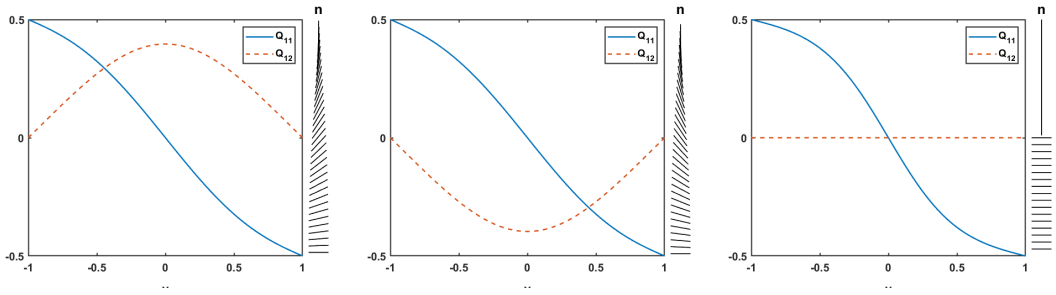

Non-OR 1 Non-OR 2 OR

Figure 3.11: Solutions for $\epsilon = 30$, when $\theta_1 = \frac{\pi}{2}$.

s has a single non-zero minimum, and s approaches one everywhere since ϵ is small. However, the θ-profile associated with Non-OR 2, will not be a solution of (3.1.12) since the inequalities $W \geq 0$ (Remark 3.1.1) and (3.1.17), are violated. This θ-profile is effectively the negative of θ in Non-OR 1. Note, this is still consistent with Theorem 3.2.6, since we require $\theta \geq 0$. The negativity and jump discontinuity in θ here, is a numerical artefact due to extracting it from $\mathbf{Q}$ using (3.1.15).

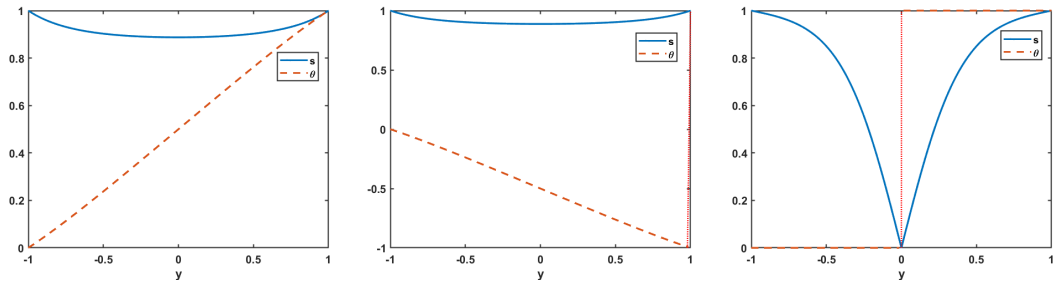

Non-OR 1 Non-OR 2 OR

Figure 3.12: The associated $(s, \theta/\theta_1)$-profiles for the solutions in Figure 3.11.

Moving on, we now consider the boundary conditions $\theta_1 = \frac{\pi}{8}, \frac{\pi}{4}, \frac{3\pi}{8}$, for $\epsilon = 100$, to demonstrate non-uniqueness when $W < 0$ is permitted. In Figure 3.13, Figure 3.14 and Figure 3.15, we plot two new $\mathbf{Q}$ solutions and their associated (s, θ)-profiles for $\theta_1 = \frac{\pi}{8}, \frac{\pi}{4}, \frac{3\pi}{8}$ respectively (see the previous section for the single solution with $W > 0$). These new solutions each have $W < 0$ and are found simulating

our numerical method 100 times with random initial conditions. The defining feature of these solutions with $W < 0$, is that the director rotates such that it is orthogonal to the channel walls at some point in the domain. This is a direct result of having negative W in (3.2.23), which ensures the corresponding director angle θ (as extracted from (3.1.15)) need not remain positive or be continuous throughout Ω, and this allows for non-uniqueness.

Although we have non-uniqueness when $\epsilon = 100$ for all three boundary conditions, uniqueness can be achieved for sufficiently small ϵ, as predicted by Lemma 8.2 in [64]. We find that as θ_1 increase, the value of ϵ for which we can have uniqueness decreases. Completing 100 simulations with random initial conditions for $\theta_1 = \frac{\pi}{8}, \frac{\pi}{4}, \frac{3\pi}{8}$, we find only one solution for $\epsilon = 87, 60, 35$ respectively, but three solutions for $\epsilon = 88, 61, 36$. For $\epsilon = 1, 10$ we find only one solution in all three cases (the unique solution with $W > 0$ predicted by Theorem 3.2.6), indicating we have a unique solutions for $\epsilon \leq 87, 60, 35$ when $\theta_1 = \frac{\pi}{8}, \frac{\pi}{4}, \frac{3\pi}{8}$ respectively. This demonstrates that boundary conditions can be used to tune the windows of uniqueness and multistability, not only material properties (i.e. K and A) and domain size (i.e. D) through ϵ. Finally, we note that for all boundary conditions and all values of ϵ, we find either one or three solutions.

3.5 Summary

In this chapter, we rigorously investigate the impact that the Dirichlet boundary conditions imposed on the nematic director have on the multiplicity of solutions. In the **Q**-formulation, when $\theta_1 = \frac{\pi}{2}$ (recall θ_1 is the angle between the director and the channel wall at $y = 1$ (see Figure 3.1)), we find a unique OR solution for small ϵ and non-uniqueness for large ϵ, consistent with the results in [64],

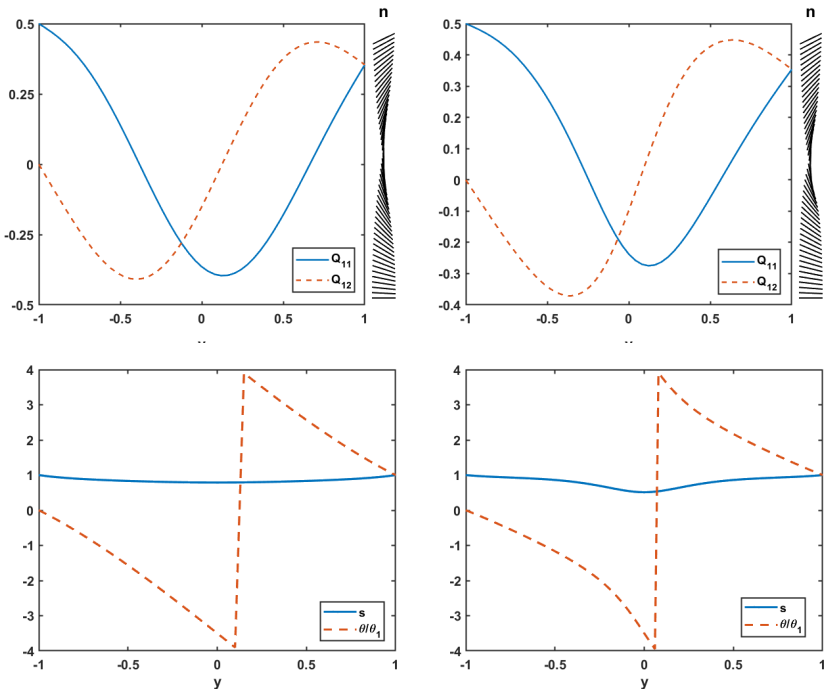

Figure 3.13: **Q** solutions of (3.2.20) with $W < 0$ when $\theta_1 = \frac{\pi}{8}$ and $\epsilon = 100$, with their associated (s, θ)-profiles plotted below.

but we additionally show this is the only boundary condition compatible with OR solutions. While in the (s, θ)-framework, we show we have a unique solution whenever an OR solution does not exist. As has been noted in [88], orthogonal boundary conditions allow for solutions in the **Q**-formalism (solutions of (3.2.20)) that have a constant set of eigenvectors in space, but non-constant eigenvalues. These solutions, with a constant set of eigenvectors, are precisely the OR solutions, which are disallowed for non-orthogonal boundary conditions. Thus, whilst the conclusion of Theorem 3.2.8 is not surprising, we now provide a proof of this fact. Hence, if polydomain structures are the goal in experiments, orthogonal boundary conditions on the channel walls should be the focus.

In Section 3.3, we study in detail the $\epsilon \to 0$ limit for both the (s, θ)- and **Q**-formulations. This limit is independent of bulk effects and therefore allows us to

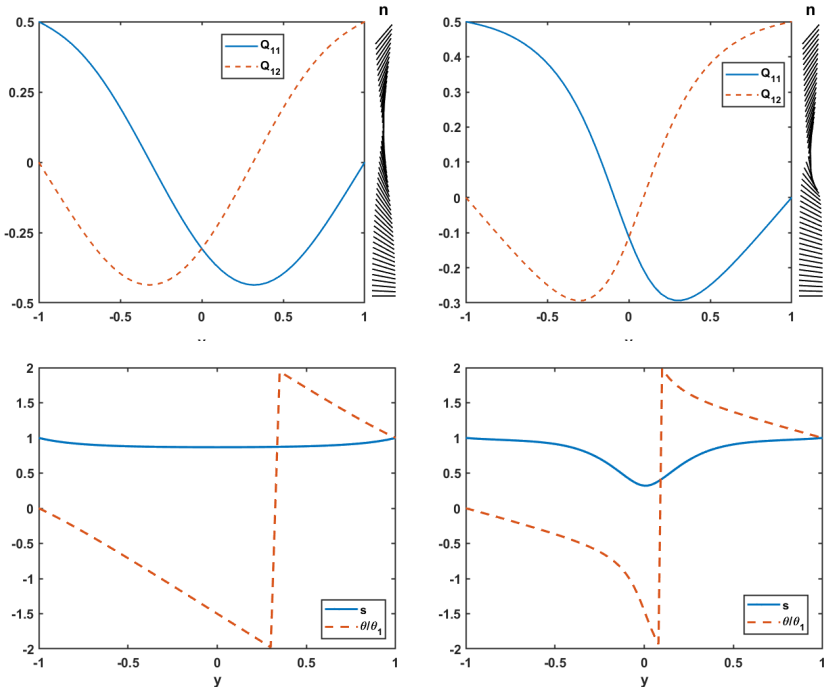

Figure 3.14: **Q** solutions of (3.2.20) with $W < 0$ when $\theta_1 = \frac{\pi}{4}$ and $\epsilon = 100$, with their associated (s, θ)-profiles plotted below.

explicitly solve the governing equations in both formulations, yielding useful and informative limiting profiles. As a result, we are able to independently verify many of the properties of solutions predicted in Section 3.2. In particular, we verify the symmetry of s profiles and that OR solutions are compatible with $\theta_1 = \frac{\pi}{2}$ only.

Finally, in Section 3.4, we numerically compute solutions of the **Q**-Euler-Lagrange equations. We begin by assessing the accuracy of the limiting profiles computed in Section 3.3, which as well as being excellent approximations to the numerical solutions for $\epsilon \leq 0.1$, are also good initial conditions for finding solutions with $W > 0$. When $W > 0$, and OR solutions are therefore not permitted, we find a unique (s, θ)-profile corresponding to the single solution in the **Q**-formulation with $W > 0$. This corroborates Theorem 3.2.3 and Theorem 3.2.6. For these profiles with $W > 0$, we investigate the effects of both θ_1 and ϵ on solution

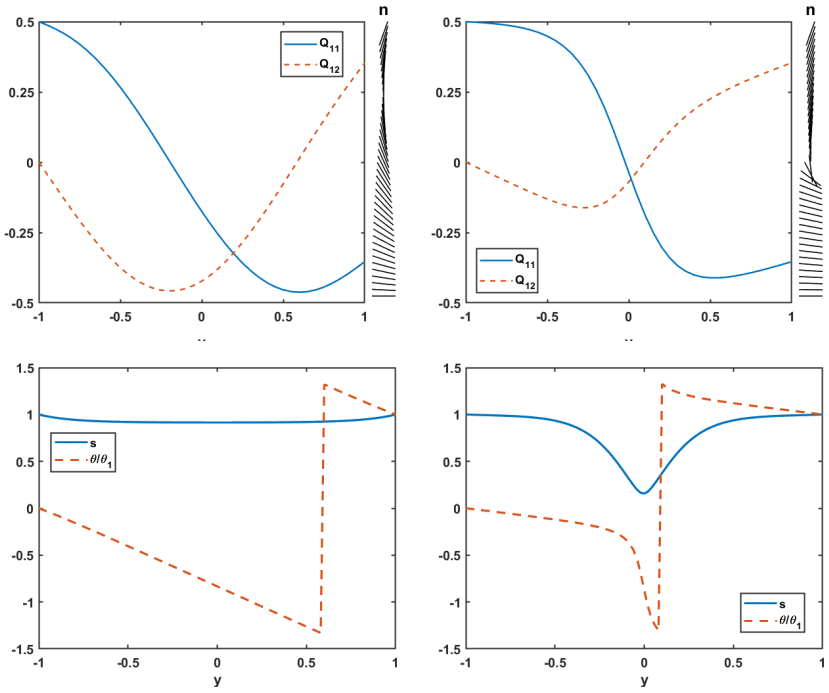

Figure 3.15: **Q** solutions of (3.2.20) with $W < 0$ when $\theta_1 = \frac{3\pi}{8}$ and $\epsilon = 100$, with their associated (s, θ)-profiles plotted below.

profiles, where we find decreasing θ_1, increasing ϵ, or both, lead to increased order about the nematic director $\mathbf{n}$, along with smoother and more gradual rotation of $\mathbf{n}$. When $W \leq 0$ is allowed, we find non-uniqueness in the $\mathbf{Q}$-formulation even for boundary conditions that do not permit OR solutions. This highlights the difference between the (s, θ)- and $\mathbf{Q}$-frameworks, and in particular, how solutions are lost in the (s, θ)-framework due to the physical equivalence of $\mathbf{n}$ and $-\mathbf{n}$ not being respected.

In Chapter 4, we build upon the work presented here as follows:

1. We show that many of the results in Section 3.2, can be applied to the dynamic setting of nematodynamics with constant fluid velocity and constant pressure.

2. We apply these analytical ingredients for flows with constant velocity and pressure, to gain informative insight into the complex cases of passive and active nematodynamics with non-constant flow and pressure.

Chapter 4

Passive and active nematodynamics

This chapter is derived from Dalby, Han, Majumdar and Mrad (2022) [1].

4.1 The problem

In this chapter, we seek to demonstrate the universality of order reconstruction (OR) solutions by investigating them in the context of passive and active nematodynamics, i.e., dynamic situations where our liquid crystal is able to flow. OR solutions are well understood for conventional nematics. We now show OR solutions exist for passive flows with constant velocity and pressure, whilst OR-type solutions (introduced in Section 4.3) can be found without such constraints for both passive and active nematic flows. Our present study focuses on long shallow channels relevant for microfluidic problems for which we employ the Beris-Edwards framework for nematodynamics. As in Chapter 3, we investigate the compatibility of OR solutions with certain boundary conditions for the nematic director. In the

setting of passive flows with constant velocity and pressure, we see many of the results from Chapter 3, Section 3.2, can be applied directly, or modified to suit the new setting. This gives us invaluable insight into the more complex settings considered in Section 4.3, in that it guides our asymptotic constructions in the limit of large domain sizes. In particular, these asymptotics suggest OR-type solutions are possible for both passive and active flows with non-constant velocity and pressure for sufficiently large domains. This is then verified by numerical experiments in Section 4.4, which confirm they are excellent approximations in the limiting regimes considered. We also explore the multiplicity of OR-type solutions in Section 4.4, where we find a plethora of such solutions.

This study of passive and active nematodynamics in microfluidic channels, enables us to model polydomain structures and singular lines (disclination lines) or domain walls in such channels. These phenomena can be captured by OR and OR-type solutions and are of clear physical interest having been observed in experiments. Referring to the experimental results in [18] for passive nematic liquid crystals (NLCs), the authors find disclination lines at the centre of a microfluidic channel filled with the liquid crystal 5CB, with flow, and with and without an applied electric field (Figure 2.3). In the active case, there are similar experimental results in [86]. Here, the authors use an applied magnetic field to control an active nematic system (8CB with a water based active gel), and observe parallel lanes of defect cores in the active nematic, aligned perpendicularly to the magnetic field. In general, analysis of liquid crystals with polydomains and domain walls is a field that could benefit from rigorous analyses of experimental phenomena as discussed in this chapter.

4.1.1 Theory

We consider the same channel geometry as in Chapter 3, which can again be reduced to an effectively one-dimensional problem: $\bar{\Omega} = [-D, D]$. There are two macroscopic variables - the fluid velocity $\mathbf{u}$, and a reduced Landau-de Gennes (LdG) $\mathbf{Q}$-tensor order parameter as seen in Section 2.2 and Section 3.1.1, i.e., $\mathbf{Q} \in S_0 \coloneqq \{\mathbf{Q} \in \mathbb{M}^{2\times 2} : Q_{ij} = Q_{ji}, Q_{ii} = 0\}$ and

$$\mathbf{Q} = s\left(\mathbf{n} \otimes \mathbf{n} - \frac{1}{2}\mathbf{I}_2\right), \tag{4.1.1}$$

where s is the scalar order parameter and $\mathbf{n}$ is the nematic director. For $\mathbf{n} = (\cos\theta, \sin\theta)$ (θ denotes the angle between $\mathbf{n}$ and the x-axis), the two independent components of $\mathbf{Q}$ are again given by

$$Q_{11} = \frac{s}{2}\cos 2\theta, \quad Q_{12} = \frac{s}{2}\sin 2\theta, \tag{4.1.2}$$

and we have the relationships in (3.1.4) between (s, θ) and $\mathbf{Q}$.

We work within the Beris-Edwards framework for nematodynamics [91]. In the passive case (which we consider until Section 4.3.2) there are three governing equations: an incompressibility constraint for $\mathbf{u}$, an evolution equation for $\mathbf{u}$ (essentially the Navier–Stokes equation with an additional stress due to the nematic ordering σ), and an evolution equation for $\mathbf{Q}$ which has an additional stress induced by the fluid vorticity [37]. These equations are given below,

$$\begin{aligned} &\nabla \cdot \mathbf{u} = 0, \quad \rho\frac{D\mathbf{u}}{Dt} = -\nabla p + \nabla \cdot (\mu(\nabla\mathbf{u} + (\nabla\mathbf{u})^T) + \sigma), \\ &\frac{D\mathbf{Q}}{Dt} = \zeta\mathbf{Q} - \mathbf{Q}\zeta + \frac{1}{\gamma}\mathbf{H}. \end{aligned}$$

Here, ρ and μ are the fluid density and viscosity respectively, p is the hydrodynamic pressure, ζ is the anti-symmetric part of the velocity gradient tensor, and γ is the

rotational diffusion constant. The nematic stress is defined to be

$$\sigma = \mathbf{QH} - \mathbf{HQ} \quad \text{and} \quad \mathbf{H} = K\triangle\mathbf{Q} - A\mathbf{Q} - C|\mathbf{Q}|^2\mathbf{Q},$$

where $\mathbf{H}$ is the molecular field related to the LdG free energy, K is the nematic elasticity constant, $A < 0$ is a material and temperature dependent constant, $C > 0$ is a material dependent constant, and $|\mathbf{Q}| = \sqrt{\text{tr}\mathbf{Q}^2}$, is the matrix norm. Finally, we assume that all quantities depend on y alone and work with a unidirectional channel flow, so that $\mathbf{u} = (u(y), 0)$. The incompressibility constraint is automatically satisfied. To render the equations nondimensional, we use the following scalings, as in [37],

$$y = D\bar{y},\ t = \frac{\gamma D^2}{K}\bar{t},\ u = \frac{K}{\gamma D}\bar{u},\ Q_{11} = \sqrt{\frac{-2A}{C}}\bar{Q}_{11},\ Q_{12} = \sqrt{\frac{-2A}{C}}\bar{Q}_{12},\ p_x = \frac{\mu K}{\gamma D^3}\bar{p}_x,$$

and then drop bars for simplicity. Our rescaled domain is $\Omega = [-1, 1]$ and the evolution equations become

$$\frac{\partial Q_{11}}{\partial t} = u_y Q_{12} + Q_{11,yy} + \frac{1}{L^*}Q_{11}(1 - 4(Q_{11}^2 + Q_{12}^2)), \tag{4.1.3a}$$

$$\frac{\partial Q_{12}}{\partial t} = -u_y Q_{11} + Q_{12,yy} + \frac{1}{L^*}Q_{12}(1 - 4(Q_{11}^2 + Q_{12}^2)), \tag{4.1.3b}$$

$$L_1\frac{\partial u}{\partial t} = -p_x + u_{yy} + 2L_2(Q_{11}Q_{12,yy} - Q_{12}Q_{11,yy})_y, \tag{4.1.3c}$$

where $L_1 = \frac{\rho K}{\mu\gamma}$, $L^* = \frac{K}{|A|D^2}$, and $L_2 = \frac{2|A|\gamma}{C\mu} = \frac{2|A|Er^*}{CEr}$ are dimensionless parameters. Here, $Er = u_0 D\mu/K$ is the Ericksen number (u_0 is the characteristic length scale of the fluid velocity) and $Er^* = u_0 D\gamma/K$ is analogous to the Ericksen number in terms of the rotational diffusion constant γ, rather than viscosity μ. L^* is a scaled elastic constant (note $L^* = 1/\epsilon$, where ϵ is as in (3.1.11)), which we interpret as a measure of domain size. The parameter L_2 is the product of the ratio of material and temperature-dependent constants and the ratio of rotational to momentum diffusion [37]. Analytically, we focus on the static problem where L_1

does not appear, and when we solve (4.1.3) numerically via gradient flow methods to compute solutions of the static problem, we take $L_1 = 1$. As such, we do not comment on the physical significance of L_1.

From (4.1.3), it follows that the static governing equations for $\mathbf{Q}$ are

$$Q_{11,yy} = -u_y Q_{12} + \frac{1}{L^*} Q_{11}(4(Q_{11}^2 + Q_{12}^2) - 1), \tag{4.1.4a}$$

$$Q_{12,yy} = u_y Q_{11} + \frac{1}{L^*} Q_{12}(4(Q_{11}^2 + Q_{12}^2) - 1), \tag{4.1.4b}$$

$$u_{yy} = p_x - 2L_2(Q_{11}Q_{12,yy} - Q_{12}Q_{11,yy})_y. \tag{4.1.4c}$$

From the above system, we can derive the static governing equations for (s, θ), using (4.1.2):

$$s_{yy} = 4s\theta_y^2 + \frac{1}{L^*} s(s^2 - 1), \tag{4.1.5a}$$

$$s\theta_{yy} = \frac{1}{2} s u_y - 2 s_y \theta_y, \tag{4.1.5b}$$

$$u_{yy} = p_x - L_2(s^2 \theta_y)_{yy}. \tag{4.1.5c}$$

This formulation in terms of (s, θ) gives informative insight into the solution profiles and avoids some of the degeneracy conditions coded in the $\mathbf{Q}$-formulation. We work with Dirichlet conditions for (s, θ) as given below:

$$s(-1) = s(1) = 1, \tag{4.1.6a}$$

$$\theta(-1) = -\omega\pi,\ \theta(1) = \omega\pi, \tag{4.1.6b}$$

where $\omega \in \left[-\frac{1}{2}, \frac{1}{2}\right]$ is the winding number, which encodes information about the director alignment at the channel walls (see Figure 4.1 for a sketch of these boundary conditions). This translates to the following boundary conditions for

Q:

$$Q_{11}(\pm 1) = \frac{1}{2}\cos(2\omega\pi),\ Q_{12}(-1) = -\frac{1}{2}\sin(2\omega\pi),\ Q_{12}(1) = \frac{1}{2}\sin(2\omega\pi). \quad (4.1.7)$$

The boundary conditions in (4.1.6a), imply that the nematic ordering is equal to the bulk energy minimiser s_+ on the bounding plates. We consider asymmetric Dirichlet boundary conditions in (4.1.6b) for the angle θ. From (3.1.4), the range of θ is $(-\frac{\pi}{4}, \frac{\pi}{4})$, but our boundary conditions extend to $\pm\frac{\pi}{2}$. As in Chapter 3, we avoid this issue by using the function atan2$(y, x) \in (-\pi, \pi]$ (and the identities in (3.1.15)), which returns the angle between the line connecting the point (x, y) to the origin and the positive x axis. For the flow field, we consider the typical

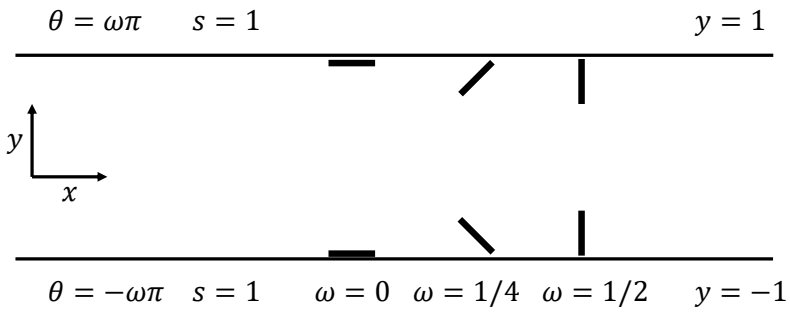

Figure 4.1: Boundary conditions for s and θ and some example director boundary conditions.

no-slip boundary conditions, namely

$$u(-1) = u(1) = 0, \quad (4.1.8)$$

and assume that the pressure p is uniform in the y-direction, hence it depends on x only.

4.2 Passive flows with constant velocity and pressure

In this section, we identify situations for passive nematodynamics which are compatible with OR solutions. Recall from Chapter 3, that OR solutions are characterised by sub-intervals with constant θ, separated by nodal points with $s = 0$ (see Remark 3.1.2). From (4.1.5b), constant θ implies constant fluid velocity u, and from (4.1.5c), constant pressure, p. Therefore, in order to study OR solutions, we assume constant velocity and pressure in this section. This means both our fluid velocity and system pressure, are constant in all spatial directions and with respect to time. This framework, though somewhat artificial (and unlikely to be physically observed), allows for OR solutions, although OR-type solutions exist in more generic situations with non-constant flows as we show in subsequent sections. The current setting serves as a rough approximation of these more generic scenarios. We work with both the **Q**- and (s, θ)-frameworks in this section. Many of the results from Chapter 3, Section 3.2, still hold true in this setting, or can be adapted to suit. This gives us informative insight into the more complex cases considered in Section 4.3. Although many details are analogous to those in Section 3.1.2, there are differences due to our choice of Dirichlet boundary conditions for θ (4.1.6b), so we briefly recap them for completeness and clarity. We let $'$ denote differentiation with respect to y in this section (Section 4.2).

We study **Q**-tensors that belong to the admissible space, $W^{1,2}([-1,1];S_0)$ (i.e. the Sobolev space), and satisfy the boundary conditions (4.1.7). In the setting of constant u and p, (4.1.4a)-(4.1.4b) become

$$Q_{11}'' = \frac{1}{L^*} Q_{11}(4(Q_{11}^2 + 4Q_{12}^2) - 1), \tag{4.2.1a}$$

$$Q_{12}'' = \frac{1}{L^*} Q_{12}(4(Q_{11}^2 + 4Q_{12}^2) - 1). \tag{4.2.1b}$$

From these equations, it follows that (4.1.4c) is satisfied. The equations (4.2.1a)-(4.2.1b) are the Euler-Lagrange equations associated with the energy

$$F(Q_{11}, Q_{12}) = \int_{-1}^{1} \left((Q_{11}')^2 + (Q_{12}')^2 \right) + \frac{1}{L^*} (Q_{11}^2 + Q_{12}^2)(2(Q_{11}^2 + Q_{12}^2) - 1) \, \mathrm{d}y. \tag{4.2.2}$$

The stable and physically observable configurations correspond to local or global minimisers of (4.2.2), in the prescribed admissible space.

In the static case, with constant u and p, the corresponding equations for (s, θ) can be deduced from (4.1.5a), (4.1.5b) :

$$s'' = 4s(\theta')^2 + \frac{1}{L^*} s(s^2 - 1), \tag{4.2.3a}$$

$$\left(s^2 \theta' \right)' = 0 \implies s^2 \theta' = W, \tag{4.2.3b}$$

whilst (4.1.5c) is automatically satisfied. In the above, W is a fixed constant of integration and

$$W = \theta'(-1) = \theta'(1) \tag{4.2.4}$$

Many of the comments from Remark 3.1.1 apply here too. When $\omega \geq 0$ and recalling the boundary conditions for θ, there exists a point y_0 such that $\theta'(y_0) \geq 0$, hence $W \geq 0$, and $\theta' \geq 0$ for all $y \in [-1, 1]$. Thus, we have

$$-\omega\pi \leq \theta \leq \omega\pi, \ \forall y \in [-1, 1] \text{ and } \forall \omega \in \left[0, \frac{1}{2} \right]. \tag{4.2.5}$$

Similar comments apply when $\omega \leq 0$, for which $W \leq 0$, and $\theta' \leq 0$ for all $y \in [-1, 1]$. If $W = 0$, we either have $s = 0$ or θ=constant almost everywhere, compatible with the definition of an OR solution (unless $\omega = 0$, and $(s, \theta) = (1, 0)$,

which is not an OR solution). Conversely, an OR solution, by definition, has $W = 0$ since they have piecewise constant θ-profiles. In other words, if $\omega \neq 0$, OR solutions exist if and only if $W = 0$. If $W \neq 0$, then OR solutions are necessarily disallowed because a non-zero value of W implies that $s \neq 0$ on Ω. The following results show that the choice of W is in turn dictated by ω, or the Dirichlet boundary conditions.

Note that, (4.2.3a) and (4.2.3b) are the Euler-Lagrange equations of the following energy,

$$F(s,\theta) = \int_{-1}^{1} \left(\frac{(s')^2}{4} + s^2(\theta')^2 \right) + \frac{s^2}{4L^*} \left(\frac{s^2}{2} - 1 \right) \, \mathrm{d}y, \tag{4.2.6}$$

but we only consider smooth, classical solutions of (4.2.3a) and (4.2.3b), subject to the boundary conditions in (4.1.6a)-(4.1.6b), and not OR solutions. We first prove that OR solutions only exist for the special values, $\omega = \pm\frac{1}{4}$, in the **Q**-framework. If $\omega = \pm\frac{1}{4}$, then $W = 0$ can be either zero or non-zero for different solution branches, especially for small values of L^* that admit multiple solution branches. Once the correspondence between ω, $W = 0$ and OR solutions is established, we present several qualitative properties of the corresponding (s,θ)-profiles.

4.2.1 Qualitative results

Our first result regards the compatibility of OR solutions with the boundary conditions. We refer the reader to Remark 3.2.5 for the characterisation of OR solutions in the **Q**-framework. The proof requires different arguments to those presented in Theorem 3.2.8, because of the boundary conditions (4.1.7).

Theorem 4.2.1. *For constant u and p, and all $L^* \geq 0$, there exists a minimiser of the energy* (4.2.2)*, in the admissible space*

$$\mathcal{A} := \Big\{ \mathbf{Q} \in W^{1,2}\left([-1,1]; S_0\right); Q_{11}(\pm 1) = \frac{\cos(2\omega\pi)}{2}, \\ Q_{12}(-1) = -\frac{\sin 2\omega\pi}{2}, Q_{12}(1) = \frac{\sin 2\omega\pi}{2} \Big\}. \quad (4.2.7)$$

Moreover, the system (4.2.1) admits an analytic solution for all $L^* \geq 0$, in $\mathcal{A}$. OR solutions only exist for $\omega = \pm\frac{1}{4}$ in (4.1.7). In this case, $Q_{11} \equiv 0$ while Q_{12} is odd, increasing, and $Q_{12} = 0$ at $y = 0$ only.

Proof. The existence of an energy minimiser for (4.2.2) in $\mathcal{A}$, is immediate from the direct methods in the calculus of variations, for all L^* and ω, and the minimiser is a classical solution of the associated Euler-Lagrange equations (4.2.1), for all ϵ and ω. In fact, using arguments in elliptic regularity, one can show that all solutions of the system (4.2.1) are analytic [65] (recall the discussion in Section 2.2).

The key observation is

$$(Q'_{12}Q_{11} - Q'_{11}Q_{12})' = Q''_{12}Q_{11} + Q'_{12}Q'_{11} - Q'_{12}Q'_{11} - Q_{12}Q''_{11} = 0,$$

and hence, $Q'_{12}Q_{11} - Q'_{11}Q_{12}$ is a constant. In fact, using (3.1.15), we see that

$$(s^2\theta')' = 2(Q''_{12}Q_{11} - Q''_{11}Q_{12}) = 0 \implies s^2\theta' = 2(Q'_{12}Q_{11} - Q'_{11}Q_{12}) = W,$$

where W is as in (4.1.5b). Now let $W = 0$ (so that OR solutions are possible), then

$$Q'_{12}Q_{11} = Q'_{11}Q_{12} \quad \forall y \in [-1,1]. \quad (4.2.8)$$

There are two obvious solutions of (4.2.8), $Q_{11} \equiv 0$ (i.e., $\omega = \pm\frac{1}{4}$), or $Q_{12} \equiv 0$ (i.e., $\omega = 0, \pm\frac{1}{2}$), everywhere on Ω.

For the case $Q_{12} \equiv 0$ and $\omega = \pm\frac{1}{2}$, the **Q**-Euler-Lagrange equations reduce to

$$\begin{cases} Q_{11}'' = \frac{1}{L^*} Q_{11}(4Q_{11}^2 - 1), \\ Q_{11}(-1) = -\frac{1}{2},\ Q_{11}(1) = -\frac{1}{2}. \end{cases} \tag{4.2.9}$$

This is essentially the ordinary differential equation considered in equation (20) of [64]. Applying the arguments in Lemma 5.4 of [64], the solution Q_{11} of (4.2.9) must satisfy $Q_{11}'(-1) = 0$, or Q_{11}' is always positive. However, the latter is not possible since we have symmetric boundary conditions. Hence, when $\omega = \pm\frac{1}{2}$, the unique solution to (4.2.9) is the constant solution $(Q_{11}, Q_{12}) = (-\frac{1}{2}, 0)$. This corresponds to $s = 1$ everywhere in Ω, inconsistent with an OR solution. The same arguments apply to the case $Q_{12} \equiv 0$ and $\omega = 0$. In this case, the boundary conditions are $Q_{11}(\pm 1) = \frac{1}{2}$, and the corresponding solution is $(Q_{11}, Q_{12}) = (\frac{1}{2}, 0)$. Again, this is not an OR solution.

When $Q_{11} \equiv 0$ ($\omega = \pm\frac{1}{4}$), the **Q** system becomes

$$\begin{cases} Q_{12}'' = \frac{1}{L^*} Q_{12}(4Q_{12}^2 - 1), \\ Q_{12}(-1) = -\frac{1}{2},\ Q_{12}(1) = \frac{1}{2}. \end{cases} \tag{4.2.10}$$

Applying the arguments in Lemma 5.4 of [64], we see (4.2.10) has a unique solution which is odd and increasing, with a single zero at $y = 0$ - the centre of the channel. This is an OR solution, since $Q_{11} = 0$ implies that θ is necessarily constant on either side of $y = 0$.

It remains to show that there are no solutions (Q_{11}, Q_{12}) of (4.2.1), which satisfy (4.2.8), other than the possibilities considered above. To this end, we assume that we have non-trivial solutions, Q_{11} and Q_{12} such that (4.2.8) holds. We recall that all solution pairs, (Q_{11}, Q_{12}) of (4.2.1) are analytic and hence, can only have

zeroes at a discrete set of points in $\Omega = [-1, 1]$. This means that there exists a finite number of intervals $(y_0 = -1, y_1), \ldots, (y_{n-1}, y_n = 1)$, such that $Q_{11} \neq 0$ and $Q_{12} \neq 0$ in the interior of these intervals, whilst either $Q_{11}(y_i)$, $Q_{12}(y_i)$, or both, equal zero at each interval end-points. On such intervals we can rearrange and then integrate (4.2.8), i.e.,

$$\frac{Q_{12}'}{Q_{12}} = \frac{Q_{11}'}{Q_{11}} \implies |Q_{11}| = c_i |Q_{12}| \text{ for } y \in (y_{i-1}, y_i)$$

for constants $c_i > 0$ and $i = 0, \ldots, n$. Therefore, there exists an interval, (y_{i-1}, y_i), for which Q_{11} and Q_{12} have the same, or opposite signs. Assume without loss of generality Q_{11} and Q_{12} have the same sign on an interval, then the analytic function

$$f(y) := Q_{11}(y) - c_i Q_{12}(y) = 0, \text{ for } y \in (y_{i-1}, y_i).$$

Therefore, $f(y) = 0$ for all $y \in [-1, 1]$. Evaluating at $y = \pm 1$, we have

$$\cos(2\omega\pi) = -\sin(2\omega\pi)c_i \text{ and } \cos(2\omega\pi) = \sin(2\omega\pi)c_i,$$

and this is only possible if $\cos(2\omega\pi) = 0$ and $\sin(2\omega\pi)c_i = 0$, which implies $\omega = \pm\frac{1}{4}$ and $c_i = 0$. Hence, there are only three possibilities $\omega = 0, \pm\frac{1}{4}, \pm\frac{1}{2}$ that are consistent with (4.2.8), of which OR solutions are only compatible with $\omega = \pm\frac{1}{4}$. □

In the remainder of this section, we consider smooth classical solutions of the (s, θ)-equations (4.2.3). We have seen above that the dynamic equations (4.1.5), reduce to (4.2.3) in the setting of constant flow and pressure, and these are the same equations considered in Chapter 3 (i.e, (3.1.12)). Hence, the results of Section 3.2 apply in certain dynamic scenarios and we now restate them in the current setting for clarity. These results then inform our asymptotic and numerical studies in the

sections that follow.

Theorem 4.2.2. *(Maximum Principle) Let u and p be constant, and let s and θ be solutions of* (4.1.5)*, where s is at least C^2 and θ is at least C^1, then*

$$0 < s \leq 1 \quad \forall y \in [-1, 1]. \tag{4.2.11}$$

Theorem 4.2.3. *For constant u and p, any non-constant and non-OR solution, s, of the system* (4.1.5)*, has a single critical point which is necessarily a non-zero global minimum at some $y^* \in (-1, 1)$.*

We next present our uniqueness result for $W \neq 0$. The result follows from Theorem 3.2.3, however, there is the additional possibility of $W < 0$ when $\omega < 0$. This requires only minor modifications to the proof, and as such we omit it.

Theorem 4.2.4. *For constant u and p, and for a given $W \neq 0$, the system* (4.1.5)*, subject to the boundary conditions* (4.1.6)*, has a unique solution for a fixed L^* and ω.*

Combined, Theorem 4.2.3 and Theorem 4.2.4 yield the following result.

Theorem 4.2.5. *For constant u and p, and for $W \neq 0$, the unique solution, (s, θ) of* (4.1.5)*, has the following symmetry properties:*

$$s(y) = s(-y) \text{ and } \theta(y) = -\theta(-y) \quad \forall y \in [-1, 1].$$

Then s has a unique non-zero minimum at $y = 0$.

Remark 4.2.6. As commented on in Section 3.2, using the arguments in [64], it can be proved that for $\omega = \pm\frac{1}{4}$, OR solutions exist for all $L^* \geq 0$ and are globally stable as $L^* \to \infty$, but lose stability as L^* decreases. Stable non-OR solutions emerge as L^* decreases which do not have polydomain structures. From this

section, we see these conclusions hold true in a dynamic situation with constant u and p.

4.3 Asymptotics for OR-type solutions in the $L^* \to 0$ limit

In this section, we compute asymptotic expansions for OR-type solutions of the system (4.1.5), in the $L^* \to 0$ limit relevant to micron-scale channels. An OR-type solution is simply a solution of (4.1.5) with a non-empty nodal set for the scalar order parameter, such that θ has a jump discontinuity at the zeroes of s. Unlike OR solutions, OR-type solutions need not have constant θ-profiles. We consider conventional passive nematodynamics (Section 4.3.1) and active nematodynamics (Section 4.3.2) in generic scenarios with non-constant velocity and pressure. Our asymptotic methods are adapted from [92], where the authors investigate a chevron texture characterised specifically by a $\pm\pi/4$ jump in θ, using an Ericksen model for uniaxial NLCs. These asymptotic methods, now placed within the Beris-Edwards framework, allow us to explicitly construct solutions characterised by an isotropic line, with a jump discontinuity in the nematic director, which are strongly reminiscent of disclination lines seen in experiments [18, 82].

4.3.1 Passive nematodynamics

Consider the system of coupled equations, (4.1.5), in the $L^* \to 0$ limit. Motivated by the results of Section 4.2 (in particular, theorem 4.2.1 and Theorem 4.2.5), and for simplicity, we assume s attains a single minimum at $y = 0$, s is even and θ is odd, throughout this section. The first step is to calculate the flow gradient

u_y. We multiply (4.1.5b) by s so that

$$(s^2\theta_y)_y = \frac{s^2}{2}u_y. \tag{4.3.1}$$

Substituting $(s^2\theta_y)_y$ from (4.3.1) into (4.1.5c), we obtain

$$\left(u_y + \frac{L_2}{2}s^2 u_y\right)_y = p_x. \tag{4.3.2}$$

Both sides of (4.3.2) equal a constant, since the left hand side is independent of x, and p_x is independent of y. Integrating (4.3.2), we find

$$u_y = \frac{p_x y}{g(s)} + \frac{B_0}{g(s)}, \tag{4.3.3}$$

where B_0 is a constant and

$$g(s) = 1 + \frac{L_2}{2}s^2 > 0, \ \forall s \in \mathbb{R}. \tag{4.3.4}$$

Integrating (4.3.3), we have

$$u(y) = \int_{-1}^{y} \frac{p_x Y}{g(s(Y))} + \frac{B_0}{g(s(Y))} \, \mathrm{d}Y, \tag{4.3.5}$$

since $u(-1) = 0$ from (4.1.8). Using the no-slip condition, $u(1) = 0$ and the fact that $\int_{-1}^{1} \frac{Y}{g(s(Y))} \, \mathrm{d}Y = 0$ (since $\frac{y}{g(s(y))}$ is odd), we see $B_0 = 0$ so that the flow velocity is given by

$$u(y) = \int_{-1}^{y} \frac{p_x Y}{g(s(Y))} \, \mathrm{d}Y, \tag{4.3.6}$$

and the corresponding velocity gradient is

$$u_y(y) = \frac{p_x y}{g(s)}. \tag{4.3.7}$$

Following the method in [92], we seek the following asymptotic expansions for

(s, θ):

$$s(y) = S(y) + IS(\lambda) + \mathcal{O}(L^*), \tag{4.3.8a}$$

$$\theta(y) = \Theta(y) + I\Theta(\lambda) + \mathcal{O}(L^*), \tag{4.3.8b}$$

where S, Θ represent the outer solutions away from the jump point at $y = 0$, $IS, I\Theta$ represent the inner solutions around $y = 0$, and λ is our inner variable. Substituting these expansions into (4.1.5a) and (4.1.5b) yields

$$L^* S_{yy} + L^* IS_{yy} = 4L^*(S + IS)(\Theta_y + I\Theta_y)^2 + (S + IS)((S + IS)^2 - 1), \tag{4.3.9a}$$

$$(S + IS)(\Theta_{yy} + I\Theta_{yy}) = \frac{1}{2}(S + IS)u_y(y) - 2(S_y + IS_y)(\Theta_y + I\Theta_y). \tag{4.3.9b}$$

It is clear that (4.3.9a) is a singular problem in the $L^* \to 0$ limit, and as such we rescale y and set

$$\lambda = \frac{y}{\sqrt{L^*}}, \tag{4.3.10}$$

to be our inner variable.

The outer solution is simply the solution of (4.3.9a) and (4.3.9b), away from $y = 0$, for $L^* = 0$ and when internal contributions are ignored. In this case, (4.3.9a) reduces to

$$S(S^2 - 1) = 0, \tag{4.3.11}$$

which implies

$$S(y) = 1, \quad \text{for } y \in [-1, 0) \cap (0, 1] \tag{4.3.12}$$

is the outer solution. Here we have ignored the trivial solution $S = 0$, and $S = -1$, as these solutions do not satisfy the boundary conditions.

Ignoring internal contributions, (4.3.9b) reduces to

$$\Theta_{yy}(y) = \frac{1}{2} u_y(y) \quad \text{for } y \in [-1, 0) \cap (0, 1]. \tag{4.3.13}$$

From the above, $s = 1$ for $y \in [-1, 0) \cap (0, 1]$, so integrating (4.3.7) and imposing the no-slip boundary conditions (4.1.8), we obtain

$$u(y) = \frac{p_x}{2 + L_2}(y^2 - 1). \tag{4.3.14}$$

We take $u(0) = -\frac{p_x}{2+L_2}$, consistent with the above expression. Solving for $0 < y \leq 1$, we integrate (4.3.13) to obtain

$$\begin{aligned} \Theta_y(y) &= \int_0^y \frac{u_y(Y)}{2} \, \mathrm{d}Y + \Theta_y(0+) \\ \implies \Theta_y(y) &= \frac{u(y) - u(0)}{2} + \Theta_y(0+). \end{aligned} \tag{4.3.15}$$

Similarly, for $-1 \leq y < 0$, integrating (4.3.13) yields

$$\Theta_y(y) = \frac{u(y) - u(0)}{2} + \Theta_y(0-). \tag{4.3.16}$$

Since $\Theta_y(0\pm)$ is unknown, we enforce the following boundary conditions at $y = 0$ to give us an explicitly computable expression

$$\Theta(0+) = \omega\pi - \frac{k\pi}{2}, \ k \in \mathbb{Z}, \tag{4.3.17a}$$

$$\Theta(0-) = -\omega\pi + \frac{k\pi}{2}, \ k \in \mathbb{Z}. \tag{4.3.17b}$$

We now justify this jump condition. In the case of constant flow and pressure, OR solutions jump by $\frac{\pi}{2}$ (in the $\mathbf{Q}$ formulation), but OR-type solutions could have different jump conditions across the domain walls, hence the inclusion of the $\frac{k\pi}{2}$ term.

Substituting (4.3.14) into (4.3.15), integrating, and imposing the boundary con-

ditions, we have that

$$\Theta(y) = \frac{p_x}{(2+L_2)}\left(\frac{y^3}{6} - \frac{y}{6}\right) + \frac{k\pi}{2}(y-1) + \omega\pi \quad \text{for } y \in (0,1]. \tag{4.3.18}$$

Analogously, (4.3.16) yields

$$\Theta(y) = \frac{p_x}{(2+L_2)}\left(\frac{y^3}{6} - \frac{y}{6}\right) + \frac{k\pi}{2}(y+1) - \omega\pi \quad \text{for } y \in [-1,0). \tag{4.3.19}$$

We now compute the inner solutions $IS, I\Theta$. Substituting the inner variable (4.3.10), into (4.3.9a) and (4.3.9b), they become

$$\begin{aligned} L^* S_{yy} + \ddot{IS} &= 4L^*(S+IS)\left(\Theta_y + \frac{\dot{I\Theta}}{\sqrt{L^*}}\right)^2 + (S+IS)((S+IS)^2-1), \\ (S+IS)(L^*\Theta_{yy} + \ddot{I\Theta}) &= \frac{L^*}{2}(S+IS)u_y(\lambda\sqrt{L^*}) \\ &\quad - 2L^*\left(S_y + \frac{\dot{IS}}{\sqrt{L^*}}\right)\left(\Theta_y + \frac{\dot{I\Theta}}{\sqrt{L^*}}\right), \end{aligned}$$

where $\dot{()}$ denotes differentiation with respect to λ. Letting $L^* \to 0$, we have that the leading order equations are

$$\ddot{IS} = 4(S+IS)(\dot{I\Theta})^2 + (S+IS)((S+IS)^2-1), \tag{4.3.20a}$$

$$(S+IS)\ddot{I\Theta} = -2\dot{IS}\dot{I\Theta}, \tag{4.3.20b}$$

or equivalently, after recalling $S = 1$,

$$\begin{aligned} \ddot{IS} &= 2IS + q_1(IS, \dot{I\Theta}), \\ \ddot{I\Theta} &= q_2(IS, \dot{IS}, \dot{I\Theta}, \ddot{I\Theta}), \end{aligned}$$

where q_1, q_2 represent the nonlinear terms of the equation. The linearised system is

$$\ddot{IS} = 2IS, \tag{4.3.21a}$$

$$I\ddot{\Theta} = 0, \tag{4.3.21b}$$

subject to the boundary and matching conditions

$$\lim_{\lambda \to \pm\infty} IS(\lambda) = 0, \; IS(0) = s_{min} - 1, \tag{4.3.22a}$$

$$\lim_{\lambda \to \pm\infty} I\Theta(\lambda) = 0, \tag{4.3.22b}$$

where $s_{min} \in [0, 1]$, is the minimum value of s. We note that the second condition in (4.3.22a) ensures $s(0) = s_{min}$.

Using the conditions (4.3.22a), the general solution of (4.3.21a) is

$$s(y) = \begin{cases} 1 + (s_{min} - 1)e^{-\sqrt{2}\frac{y}{\sqrt{L^*}}} & \text{for } 0 \leq y \leq 1 \\ 1 + (s_{min} - 1)e^{\sqrt{2}\frac{y}{\sqrt{L^*}}} & \text{for } -1 \leq y \leq 0. \end{cases} \tag{4.3.23}$$

With IS determined, we calculate $I\Theta$. Solving (4.3.21b) subject to the limiting conditions (4.3.22b), it is clear that $I\Theta = 0$. Hence,

$$\theta(y) = \begin{cases} \frac{p_x}{(2+L_2)}\left(\frac{y^3}{6} - \frac{y}{6}\right) + \frac{k\pi}{2}(y-1) + \omega\pi & \text{for } 0 < y \leq 1 \\ \frac{p_x}{(2+L_2)}\left(\frac{y^3}{6} - \frac{y}{6}\right) + \frac{k\pi}{2}(y+1) - \omega\pi & \text{for } -1 \leq y < 0. \end{cases} \tag{4.3.24}$$

The expressions, (4.3.23) and (4.3.24), are consistent with our definition of an OR-type solution. In principle, in this (s, θ, u) formulation, OR-type solutions are compatible with any choice of ω.

4.3.2 Active nematodynamics

Next, we consider a system of uniaxial active nematics in a channel geometry i.e., a system that is constantly driven out of equilibrium by internal stresses and activity [93]. There are three dependent variables to solve for - the concentration, c, of active particles, the fluid velocity $\mathbf{u}$, and the nematic order parameter, $\mathbf{Q}$. The

corresponding evolution equations are taken from [44, 94], with additional stresses from the self-propelled motion of the active particles and the non-equilibrium intrinsic activity, referred to as *active stresses*:

$$\frac{Dc}{Dt} = \nabla \cdot \left(\mathbf{D} \nabla c + \alpha_1 c^2 (\nabla \cdot \mathbf{Q}) \right), \tag{4.3.25a}$$

$$\nabla \cdot \mathbf{u} = 0, \quad \rho \frac{D\mathbf{u}}{Dt} = -\nabla p + \nabla \cdot (\mu(\nabla \mathbf{u} + (\nabla \mathbf{u})^T) + \tilde{\sigma}), \tag{4.3.25b}$$

$$\frac{D\mathbf{Q}}{Dt} = \lambda s \mathbf{W} + \zeta \mathbf{Q} - \mathbf{Q}\zeta + \frac{1}{\gamma}\mathbf{H}, \tag{4.3.25c}$$

where $\mathbf{W}$ is the symmetric part of the velocity gradient tensor, $D_{ij} = D_0 \delta_{ij} + D_1 Q_{ij}$ is the anisotropic diffusion tensor ($D_0 = (D_\parallel + D_\perp)/2$, $D_1 = D_\parallel - D_\perp$ $D_\parallel$ and $D_\perp$ are, respectively, the bare diffusion coefficients along the parallel and perpendicular directions of the director field), α_1 is an activity parameter and λ is the nematic alignment parameter, which characterises the relative dominance of the strain and the vorticity in affecting the alignment of particles with the flow [95]. For $|\lambda| < 1$, the rotational part of the flow dominates, while for $|\lambda| > 1$, the director will tend to align at a unique angle to the flow direction [96]. The value of λ is also determined by the shape of the active particles [97]. The stress tensor, $\tilde{\sigma} = \sigma^e + \sigma^a$, is the sum of an elastic stress due to nematic elasticity

$$\sigma^e = -\lambda s \mathbf{H} + \mathbf{Q}\mathbf{H} - \mathbf{H}\mathbf{Q}, \tag{4.3.26}$$

and an active stress defined by

$$\sigma^a = \alpha_2 c^2 \mathbf{Q}. \tag{4.3.27}$$

Here, α_2 is a second activity parameter, which describes extensile (contractile) stresses exerted by the active particles when $\alpha_2 < 0$ ($\alpha_2 > 0$). $\mathbf{H}$, μ, ξ, p and ρ, are as introduced in Section 4.1.1.

We again consider a one-dimensional static problem, with a unidirectional flow

in the x direction and take $\lambda = 0$ for simplicity. Then the evolution equations for $\mathbf{Q}$ are the same as those considered in the passive case, hence, making it easier to adapt the calculations in Section 4.3.1 and draw comparisons between the passive and active cases. The isotropic to nematic phase transition is driven by the concentration of active particles and as such, we take $A = K(c^* - c)/2$ and $C = Kc$, where $c^* = \sqrt{3\pi/2L^2}$ is the critical concentration at which this transition occurs [44, 93]. As in the passive case, we work with $A < 0$ i.e. with concentrations that favour nematic ordering.

The continuity equation (4.3.25a), follows from the fact that the total number of active particles must remain constant [93]. This is compatible with constant concentration, c, although solutions with constant concentration do not exist for $\alpha_1 \neq 0$. As in [98], we consider the case of constant concentration c, which is not unreasonable for small values of α_1 (see (4.3.25a), which can admit approximately constant solutions, $c(y)$ in the $\alpha_1 \to 0$ limit), and do not consider the concentration equation, (4.3.25a), in this work. We nondimensionalise the system as before, but additionally scale c and c^* by D^{-2} (e.g, $c = D^{-2}\tilde{c}$, where $\tilde{c}$ is dimensionless). In terms of $\mathbf{Q}$, the evolution equations are given by

$$\frac{\partial Q_{11}}{\partial t} = u_y Q_{12} + Q_{11,yy} + \frac{1}{L^*} Q_{11}(1 - 4(Q_{11}^2 + Q_{12}^2)), \tag{4.3.28a}$$

$$\frac{\partial Q_{12}}{\partial t} = -u_y Q_{11} + Q_{12,yy} + \frac{1}{L^*} Q_{12}(1 - 4(Q_{11}^2 + Q_{12}^2)), \tag{4.3.28b}$$

$$L_1 \frac{\partial u}{\partial t} = -p_x + u_{yy} + 2L_2(Q_{11}Q_{12,yy} - Q_{12}Q_{11,yy})_y + \Gamma(Q_{12}c^2)_y, \tag{4.3.28c}$$

where $\Gamma = \frac{\alpha_2 \gamma}{K\mu D^2}\sqrt{-\frac{2A}{C}}$ is a measure of activity. In the steady case, and in terms of (s, θ), the system (4.3.28) reduces to

$$s_{yy} = 4s\theta_y^2 + \frac{s}{L^*}\left(s^2 - 1\right), \tag{4.3.29a}$$

$$s\theta_{yy} = \frac{1}{2} s u_y - 2 s_y \theta_y, \tag{4.3.29b}$$

$$u_{yy} = p_x - L_2(s^2\theta_y)_{yy} - \Gamma\left(\frac{c^2 s}{2}\sin(2\theta)\right)_y. \tag{4.3.29c}$$

Regarding boundary conditions, we impose the same boundary conditions on s, θ and u, as in the passive case.

The equations, (4.3.29a) and (4.3.29b), are identical to the equations, (4.1.5a) and (4.1.5b), respectively. Hence, the asymptotics in Section 4.3.1 remain largely unchanged, with differences coming from (4.3.29c), due to the additional active stress. Substituting (4.3.1) into (4.3.29c), we obtain

$$\left(u_y + \frac{L_2}{2}s^2 u_y + \frac{\Gamma}{2}c^2 s\sin(2\theta)\right)_y = p_x. \tag{4.3.30}$$

Following the same steps as in Section 4.3.1 to obtain equation (4.3.5), we compute

$$u(y) = \int_{-1}^{y} \frac{2p_x Y + 2B_0 - \Gamma c^2 s(Y)\sin(2\theta(Y))}{2g(s(Y))}\,\mathrm{d}Y,$$

where B_0 is a constant and g is given by (4.3.4). Using $u(1) = 0$ and rearranging, we see that

$$B_0 = \frac{-\int_{-1}^{1} \frac{2p_x Y - \Gamma c^2 s(Y)\sin(2\theta(Y))}{2g(s(Y))}\,\mathrm{d}Y}{\int_{-1}^{1} g(s(Y))^{-1} dY}.$$

From our assumption that s is even and θ is odd, it follows that $\frac{y}{g(s)}$ and $\frac{s\sin(2\theta)}{g(s)}$ are odd, and consequently, $B_0 = 0$. Therefore, the flow velocity is given by

$$u(y) = \int_{-1}^{y} \frac{2p_x Y - \Gamma c^2 s(Y)\sin(2\theta(Y))}{2g(s(Y))}\,\mathrm{d}Y, \tag{4.3.31}$$

and the velocity gradient by

$$u_y(y) = \frac{p_x y}{g(s(y))} - \frac{\Gamma c^2 s(y)\sin(2\theta(y))}{2g(s(y))}. \tag{4.3.32}$$

Here, the active contribution is captured by the second term, assuming a constant concentration c.

As (4.3.29a) and (4.3.29b) are identical to equations (4.1.5a) and (4.1.5b) respectively, much of the calculations are the same as in Section 4.3.1. In particular, we pose asymptotic expansions as in (4.3.8a) and (4.3.8b), for s and θ respectively in the $L^* \to 0$ limit, which yields (4.3.9a) and (4.3.9b). In fact, the expression for s is given by (4.3.23), in the active case too. We highlight the differences for the outer solution Θ, as a result of the velocity gradient (4.3.32). We again solve (4.3.13) and find an implicit representation for Θ as given below:

$$\Theta(y) = \begin{cases} \int_y^1 \frac{u(0)-u(Y)}{2}\,\mathrm{d}Y + \left(\frac{k\pi}{2} - \int_0^1 \frac{u(Y)-u(0)}{2}\,\mathrm{d}Y\right)(y-1) + \omega\pi, \ 0 < y \leq 1, \\ \int_{-1}^y \frac{u(Y)-u(0)}{2}\,\mathrm{d}Y + \left(\frac{k\pi}{2} - \int_{-1}^0 \frac{u(Y)-u(0)}{2}\,\mathrm{d}Y\right)(y+1) - \omega\pi, \ -1 \leq y < 0, \end{cases} \tag{4.3.33}$$

where $u(y)$ is given by (4.3.31). Moving to the inner solution $I\Theta$, we need to solve (4.3.21b), subject to the matching condition (4.3.22b). As before, we find $I\Theta = 0$, and our composite expansion for θ is just the outer solution presented above. We deduce that OR-type solutions are still possible in an active setting, for the case $\lambda = 0$.

We now consider a simple case for which (4.3.33) can be solved explicitly. In (4.3.31), we assume $s = 1$ and $\sin 2\theta = 1$ for $-1 \leq y < 0$, and $\sin(2\theta) = -1$ for $0 < y \leq 1$ i.e., we assume an OR solution with $\theta = \mp\frac{\pi}{4}$ and $\omega = -\frac{1}{4}$. Under these assumptions, integrating (4.3.32) yields

$$u(y) = \begin{cases} \frac{p_x}{2+L_2}(y^2-1) + \frac{\Gamma c^2}{2+L_2}(y-1), & \text{for } 0 < y \leq 1, \\ \frac{p_x}{2+L_2}(y^2-1) - \frac{\Gamma c^2}{2+L_2}(y+1), & \text{for } -1 \leq y < 0. \end{cases} \tag{4.3.34}$$

Substituting the above into (4.3.33), we find

$$\theta(y) = \begin{cases} \frac{p_x}{2+L_2}\left(\frac{y^3}{6} - \frac{y}{6}\right) + \frac{\Gamma c^2}{2+L_2}(\frac{y^2}{4} - \frac{y}{4}) + \frac{k\pi}{2}(y-1) + \omega\pi, & \text{for } 0 < y \leq 1, \\ \frac{p_x}{2+L_2}\left(\frac{y^3}{6} - \frac{y}{6}\right) - \frac{\Gamma c^2}{2+L_2}(\frac{y^2}{4} + \frac{y}{4}) + \frac{k\pi}{2}(y+1) - \omega\pi & \text{for } -1 \leq y < 0. \end{cases} \tag{4.3.35}$$

We expect (4.3.34) and (4.3.35) to be good approximations to OR-type solutions with $\omega = -\frac{1}{4}$, in the limit of small Γ (small activity) and small pressure gradient, when the outer solution is well approximated by an OR solution.

4.4 Numerical results

The numerical results of this section were produced by Dr. Yucen Han [1], and guided by the author.

We now validate our asymptotics and confirm the existence of OR-type solutions for passive and active nematodynamics (with non-constant pressure and flow), with extensive numerical experiments, for large and small values of L^*.

Numerical Method

We solve the dynamical systems (4.1.3) and (4.3.28) with finite element methods, and all simulations are performed using the open-source package FEniCS [99]. We write the dynamical systems in their weak formulation. For example, the weak formulation of the complicated active system (4.3.28), is the following:

$$\int_{-1}^{1} \frac{\partial Q_{11}}{\partial t} v_1 \, \mathrm{d}y = \int_{-1}^{1} u_y Q_{12} v_1 - Q_{11,y} v_{1y} + \frac{1}{L^*} Q_{11}(1 - 4(Q_{11}^2 + Q_{12}^2)) v_1 \, \mathrm{d}y, \tag{4.4.1a}$$

$$\int_{-1}^{1} \frac{\partial Q_{12}}{\partial t} v_2 \, \mathrm{d}y = \int_{-1}^{1} -u_y Q_{11} v_2 - Q_{12,y} v_{2y} + \frac{1}{L^*} Q_{12}(1 - 4(Q_{11}^2 + Q_{12}^2)) v_2 \, \mathrm{d}y, \tag{4.4.1b}$$

$$\int_{-1}^{1} \frac{\partial u}{\partial t} v_3 \, \mathrm{d}y = \int_{-1}^{1} -p_x v_3 - \left(u_y + 2L_2(Q_{11}Q_{12,yy} - Q_{12}Q_{11,yy}) + \Gamma(Q_{12}c^2) \right) v_{3y} \, \mathrm{d}y, \tag{4.4.1c}$$

for all $v_1, v_2, v_3 \in W_0^{1,2}([-1,1])$ with Dirichlet boundary conditions for Q_{11}, Q_{12} and u, given in (4.1.7) and (4.1.8), respectively. We partition the domain $[-1,1]$ into a uniform mesh with mesh size $1/256$. Due to the third order partial derivatives with respect to y in (4.3.28), Lagrange elements of order 2 are used for the spatial discretization.

We also study the linear stability of the equilibrium solutions in (4.1.3) and (4.3.28). The systems can be written as $\frac{\partial \mathbf{x}}{\partial t} = F(\mathbf{x}(t))$. Let $\mathbf{x}_0$ denote an equilibrium point i.e. $F(\mathbf{x}_0) = \mathbf{0}$, and let $J(\mathbf{x}_0) = \nabla F(\mathbf{x}_0)$ be the Jacobian matrix of F at $\mathbf{x}_0$. We can then determine the stability of $\mathbf{x}_0$ by checking the sign of the largest real part amongst all eigenvalues of $J(\mathbf{x}_0)$. If the largest real part is negative (positive), then the equilibrium point is stable (unstable).

For stable states of the system (4.1.3), we use the semi-implicit Euler method for time discretization and the initial conditions

$$Q_{11} = \cos(2\omega\pi y)/2, \; Q_{12} = \sin(2\omega\pi y)/2, \; u = -p_x(1-y^2)/2. \tag{4.4.2}$$

For the unstable OR-type solutions, we assume that the partial derivatives with respect to t are zero, and solve the passive or active flow systems using a Newton solver with a linear LU solver at each iteration. Newton's method strongly depends on the initial condition, so we use the asymptotic expressions (4.3.23) and (4.3.24) as initial conditions for the passive flow system, and (4.3.23) and (4.3.35) as initial conditions for the active flow system with small Γ. In the numerical results that follow, we extract the s-profile from $\mathbf{Q}$, using (3.1.15).

Passive flows

We begin by investigating whether OR-type solutions exist for the passive system (4.1.3) when L^* is large, that is, for small nano-scale channel domains. When $\omega = \pm\frac{1}{4}$ and $p_x = -1$, we find stable profiles which are small perturbations of OR solutions for large L^* with $p_x = u_y = 0$ (see Figure 4.2), i.e., the following limiting profiles as $L^* \to \infty$ with $\omega = \pm\frac{1}{4}$ and $p_x = u_y = 0$,

$$s_\infty = \begin{cases} -y \quad \text{for } -1 \le y \le 0 \\ y \quad 0 \le y \le 1 \end{cases} \tag{4.4.3a}$$

$$\theta_\infty = \begin{cases} -\frac{\pi}{4} \quad \text{for } -1 \le y < 0 \\ \frac{\pi}{4} \quad \text{for } 0 < y \le 1. \end{cases} \tag{4.4.3b}$$

These profiles are computed following the same steps as in Section 3.3. We regard the solutions in the first column of Figure 4.2 as being OR-type solutions although $s(0) \neq 0$ but $s(0) \ll 1$, as the director profile resembles a polydomain structure. As $|p_x|$ increases, we lose this approximate zero in s i.e., we lose the approximate domain wall and $s \to 1$ almost everywhere. It is also worth noting, that the director represents a splay deformation when $\omega = -\frac{1}{4}$, and a bend deformation when $\omega = \frac{1}{4}$, which becomes more pronounced as $|p_x|$ increases.

To highlight the effect of $|p_x|$, we can compute asymptotic expansions for Q_{11} and Q_{12} in the $L^* \to \infty$ limit, for small values of p_x by setting $\frac{1}{L^*} = p_x$ in the governing equations, and expanding around the OR solution $(Q_{11}, Q_{12}) = (0, -\frac{y}{2})$ i.e.,

$$Q_{11} = p_x g_2(y) + p_x^2 g_3(y) + \mathcal{O}\left(p_x^3\right), \quad Q_{12} = \frac{y}{2} + p_x f_2(y) + p_x^2 f_3(y) + \mathcal{O}\left(p_x^3\right),$$

where $g_2(\pm 1) = g_3(\pm 1) = f_2(\pm 1) + f_3(\pm 1) = 0$. We also take $L_2 = 0$, since L_2 is

small in Figure 4.2. Substituting the above into the system (4.1.3) (in the static case) and assuming a constant and small flow field (since p_x is small), we obtain,

$$Q_{11} = 0, \quad Q_{12} = \frac{y}{2} + p_x \left(\frac{y^5}{40} - \frac{y^3}{12} + \frac{7y}{120} \right) + p_x^2 f_3(y) + \mathcal{O}(p_x^3), \tag{4.4.4}$$

where

$$f_3(y) = \frac{y^9}{960} - \frac{y^7}{140} + \frac{41y^5}{2400} - \frac{7y^3}{360} + \frac{853y}{10800}.$$

In practice, for small p_x the flow u is small and non-constant, hence Q_{11} is non-zero but small, i.e., $|Q_{11}| \ll 1$. Also, $Q_{12}(0) \neq 0$ but $|Q_{12}(0)| \ll 1$.

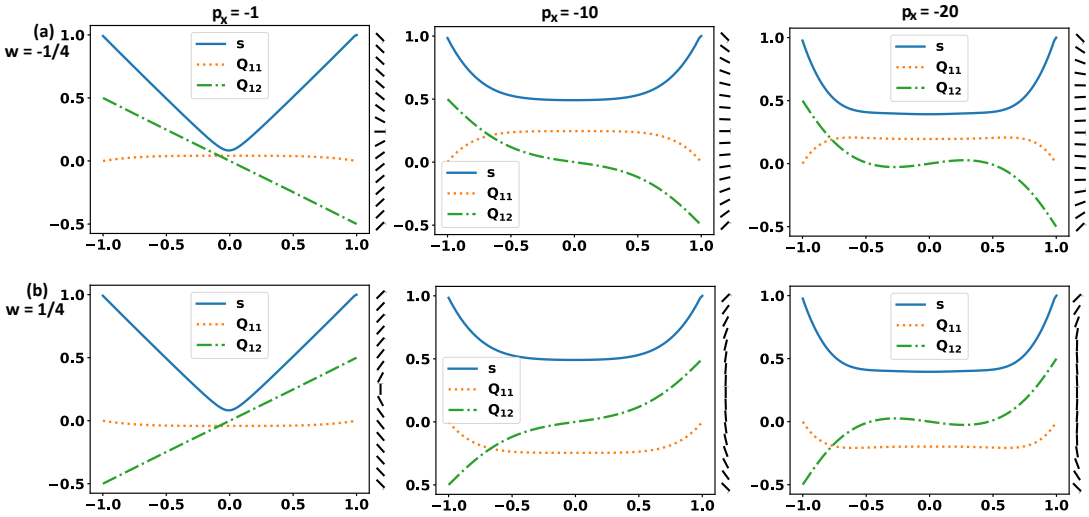

Figure 4.2: The stable solutions of (4.1.3) for $L^* = \infty$ (i.e., we remove the bulk contributions) and $L_2 = 1e-3$. The values of p_x and ω, are indicated in the plots (the same comments apply to all other figures where values are included in the plots).

We now proceed to study solutions of (4.1.3) in the $L^* \to 0$ limit, relevant for micron-scale channel domains. We are interested in the stable equilibrium solutions and the existence of OR-type solutions in this limit, and how well the OR-type solutions are approximated by the asymptotic expansions in Section 4.3.1. As expected, in Figure 4.3 we find stable equilibria which satisfy $s = 1$ almost everywhere. We also report unstable OR-type solutions in Figure 4.4, when

$\omega = -\frac{1}{4}$. We again consider these to be OR-type solutions despite $s(0) \neq 0$, since their behaviour is consistent with the asymptotic expressions (4.3.23) and (4.3.24), and we also have approximate polydomain structures. We also find these OR-type solutions for $\omega = \frac{1}{4}$, but do not report them as they are similar to the $\omega = -\frac{1}{4}$ case (the same is true in the next subsection). In fact, $\omega = \pm\frac{1}{4}$ are the only boundary conditions for which we have been able to identify OR-type solutions (identical comments apply to the active case).

In Figure 4.4, we present three distinct OR-type solutions which vary in their Q_{11} and Q_{12} profiles, or equivalently the rotation of θ between the bounding plates at $y = \pm 1$. These numerical solutions are found by taking (4.3.23) (with $s_{min} = 0$) and (4.3.24) with different values of k ($k = 0, 1, 2$), as the initial condition in our Newton solver. We conjecture that one could build a hierarchy of OR-type solutions corresponding to arbitrary integer values of k in (4.3.17), or different jumps in θ at $y = 0$ in (4.3.17), when $\omega = \pm\frac{1}{4}$. OR-type solutions are unstable, and we speculate that the solutions corresponding to different values of k in (4.3.17) are unstable equilibria with different Morse indices, where the Morse index is a measure of the instability of an equilibrium point [100]. A higher value of k could correspond to a higher Morse index or informally speaking, a more unstable equilibrium point with more directions of instability. A further relevant observation is that according to the asymptotic expansion (4.3.24), $Q_{11}(0\pm) = 0$ and $Q_{12}(0\pm) = \pm\frac{1}{2}$ for $\omega = \pm\frac{1}{4}$, and hence the energy of the domain wall does not depend strongly on k. The far-field behavior does depend on k in (4.3.24), and we conjecture that this k-dependence generates the family of k-dependent OR-type equilibrium solutions. We note that OR-type solutions generally do not satisfy $s(0) = 0$, but typically exhibit approximate polydomain structures in θ, or equivalently the director $\mathbf{n} = (\cos\theta, \sin\theta)$. However, as $L^* \to 0$, we find $s(0) \to 0$

for OR-type solutions, for a fixed p_x (see Figure 4.5).

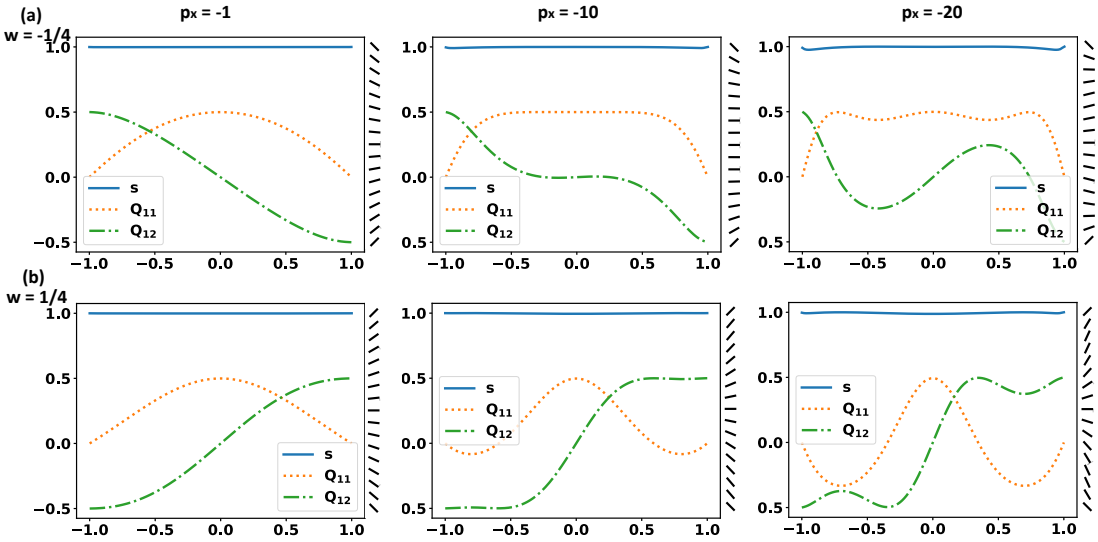

Figure 4.3: Some example stable solutions of (4.1.3) for $L^* = 1e-3$ and $L_2 = 1e-3$. With $A = 3900\text{Nm}^{-2}$ and $K = 10^{-11}$, this value of L^* corresponds to a channel of width $2D = 3.2 \times 10^{-6}$m.

To conclude this section on passive flows, we assess the accuracy of our asymptotic expansions in Section 4.3.1. In Figure 4.6, we plot the error between the asymptotic expressions ((4.3.23) and (4.3.24)) and the corresponding numerical solutions of (4.1.3), for the parameter values $L^* = 1e-4$, $L_2 = 1e-3$, $p_x = -20$ and $\omega = -\frac{1}{4}$. More precisely, we use these parameter values along with $k = 1, 2, 3$ in (4.3.24), and (4.3.23) with $s_{min} = 0$, to construct the asymptotic profiles. We then use these asymptotic profiles as initial conditions to find the corresponding numerical solutions. Hence, we have three comparison plots in Figure 4.6, corresponding to $k = 1, 2, 3$ respectively. By error, we refer to the difference between the asymptotic profile and the corresponding numerical solution. We label the asymptotic profiles using the superscript 0, in the $L^* \to 0$ limit, whilst a non-zero superscript identifies the numerical solution along with the the value of L^* used in the numerics (these comments also apply to the active case in the next section).

We find good agreement between the asymptotics and numerics, especially for the s-profiles, where any error is confined to a narrow interval around $y = 0$ and does not exceed 0.07 in magnitude. Using (4.1.2), (4.3.23), and (4.3.24), we construct the corresponding asymptotic profile $\mathbf{Q}^0$. Looking at the differences between $\mathbf{Q}^0$ and the numerical solutions $\mathbf{Q}^{1e-4}$ (for $k = 1, 2, 3$), the error does not exceed 0.06 in magnitude. This implies good agreement between the asymptotic and numerically computed θ-profiles, at least for the parameter values under consideration. While the fluid velocity u is not the focus of this work, we note that our asymptotic profile (4.3.14), gives almost perfect agreement with the numerical solution for u.

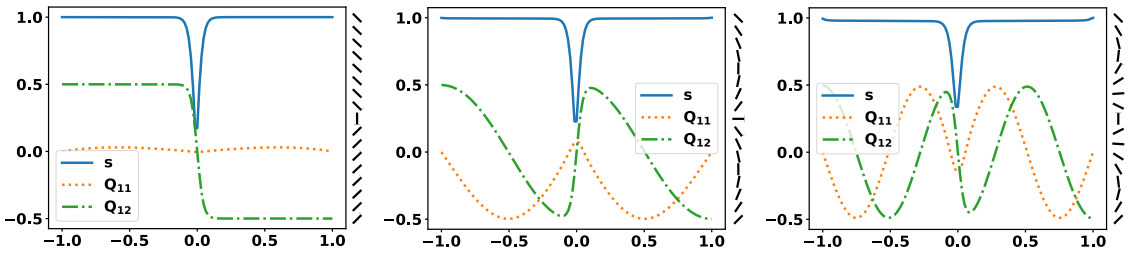

Figure 4.4: Three unstable OR-type solutions (in the sense that they have transition layer profiles for s) of (4.1.3) for $L^* = 1e-3$, $L_2 = 1e-3$, $p_x = -1$ and $\omega = -\frac{1}{4}$. The initial conditions used are (4.3.23) (with $s_{min} = 0$) and (4.3.24) with $k = 0, 1, 2$ (from left to right), along with the parameter values just stated.

Active flows

As explained previously, we consider active flows with constant concentration c, and take $c > c^*$. To this end, we fix $c = \sqrt{2\pi}$ in the following numerical experiments. For L^* large (small nano-scale channel domains), we find OR-type solutions when $\omega = \pm\frac{1}{4}$, and these are stable. In Figure 4.7, we plot these solutions when $p_x = -1$ and for three different values of Γ, which we recall is proportional to the activity parameter α_2. We only have $s(0) < 0.5$ when $\Gamma = 1$, in which case

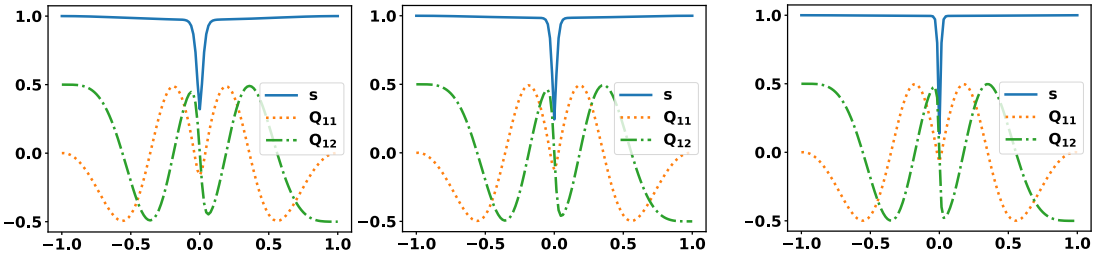

Figure 4.5: Plot of an OR-type solution for $L^* = 5e-4$, $3e-4$, $1e-4$ (from left to right). The remaining parameter values are $L_2 = 1e-3$, $p_x = -20$ and $\omega = -\frac{1}{4}$. The initial conditions used are (4.3.23) (with $s_{min} = 0$) and (4.3.24) with $k = 2$, along with the parameter values just stated.

the director profile exhibits approximate polydomain structures. As Γ increases, $s(0)$ increases and $s \to 1$ almost everywhere, so that OR-type solutions are only possible for small values of p_x and Γ. Increasing $|p_x|$ for a fixed value of Γ, also drives $s \to 1$ everywhere. Looking at Figure 4.2 and Figure 4.7 together, we notice that if Q_{11} is positive in the interior, the nematic director has a splay deformation and if Q_{11} is negative in the interior, the director has a bend deformation.

As in the passive case, we also find unstable OR-type solutions consistent with the limiting asymptotic expression (4.3.23), along with a discontinuous θ-profile as in (4.3.33), for small values of L^* that correspond to micron-scale channels. The stable solutions have $s \approx 1$ almost everywhere (see Figure 4.8). In Figure 4.9, we find unstable OR-type solutions when $L^* = 1e-3$, $L_2 = 1e-3$ and $\omega = -\frac{1}{4}$, for a range of values of p_x and Γ. To numerically compute these solutions, we use the stated parameter values in (4.3.23) (with $s_{min} = 0$) and (4.3.35), along with $k = 0$, as our initial condition. We only have $s(0) \approx 0$ provided $|p_x|$ and Γ are not too large, however, $s(0) \to 0$ in the $L^* \to 0$ limit for fixed values of p_x and Γ. This illustrates the robustness of OR-type solutions in an active setting. In Figure 4.10, we plot three further distinct OR-type solutions, obtained by taking (4.3.23)

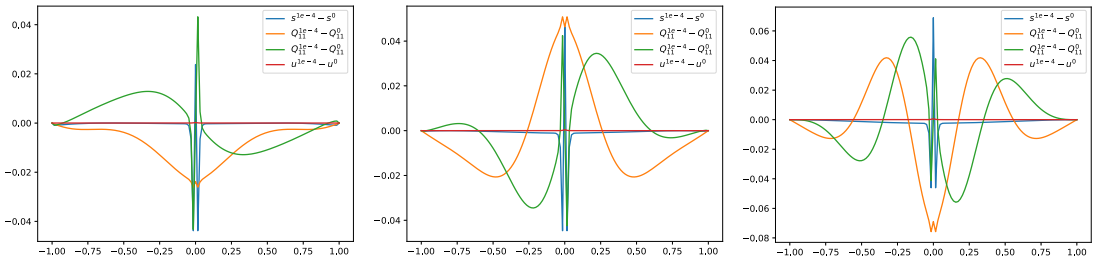

Figure 4.6: Plot of $\mathbf{Q}^{1e-4} - \mathbf{Q}^0$, $s^{1e-4} - s^0$, and $u^{1e-4} - u^0$. Here, $\mathbf{Q}^0$ is the asymptotic profile given by (4.3.23) and (4.3.24) with, $s_{min} = 0$, $k = 1, 2, 3$ (from left to right), $L^* = 1e-4$, $L_2 = 1e-3$, $p_x = -20$ and $\omega = -1/4$, whilst $\mathbf{Q}^{1e-4}$ denotes the corresponding numerical solution of (4.1.3). s^0 is given by (4.3.23) and s^{1e-4} is extracted from $\mathbf{Q}^{1e-4}$. The numerical solutions are found by using $\mathbf{Q}^0$ as the initial condition. Identical comments apply to $u^0 - u^{1e-4}$, where u^0 is given by (4.3.14) and u^{1e-4} is the numerical solution of (4.1.3).

(with $s_{min} = 0$) and (4.3.35) with $k = 1, 2, 3$ as our initial condition. Hence, for the same reasons as in the passive case, we believe there maybe multiple unstable OR-type solutions, corresponding to different values of k in (4.3.17).

By analogy with the passive case, we now compare the asymptotic expressions (4.3.23), (4.3.34) and (4.3.35), with the numerical solutions. The error plots are given in Figure 4.11. Once again, there is good agreement between the limiting s-profile (4.3.23) and the numerical solutions, where any error is confined to a small interval around $y = 0$. There is also good agreement between the asymptotic and numerically computed θ-profiles (coded in terms of Q_{11} and Q_{12}) and flow profile u, provided $|p_x|$, Γ, or both, are not too large. When $|p_x|$ and Γ are large (say much greater than 1), the accuracy of the asymptotics breaks down, especially for the u-profile. However, OR-type solutions are still possible for large values of $|p_x|$ and Γ, as elucidated by Figure 4.9.

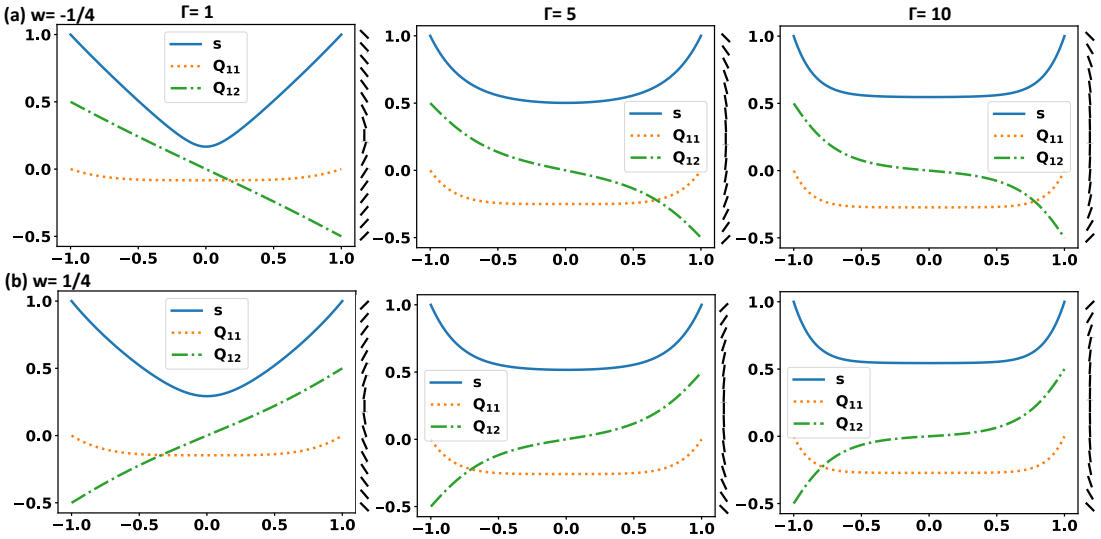

Figure 4.7: The stable solutions of (4.3.28) for $L^* = \infty$, $L_2 = 1e-3$, $c = \sqrt{2\pi}$ and $p_x = -1$.

4.5 Summary

The conclusions of this chapter can be summarised as follows:

- We provide another example of OR solutions in NLC-filled channels, hence supporting the idea that these solutions maybe universal. Section 4.2 focuses on the simple and idealised case of constant flow and pressure to give some preliminary insight into the more complex systems considered in Section 4.3. Many of the results from Section 3.2 are applied/adapted to the case of nematodynamics with constant flow and constant pressure. In particular, we find OR solutions are only compatible with orthogonal boundary conditions on the nematic director.

- In Section 4.3, we calculate useful asymptotic expansions for OR-type solutions in the limit of large domains, for both passive and active nematics without the assumptions of constant velocity and pressure. The asymptotics are validated by numerically computed OR-type solutions for small and large

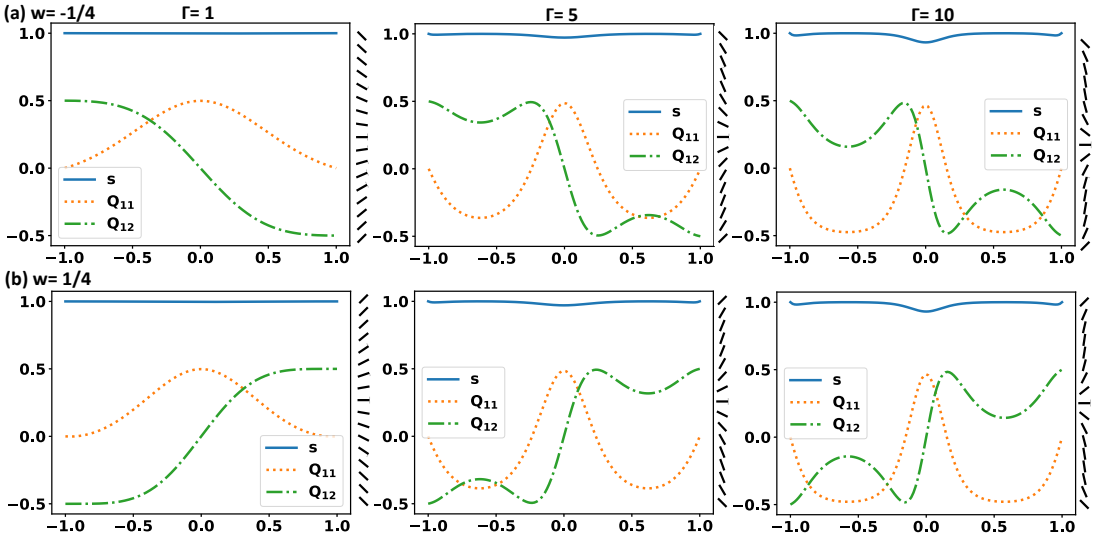

Figure 4.8: The stable solutions of (4.3.28) for $L^* = 1e-3$, $L_2 = 1e-3$, $c = \sqrt{2\pi}$ and $p_x = -1$.

values of L^*, using the asymptotic expansions as initial conditions. There is good agreement between the asymptotics and the numerical solutions, and the asymptotics give good insight into the internal structure of domain walls of OR-type solutions and the outer far-field solutions. In fact, as with OR solutions for constant flow and pressure, we find OR-type solutions to be compatible with $\omega = \pm\frac{1}{4}$ only, or orthogonal boundary conditions, in these general passive and active settings.

- The strength and power of our asymptotic expressions and numerically obtained OR-type solutions, lies in their ability to describe (qualitatively) experimentally observed phenomena. Referring again to the experimental results in [18] for passive nematodynamics confined to microfluidic channels, the authors observe disclination lines in the channel centre. These disclination lines are captured beautifully (in a visual sense) by our OR-type solutions after extrapolating the profiles across the length of the channel (this can be done based on our modelling assumption that structural proper-

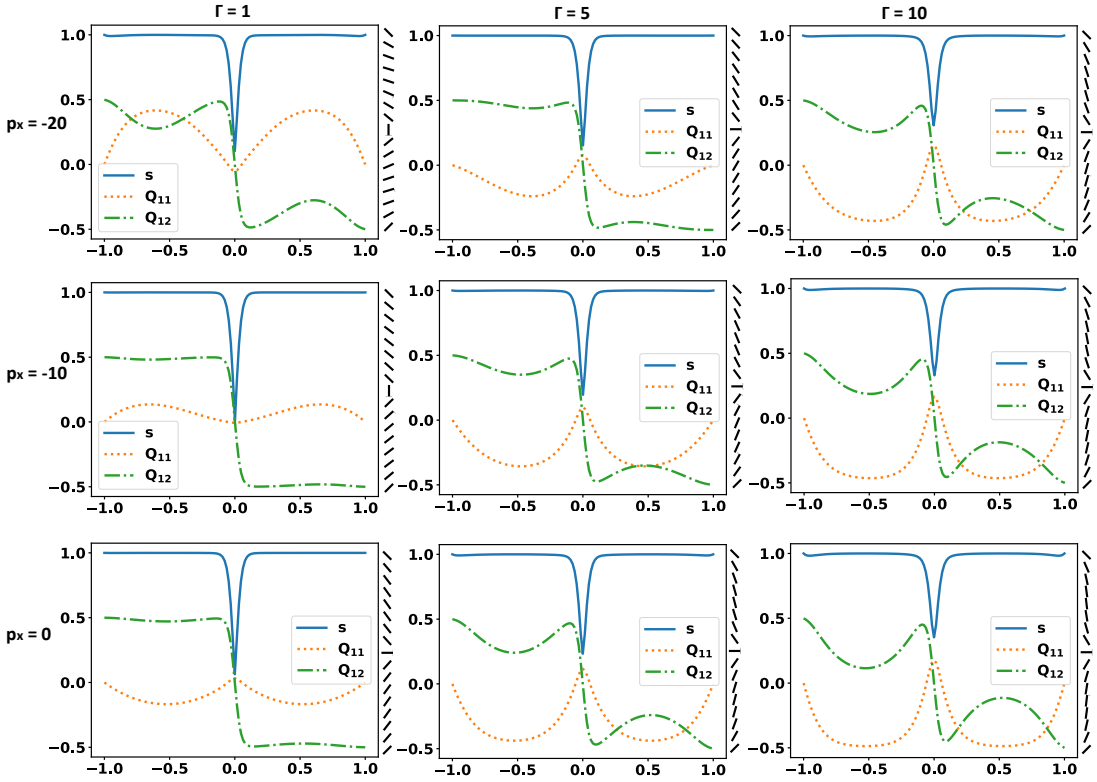

Figure 4.9: Unstable OR-type solutions (in the sense that they have transition layer profiles for s) of (4.3.28), for $L^* = 1e-3$, $L_2 = 1e-3$, $c = \sqrt{2\pi}$ and $\omega = -\frac{1}{4}$. The initial conditions used are (4.3.23) (with $s_{min} = 0$) and (4.3.35) with $k = 0$.

ties will be uniform across the length of the channel). Moreover, the authors observe a $\pi/2$ reorientation of the director across disclination lines and this is in agreement with our observation of OR-type solutions for orthogonal boundary conditions only, where the director undergoes an approximate $\pi/2$ reorientation across the single central domain wall. For the active case, the authors in [86] observe multiple parallel lanes of defect cores in their active system, which is confined to a cylindrical cell. Hence, for the same reasons as above, our active OR-type solutions describe well a single defect core. For an active system confined to a microfluidic channel, it may be the case that a single defect core is observed and our results would again

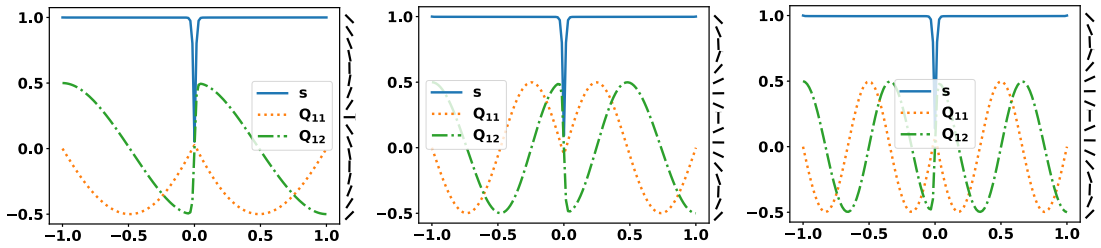

Figure 4.10: Three unstable OR-type solutions of (4.3.28) for $L^* = 1e-3$, $L_2 = 1e-3$, $p_x = -1$, $\Gamma = 0.7$ and $\omega = -\frac{1}{4}$. The initial conditions used are (4.3.23) (with $s_{min} = 0$) and (4.3.35) with $k = 1, 2, 3$ (from left to right), along with the parameter values just stated.

be a very good match to experiments. Details of the reorientation of the director across defect cores are not given in [86], so whether orthogonality of the director is key here is unclear.

- In Section 4.4, the OR-type solutions are unstable for small L^* or large channels. However, the experimental results in [18, 86] show that flows containing disclination lines or domain walls, can be stabilised in experiments via electric fields in the passive case, and magnetic fields in the active case. So, while these OR-type solutions are unstable mathematically, they can be stabilised or controlled/exploited for transport phenomena and cargo transport in experiments, making such solutions of physical interest. In general, we argue that unstable solutions are of independent interest since they play crucial roles in the connectivity of solution landscapes of complex systems [100] (also see Chapter 6).

Future work would be:

1. To thoroughly investigate solution landscapes for these passive and active nematodynamic systems, with a focus on understanding the multiplicity of

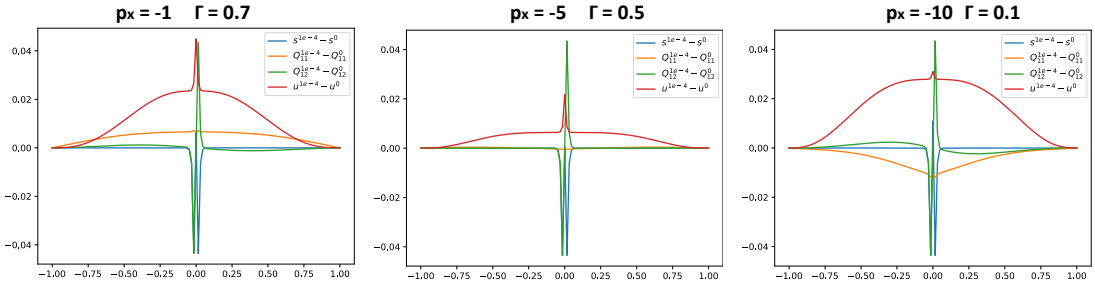

Figure 4.11: Plot of $\mathbf{Q}^{1e-4} - \mathbf{Q}^0$, $s^{1e-4} - s^0$, and $u^{1e-4} - u^0$. Here, $\mathbf{Q}^0$ is given by (4.3.23) and (4.3.35) with, $s_{min} = 0$, $k = 0$, $c = \sqrt{2\pi}$, $L^* = 1e-4$, $L_2 = 1e-3$, p_x and Γ as stated in the figure, and $\omega = -1/4$, whilst $\mathbf{Q}^{1e-4}$ is the numerical solution of (4.3.28), with the same parameter values. s^0 is given by (4.3.23) and s^{1e-4} is extracted from $\mathbf{Q}^{1e-4}$. The numerical solutions are found by using $\mathbf{Q}^0$ as the initial condition. Identical comments apply to $u^0 - u^{1e-4}$, where u^0 is given by (4.3.34) and u^{1e-4} is the numerical solution of (4.3.28).

OR-type solutions and how our asymptotic profiles may be used to generate such solutions.

2. To investigate passive and active nematodynamics in other non-trivially shaped geometries, such as wedge shaped or curved channels.

To conclude this chapter, we argue why OR/OR-type solutions maybe universal in variational theories, with free energies that employ a Dirichlet elastic energy for the unknowns, e.g. $y_1 \dots y_n$ for $n \in \mathbb{N}$. Working in a one-dimensional setting, consider an energy of the form

$$\int_\Omega y_1'(x)^2 + \dots y_n'(x)^2 + \frac{1}{L^*} h(y_1, \dots y_n)(x) \, \mathrm{d}x, \tag{4.5.1}$$

subject to Dirichlet boundary conditions, for a material-dependent positive elastic constant L^*. The function, h, models a bulk energy that only depends on $y_1, \dots, y_n$. As $L^* \to \infty$, the limiting Euler-Lagrange equations admit unique

solutions of the form $y_j = ax + b$, for constants a and b. For specific choices of Ω and asymmetric boundary conditions, we can have domain walls at $x = x^*$ such that $y_j(x^*) = 0$ for $j = 1, \ldots, n$. Writing each $y_j = |y_j| sgn(y_j)$, the domain wall separates sub-domains with phases differentiated by different values of $sgn(y_j)$. Furthermore, if the bulk contribution h, is such that the Euler-Lagrange equations are satisfied when $y_1 = \ldots = y_n = 0$ for any value of L^*, we may always find solutions with domain walls.

Chapter 5

One-dimensional ferronematics

This chapter is derived from Dalby, Farrell, Majumdar and Xia (2022) [2].

5.1 The problem

In this chapter we study ferronematics, i.e., a mixture consisting of magnetic nanoparticles (MNPs) suspended in a nematic liquid crystal (NLC). Ferronematics are interesting since they have the potential to extend applications of nematics to magnetic field driven devices. This is a result of their substantially increased magnetic response. They are also a relatively new and unexplored material from an applications perspective, with the first stable ferronematic only being reported in [35] in 2013. Of particular interest our ferronematic systems that support multiple stable ferronematic states, without external magnetic fields. This is analogous to multistable nematic systems, such as bistable liquid crystal displays, but ferronematics have additional magnetic order that allows for greater complexity in the observable equilibria. As such, ferronematics represent an exciting material in need of greater understanding and are therefore worthy of an in-depth mathemat-

ical study as performed in this chapter. The work in this chapter is a first step in the rigorous analytical and numerical study of multistable ferronematic systems, without external magnetic fields. Once understood, magnetic fields could then be incorporated to switch between the distinct stable ferronematic states, to control non-equilibrium behaviour for multistable systems.

We prove useful qualitative results for a model for ferronematics first proposed in [69, 70]. In [69, 70] the authors numerically study this model in one- and two-dimensions respectively, and begin to explore the effects of model parameters. We instead answer key questions regarding the existence, uniqueness, and stability of solutions of this model. We also investigate solution types, specifically, order reconstruction (OR) and non-OR solutions. OR solutions were introduced in Section 2.3 and they are well documented for conventional nematics, but surprisingly, we find that OR solutions exist for this ferronematic system too. In fact, an OR solution is the unique global minimiser of the ferronematic free energy for small domain sizes and then loses stability for large domains, where we also find multiple OR solutions. There are similarities and differences between the interpretation of OR solution in the context of ferronematics and conventional nematics, and this will be explained in due course. Once our analytic results are proven, we perform complementary numerical experiments which support our results and also shed some preliminary insight into the ferronematic solution landscape. In particular, we numerically observe a pitchfork bifurcation away from the unique OR solution and the emergence of multiple stable states, highlighting mutlistability is possible for one-dimensional ferronematic suspensions. The exploration of ferronematic solution landscapes is then built upon in Chapter 6.

5.1.1 Modelling framework

We study a dilute suspension of MNPs in a NLC filled channel. We assume a uniform distribution of MNPs (much smaller than the physical domain dimensions) such that the average distance between the MNPs is much larger than the MNP size, and the total volume fraction of MNPs is small. Our geometry is the same as the previous two chapters, namely a long thin shallow channel geometry, which is reduced to an effectively one-dimensional problem: $\bar{\Omega} = [-D, D]$

Since the MNPs generate a spontaneous magnetisation even without an external magnetic field, by means of the MNP-NLC interactions, the ferronematic suspension is described by two order parameters: (i) a reduced Landau–de Gennes (LdG) nematic $\mathbf{Q}$-tensor with two degrees of freedom (as explained in Section 2.2), that contains information about the nematic director (i.e., the eigenvector of $\mathbf{Q}$ with a positive eigenvalue) and the degree of nematic ordering, and (ii) a magnetisation vector $\mathbf{M}$ generated by the suspended MNPs. Specifically, $\mathbf{Q}$ is a symmetric traceless 2×2 matrix, i.e., $\mathbf{Q} \in S_0 \coloneqq \{\mathbf{Q} \in \mathbb{M}^{2\times 2} : Q_{ij} = Q_{ji}, Q_{ii} = 0\}$, and $\mathbf{M} = (M_1, M_2)$ is a two-dimensional vector. The nematic order parameter $\mathbf{Q}$ can be written as

$$\mathbf{Q} = s(2\mathbf{n} \otimes \mathbf{n} - \mathbf{I}_2), \tag{5.1.1}$$

where s is a scalar order parameter and $\mathbf{n}$ is the nematic director. Compared to the previous chapters, we have rescaled the reduced $\mathbf{Q}$-tensor by a factor of two for mathematical convenience. We denote the two independent components of $\mathbf{Q}$, by Q_{11} and Q_{12} such that

$$Q_{11} = s\cos 2\vartheta, \quad Q_{12} = s\sin 2\vartheta,$$

when $\mathbf{n} = (\cos\vartheta, \sin\vartheta)$ and ϑ denotes the angle between $\mathbf{n}$ and the x-axis.

Following the methods in [35, 69], the ferronematic free energy is given by the sum of three energies for low temperatures: a LdG type nematic energy for $\mathbf{Q}$,

$$f_{nem}(\mathbf{Q}, \nabla\mathbf{Q}) = \frac{K}{2}|\nabla\mathbf{Q}|^2 + 2A\text{tr}\mathbf{Q}^2 + C\text{tr}\mathbf{Q}^4 + \frac{|A|^2}{C}, \tag{5.1.2}$$

(when compared to the previous two chapters, we have rescaled the bulk contribution and introduced an additive constant for mathematical convenience) a magnetisation energy for $\mathbf{M}$,

$$f_{mag}(\mathbf{M}, \nabla\mathbf{M}) = \frac{\kappa}{2}|\nabla\mathbf{M}|^2 + \frac{\alpha}{2}|\mathbf{M}|^2 + \frac{\beta}{4}|\mathbf{M}|^4 + \frac{|\alpha|^2}{4\beta}, \tag{5.1.3}$$

and a coupling energy between $\mathbf{Q}$ and $\mathbf{M}$,

$$f_{coupling} = -\gamma\mu_0 M_i Q_{ij} M_j = -\gamma\mu_0(2(\mathbf{n}\cdot\mathbf{M})^2 - |\mathbf{M}|^2). \tag{5.1.4}$$

In (5.1.2), K is again a nematic elasticity constant, $A < 0$ is a material and temperature dependent constant, and $C > 0$ is a material dependent constant (as in (1.5.11a)). As seen previously, (5.1.2) is a sum of elastic and bulk effects (Section 1.5.2). (5.1.3) is a Ginzburg-Landau energy, where $\alpha < 0$ and $\beta > 0$ are Landau coefficients describing the ferronematic transition [35], and κ is a magnetic stiffness constant associated to the elastic energy density [70]. Finally, in (5.1.4), γ is an MNP-NLC coupling parameter such that positive values of γ coerce $\mathbf{n}$ and $\mathbf{M}$ to be parallel or anti-parallel, whereas negative values of γ coerce $\mathbf{n}$ and $\mathbf{M}$ to be perpendicular to each other [69] (μ_0 is the vacuum permeability [35]). Moreover, γ can be related to the shape and size of the MNPs, as well as the strength of the surface-mediated MNP-NLC interactions via the surfaces of the MNPs [70].

We use the following scalings, $\bar{\mathbf{Q}} = \sqrt{\frac{2C}{|A|}}\mathbf{Q}$, $\bar{\mathbf{M}} = \sqrt{\frac{\beta}{|\alpha|}}\mathbf{M}$ and $\bar{y} = yD$, which leads

to four dimensionless parameters [69]:

$$L^* = \frac{K}{D^2|A|},\ l_2 = \frac{\kappa}{D^2|\alpha|},\ c = \frac{\gamma\mu_0}{|A|}\sqrt{\frac{C}{2|A|}}\frac{|\alpha|}{\beta},\ \xi = \frac{C}{|A|^2}\frac{|\alpha|^2}{\beta}. \tag{5.1.5}$$

Here, $L^* > 0$ (seen previously) and $l_2 > 0$ are scaled elastic constants (inversely proportional to D^2, i.e., the physical channel width squared). ξ is a measure of magnetic order, such that large values of ξ coerce the system to minimise the magnetisation energy. c is a coupling parameter and we take $c > 0$ in this work so that the coupling energy favours $\mathbf{n} \cdot \mathbf{M} = \pm 1$. After dropping bars, our rescaled domain is $\Omega = [-1, 1]$, while the total rescaled and dimensionless ferronematic free energy is

$$\begin{aligned} F(Q_{11}, Q_{12}, M_1, M_2) = \int_{-1}^{1} \Bigg\{ & \frac{L^*}{2}\left[\left(\frac{\mathrm{d}Q_{11}}{\mathrm{d}y}\right)^2 + \left(\frac{\mathrm{d}Q_{12}}{\mathrm{d}y}\right)^2\right] + \left(Q_{11}^2 + Q_{12}^2 - 1\right)^2 \\ & + \frac{\xi l_2}{2}\left[\left(\frac{\mathrm{d}M_1}{\mathrm{d}y}\right)^2 + \left(\frac{\mathrm{d}M_2}{\mathrm{d}y}\right)^2\right] + \frac{\xi}{4}\left(M_1^2 + M_2^2 - 1\right)^2 \\ & - cQ_{11}\left(M_1^2 - M_2^2\right) - 2cQ_{12}M_1M_2 \Bigg\}\,\mathrm{d}y. \end{aligned} \tag{5.1.6}$$

Regarding boundary conditions, we work with Dirichlet conditions for $\mathbf{Q}$ and $\mathbf{M}$ on the boundaries $y = \pm 1$ i.e.,

$$\begin{aligned} & Q_{11}(-1) = M_1(-1) = 1, \\ & Q_{12}(-1) = Q_{12}(1) = M_2(-1) = M_2(1) = 0, \\ & Q_{11}(1) = M_1(1) = -1. \end{aligned} \tag{5.1.7}$$

Here, the boundary conditions for $\mathbf{Q}$ correspond to $\mathbf{n} = (1, 0)$ on $y = -1$ and $\mathbf{n} = (0, 1)$ on $y = 1$ (with $s(\pm 1) = 1$), hence, we have planar boundary conditions on $y = -1$ and normal/homeotropic boundary conditions on $y = +1$. Furthermore, the boundary conditions for $\mathbf{M}$ describe a π-rotation between the bounding plates,

$y = \pm 1$.

The admissible space is given by

$$\mathcal{A} := \left\{ \mathbf{Q} \in W^{1,2}\left(\Omega; S_0\right), \mathbf{M} \in W^{1,2}\left(\Omega; \mathbb{R}^2\right) : \right.$$
$$\left. \mathbf{Q} \text{ and } \mathbf{M} \text{ satisfy the boundary conditions (5.1.7)} \right\}. \quad (5.1.8)$$

The Sobolev space $W^{1,2}$ is the space of all square-integrable $(\mathbf{Q}, \mathbf{M})$ with square-integrable first derivatives, which is a standard choice for such variational problems. The stable, physically relevant and potentially observable $(\mathbf{Q}, \mathbf{M})$-profiles are local or global energy minimisers of the full energy (5.1.6) subject to the boundary conditions in (5.1.7), in $\mathcal{A}$. They are in fact, solutions of the associated Euler–Lagrange equations [69]

$$L^* \frac{\mathrm{d}^2 Q_{11}}{\mathrm{d}y^2} = 4Q_{11}(Q_{11}^2 + Q_{12}^2 - 1) - c\left(M_1^2 - M_2^2\right), \quad (5.1.9a)$$
$$L^* \frac{\mathrm{d}^2 Q_{12}}{\mathrm{d}y^2} = 4Q_{12}(Q_{11}^2 + Q_{12}^2 - 1) - 2cM_1M_2, \quad (5.1.9b)$$
$$\xi l_2 \frac{\mathrm{d}^2 M_1}{\mathrm{d}y^2} = \xi M_1\left(M_1^2 + M_2^2 - 1\right) - 2cQ_{11}M_1 - 2cQ_{12}M_2, \quad (5.1.9c)$$
$$\xi l_2 \frac{\mathrm{d}^2 M_2}{\mathrm{d}y^2} = \xi M_2\left(M_1^2 + M_2^2 - 1\right) + 2cQ_{11}M_2 - 2cQ_{12}M_1. \quad (5.1.9d)$$

5.2 Qualitative results

To avoid writing $\mathbf{Q}$ in the matrix form $\left[\begin{smallmatrix} Q_{11} & Q_{12} \\ Q_{12} & -Q_{11} \end{smallmatrix}\right]$, we henceforth label $\mathbf{Q}$ in terms of its two independent components (Q_{11}, Q_{12}). We therefore define the vector norm, $|\mathbf{Q}| = \sqrt{Q_{11}^2 + Q_{12}^2}$, as opposed to a matrix norm (the difference is a factor of 2) **in this chapter and Chapter 6 only**. The first result concerns a brief proof of the existence of a global minimiser of the free energy (5.1.6), in $\mathcal{A}$.

Theorem 5.2.1. *For all positive values of (L^*, l_2, c, ξ), there exists at least one*

minimiser $(Q_{11}^*, Q_{12}^*, M_1^*, M_2^*)$ *of the ferronematic free energy* (5.1.6)*, in the admissible space* (5.1.8)*. Moreover, this minimiser is a (classical) solution of the Euler–Lagrange equations* (5.1.9a)-(5.1.9d) *subject to the boundary conditions* (5.1.7)*.*

Remark 5.2.2. For brevity of notations, we omit $(\Omega; S_0)$ and $(\Omega; \mathbb{R}^2)$ in the Sobolev spaces hereafter in this chapter, whenever it causes no confusions.

Proof. The admissible space (5.1.8) is nonempty as

$$(Q_{11}, Q_{12}, M_1, M_2) = (-y, 0, -y, 0) \in \mathcal{A}.$$

The ferronematic energy (5.1.6) is quadratic and thus, convex in the gradient of all four state variables $(Q_{11}, Q_{12}, M_1, M_2)$ and hence, weakly lower semi-continuous [74]. Furthermore, the coupling energy can be decomposed as follows

$$\begin{aligned}
-cQ_{11}\left(M_1^2 - M_2^2\right) - 2cQ_{12}M_1M_2 &\geq -c(M_1^2 + M_2^2)(|Q_{11}| + |Q_{12}|) \\
&\geq -\frac{c}{2}\left(\epsilon\left(|Q_{11}| + |Q_{12}|\right)^2 + \frac{1}{\epsilon}\left(M_1^2 + M_2^2\right)^2\right) \\
&\geq -\frac{c}{2}\left(2\epsilon\left(Q_{11}^2 + Q_{12}^2\right) + \frac{1}{\epsilon}\left(M_1^2 + M_2^2\right)^2\right),
\end{aligned}$$

where $\epsilon > 0$ is arbitrary. Hence, the energy density is bounded from below as

$$\begin{aligned}
&\frac{L^*}{2}\left[\left(\frac{\mathrm{d}Q_{11}}{\mathrm{d}y}\right)^2 + \left(\frac{\mathrm{d}Q_{12}}{\mathrm{d}y}\right)^2\right] + \left(Q_{11}^2 + Q_{12}^2 - 1\right)^2 + \frac{\xi l_2}{2}\left[\left(\frac{\mathrm{d}M_1}{\mathrm{d}y}\right)^2 + \left(\frac{\mathrm{d}M_2}{\mathrm{d}y}\right)^2\right] \\
&\quad + \frac{\xi}{4}\left(M_1^2 + M_2^2 - 1\right)^2 - cQ_{11}\left(M_1^2 - M_2^2\right) - 2cQ_{12}M_1M_2 \\
&\geq \frac{L^*}{2}\left[\left(\frac{\mathrm{d}Q_{11}}{\mathrm{d}y}\right)^2 + \left(\frac{\mathrm{d}Q_{12}}{\mathrm{d}y}\right)^2\right] + \frac{\xi l_2}{2}\left[\left(\frac{\mathrm{d}M_1}{\mathrm{d}y}\right)^2 + \left(\frac{\mathrm{d}M_2}{\mathrm{d}y}\right)^2\right] \\
&\quad + \left[Q_{11}^2 + Q_{12}^2 - \left(1 + \frac{c\epsilon}{2}\right)\right]^2 + \left(\frac{\xi\epsilon - 2c}{4\epsilon}\right)\left(M_1^2 + M_2^2 - \frac{\epsilon\xi}{\xi\epsilon - 2c}\right)^2 \\
&\quad - \left(c\epsilon + \frac{c^2\epsilon^2}{4} + \frac{c\xi}{2(\xi\epsilon - 2c)}\right),
\end{aligned}$$

and thus the full energy (5.1.6) is coercive provided $\epsilon > \frac{2c}{\xi}$. The existence of a minimiser in the admissible space $\mathcal{A}$ therefore follows by the direct method in the calculus of variations [74]. We can follow the arguments from elliptic regularity in [65] to deduce that minimisers, and in fact all critical points of the free energy, are classical solutions of (5.1.9a)-(5.1.9d). □

5.2.1 Full problem: homogeneous solutions and asymptotics as $c \to 0$ and $c \to \infty$

We now complete a useful study of the homogeneous solutions of the problem, that is, the critical points of the bulk energy density (which consists of the non-gradient contributions to the free energy (5.1.6)). In particular, we look at the bulk energy minimisers for different values of (c, ξ), as these are crucial for the analysis of the full variational problem. We denote the bulk energy density by

$$\begin{aligned} f(Q_{11}, Q_{12}, M_1, M_2) \coloneqq &\left(Q_{11}^2 + Q_{12}^2 - 1\right)^2 + \frac{\xi}{4}\left(M_1^2 + M_2^2 - 1\right)^2 \\ &- cQ_{11}\left(M_1^2 - M_2^2\right) - 2cQ_{12}M_1M_2. \end{aligned} \tag{5.2.1}$$

Using the substitutions

$$\begin{aligned} Q_{11} &= \rho\cos(\theta), Q_{12} = \rho\sin(\theta), \\ M_1 &= \sigma\cos(\phi), M_2 = \sigma\sin(\phi), \end{aligned} \tag{5.2.2}$$

the bulk energy density becomes

$$f(\rho, \sigma, \theta, \phi) = (\rho^2 - 1)^2 + \frac{\xi}{4}(\sigma^2 - 1)^2 - c\rho\sigma^2\cos(2\phi - \theta). \tag{5.2.3}$$

The critical points $(\rho(c, \xi), \sigma(c, \xi))$, $\rho, \sigma \geq 0$ are solutions of the following system of algebraic equations:

$$4\rho\cos(\theta)\left(\rho^2 - 1\right) - c\sigma^2\cos(2\phi) = 0, \tag{5.2.4a}$$

$$4\rho\sin(\theta)\left(\rho^2-1\right)-c\sigma^2\sin(2\phi)=0, \tag{5.2.4b}$$

$$\xi\sigma\cos(\phi)\left(\sigma^2-1\right)-2\sigma\rho c\cos(\theta-\phi)=0, \tag{5.2.4c}$$

$$\xi\sigma\sin(\phi)\left(\sigma^2-1\right)-2\sigma\rho c\sin(\theta-\phi)=0. \tag{5.2.4d}$$

There are two trivial solutions, i.e., $\rho=\sigma=0$; $\rho=1$ and $\sigma=0$, which exist for all real-valued c and ξ. For these trivial solutions, θ and ϕ are undetermined. For ferronematic solutions, we need $\rho,\sigma\neq 0$ in order to capture the nemato-magnetic coupling. The equations (5.2.4) can be explicitly solved; firstly, (5.2.4c) and (5.2.4d) give

$$\sigma^2=1+\frac{2\rho c\cos(\theta-\phi)}{\xi\cos(\phi)} \text{ and } \sigma^2=1+\frac{2\rho c\sin(\theta-\phi)}{\xi\sin(\phi)},$$

respectively, which in turn require that

$$\frac{\cos(\theta-\phi)}{\cos(\phi)}=\frac{\sin(\theta-\phi)}{\sin(\phi)} \implies 2\phi-\theta=n\pi \quad \text{for } n\in\mathbb{Z}, \tag{5.2.5}$$

imposing constraints on the relative alignment of $\mathbf{n}$ and $\mathbf{M}$. Furthermore, multiplying (5.2.4a) by $\sin(\theta)$, (5.2.4b) by $\cos(\theta)$, following similar steps for (5.2.4c) and (5.2.4d), and using the constraint $2\phi=\theta+n\pi$, we obtain

$$\rho^3-\rho\left(1+\frac{c^2}{2\xi}\right)-\frac{c}{4}=0, \tag{5.2.6a}$$

$$\rho^3-\rho\left(1+\frac{c^2}{2\xi}\right)+\frac{c}{4}=0. \tag{5.2.6b}$$

Here, (5.2.6a) corresponds to $2\phi-\theta=2n\pi$ whereas (5.2.6b) corresponds to $2\phi-\theta=(2n+1)\pi$, i.e., an odd multiple of π. Once ρ is determined by (5.2.6), σ is given by

$$\sigma^2=1+\frac{2\rho c}{\xi}, \tag{5.2.7a}$$

$$\sigma^2=1-\frac{2\rho c}{\xi}; \tag{5.2.7b}$$

where (5.2.7a) (respectively (5.2.7b)) is associated with (5.2.6a) (respectively (5.2.6b)).

To solve (5.2.6a), let $\rho = S+T$ and recall that $(S+T)^3-3ST(S+T)-(S^3+T^3) = 0$, then we have

$$ST = \frac{1}{3}\left(1+\frac{c^2}{2\xi}\right), \qquad S^3+T^3 = \frac{c}{4},$$

from which we deduce that S^3 and T^3 are roots of the quadratic equation

$$z^2 - \frac{c}{4}z + \frac{1}{27}\left(1+\frac{c^2}{2\xi}\right)^3 = 0,$$

i.e., $z_\pm = \frac{c}{8} \pm \sqrt{\frac{c^2}{64} - \frac{1}{27}\left(1+\frac{c^2}{2\xi}\right)^3}$. Hence, S and T are given by

$$S = \omega_j \left(\frac{c}{8} + \sqrt{\frac{c^2}{64} - \frac{1}{27}\left(1+\frac{c^2}{2\xi}\right)^3}\right)^{\frac{1}{3}} =: \omega_j \Theta_1, \tag{5.2.8a}$$

$$T = \omega_k \left(\frac{c}{8} - \sqrt{\frac{c^2}{64} - \frac{1}{27}\left(1+\frac{c^2}{2\xi}\right)^3}\right)^{\frac{1}{3}} =: \omega_k \Theta_2, \tag{5.2.8b}$$

for $j,k \in \{1,2,3\}$, where $\omega_1 = 1, \omega_2 = \frac{-1+\sqrt{3}\mathrm{i}}{2}$ and $\omega_3 = \frac{-1-\sqrt{3}\mathrm{i}}{2}$ are the cube roots of unity. Throughout this chapter, we use the notation $\mathrm{i} = \sqrt{-1}$. This yields nine possible roots of (5.2.6a), of which only three are viable choices since $ST = \frac{1}{3}\left(1+\frac{c^2}{2\xi}\right)$ and thus, $\omega_j\omega_k = 1$. Therefore, the viable roots of (5.2.6a) are given by, for $k \in \{1,2,3\}$,

$$\rho = \omega_k\Theta_1 + \omega_k^2\Theta_2, \tag{5.2.9}$$

and the corresponding values of σ are

$$\sigma = \sqrt{1 + \frac{2c}{\xi}(\omega_k\Theta_1 + \omega_k^2\Theta_2)}, \tag{5.2.10}$$

with $2\phi - \theta$ being an even multiple of π.

The cubic equation (5.2.6b) can be tackled similarly so that the relevant roots of (5.2.6b) and the corresponding values of σ are given by

$$\rho = \omega_k \left(-\frac{c}{8} + \sqrt{\frac{c^2}{64} - \frac{1}{27}\left(1 + \frac{c^2}{2\xi}\right)^3} \right)^{\frac{1}{3}} + \omega_k^2 \left(-\frac{c}{8} - \sqrt{\frac{c^2}{64} - \frac{1}{27}\left(1 + \frac{c^2}{2\xi}\right)^3} \right)^{\frac{1}{3}}$$
$$=: \omega_k \Lambda_1 + \omega_k^2 \Lambda_2, \tag{5.2.11}$$

and

$$\sigma = \sqrt{1 - \frac{2c}{\xi}(\omega_k \Lambda_1 + \omega_k^2 \Lambda_2)}, \tag{5.2.12}$$

with $2\phi - \theta$ being an odd multiple of π, for $k \in \{1, 2, 3\}$. Hence, the solution pairs $(\rho(c, \xi), \sigma(c, \xi))$ for the algebraic system (5.2.4) are given by ((5.2.9),(5.2.10)) and ((5.2.11),(5.2.12)). This yields six possibilities for ρ, and twelve possibilities for σ.

Amongst the admissible critical points, we require ρ and σ to be non-negative and real-valued. In fact, if $27c^2 \leq 64\left(1 + \frac{c^2}{2\xi}\right)$ then both (5.2.9) and (5.2.11) yield a real-valued ρ for each $k \in \{1, 2, 3\}$ (one can check this with De Moivre's formula), whilst for $27c^2 > 64\left(1 + \frac{c^2}{2\xi}\right)$, (5.2.9) and (5.2.11) have a real solution for $k = 1$ only. Furthermore, if ρ is real, (5.2.10) gives a real-valued σ when $-\frac{2c}{\xi}\rho \leq 1$, whilst (5.2.12) yields a real-valued σ if $\frac{2c}{\xi}\rho \leq 1$. Regarding non-negative solution pairs, we simply enumerate the solution pairs with $\rho \geq 0$ and choose the positive root for σ.

For simplicity, we now focus on the special case of $\xi = 1$. The inequality $27c^2 < 64\left(1 + \frac{c^2}{2}\right)^3$ holds for all $c \geq 0$, and hence, both (5.2.9) and (5.2.11) yield real-valued ρ. Therefore, ignoring negative solutions (see Figure 5.1 for a plot of all the roots), we have the following positive real solutions:

$$\rho = \Theta_1 + \Theta_2, \tag{5.2.13a}$$

$$\rho = \Lambda_1 + \Lambda_2, \tag{5.2.13b}$$

$$\rho = \omega_3\Lambda_1 + \omega_2\Lambda_2, \tag{5.2.13c}$$

and the corresponding values of σ are

$$\sigma = \sqrt{1 + 2c\,(\Theta_1 + \Theta_2)}, \tag{5.2.14a}$$

$$\sigma = \sqrt{1 - 2c\,(\Lambda_1 + \Lambda_2)}, \tag{5.2.14b}$$

$$\sigma = \sqrt{1 - 2c\,(\omega_3\Lambda_1 + \omega_2\Lambda_2)}. \tag{5.2.14c}$$

Moreover, the solutions in (5.2.14a) and (5.2.14c) correspond to a real-valued σ for all $c > 0$, while (5.2.14b) is real for $c \leq \frac{1}{2}$. Henceforth, we do not consider the solution pair ((5.2.13b),(5.2.14b)).

The next task is to determine which solution pair, (ρ, σ), minimises the bulk energy density (5.2.3), for $c \geq 0$. It is enough to observe that $f(0,0) = \frac{5}{4}$ and $f(1,0) = \frac{1}{4}$, and identify which of the non-trivial solution pairs, if any, satisfy $f(\rho,\sigma) < \frac{1}{4}$. In Figure 5.2, we plot the bulk energy density (5.2.3) as a function of c, for each non-trivial solution pair ((5.2.13a), (5.2.14a)), ((5.2.13c), (5.2.14c)) and observe that ((5.2.13a),(5.2.14a)) is the global energy minimiser for all positive values of c.

Next, we compute asymptotic expansions for the minimising pair $((5.2.13a), (5.2.14a))$ as $c \to 0$ and $c \to \infty$ respectively. As $c \to 0$, we expect the minimising pair to approach $(\rho, \sigma) \to (1, 1)$, since $(\rho, \sigma) = (1, 1)$ is the minimiser of the bulk energy density with $c = 0$. To this end, we first approximate the square root terms in (5.2.13a) as

$$\sqrt{-\frac{c^2}{64} + \frac{1}{27}\left(1 + \frac{c^2}{2}\right)^3} \approx \frac{1}{3\sqrt{3}}\left(1 + \frac{69c^2}{128}\right),$$

by applying the binomial formula. Then using De Moivre's formula and an

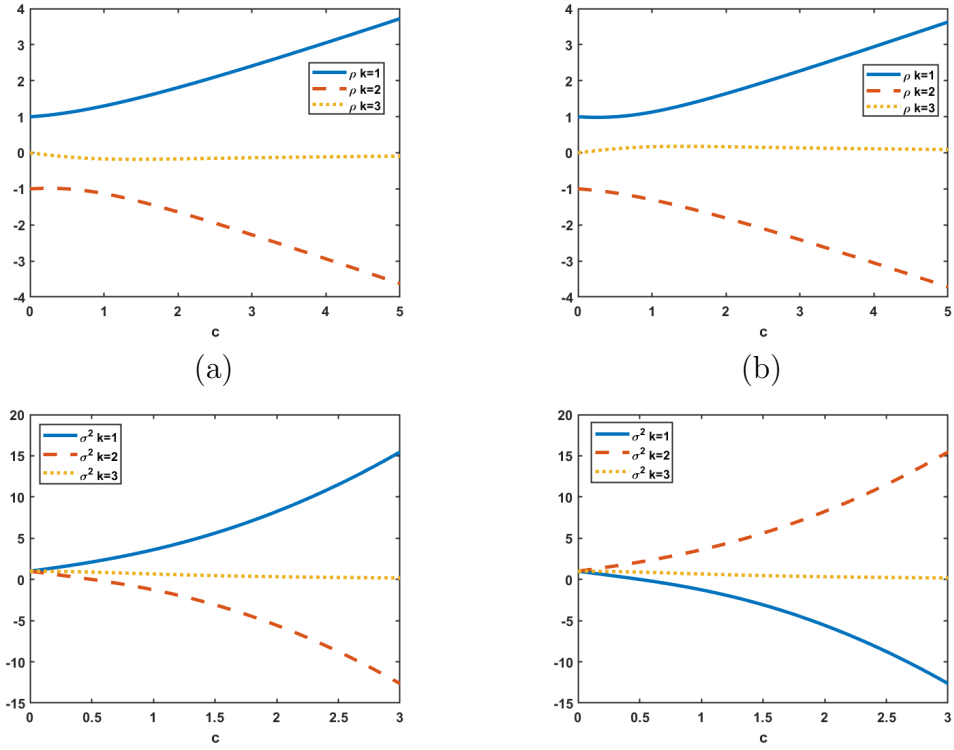

Figure 5.1: (a) Plot of the roots in (5.2.9), and (c) a plot of the corresponding σ^2 values in (5.2.10), when $\xi = 1$. (b) Plot of the roots in (5.2.11) and (d), a plot of the corresponding σ^2 values in (5.2.12), when $\xi = 1$.

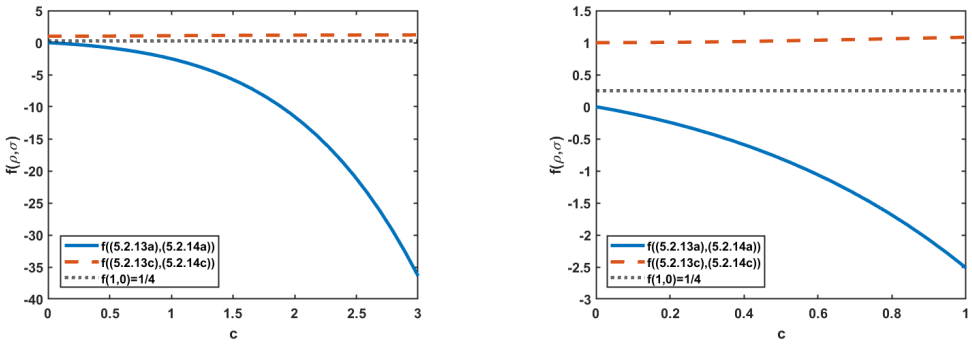

Figure 5.2: Plots of the bulk energy density (5.2.3) at $(\rho, \sigma) =$ ((5.2.13a),(5.2.14a)) and ((5.2.13c),(5.2.14c)) as functions of c with $\xi = 1$ for (left) $c \in [0, 3]$ and (right) $c \in [0, 1]$.

appropriate binomial formula, the first cube root is approximated by

$$\begin{aligned}\Theta_1 = \left(\frac{c}{8} + \sqrt{\frac{c^2}{64} - \frac{1}{27}\left(1+\frac{c^2}{2}\right)^3}\right)^{\frac{1}{3}} &\approx \left(\frac{\mathrm{i}}{3\sqrt{3}}\right)^{\frac{1}{3}} \left(1 + \left(\frac{3\sqrt{3}c}{8\mathrm{i}} + \frac{69c^2}{128}\right)\right)^{\frac{1}{3}} \\ &= \left(\frac{1}{2} + \frac{\sqrt{3}\mathrm{i}}{6}\right)\left(1 + \frac{\sqrt{3}c}{8\mathrm{i}} + \frac{23c^2}{128} + \mathcal{O}(c^3)\right) \\ &\approx \frac{1}{2} + \frac{c}{16} + \mathrm{i}P(c).\end{aligned}$$

In the last approximation, we have ignored $\mathcal{O}(c^2)$ terms for small c and $P(c) \coloneqq \frac{\sqrt{3}}{6} - \frac{\sqrt{3}c}{16}$. The second cube root is the complex conjugate of the first cube root in (5.2.13a), and thus for the solution pair ((5.2.13a), (5.2.14a)), we have as $c \to 0$ that

$$\rho \approx 1 + \frac{c}{8}, \tag{5.2.15a}$$

$$\sigma^2 \approx 1 + 2c + \frac{c^2}{4}, \tag{5.2.15b}$$

and we indeed recover the solution $(\rho, \sigma) = (1, 1)$ for $c = 0$.

For large $c \gg 1$, the square root in (5.2.13a) is given to leading order by,

$$\sqrt{\frac{1}{27}\left(1+\frac{c^2}{2}\right)^3 - \frac{c^2}{64}} \approx \frac{\sqrt{6}c^3}{36}. \tag{5.2.16}$$

Similarly, the first cube root in (5.2.13a) can be approximated to leading order as

$$\Theta_1 \approx \left(\frac{c}{8} + \mathrm{i}\frac{\sqrt{6}c^3}{36}\right)^{\frac{1}{3}} \approx \left(\frac{\sqrt{3}+\mathrm{i}}{2}\right)\left(\frac{\sqrt{6}}{36}\right)^{\frac{1}{3}} c.$$

Applying similar arguments to the second cube root, we deduce that for $c \gg 1$

$$\rho \approx \left(\frac{\sqrt{2}}{4}\right)^{\frac{1}{3}} c, \tag{5.2.17a}$$

$$\sigma^2 \approx 1 + \sqrt{2}c^2. \tag{5.2.17b}$$

Hence, both ρ and σ grow linearly with c for large $c \gg 1$, for the bulk energy

minimiser ((5.2.13a), (5.2.14a)).

Remark 5.2.3. For the uncoupled problem with $c = 0$, we have nine solution pairs (ρ, σ) (with θ, ϕ undetermined) of the system (5.2.4), namely,

$$(0,0),\ (0,\pm 1),\ (\pm 1,0),\ (\pm 1,\pm 1), \tag{5.2.18}$$

where all sign combinations are possible. In the $c \to 0$ limit, we expect each of the solution pairs $((5.2.9),(5.2.10))$ and $((5.2.11),(5.2.12))$ to reduce to a solution of the uncoupled problem. From (5.2.15), we see (5.2.13a) and (5.2.14a) recover the solutions $(1, \pm 1)$ as $c \to 0$. Applying analogous asymptotic analysis for small c to the remaining roots of $((5.2.9),(5.2.10))$ and $((5.2.11),(5.2.12))$ (also see Figure 5.1), we recover all of the solution pairs in (5.2.18), except $(0,0)$ and $(\pm 1, 0)$. However, these unrecovered solution pairs, $(\rho, \sigma) = \{(0,0),(\pm 1,0)\}$ are solutions of the system (5.2.4) for arbitrary $c \geq 0$, and thus not perturbed for $c > 0$.

5.2.2 Maximum principle and uniqueness results

For simplicity and brevity, we take $L^* = l_2 =: l$ and $\xi = 1$ hereafter. The cases of $L^* \neq l_2$ and $\xi \neq 1$ can be tackled using similar mathematical methods, although ξ is necessarily small for dilute ferronematic suspensions where nematic effects dominate magnetic effects.

Theorem 5.2.4. *(Maximum Principle) There exists an L^∞ bound for the solutions, $(Q_{11}, Q_{12}, M_1, M_2)$ of the system (5.1.9a)-(5.1.9d), subject to the boundary conditions (5.1.7). Specifically,*

$$Q_{11}^2(y) + Q_{12}^2(y) \leq (\rho^*)^2,\ M_1^2(y) + M_2^2(y) \leq 1 + 2c\rho^* \quad \forall y \in [-1,1], \tag{5.2.19}$$

where ρ^* is given by

$$\rho^* = \left(\frac{c}{8} + \sqrt{\frac{c^2}{64} - \frac{1}{27}\left(1 + \frac{c^2}{2}\right)^3}\right)^{\frac{1}{3}} + \left(\frac{c}{8} - \sqrt{\frac{c^2}{64} - \frac{1}{27}\left(1 + \frac{c^2}{2}\right)^3}\right)^{\frac{1}{3}}. \quad (5.2.20)$$

Proof. Assume that, $|\mathbf{Q}| = \sqrt{Q_{11}^2 + Q_{12}^2}$, and, $|\mathbf{M}| = \sqrt{M_1^2 + M_2^2}$, attain their maxima at two distinct points $y_1, y_2 \in (-1, 1)$, respectively, then we have

$$\frac{\mathrm{d}^2}{\mathrm{d}y^2}\left(\frac{1}{2}|\mathbf{Q}|^2\right)(y_1) \leq 0 \text{ and } \frac{\mathrm{d}^2}{\mathrm{d}y^2}\left(\frac{1}{2}|\mathbf{M}|^2\right)(y_2) \leq 0.$$

Multiplying (5.1.9a) by Q_{11}, (5.1.9b) by Q_{12}, adding the resulting equations, and using the identity $\frac{\mathrm{d}^2}{\mathrm{d}y^2}\left(\frac{1}{2}|\mathbf{Q}|^2\right) = \frac{\mathrm{d}^2 Q_{11}}{\mathrm{d}y^2}Q_{11} + \frac{\mathrm{d}^2 Q_{12}}{\mathrm{d}y^2}Q_{12} + \left(\frac{\mathrm{d}Q_{11}}{\mathrm{d}y}\right)^2 + \left(\frac{\mathrm{d}Q_{12}}{\mathrm{d}y}\right)^2$, we obtain the necessary condition

$$\left[4\left(Q_{11}^2 + Q_{12}^2\right)\left(Q_{11}^2 + Q_{12}^2 - 1\right) - c\left(Q_{11}(M_1^2 - M_2^2) + 2Q_{12}M_1M_2\right)\right]\Big|_{y=y_1} \leq 0. \quad (5.2.21)$$

Similarly, we have

$$\left[\left(M_1^2 + M_2^2\right)\left(M_1^2 + M_2^2 - 1\right) - 2c\left(Q_{11}(M_1^2 - M_2^2) + 2Q_{12}M_1M_2\right)\right]\Big|_{y=y_2} \leq 0. \quad (5.2.22)$$

Substituting (5.2.2) with $\rho = |\mathbf{Q}| \geq 0$ and $\sigma = |\mathbf{M}| \geq 0$, with arbitrary θ and ϕ, into (5.2.21) and (5.2.22), we obtain

$$0 \geq \left[4\rho^2(\rho^2 - 1) - c\rho\sigma^2\cos(\theta - 2\phi)\right]\Big|_{y=y_1} \geq \left[4\rho^2(\rho^2 - 1) - c\rho\sigma^2\right]\Big|_{y=y_1},$$
$$\implies \left(\rho^3 - \rho - \frac{c\sigma^2}{4}\right)\Big|_{y=y_1} \leq 0, \quad (5.2.23)$$

and

$$0 \geq \left[\sigma^2(\sigma^2 - 1) - 2c\rho\sigma^2\cos(\theta - 2\phi)\right]\Big|_{y=y_2} \geq \left[\sigma^2(\sigma^2 - 1) - 2c\rho\sigma^2\right]\Big|_{y=y_2},$$
$$\implies \left(\sigma^2 - 1 - 2c\rho\right)\Big|_{y=y_2} \leq 0,$$

respectively. We then immediately deduce that $\sigma^2(y) \leq 1 + 2c\rho(y_2)$ for all $y \in [-1, 1]$, as $|\mathbf{M}|$ attains its maximum at y_2. Since $\rho(y_1) \geq \rho(y_2)$ (as $|\mathbf{Q}|$ attains its maximum at y_1), we further have $\sigma^2(y_1) \leq 1 + 2c\rho(y_1)$. Using this in (5.2.23), we get

$$0 \geq \left(\rho^3 - \rho - \frac{c\sigma^2}{4}\right)\Big|_{y=y_1} \geq \left(\rho^3 - \rho\left(1 + \frac{c^2}{2}\right) - \frac{c}{4}\right)\Big|_{y=y_1}, \tag{5.2.24}$$

which holds (on an interval) provided that ρ is less than or equal to the largest positive root of the cubic polynomial, $\rho^3 - \rho\left(1 + \frac{c^2}{2}\right) - \frac{c}{4}$. From the detailed calculations in Section 5.2.1, the largest positive root is given by

$$\rho = \left(\frac{c}{8} + \sqrt{\frac{c^2}{64} - \frac{1}{27}\left(1 + \frac{c^2}{2}\right)^3}\right)^{\frac{1}{3}} + \left(\frac{c}{8} - \sqrt{\frac{c^2}{64} - \frac{1}{27}\left(1 + \frac{c^2}{2}\right)^3}\right)^{\frac{1}{3}},$$

and thus $\rho(y_1) \leq \rho^*$. The L^∞ bounds for ρ and σ are an immediate consequence, i.e.,

$$\rho(y) \leq \rho^*, \ \sigma^2(y) \leq 1 + 2c\rho^* \quad \forall y \in [-1, 1].$$

Note that if $y_1 = y_2$, the proof is unchanged since $\rho(y_1) = \rho(y_2)$. □

Remark 5.2.5. For $c = 0$, the upper bounds (5.2.19) reduce to $Q_{11}^2 + Q_{12}^2 \leq 1$, $M_1^2 + M_2^2 \leq 1$, which are the Ginzburg–Landau bounds in [60] for $\mathbf{Q}$ and $\mathbf{M}$. Moreover, the calculations in the previous section show we can expand ρ^* in powers of c to deduce that $Q_{11}^2 + Q_{12}^2 \leq 1 + \frac{c}{4}$, $M_1^2 + M_2^2 \leq 1 + 2c$ for small c, and $Q_{11}^2 + Q_{12}^2 \leq \left(\frac{\sqrt{2}}{4}\right)^{\frac{2}{3}} c^2$, $M_1^2 + M_2^2 \leq 1 + \sqrt{2}c^2$ for large c. Hence, the nemato-magnetic coupling perturbs the Ginzburg–Landau bounds linearly, for small c.

With the L^∞ bounds at hand, we prove that there is a unique critical point of (5.1.6), which is necessarily the global energy minimiser, in the $l \to \infty$ limit. In the pure nematic case ($c = 0$), the model problem admits a unique order reconstruction (OR) solution for $D \ll c_2\xi_n$, for some positive constant c_2 independent

of model parameters, and where $\xi_n = \sqrt{\frac{K}{|A|}}$ is the temperature-dependent nematic correlation length [64]. We find the qualitative features are unchanged in the ferronematic case.

Theorem 5.2.6. *(Uniqueness of minimisers for sufficiently large l) For a fixed c and for $L^* = l_2 =: l$ sufficiently large and $\xi = 1$, there exists a unique critical point (and hence global minimiser) of the full energy (5.1.6), in the admissible space (5.1.8).*

Proof. We first show that the free energy (5.1.6) is strictly convex using the maximum principle. We let $(\mathbf{Q}, \mathbf{M}), \left(\overline{\mathbf{Q}}, \overline{\mathbf{M}}\right) \in \mathcal{A}$ so that $\left(\mathbf{Q} - \overline{\mathbf{Q}}\right) \in W_0^{1,2}$ and $\left(\mathbf{M} - \overline{\mathbf{M}}\right) \in W_0^{1,2}$, where $W_0^{1,2}$ is the closure of C_0^∞ with respect to the $W^{1,2}$-norm. With $\xi = 1$, note that

$$\begin{aligned} F\left(\frac{\mathbf{Q}+\overline{\mathbf{Q}}}{2}, \frac{\mathbf{M}+\overline{\mathbf{M}}}{2}\right) =& \frac{1}{2}\left[F(\mathbf{Q}, \mathbf{M}) + F\left(\overline{\mathbf{Q}}, \overline{\mathbf{M}}\right)\right] + \int_{-1}^{1} \Bigg\{ f\left(\frac{\mathbf{Q}+\overline{\mathbf{Q}}}{2}, \frac{\mathbf{M}+\overline{\mathbf{M}}}{2}\right) \\ & - \frac{1}{2}\left[f(\mathbf{Q}, \mathbf{M}) + f\left(\overline{\mathbf{Q}}, \overline{\mathbf{M}}\right)\right] - \frac{l}{8}\left[\left(\frac{\mathrm{d}\mathbf{Q}}{\mathrm{d}y}\right) - \left(\frac{\mathrm{d}\overline{\mathbf{Q}}}{\mathrm{d}y}\right)\right]^2 \\ & - \frac{l}{8}\left[\left(\frac{\mathrm{d}\mathbf{M}}{\mathrm{d}y}\right) - \left(\frac{\mathrm{d}\overline{\mathbf{M}}}{\mathrm{d}y}\right)\right]^2 \Bigg\} \, \mathrm{d}y \\ \leq & \frac{1}{2}\left[F(\mathbf{Q}, \mathbf{M}) + F\left(\overline{\mathbf{Q}}, \overline{\mathbf{M}}\right)\right] + \int_{-1}^{1} \Bigg\{ f\left(\frac{\mathbf{Q}+\overline{\mathbf{Q}}}{2}, \frac{\mathbf{M}+\overline{\mathbf{M}}}{2}\right) \\ & - \frac{1}{2}\left[f(\mathbf{Q}, \mathbf{M}) + f\left(\overline{\mathbf{Q}}, \overline{\mathbf{M}}\right)\right] \Bigg\} \, \mathrm{d}y - \frac{l}{8}\|\mathbf{Q} - \overline{\mathbf{Q}}\|_{L^2}^2 \\ & - \frac{l}{8}\|\mathbf{M} - \overline{\mathbf{M}}\|_{L^2}^2, \end{aligned} \tag{5.2.25}$$

where f is the bulk energy density (5.2.1), F is the energy (5.1.6), and we have used the Poincaré inequality with the Poincaré constant $c_p = 1$ (this can be shown via a quick calculation using the Cauchy-Schwarz inequality) in the last inequality. We estimate the second partial derivatives of f, using the L^∞ bounds

above, yielding

$$\begin{aligned}
&\left|\frac{\partial^2 f}{\partial Q_{1i}\partial Q_{1j}}\right| = \left|4\delta_{ij}\left(Q_{11}^2+Q_{12}^2-1\right)+8Q_{1i}Q_{1j}\right| \leq 4\left(3(\rho^*)^2-1\right) =: a_1,\\
&\left|\frac{\partial^2 f}{\partial M_i\partial M_j}\right| \leq A_0(5c\rho^*+1) =: a_2,\\
&\left|\frac{\partial^2 f}{\partial Q_{1i}\partial M_j}\right| \leq B_0 c\sqrt{1+2c\rho*} =: a_3,
\end{aligned}$$

for $i,j \in \{1,2\}$, where δ_{ij} is the Kronecker delta symbol and A_0, B_0 are constants independent of c. Using methods parallel to [64, Lemma 8.2], we have

$$\begin{aligned}
&\int_{-1}^{1}\left\{f\left(\frac{\mathbf{Q}+\overline{\mathbf{Q}}}{2},\frac{\mathbf{M}+\overline{\mathbf{M}}}{2}\right)-\frac{1}{2}\left[f\left(\mathbf{Q},\mathbf{M}\right)+f\left(\overline{\mathbf{Q}},\overline{\mathbf{M}}\right)\right]\right\}\mathrm{d}y\\
&\qquad\leq a_1\|\mathbf{Q}-\overline{\mathbf{Q}}\|_{L^2}^2+a_2\|\mathbf{M}-\overline{\mathbf{M}}\|_{L^2}^2+a_3\|\mathbf{Q}-\overline{\mathbf{Q}}\|_{L^2}\|\mathbf{M}-\overline{\mathbf{M}}\|_{L^2}.
\end{aligned} \tag{5.2.26}$$

This follows since the second derivatives of f are bounded so that $f \in W^{2,\infty}$, hence after Taylor expanding, we can bound f by its second derivatives as in (5.2.26). Note that,

$$\left\|\mathbf{Q}-\overline{\mathbf{Q}}\right\|_{L^2}\left\|\mathbf{M}-\overline{\mathbf{M}}\right\|_{L^2} \leq \frac{1}{2}\left(\epsilon\left\|\mathbf{Q}-\overline{\mathbf{Q}}\right\|_{L^2}^2+\epsilon^{-1}\left\|\mathbf{M}-\overline{\mathbf{M}}\right\|_{L^2}^2\right) \quad \forall\epsilon>0.$$

We take $\epsilon = 2$ for convenience and then substitute (5.2.26) into (5.2.25), so that

$$\begin{aligned}
F\left(\frac{\mathbf{Q}+\overline{\mathbf{Q}}}{2},\frac{\mathbf{M}+\overline{\mathbf{M}}}{2}\right) \leq \frac{1}{2}\left[F\left(\mathbf{Q},\mathbf{M}\right)+F\left(\overline{\mathbf{Q}},\overline{\mathbf{M}}\right)\right]+\left(a_1+a_3-\frac{l}{8}\right)\|\mathbf{Q}-\overline{\mathbf{Q}}\|_{L^2}^2\\
+\left(a_2+\frac{a_3}{4}-\frac{l}{8}\right)\|\mathbf{M}-\overline{\mathbf{M}}\|_{L^2}^2.
\end{aligned}$$

Hence, for $l > l^*(c) = \max\{8(a_1+a_3), 2(4a_2+a_3)\}$, it holds that

$$F\left(\frac{\mathbf{Q}+\overline{\mathbf{Q}}}{2},\frac{\mathbf{M}+\overline{\mathbf{M}}}{2}\right) < \frac{1}{2}F\left(\mathbf{Q},\mathbf{M}\right)+\frac{1}{2}F\left(\overline{\mathbf{Q}},\overline{\mathbf{M}}\right)$$

for all $\mathbf{Q},\overline{\mathbf{Q}} \in W^{1,2}$ and $\mathbf{M},\overline{\mathbf{M}} \in W^{1,2}$ such that $\mathbf{Q} \neq \overline{\mathbf{Q}}$, $\mathbf{M} \neq \overline{\mathbf{M}}$. Therefore, F is strictly convex.

Now assume that for $l \in (l^*,\infty)$, there exist two solutions $(\mathbf{Q},\mathbf{M})$ and $\left(\overline{\mathbf{Q}},\overline{\mathbf{M}}\right)$ of

(5.1.9a)-(5.1.9d) in the admissible space $\mathcal{A}$. Then the mapping

$$[0,1] \ni t \mapsto g(t) = F\left(t\mathbf{Q} + (1-t)\overline{\mathbf{Q}}, t\mathbf{M} + (1-t)\overline{\mathbf{M}}\right)$$

is C^1 (continuously differentiable) and its derivative vanishes at $t = 0, 1$. Evaluating the inequality $(t_1 - t_0)\frac{\mathrm{d}g}{\mathrm{d}t}(t_0) < g(t_1) - g(t_0)$ at $t_0 = 0,\ t_1 = 1$ and $t_0 = 1,\ t_1 = 0$, we find $F(\overline{\mathbf{Q}}, \overline{\mathbf{M}}) < F(\mathbf{Q}, \mathbf{M})$ and $F(\mathbf{Q}, \mathbf{M}) < F(\overline{\mathbf{Q}}, \overline{\mathbf{M}})$. This is a contradiction and hence, the uniqueness result follows. □

Remark 5.2.7. The methods in our existence, uniqueness, and maximum principle results, could be adapted for two- and three-dimensional problems, as well as the case when $L^* \neq l_2$ and $\xi \neq 1$. Recall the definitions of the dimensionless parameters in (5.1.5). From Theorem 5.2.6, the conditions $l := L^* = l_2 > l^*(c) = \max\{8(a_1 + a_3), 2(4a_2 + a_3)\}$ guarantee the uniqueness of a solution for the system (5.1.9a)-(5.1.9d). The parameters a_1, a_2, a_3 grow as c^2 for large c, and thus the condition $l > l^*(c)$ is equivalent to $\frac{c_1^2 K}{D^2|A|\left(c_0^2 + c^2\right)} \gg 1$ for some constants c_0, c_1, or $D \ll \sqrt{\frac{c_1^2 K}{|A|\left(c_0^2 + c^2\right)}} =: c_1 \frac{\xi_n}{\sqrt{c_0^2 + c^2}}$, i.e., when the physical length D is much smaller than an enhanced material-dependent length scale $c_1 \frac{\xi_n}{\sqrt{c_0^2 + c^2}}$. For $c = 0$, we recover the uniqueness results reported in [64] and [66].

5.2.3 Convergence analysis for $l \to \infty$ and $l \to 0$

For a fixed $c > 0$, the $l \to \infty$ limit corresponds to very narrow channels with $D \ll \sqrt{\frac{c_1^2 K}{|A|(c_0^2 + c^2)}}$ as discussed in Remark 5.2.7. From the maximum principle Theorem 5.2.4, $\|\mathbf{Q}\|_{L^\infty}$ and $\|\mathbf{M}\|_{L^\infty}$ are bounded independently of l, as shown in (5.2.19). Furthermore, in the $l \to \infty$ limit, one can see that (5.1.9a)-(5.1.9d)

reduce to the Laplace equations

$$\begin{aligned} \frac{\mathrm{d}^2 Q_{11}}{\mathrm{d}y^2} = 0, \quad \frac{\mathrm{d}^2 Q_{12}}{\mathrm{d}y^2} = 0, \\ \frac{\mathrm{d}^2 M_1}{\mathrm{d}y^2} = 0, \quad \frac{\mathrm{d}^2 M_2}{\mathrm{d}y^2} = 0, \end{aligned} \tag{5.2.27}$$

subject to (5.1.7), which admits the unique solution as shown below:

$$(\mathbf{Q}^\infty, \mathbf{M}^\infty) = (Q_{11}^\infty, Q_{12}^\infty, M_1^\infty, M_2^\infty) = (-y, 0, -y, 0). \tag{5.2.28}$$

In fact, (5.2.28) is an order reconstruction (OR) solution, as introduced in Section 5.3, with linear profiles for Q_{11} and M_1. In the next theorem, we use the method of sub- and super-solutions, as in [89], to study the convergence of solutions of (5.1.9a)-(5.1.9d) to $(\mathbf{Q}^\infty, \mathbf{M}^\infty)$, as $l \to \infty$.

Theorem 5.2.8. *(Convergence result for $l \to \infty$) Let $(\mathbf{Q}^l, \mathbf{M}^l)$ be the unique solution of the Euler–Lagrange equations (5.1.9a)-(5.1.9d) in (5.1.8). Then, for sufficiently large l, $(\mathbf{Q}^l, \mathbf{M}^l)$ converge to $(\mathbf{Q}^\infty, \mathbf{M}^\infty)$ with the following estimates:*

$$\forall j = 1, 2, \quad \|Q_{1j}^l - Q_{1j}^\infty\|_{L^\infty} \leq W_1 l^{-1}, \ \|M_j^l - M_j^\infty\|_{L^\infty} \leq W_2 l^{-1}, \tag{5.2.29}$$

for positive constants W_1, W_2 which depend on c only.

Proof. Recalling [89, Proposition 3.1] and comparing equations (5.1.9a)-(5.1.9d) with the Laplace equations (5.2.27), we have for $j = 1, 2$,

$$-l^{-1}\left(4\rho^*\left((\rho^*)^2 - 1\right) + c\,(1 + 2c\rho^*)\right) \leq \frac{\mathrm{d}^2}{\mathrm{d}y^2}\left(Q_{1j}^l - Q_{1j}^\infty\right) \tag{5.2.30a}$$

$$\leq l^{-1}\left(4\rho^*\left((\rho^*)^2 - 1\right) + c\,(1 + 2c\rho^*)\right) \text{ in } \Omega,$$

$$Q_{1j}^l - Q_{1j}^\infty = 0 \text{ on } \partial\Omega, \tag{5.2.30b}$$

$$-l^{-1} 6c\rho^*(1 + 2c\rho^*)^{\frac{1}{2}} \leq \frac{\mathrm{d}^2}{\mathrm{d}y^2}(M_j^l - M_j^\infty) \leq l^{-1} 6c\rho^*(1 + 2c\rho^*)^{\frac{1}{2}} \text{ in } \Omega, \tag{5.2.30c}$$

$$M_j^l - M_j^\infty = 0 \text{ on } \partial\Omega. \tag{5.2.30d}$$

The L^∞ bounds (5.2.19) has been used in the inequalities above. Let $v_k \in C^\infty(\Omega;\mathbb{R})$, $k=1,2$, be solutions of

$$\begin{cases} \dfrac{\mathrm{d}^2 v_1}{\mathrm{d}y^2} = 4\rho^*\left((\rho^*)^2-1\right) + c\,(1+2c\rho^*) := 2W_1(c) & \text{in } \Omega, \\ \dfrac{\mathrm{d}^2 v_2}{\mathrm{d}y^2} = 6c\rho^*\,(1+2c\rho^*)^{\frac{1}{2}} := 2W_2(c) & \text{in } \Omega, \\ v_k = 0 \quad \text{for } k=1,2 & \text{on } \partial\Omega. \end{cases}$$

Then each v_k only depends on the coupling parameter c. In fact, $v_k(y) = W_k(c)(y^2-1) \le W_k(c)$.

We say $\tilde{u}$ is a sub-solution (super-solution) of $-\frac{d^2u}{dy^2} = f(u)$, subject to $u=g$ on $\partial\Omega$, for some smooth functions f and g, if $-\frac{d^2\tilde{u}}{dy^2} \le f(\tilde{u})$ ($f(\tilde{u}) \le -\frac{d^2\tilde{u}}{dy^2}$) and $\tilde{u} \le g$ ($\tilde{u} \ge g$) on $\partial\Omega$. Defining

$$\begin{aligned} \begin{pmatrix} \frac{\mathrm{d}^2}{\mathrm{d}y^2}\left(Q_{11}^l - Q_{11}^\infty\right) \\ \frac{\mathrm{d}^2}{\mathrm{d}y^2}\left(Q_{12}^l - Q_{12}^\infty\right) \\ \frac{\mathrm{d}^2}{\mathrm{d}y^2}\left(M_1^l - M_1^\infty\right) \\ \frac{\mathrm{d}^2}{\mathrm{d}y^2}\left(M_2^l - M_2^\infty\right) \end{pmatrix} &= \begin{pmatrix} \frac{1}{l}\left(4Q_{11}(Q_{11}^2+Q_{12}^2-1) - c\,(M_1^2-M_2^2)\right) \\ \frac{1}{l}\left(4Q_{12}(Q_{11}^2+Q_{12}^2-1) - 2cM_1M_2\right) \\ \frac{1}{l}\left(M_1\,(M_1^2+M_2^2-1) - 2cQ_{11}M_1 - 2cQ_{12}M_2\right) \\ \frac{1}{l}\left(M_2\,(M_1^2+M_2^2-1) + 2cQ_{11}M_2 - 2cQ_{12}M_1\right) \end{pmatrix} \\ &:= \mathbf{f}(Q_{11},Q_{12},M_1,M_2), \end{aligned}$$

$l^{-1}v_1$ will be a sub-solution and $-l^{-1}v_1$ a super-solution for each component of $(\mathbf{Q}^l - \mathbf{Q}^\infty)$, and similarly, $l^{-1}v_2$ will be a sub-solution and $-l^{-1}v_2$ a super-solution for each of the vector components of $(\mathbf{M}^l - \mathbf{M}^\infty)$, if

$$-\frac{1}{l}\frac{\mathrm{d}^2}{\mathrm{d}y^2}(v_1,v_1,v_2,v_2) \le \mathbf{f}(l^{-1}v_1, l^{-1}v_1, l^{-1}v_2, l^{-1}v_2) \tag{5.2.31a}$$

$$\mathbf{f}(-l^{-1}v_1, -l^{-1}v_1, -l^{-1}v_2, -l^{-1}v_2) \le \frac{1}{l}\frac{\mathrm{d}^2}{\mathrm{d}y^2}(v_1,v_1,v_2,v_2). \tag{5.2.31b}$$

Looking at the first component of (5.2.31b), we require

$$-\frac{2v_1}{l}\left(\frac{2v_1^2}{l^2}-1\right) \le W_1(c).$$

Substituting our expression for v_1 into the above, this inequality holds provided $l \geq (4W_1^2(c))^{\frac{1}{3}}$. It follows $-l^{-1}v_1$ is a super-solution of $Q_{11}^l - Q_{11}^\infty$, after noting both equal zero on $\partial\Omega$. Applying analogous arguments to the remaining inequalities in (5.2.31), they all hold provided $l \geq \max\left\{(4W_1^2(c))^{\frac{1}{3}}, (4W_2^2(c))^{\frac{1}{3}}\right\} := W$. For $l \geq W$, the estimates then follow and the proof is complete. □

Next, we consider the $l \to 0$ limit for fixed c, which is valid for large channel widths D, much greater than the nematic correlation length. To this end, we rewrite the free energy (5.1.6) as

$$\begin{aligned}\frac{1}{l}F(Q_{11}, Q_{12}, M_1, M_2) \coloneqq \int_{-1}^{1} \Bigg\{ &\frac{1}{2}\left[\left(\frac{\mathrm{d}Q_{11}}{\mathrm{d}y}\right)^2 + \left(\frac{\mathrm{d}Q_{12}}{\mathrm{d}y}\right)^2\right] \\ &+\frac{1}{2}\left[\left(\frac{\mathrm{d}M_1}{\mathrm{d}y}\right)^2 + \left(\frac{\mathrm{d}M_2}{\mathrm{d}y}\right)^2\right] + \frac{1}{l}\bar{f}(Q_{11}, Q_{12}, M_1, M_2)\Bigg\}\,\mathrm{d}y,\end{aligned} \tag{5.2.32}$$

where

$$\begin{aligned}\bar{f}(Q_{11}, Q_{12}, M_1, M_2) \coloneqq &\left(Q_{11}^2 + Q_{12}^2 - 1\right)^2 + \frac{1}{4}\left(M_1^2 + M_2^2 - 1\right)^2 \\ &- cQ_{11}\left(M_1^2 - M_2^2\right) - 2cQ_{12}M_1M_2 - \alpha_0(c) \geq 0\end{aligned} \tag{5.2.33}$$

and the c-dependent constant, $\alpha_0(c)$, is the minimum value of the bulk energy density. The set of minimisers of $\bar{f}$ plays a crucial role in the analysis, and belong to the set

$$\begin{aligned}\mathcal{A}_{\min} \coloneqq &\{(Q_{11}, Q_{12}, M_1, M_2) \\ &= \left(\rho^* \cos 2\phi, \rho^* \sin 2\phi, \sqrt{1 + 2c\rho^*}\cos\phi, \sqrt{1 + 2c\rho^*}\sin\phi\right)\Big\},\end{aligned} \tag{5.2.34}$$

where ρ^* is given by (5.2.20) and ϕ is an arbitrary angle (see Section 5.2.1).

Consider the following admissible test maps for sufficiently small l, with $Q_{12}^t(y) =$

$M_2^t(y) \equiv 0$ for $y \in [-1, 1]$ and

$$Q_{11}^t(y) = \begin{cases} g(y), & y \in \left[-1, -1+\sqrt{l}\right), \\ \rho^*, & y \in \left(-1+\sqrt{l}, 1-\sqrt{l}\right), \\ h(y), & y \in \left(1-\sqrt{l}, 1\right]. \end{cases}$$

Here, g linearly interpolates between ρ^* and $g(-1) = 1$; h linearly interpolates between ρ^* and $h(1) = -1$. Similarly, we use the following test map for M_1:

$$M_1^t(y) = \begin{cases} g^*(y), & y \in \left[-1, -1+\sqrt{l}\right), \\ \sqrt{1+2c\rho^*}, & y \in \left(-1+\sqrt{l}, 1-\sqrt{l}\right), \\ h^*(y), & y \in \left(1-\sqrt{l}, 1\right]. \end{cases}$$

Here, g^* linearly interpolates between $\sqrt{1+2c\rho^*}$ and $g^*(-1) = 1$; h^* linearly interpolates between $\sqrt{1+2c\rho^*}$ and $h^*(1) = -1$. We have seen in Section 5.2.1, that the pair $(\rho, \sigma) = (\rho^*, \sqrt{1+2c\rho^*})$ is the bulk energy minimiser when $2\phi - \theta = 2n\pi$ for $n \in \mathbb{Z}$, hence taking $\phi = 0$ and $\theta = 2n\pi$, we have $\bar{f}\left(\rho^*, 0, \sqrt{1+2c\rho^*}, 0\right) = 0$. The gradients of $g,\ h,\ g^*,\ h^*$ are all of the form $\frac{1}{\sqrt{l}}$ times a constant independent of l, it is then straightforward to check that

$$\frac{1}{l} F\left(Q_{11}^t, 0, M_1^t, 0\right) \leq \frac{C_1}{\sqrt{l}} + \frac{C_2}{l} \leq \frac{C_3}{\sqrt{l}},$$

for positive constants $C_1,\ C_2,\ C_3$ independent of l, with l small enough. Hence, for an energy minimiser $(\mathbf{Q}^l, \mathbf{M}^l)$ of the full energy (5.1.6), we necessarily have that

$$\frac{1}{l} F\left(Q_{11}^l, Q_{12}^l, M_1^l, M_2^l\right) \leq \frac{C_3}{\sqrt{l}},$$

and hence,

$$\int_{-1}^{1} \bar{f}\left(Q_{11}^l, Q_{12}^l, M_1^l, M_2^l\right)\, \mathrm{d}y \leq C_3\sqrt{l} \to 0 \quad \text{as } l \to 0.$$

Furthermore, since $\bar{f} \geq 0$ by its definition (5.2.33), we deduce that

$$\bar{f}\left(Q_{11}^l, Q_{12}^l, M_1^l, M_2^l\right) \equiv 0$$

almost everywhere, as $l \to 0$. Hence, in the $l \to 0$ limit, we expect the energy minimisers, $\left(\mathbf{Q}^l, \mathbf{M}^l\right)$ to minimise the Dirichlet energy of $\mathbf{Q}$ and $\mathbf{M}$ in the constrained set $\mathcal{A}_{\min}$ defined above, so that the limiting minimisers are given by:

$$\mathbf{Q}^0(c,y) = \rho^*(\cos(2\phi_0(y)), \sin(2\phi_0(y))), \tag{5.2.35a}$$

$$\mathbf{M}^0(c,y) = \sqrt{1+2c\rho^*}\left(\cos(\phi_0(y)), \sin(\phi_0(y))\right), \tag{5.2.35b}$$

where there are two choices of ϕ_0, dictated by the boundary conditions for $\mathbf{M}$:

$$\frac{\mathrm{d}^2\phi_0}{\mathrm{d}y^2} = 0, \tag{5.2.36a}$$

$$\phi_0(-1) = 0, \phi_0(1) = \pi \quad \text{or} \quad \phi_0(-1) = 0, \phi_0(1) = -\pi, \tag{5.2.36b}$$

$$2\phi_0 - \theta_0 = 2n\pi, \quad n \in \mathbb{Z}. \tag{5.2.36c}$$

Here, θ_0 and ϕ_0 denote the director and magnetisation vector angles, respectively. In Section 5.4.3, we numerically demonstrate that the energy minimisers $\left(\mathbf{Q}^l, \mathbf{M}^l\right)$, indeed converge to one of the two limiting maps in $\mathcal{A}_{\min}$, defined above, almost everywhere except near $y = \pm 1$ (and interior points associated with jumps in $(2\phi_0 - \theta_0)$, since $2\phi_0 - \theta_0$ is constrained to be an even multiple of 2π, in the $l \to 0$ limit). There are necessarily boundary layers near $y = \pm 1$, since the limiting maps in $\mathcal{A}_{\min}$ do not satisfy the boundary conditions at $y = \pm 1$.

We do not prove convergence results in the $l \to 0$ limit rigorously, since this requires a delicate Γ-convergence analysis for a vector-valued problem with four degrees of freedom, with the set $\mathcal{A}_{\min}$, and additional complications from the boundary conditions. This warrants a separate study in its own right.

5.3 Order reconstruction solutions

The results in Section 5.1.1 concern the full problem (5.1.9a)-(5.1.9d) or ferronematic solutions with four degrees of freedom, $(\mathbf{Q}, \mathbf{M}) = (Q_{11}, Q_{12}, M_1, M_2)$. It is evident from the Euler–Lagrange equations (5.1.9a)-(5.1.9d), that we always have a branch of solutions with $Q_{12} = M_2 = 0$. We refer to such solutions with only two degrees of freedom, $(\mathbf{Q}, \mathbf{M}) = (Q_{11}, 0, M_1, 0)$ as OR solutions. A nematic (respectively magnetic) domain wall is defined to be a point $y = y^* \in (-1, 1)$ such that $\mathbf{Q}(y^*) = (Q_{11}(y^*), Q_{12}(y^*)) = 0$ (respectively $\mathbf{M}(y^*) = 0$). We call these points “walls" since they correspond to two-dimensional surfaces in the xz-plane. Ferronematic solutions need not have domain walls in general, but OR solutions in the admissible space (5.1.8) must have domain walls because of the imposed Dirichlet conditions. There must exist an interior point $y^* \in (-1, 1)$ such that $Q_{11}(y^*) = 0$, because $Q_{11}(-1) = 1$ and $Q_{11}(1) = -1$, and $Q_{12}(y) = 0$ for all $y \in [-1, 1]$ by definition; similar remarks apply to the domain wall in $\mathbf{M}$. Furthermore, domain walls in $\mathbf{Q}$ and $\mathbf{M}$ can occur at different points, as we shall see in Section 5.4. OR solutions are special, since they describe ferronematic polydomains with domain walls separating distinctly ordered sub-domains. In fact, recall the parameterisation (5.2.2) and note that $Q_{12} = M_2 = 0$ implies $\theta = n\pi$ (for some integer n) everywhere; equivalent remarks apply to ϕ. Hence, there is necessarily a domain wall in $\mathbf{Q}$ such that $\theta = 2n\pi$ on one side of the domain wall containing $y = -1$, and $\theta = (2m + 1)\pi$ (for some integers n, m) on the other side of the domain wall containing $y = 1$; analogously, there is a domain wall in $\mathbf{M}$ that separates two sub-domains, with $\phi = 2n\pi$ and $\phi = (2m + 1)\pi$ for some integers n and m respectively. These domain walls are associated with jumps in $\mathbf{n}$ and the normalised magnetisation vector, $\mathbf{m} = \mathbf{M}/|\mathbf{M}|$. The domain

walls are not singularities of the **Q** and **M**-solutions, although they regularise singularities/jumps in **n** and **m**. Domain walls need not be associated with jumps and could just be regular zeroes of the **Q** and **M**-fields, although such domain walls would be energetically expensive.

We interpret OR solutions as critical points of the following OR energy (which is equivalent to (5.1.6) with $Q_{12} = M_2 = 0$):

$$E(Q_{11}, M_1) = \int_{-1}^{1} \left\{ \frac{l}{2} \left(\frac{\mathrm{d}Q_{11}}{\mathrm{d}y} \right)^2 + \frac{l}{2} \left(\frac{\mathrm{d}M_1}{\mathrm{d}y} \right)^2 + (Q_{11}^2 - 1)^2 + \frac{1}{4} \left(M_1^2 - 1 \right)^2 - cQ_{11}M_1^2 \right\} \mathrm{d}y, \tag{5.3.1}$$

subject to the boundary conditions

$$Q_{11}(-1) = M_1(-1) = 1, \quad Q_{11}(1) = M_1(1) = -1, \tag{5.3.2}$$

in the admissible space

$$\mathcal{A}' = \left\{ Q_{11}, M_1 \in W^{1,2}(\Omega; \mathbb{R}) : Q_{11} \text{ and } M_1 \text{ satisfy the boundary conditions (5.3.2)} \right\}. \tag{5.3.3}$$

The OR bulk energy density is given by:

$$f^{OR}(Q_{11}, M_1) = (Q_{11}^2 - 1)^2 + \frac{1}{4}(M_1^2 - 1)^2 - cQ_{11}M_1^2, \tag{5.3.4}$$

Hence, OR solutions are classical solutions of the following coupled ordinary differential equations,

$$\begin{aligned} l\frac{\mathrm{d}^2 Q_{11}}{\mathrm{d}y^2} &= 4Q_{11}(Q_{11}^2 - 1) - cM_1^2, \\ l\frac{\mathrm{d}^2 M_1}{\mathrm{d}y^2} &= M_1(M_1^2 - 1) - 2cQ_{11}M_1. \end{aligned} \tag{5.3.5}$$

In general, we expect multiple OR solutions for fixed values of (l, c) and the optimal OR solution is a minimiser of the energy (5.3.1) in $\mathcal{A}'$. We give a straightforward existence theorem below, which follows immediately from the direct method in the calculus of variations [74], along with some qualitative properties.

Theorem 5.3.1. *(Existence, uniqueness and maximum principle) For all values of (l, c), there exists a minimiser, (Q_{11}^*, M_1^*) of the OR energy (5.3.1) in $\mathcal{A}'$. This OR minimiser, $(\mathbf{Q}^{OR}, \mathbf{M}^{OR}) = (Q_{11}^*, 0, M_1^*, 0)$, is a solution of the full system (5.1.9a)-(5.1.9d), and thus a critical point of the full energy (5.1.6). Additionally, $(\mathbf{Q}^{OR}, \mathbf{M}^{OR})$ is the unique critical point, and hence, global minimiser of the energy (5.1.6), for fixed positive c and l large enough, as in Theorem 5.2.6. Moreover, we have*

$$|Q_{11}(y)| \leq \rho^*, \ M_1^2(y) \leq 1 + 2c\rho^* \quad \forall y \in [-1, 1], \tag{5.3.6}$$

where ρ^* is given by (5.2.20).

Proof. The admissible space $\mathcal{A}'$ is non-empty as $(Q_{11}, M_1) = (-y, -y) \in \mathcal{A}'$. We observe that (5.3.1) is weakly lower semi-continuous since it is quadratic and thus, convex in both the gradients of Q_{11} and M_1 [74]. As before, the coupling energy density can be decomposed as follows, for arbitrary $\epsilon > 0$

$$-cQ_{11}M_1^2 \geq -\frac{c}{2}\left(\epsilon Q_{11}^2 + \frac{1}{\epsilon}M_1^4\right).$$

Therefore, the OR energy density is bounded from below, since f^{OR} is quartic in Q_{11} and M_1 and can absorb the terms above, for a suitable choice of ϵ. The existence of a minimiser, (Q_{11}^*, M_1^*), of the OR energy (5.3.1), is immediate from [74]. Furthermore, this minimiser is a (classical) solution of the equations (5.3.5) subject to the boundary conditions (5.3.2). It is straightforward to check that the resulting OR solution, $\left(\mathbf{Q}^{OR}, \mathbf{M}^{OR}\right) = (Q_{11}^*, 0, M_1^*, 0)$ is also a solution of the full

system, (5.1.9a)-(5.1.9d) in the admissible space (5.1.8) for all values of (l, c).

Since the full energy (5.1.6) has a unique critical point for l large enough (see Theorem 5.2.6), we deduce that $\left(\mathbf{Q}^{OR}, \mathbf{M}^{OR}\right)$ is the unique energy minimiser of (5.1.6), in the $l \to \infty$ limit. The bounds (5.3.6) follow immediately from Theorem 5.2.4, using the L^∞ bounds for $|\mathbf{Q}|$ and $|\mathbf{M}|^2$ with $Q_{12} = M_2 = 0$. The solution branch $\left(\mathbf{Q}^{OR}, \mathbf{M}^{OR}\right)$ exists for all values of (l, c). This completes the proof. □

5.3.1 Order reconstruction system: homogeneous solutions and asymptotics as $c \to 0$ and $c \to \infty$

From the convergence result for $l \to \infty$ (Theorem 5.2.8), we have that $\left(\mathbf{Q}^{OR}, \mathbf{M}^{OR}\right) \to (-y, 0, -y, 0)$ as $l \to \infty$. The analysis in the $l \to 0$ limit is more involved, which necessitates a computation of the homogeneous solutions (with $\xi = 1$), or critical points of the OR bulk potential (5.3.4) which satisfy the following algebraic equations:

$$4Q_{11}(Q_{11}^2 - 1) - cM_1^2 = 0, \tag{5.3.7a}$$

$$M_1(M_1^2 - 1) - 2cQ_{11}M_1 = 0. \tag{5.3.7b}$$

From (5.3.7), we have either $M_1 = 0$ and $Q_{11} = \pm 1, 0$ for any real-valued c, or $M_1^2 = 2cQ_{11} + 1$. Following the approach in section 5.2.1, the non-trivial solutions of (5.3.7) are

$$Q_{11} = \Theta_1 + \Theta_2, \tag{5.3.8a}$$

$$Q_{11} = \omega_2\Theta_1 + \omega_3\Theta_2, \tag{5.3.8b}$$

$$Q_{11} = \omega_3\Theta_1 + \omega_2\Theta_2, \tag{5.3.8c}$$

and the corresponding values of M_1 are

$$M_1 = \pm\sqrt{2c\,(\Theta_1 + \Theta_2) + 1}, \tag{5.3.9a}$$

$$M_1 = \pm\sqrt{2c\,(\omega_2\Theta_1 + \omega_3\Theta_2) + 1}, \tag{5.3.9b}$$

$$M_1 = \pm\sqrt{2c\,(\omega_3\Theta_1 + \omega_2\Theta_2) + 1}. \tag{5.3.9c}$$

Again, $\omega_1 = 1$, $\omega_2 = \frac{-1+\sqrt{3}\mathrm{i}}{2}$ and $\omega_3 = \frac{-1-\sqrt{3}\mathrm{i}}{2}$ are the cube roots of unity. Therefore, the critical points of the OR bulk potential are ((5.3.8a),(5.3.9a)), ((5.3.8b),(5.3.9b)) and ((5.3.8c),(5.3.9c)). Since $27c^2 < 64\left(1 + \frac{c^2}{2}\right)^3$ for all $c \geq 0$, (5.3.8a)-(5.3.8c) are real (by De Moivre's formula) and (5.3.9a), (5.3.9c) are real for all positive c, whilst (5.3.9b) is real for $c \leq \frac{1}{2}$ (see the relevant roots in Figure 5.1). Therefore, we ignore the pair ((5.3.8b),(5.3.9b)) in what follows. Evaluating (5.3.4) at the admissible critical points, we can plot the OR bulk energy as a function of c and we see that the pair ((5.3.8a),(5.3.9a)) is the global minimiser of (5.3.4), for all values of c. The plot is identical in appearance to Figure 5.2 (and is therefore omitted), in that $f^{OR}((5.3.8a),(5.3.9b)) = f((5.2.13a),(5.2.14a))$, and $f^{OR}((5.3.8c),(5.3.9c)) = f((5.2.13c),(5.2.14c))$, whilst $f^{OR}(1,0) = \frac{1}{4}$ and $f^{OR}(0,0) = \frac{5}{4}$.

Next, we compute asymptotic expansions for ((5.3.8a),(5.3.9a)), for small and large c. We omit the details as they follow from Section 5.2.1. For small c, one can check that

$$Q_{11} \approx 1 + \frac{c}{8},\ M_1^2 \approx 1 + 2c + \frac{c^2}{4}.$$

While for large c, we deduce that

$$Q_{11} \approx \left(\frac{\sqrt{2}}{4}\right)^{\frac{1}{3}} c,\ M_1^2 \approx 1 + \sqrt{2}c^2,$$

thus, Q_{11} grows linearly in c and M_1^2 grows quadratically in c, for $c \gg 1$.

Remark 5.3.2. For $c = 0$, there are nine solution pairs (Q_{11}, M_1), given by (5.2.18). In the $c \to 0$ limit, we expect each of the solution pairs $((5.3.8a), (5.3.9a))$, $((5.3.8b), (5.3.9b))$ and $((5.3.8c), (5.3.9c))$ to reduce to a solution of the uncoupled problem. In fact, we can recover six solution pairs of the uncoupled system with $M_1 \neq 0$. The solutions of the uncoupled system with $M_1 = 0$, exist for all $c > 0$, and are hence, unperturbed by the nemato-magnetic coupling for $c > 0$.

5.3.2 Convergence analysis in the $l \to 0$ limit

Now, we study the regime of small l, which describes macroscopic domains with $D \gg \sqrt{\frac{c_1^2 K}{|A|(c_0^2+c^2)}}$, for fixed $c > 0$. We define the set of minimisers of the OR bulk potential (5.3.4):

$$\mathcal{B}^{OR} = \left\{ (Q_{11}, M_1) = \left(\rho^*, \sqrt{1+2c\rho^*}\right), (Q_{11}, M_1) = \left(\rho^*, -\sqrt{1+2c\rho^*}\right) \right\}.$$

As for the full problem, we expect minimisers of the OR energy (5.3.1) to converge to the set $\mathcal{B}^{OR}$ almost everywhere, away from $y = \pm 1$. In fact, the boundary conditions, $(Q_{11}(-1), M_1(-1)) = (1, 1)$ and $(Q_{11}(1), M_1(1)) = (-1, -1)$ do not belong to $\mathcal{B}^{OR}$, thus, OR energy minimisers must have boundary layers near $y = \pm 1$ in this limit. We make these heuristics more precise using Γ-convergence results, as in [77].

Consider the rescaled OR energy

$$\frac{1}{\sqrt{l}} E(Q_{11}, M_1) \coloneqq \int_{-1}^{1} \left\{ \frac{\sqrt{l}}{2} \left(\frac{\mathrm{d}Q_{11}}{\mathrm{d}y} \right)^2 + \frac{\sqrt{l}}{2} \left(\frac{\mathrm{d}M_1}{\mathrm{d}y} \right)^2 + \frac{1}{\sqrt{l}} \tilde{f}(Q_{11}, M_1) \right\} \mathrm{d}y, \tag{5.3.10}$$

where

$$\tilde{f}(Q_{11}, M_1) \coloneqq \left(Q_{11}^2 - 1\right)^2 + \frac{1}{4}\left(M_1^2 - 1\right)^2 - cQ_{11}M_1^2 - \beta_0(c) \geq 0, \tag{5.3.11}$$

and the c-dependent constant, $\beta_0(c)$, is the minimum value of the OR bulk potential. As in [77], we let $\mathbf{p} = (Q_{11}, M_1)$ and define the following metric d in the $\mathbf{p}$-plane, for any two points $\mathbf{p}_{-1}, \mathbf{p}_1 \in \mathbb{R}^2$:

$$d(\mathbf{p}_0, \mathbf{p}_1) = \inf \left\{ \int_{-1}^{1} \tilde{f}^{1/2}(\mathbf{p}(t)) \left| \frac{\mathrm{d}\mathbf{p}(t)}{\mathrm{d}t} \right| \, \mathrm{d}t : \right.$$
$$\left. \mathbf{p}(t) \in C^1\left([-1,1]; \mathbb{R}^2\right), \mathbf{p}(-1) = \mathbf{p}_{-1}, \mathbf{p}(1) = \mathbf{p}_1 \right\}. \quad (5.3.12)$$

This metric is degenerate as $\tilde{f}(\mathbf{p}) = 0$ for $\mathbf{p} = \mathbf{p}^* = (\rho^*, \sqrt{1+2c\rho^*})$ and $\mathbf{p} = \mathbf{p}^{**} = (\rho^*, -\sqrt{1+2c\rho^*})$. Despite such degeneracy, the infimum in (5.3.12) is indeed attained for arbitrary $\mathbf{p}_{-1}$ and $\mathbf{p}_1$ (see [101, Lemma 9] and [77]). We denote $\mathbf{p}_b(1) = (-1,-1)$ and $\mathbf{p}_b(-1) = (1,1)$. Let $\mathbf{p}_l$ be a minimiser of (5.3.10) for a fixed $c > 0$. An application of [77, Proposition 4.1] yields the following theorem.

Theorem 5.3.3. *There exists a subsequence $l_k \to 0$, such that the minimisers $\mathbf{p}_{l_k}$ of (5.3.10), converge in $L^1([-1,1])$ almost everywhere to a map of the form $\mathbf{p}_0 = \sum_{j=1}^{N} \mathbf{p}^j \chi_{E_j}$, where for any j, either $\mathbf{p}^j = \mathbf{p}^*$ or $\mathbf{p}^j = \mathbf{p}^{**}$, χ is the characteristic function of an interval, $E_j \subset (-1,1)$ such that $\cup_{j=1}^{N} E_j = (-1,1)$. Moreover, the intervals E_j minimise the following functional*

$$J[E_j] := \sum_{j=1}^{N-1} d(\mathbf{p}^*, \mathbf{p}^{**}) + d(\mathbf{p}_0, \mathbf{p}_b(-1)) + d(\mathbf{p}_0, \mathbf{p}_b(1)), \quad (5.3.13)$$

where the first term describes the number of jumps between $\mathbf{p}^*$ and $\mathbf{p}^{**}$, referred to as interior transition layers that necessarily contain a magnetic domain wall, and the energetic costs of the boundary layers are captured by the second and third terms.

We compute the following transition costs

$$d(\mathbf{p}^*, \mathbf{p}^{**}), d(\mathbf{p}^*, \mathbf{p}_b(1)), d(\mathbf{p}^{**}, \mathbf{p}_b(-1)), d(\mathbf{p}^*, \mathbf{p}_b(-1)), d(\mathbf{p}^{**}, \mathbf{p}_b(1)), \quad (5.3.14)$$

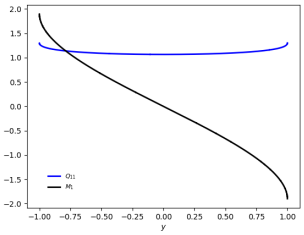

$d(\mathbf{p}^*, \mathbf{p}^{**}) \approx 3.008.$

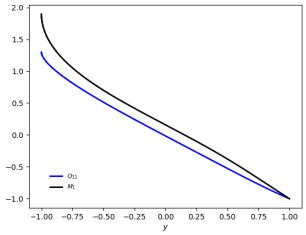

$d(\mathbf{p}^*, \mathbf{p}_b(1)) \approx 3.967.$

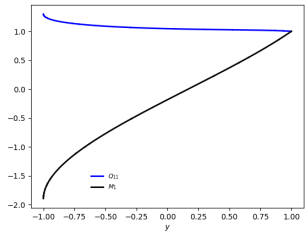

$d(\mathbf{p}^{**}, \mathbf{p}_b(-1)) \approx 2.577.$

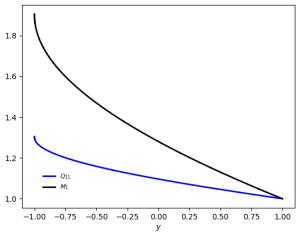

$d(\mathbf{p}^*, \mathbf{p}_b(-1)) \approx 0.455.$

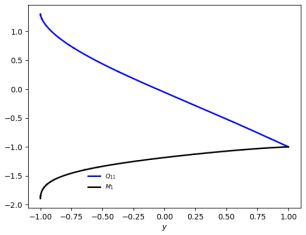

$d(\mathbf{p}^{**}, \mathbf{p}_b(1)) \approx 2.591.$

Figure 5.3: The profiles of $\mathbf{p}$ and their corresponding transition costs in (5.3.14) for $c = 1$ [2].

using the metric (5.3.12) (i.e., we numerically solve the associated Euler-Lagrange equations) for $c = 1$, and we can see from Figure 5.3 that

$$d(\mathbf{p}^*, \mathbf{p}_b(-1)) < d(\mathbf{p}^{**}, \mathbf{p}_b(-1)) < d(\mathbf{p}^{**}, \mathbf{p}_b(1)) < d(\mathbf{p}^*, \mathbf{p}^{**}) < d(\mathbf{p}^*, \mathbf{p}_b(1)).$$

It is clear that the minimiser of J in (5.3.13) is $\mathbf{p}^*$, with boundary layers near the edges $y = \pm 1$ and no interior jumps between $\mathbf{p}^*$ and $\mathbf{p}^{**}$.

5.3.3 Stability of OR solutions

The authors in [64] and [66] consider a similar OR problem with $c = 0$, in a one-dimensional channel and a two-dimensional square, respectively. In both cases, the OR solution loses stability as l decreases, or equivalently as the physical channel width/square size increases, with respect to perturbations that have non-zero Q_{12}. This motivates us to expect a similar instability result in the ferronematic setting with $c > 0$.

Theorem 5.3.4. *(Instability of the OR solution) For sufficiently small l and a fixed positive c, the OR energy minimiser, $(\mathbf{Q}^{OR}, \mathbf{M}^{OR})$, is an unstable critical point of (5.1.6), in the admissible space (5.1.8).*

Proof. For the OR solution $(\mathbf{Q}^{OR}, \mathbf{M}^{OR}) = (Q_{11}^*, 0, M_1^*, 0)$, we note that (Q_{11}^*, M_1^*) is a minimiser of the OR energy (5.3.1). Furthermore, the OR solution depends on l with fixed $c > 0$ and we suppress this explicit dependence for brevity. We compute the second variation of the free energy (5.1.6) about $\left(\mathbf{Q}^{OR}, \mathbf{M}^{OR}\right)$ with arbitrary perturbations,

$$\tilde{Q}_{11}(y) = Q_{11}^*(y) + tg(y),\ \tilde{Q}_{12}(y) = th(y),$$
$$\tilde{M}_1(y) = M_1^*(y) + tv(y),\ \tilde{M}_2(y) = tw(y).$$

Here, $t \in \mathbb{R}$ and $g(y) = h(y) = v(y) = w(y) = 0$ at $y = \pm 1$. The second variation is then given by

$$\begin{aligned}\delta^2 F[g,h,v,w] &:= \frac{\mathrm{d}^2}{\mathrm{d}t^2}\bigg|_{t=0} F(\tilde{Q}_{11}, \tilde{Q}_{12}, \tilde{M}_1, \tilde{M}_2) \\ &= \delta^2 E[g,v] + \int_{-1}^{1} \Bigg\{ l\left(\frac{\mathrm{d}h}{\mathrm{d}y}\right)^2 + l\left(\frac{\mathrm{d}w}{\mathrm{d}y}\right)^2 + 4h^2((Q_{11}^*)^2 - 1) \\ &\quad + w^2((M_1^*)^2 - 1) + 2cw^2 Q_{11}^* - 4chwM_1^* \Bigg\} \,\mathrm{d}y \\ &=: \delta^2 E[g,v] + H[h,w],\end{aligned} \tag{5.3.15}$$

where $\delta^2 E[g,v]$ is the second variation of the OR energy (5.3.1) about (Q_{11}^*, M_1^*), and thus necessarily non-negative for all admissible (g,v). To demonstrate the instability of $(\mathbf{Q}^{OR}, \mathbf{M}^{OR})$, we need to construct non-trivial h and w such that $H[h,w] < 0$. To this end, we follow methods in [64] and choose

$$h(y) = \frac{\mathrm{d}Q_{11}^*}{\mathrm{d}y} z(y) =: \tau(y)z(y), \qquad w(y) = \frac{\mathrm{d}M_1^*}{\mathrm{d}y} z(y) =: \zeta(y)z(y), \tag{5.3.16}$$

where z is a smooth cut-off function with bounded derivatives (independent of l) and $z(y) = 0$ for $|y| > 1-\eta$, $0 < \eta < \frac{1}{4}$. Since h and w vanish at $y = \pm 1$, we have

$$\int_{-1}^{1} \left(h^{'}\right)^2 \, \mathrm{d}y = -\int_{-1}^{1} hh^{''} \, \mathrm{d}y \quad \text{and} \quad \int_{-1}^{1} \left(w^{'}\right)^2 \, \mathrm{d}y = -\int_{-1}^{1} ww^{''} \, \mathrm{d}y.$$

Here and hereafter, we take $'$ ($''$) to denote first (second) derivatives with respect to y in this proof. Furthermore, one can check from (5.3.5) that

$$\begin{aligned}
&\tau^{'} = \frac{1}{l}\left[4Q_{11}^{*}\left((Q_{11}^{*})^2 - 1\right) - c(M_1^{*})^2\right], \; \tau^{''} = \frac{1}{l}\left[4\tau\left(3(Q_{11}^{*})^2 - 1\right) - 2cM_1^{*}\zeta\right], \\
&\zeta^{'} = \frac{1}{l}\left[M_1^{*}\left((M_1^{*})^2 - 1\right) - 2cQ_{11}^{*}M_1^{*}\right], \\
&\zeta^{''} = \frac{1}{l}\left[\zeta\left(3(M_1^{*})^2 - 1\right) - 2cM_1^{*}\tau - 2cQ_{11}^{*}\zeta\right].
\end{aligned} \tag{5.3.17}$$

Now noting $h^{''} = \tau^{''}z + 2\tau^{'}z^{'} + \tau z^{''}$, $w^{''} = \zeta^{''}z + 2\zeta^{'}z^{'} + \zeta z^{''}$ and substituting (5.3.16) and (5.3.17) into $H[h, w]$, we obtain

$$\begin{aligned}
H[h,w] =& \int_{-1}^{1}\left\{-8(Q_{11}^{*})^2\tau^2 z^2 + 2\zeta^2 z^2\left(2cQ_{11}^{*} - (M_1^{*})^2\right)\right\} \, \mathrm{d}y \\
&+ l\int_{-1}^{1}\left\{-2zz^{'}\tau\tau' - 2zz^{'}\zeta\zeta'\right\} \, \mathrm{d}y + \int_{-1}^{1}\left\{-lzz^{''}\left(\tau^2 + \zeta^2\right)\right\} \, \mathrm{d}y \\
=:& H_1 + H_2 + H_3.
\end{aligned} \tag{5.3.18}$$

The Γ-convergence result in Theorem 5.3.3 implies that for an interior interval $(a, b) \subset [-1, 1]$, it holds that

$$\int_a^b |Q_{11}^{*} - \rho^{*}| \, \mathrm{d}y \to 0 \quad \text{and} \quad \int_a^b \left|(M_1^{*})^2 - 1 - 2c\rho^{*}\right| \, \mathrm{d}y \to 0 \quad \text{as } l \to 0. \tag{5.3.19}$$

We use integration by parts to obtain (recall that $l\int_{-1}^{1} \tau^2 + \zeta^2 dy \le C_3\sqrt{l}$ as $l \to 0$ from the work in Section 5.2.3):

$$\int_{-1}^{1}\left\{zz^{'}\tau\tau^{'} + zz^{'}\zeta\zeta^{'}\right\} \, \mathrm{d}y = -\frac{1}{2}\int_{-1}^{1}\left\{\left(z^{'}\right)^2\left(\tau^2 + \zeta^2\right) + zz^{''}\left(\tau^2 + \zeta^2\right)\right\} \, \mathrm{d}y,$$

so that $H_2 \to 0$ as $l \to 0$. Moreover, it is straightforward to see that the third

integral H_3 in (5.3.18) vanishes in the $l \to 0$ limit. It remains to estimate the first integral in (5.3.18). By (5.3.19), we deduce that

$$H_1 \to \int_{-1}^{1} \left\{ -8\tau^2 z^2 \left(\rho^*\right)^2 - 2\zeta^2 z^2 \right\} \, \mathrm{d}y < 0 \quad \text{as } l \to 0.$$

□

5.4 Numerical results

In this section, we perform numerical experiments to validate our theoretical results and begin to understand the interplay between l and c for the solution landscapes, with fixed $\xi = 1$. For the visualisation, we plot the director $\mathbf{n}$ as lines and the normalised magnetisation vector field $\mathbf{m} = \frac{\mathbf{M}}{|\mathbf{M}|}$ as arrows.

In what follows, the presented numerical results were produced by Dr Jingmin Xia under the guidance of her then supervisor Professor Patrick Farrell. These results can be found in [2] and [102].

5.4.1 Solver details

Since the boundary-value problem is nonlinear, we use Newton's method with L^2 linesearch [103, Algorithm 2] as the outer nonlinear solver. The nonlinear solver is deemed to have converged when the Euclidean norm of the residual falls below 10^{-8}, or reduces from its initial value by a factor of 10^{-6}, whichever comes first. For the inner solver, the linearised systems are solved using the sparse LU factorisation library MUMPS [104]. The solver described above is implemented in the *Firedrake* [105] library, which relies on PETSc [106] for solving the resulting linear systems. Furthermore, we use the *deflation* technique as described in [107] to compute multiple solutions and bifurcation diagrams. Throughout this section,

we partition the whole interval $[-1,1]$ into 1000 equi-distant subintervals and numerically approximate the solutions using $\mathbb{P}^1$ finite elements (piecewise linear continuous polynomials).

5.4.2 OR solutions

We have analysed the OR solution branch with $Q_{12} = M_2 = 0$, as $l \to 0$ and as $l \to \infty$. The OR branch is fully characterised by solutions of the system (5.3.5) subject to the boundary conditions (5.3.2). OR solutions are special since they must contain separate domain walls in $\mathbf{Q}$ and $\mathbf{M}$, which can be tailored by varying l and c.

As $l \to \infty$, recall Theorem 5.3.1 to deduce that the OR solution branch is approximately given by $\left(\mathbf{Q}^{OR}, \mathbf{M}^{OR}\right) \approx (-y, 0, -y, 0)$, for a fixed c, and that $\left(\mathbf{Q}^{OR}, \mathbf{M}^{OR}\right)$ is also the unique minimiser of both the OR energy (5.3.1) and the full energy (5.1.6). In Figure 5.4, we plot the OR solution of (5.3.5) for $c = 1$ and $l = 10$. The profile is indeed linear, and we do not numerically obtain any other solutions, supporting the uniqueness result in the $l \to \infty$ limit. The OR solution vanishes at the channel centre $y = 0$, i.e. $Q_{11}(0) = M_1(0) = 0$, and thus both the nematic and magnetic domain walls coincide at $y = 0$. Therefore, the normalised magnetisation vector $\mathbf{m}$ and director $\mathbf{n}$ have a jump discontinuity at $y = 0$, i.e., $\mathbf{m}$ jumps from $\mathbf{m} = (1, 0)$ for $y < 0$ to $\mathbf{m} = (-1, 0)$ for $y > 0$, while $\mathbf{n}$ jumps from $\mathbf{n} = (1, 0)$ (modulo a sign) for $y < 0$ to $\mathbf{n} = (0, 1)$ (modulo a sign) for $y > 0$. We also plot the pointwise L^∞ bound (5.3.6) as blue solid lines in Figure 5.4, and this bound is indeed respected.

As $l \to 0$, for fixed $c > 0$, we expect $Q_{11} \to \rho^*$ and $M_1^2 \to 1 + 2c\rho^*$ uniformly away from $y = \pm 1$, for the OR energy minimiser of (5.3.1). We note that $\rho^*(c)$ defined in

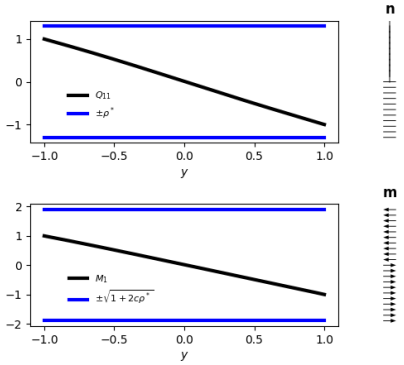

Figure 5.4: The only critical point of (5.3.1) (and (5.1.6)) for $c = \xi = 1$, and $l = 10$.

(5.2.20) is an increasing function of c and $\rho^*(0) = 1$ (see Figure 5.1 (a) for $k = 1$), thus $\rho^*(c) > 1$ for all $c > 0$. As discussed in Theorem 5.3.3, we expect a domain wall in $\mathbf{Q}$ near the edge $y = 1$, within a boundary layer where Q_{11} jumps from $Q_{11} = \rho^* > 1$ to $Q_{11}(1) = -1$. Hence, there necessarily exists a nematic domain wall where $Q_{11} = 0$, within this boundary layer close to $y = 1$. Analogously, there is a boundary layer near the other end point $y = -1$, within which Q_{11} jumps from $Q_{11}(-1) = 1$ to $Q_{11} = \rho^*$, but this boundary layer does not contain a nematic domain wall. While for $\mathbf{M}$, we expect a magnetic domain wall: near $y = 1$ if $M_1 > 0$ in the interior, or near $y = -1$ if $M_1 < 0$ in the interior respectively. In what follows, a transition layer refers to a thin interval within which M_1 jumps between $-\sqrt{1 + 2c\rho^*}$ and $\sqrt{1 + 2c\rho^*}$ and each of these transition layers necessarily contains a magnetic domain wall with $M_1 = M_2 = 0$. We expect the OR energy (5.3.1) to have multiple critical points, with multiple interior transition layers and domain walls in $\mathbf{Q}$ and $\mathbf{M}$, for l small enough. However, we expect the OR energy minimiser to be such that $Q_{11} \to \rho^*$ and $M_1 \to \sqrt{1 + 2c\rho^*}$ in the interior, with no interior domain walls or transition layers. Of course, all OR solutions are unstable critical points of the full energy (5.1.6) for l small enough, as proven in Theorem 5.3.4. We now numerically corroborate these theoretical conjectures

with $l = 0.01$ and $\xi = 1$.

In Figure 5.5, we present four example solutions with $c = 1$. They are all unstable critical points of the full energy (5.1.6) whilst being stable critical points of the OR energy (5.3.1) (in the sense that the Hessian of second variation of the OR energy at these critical points has all positive eigenvalues). As expected, these solution profiles (Q_{11}, M_1), have boundary layers near the end points. Furthermore, interior transition layers in M_1 (near the centre $y = 0$) are observed in Solutions 3 and 4. The L^∞ bounds (5.3.6) (blue solid line) for $|Q_{11}|$ and $|M_1|$ are also satisfied.

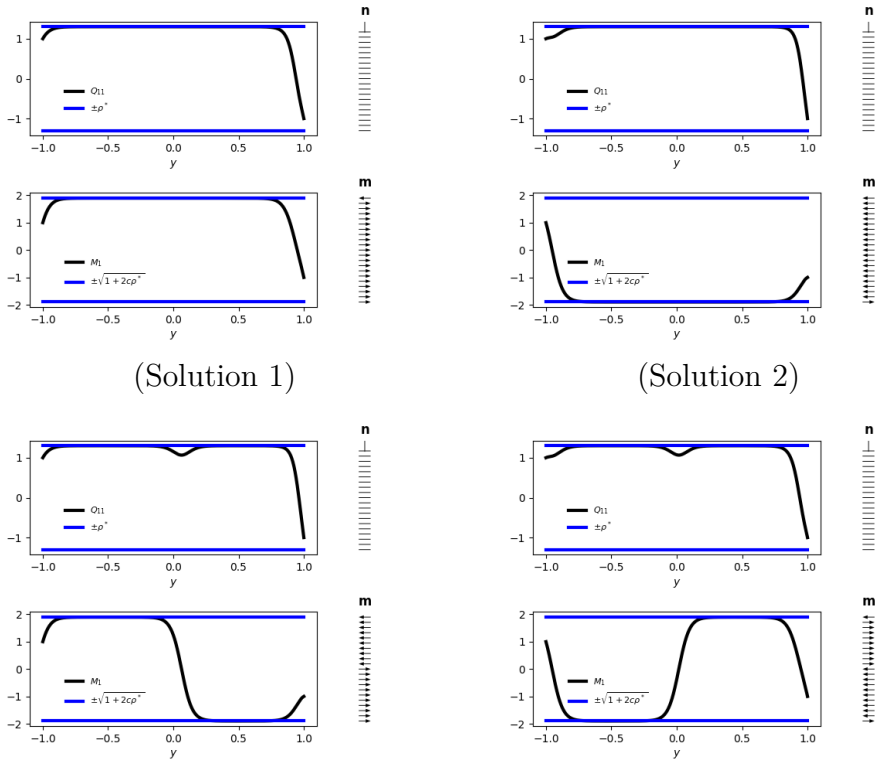

(Solution 1) (Solution 2)

(Solution 3) (Solution 4)

Figure 5.5: Four stable OR critical points of (5.3.1), with $c = \xi = 1$ and $l = 0.01$. Solution 1 is the minimiser of the OR energy (5.3.1).

In Figure 5.6, we plot the stable solutions of the OR energy (5.3.1) for a larger value $c = 5$, but again, these are unstable critical points of the full energy

(5.1.6). The two profiles in Figure 5.6, have boundary layers near $y = \pm 1$, and essentially differ in the sign of M_1 in the interior; Q_{11} only vanishes near $y = 1$ as predicted by the Γ-convergence analysis, so that we have a nematic domain wall near $y = 1$. On the other hand, M_1 can vanish either near $y = -1$ or near $y = 1$, so that the corresponding magnetic domain wall can occur near either boundary. Additionally, there are other solutions with interior transition layers for M_1, (see two examples in Figure 5.7) where single and multiple interior transition layers in M_1 are observed. They are also stable critical points of the OR energy (5.3.1). The transition layers in M_1 necessarily contain a magnetic domain wall with $M_1 = 0$, and these interior magnetic domain walls are not accompanied by associated nematic domain walls. Moreover, solutions with interior transition layers have higher OR energy (5.3.1) than solutions without interior transition layers in Figure 5.6, since each transition layer has an energetic cost of $d(\mathbf{p}^*, \mathbf{p}^{**})$ as explained in Theorem 5.3.3.

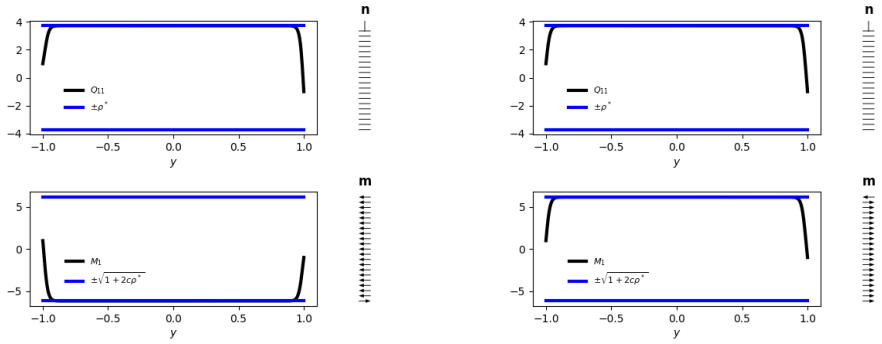

Figure 5.6: Two stable OR critical points of (5.3.1), for $c = 5$, $\xi = 1$ and $l = 0.01$. The right profile has lower OR energy than the left profile and the solutions in Figure 5.7.

These numerical experiments illustrate that we can manipulate the location and multiplicity of nematic and magnetic domain walls in OR solutions by varying l, e.g., the domain walls in the OR energy minimisers migrate from the channel

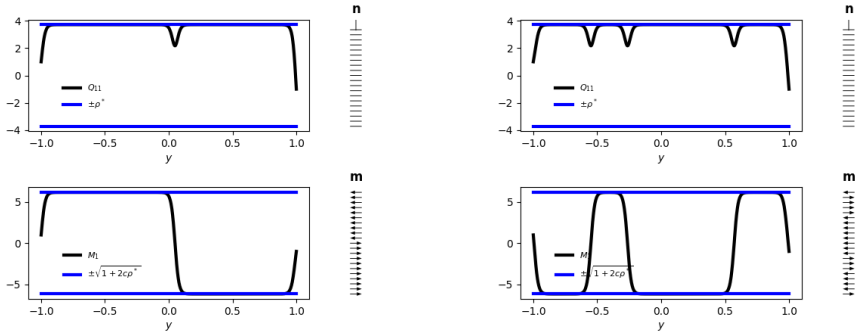

Figure 5.7: Two stable OR critical points of (5.3.1), with single (left) and multiple (right) interior transition layers for $c = 5$, $\xi = 1$ and $l = 0.01$. The left has lower OR energy.

centre to the channel boundaries at $y = \pm 1$, as l decreases.

5.4.3 Solutions of the full problem

Next, we consider the full problem (5.1.9a)-(5.1.9d) with four degrees of freedom, $(Q_{11}, Q_{12}, M_1, M_2)$. We only consider the case of small $l_1 = l_2 = l = 0.01$ with $\xi = 1$, since the OR solution branch is the unique solution of the full problem, in the $l \to \infty$ limit.

In Figure 5.8, we take $c = 1$ and present four examples of stable solutions with four degrees of freedom. We also plot the L^∞ bound (5.2.19) in the figures, illustrating that Theorem 5.2.4 is indeed satisfied. There are no interior domain walls with $|\mathbf{Q}| = |\mathbf{M}| = 0$, for small l, as discussed in Section 5.2.3. Furthermore, Solutions 1, 2 and 3 in Figure 5.8 only have boundary layers, with almost constant $|\mathbf{Q}|, |\mathbf{M}|$-profiles in the domain interior, whereas Solution 4 has interior non-zero local minima in $|\mathbf{Q}|$ and $|\mathbf{M}|$. Solutions 1 and 2 are the energy minimisers while the remaining two profiles are non-minimising stable critical points of the full energy (5.1.6). Note that the two energy minimisers differ in their **n**- and **m**-patterns

(more precisely, the sign of Q_{12} and M_2). Moreover, we compute the values of θ, ϕ (defined in (5.2.2)) by

$$\theta = \arctan\left(Q_{12}, Q_{11}\right), \ \phi = \arctan\left(M_2, M_1\right) \tag{5.4.1}$$

for each solution. It can be seen that $|\mathbf{Q}| \to \rho^*$ and $|\mathbf{M}|^2 \to 1 + 2c\rho^*$ for the energy minimiser (Solution 1), while $(2\phi - \theta)$ tends to an even multiple of π almost everywhere (consistent with (5.2.36c)), except near $y = \pm 1$ and local minima in $|\mathbf{Q}|$ and $|\mathbf{M}|$. Furthermore, the separate plots of θ and ϕ demonstrate linear behaviour except around the local minima of $|\mathbf{Q}|$ or $|\mathbf{M}|$ and the boundary layers, consistent with the limiting Laplace equation (5.2.36a) for ϕ and θ and the boundary conditions (5.2.36b), in the $l \to 0$ limit.

Now we repeat the simulations for $c = 5$. Two stable stationary profiles are illustrated in Figure 5.9. We see that $|\mathbf{Q}| \to \rho^*$ and $|\mathbf{M}|^2 \to 1 + 2c\rho^*$ almost everywhere, as expected. Here, Solution 2 has lower energy than Solution 1, since Solution 1 has more local minima in $|\mathbf{Q}|$ and $|\mathbf{M}|$ than Solution 2. Further, $(2\phi - \theta)$ is an even multiple of π almost everywhere, with the jumps being associated with the local minima in $|\mathbf{Q}|$ and $|\mathbf{M}|$, again verifying (5.2.36c). Additionally, we plot ϕ and θ in Figure 5.9, and observe almost linear profiles, except around the local minima and boundary layers. To summarise, the numerical experiments and the heuristics in Section 5.2.3 suggest that there are at least two energy minimisers, characterised by $(\rho_1, \sigma_1, \theta_1, \phi_1)$ and $(\rho_2, \sigma_2, \theta_2, \phi_2)$ of (5.1.6) in the $l \to 0$ limit, such that $\rho_1, \rho_2 \to \rho^*$, $\sigma_1^2, \sigma_2^2 \to 1 + 2c\rho^*$ almost everywhere away from $y = \pm 1$, $\theta_2 = -\theta_1$, $\phi_2 = -\phi_1$, with no domain walls and $2\phi_k - \theta_k$ (for $k = 1, 2$) an even multiple of π except near $y = 1$. The two energy minimisers differ in their sense of rotation, in $\mathbf{n}$ and $\mathbf{m}$, between $y = \pm 1$.

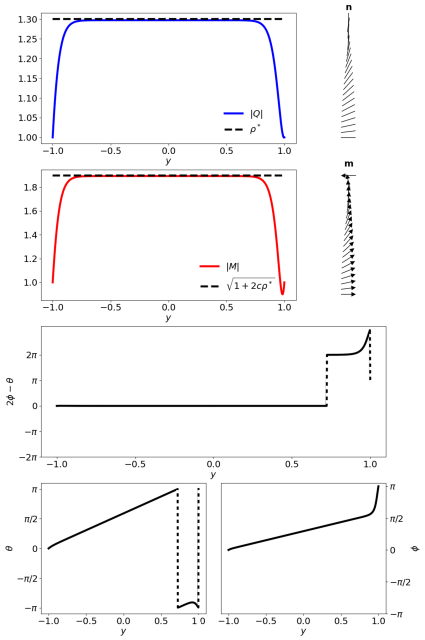

(Solution 1; stable)

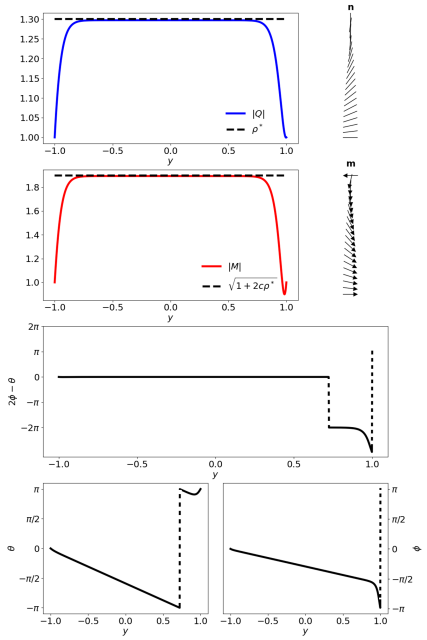

(Solution 2; stable)

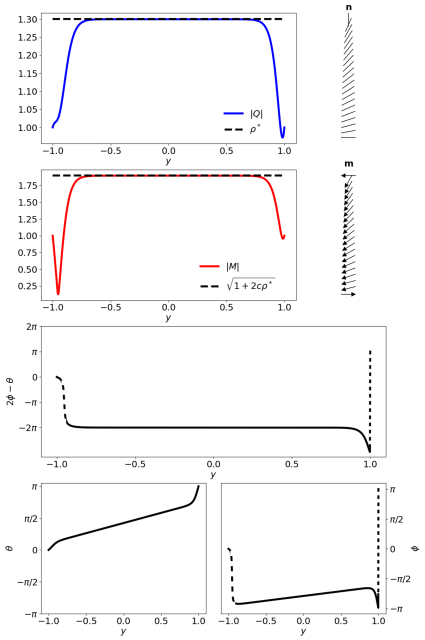

(Solution 3; stable)

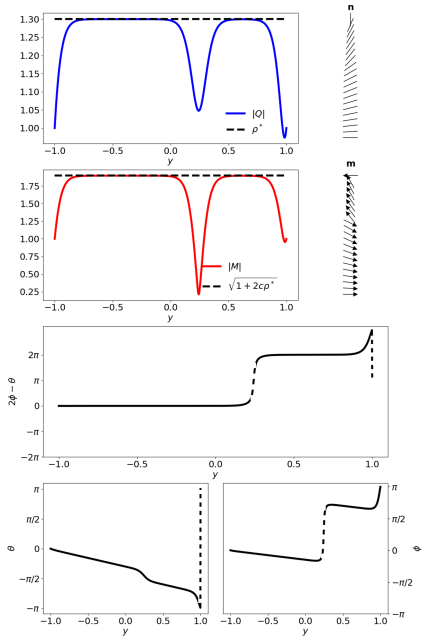

(Solution 4; stable)

Figure 5.8: Four stable critical points, $(Q_{11}, Q_{12}, M_1, M_2)$, of (5.1.6) with $l = 0.01$ and $c = \xi = 1$, along with plots of $(2\phi - \theta)$, θ and ϕ to verify the relations in (5.2.36) (dotted lines represent discontinuities). Solutions 1 and 2 have the lowest full energy value (5.1.6).

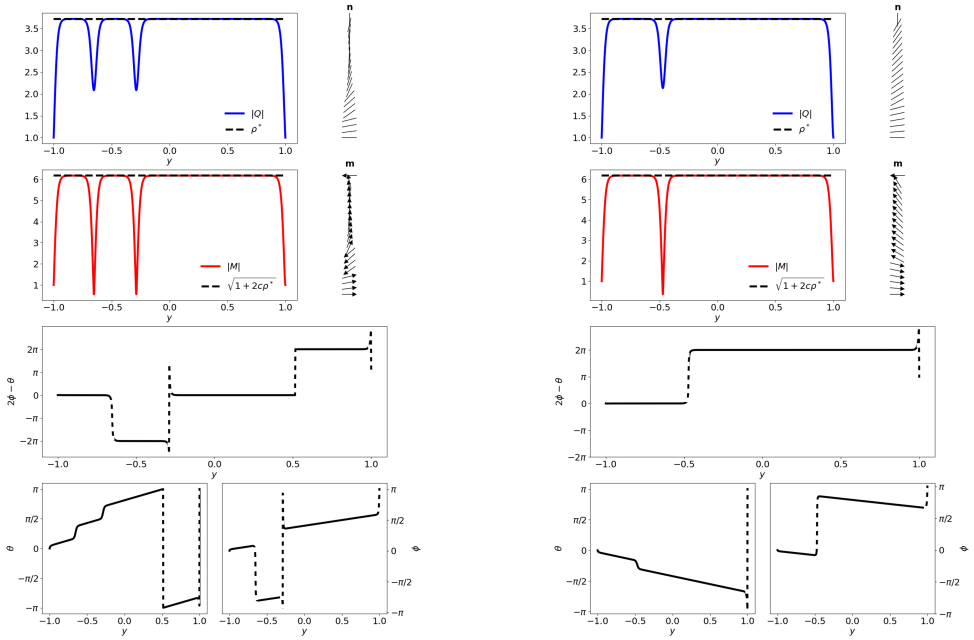

(Solution 1; stable) (Solution 2; stable)

Figure 5.9: Two examples of stable critical points $(Q_{11}, Q_{12}, M_1, M_2)$ of the full energy (5.1.6) with $l = 0.01$, $c = 5$ and $\xi = 1$. Solution 2 has lower energy than Solution 1.

5.4.4 Bifurcation diagrams with continuing l

We vary $L^* = l_2 =: l \in [0.2, 3.0]$ with step size 0.01 and $c = 1$ in Figure 5.10. There is only one stable OR solution for $l \in [1.25, 3.0]$, being the energy minimiser of the full energy (5.1.6). For $l \approx 1.25$, there is a pitchfork bifurcation consisting of two stable full solution branches and one unstable OR branch (see Figure 5.11 for the solutions). In fact, the two stable solutions (Solutions 1 and 3 in Figure 5.11) differ by the sign of Q_{12} and M_2, i.e., for every solution branch, $(Q_{11}, Q_{12}, M_1, M_2)$, there exists another solution branch with $(Q_{11}, -Q_{12}, M_1, -M_2)$. The stable solution branches correspond to a smooth rotation in $\mathbf{n}$, between $y = \pm 1$ and are the global energy minimisers for $l \leq 1.25$.

As l becomes smaller, more (stable or unstable) solutions are found. More spe-

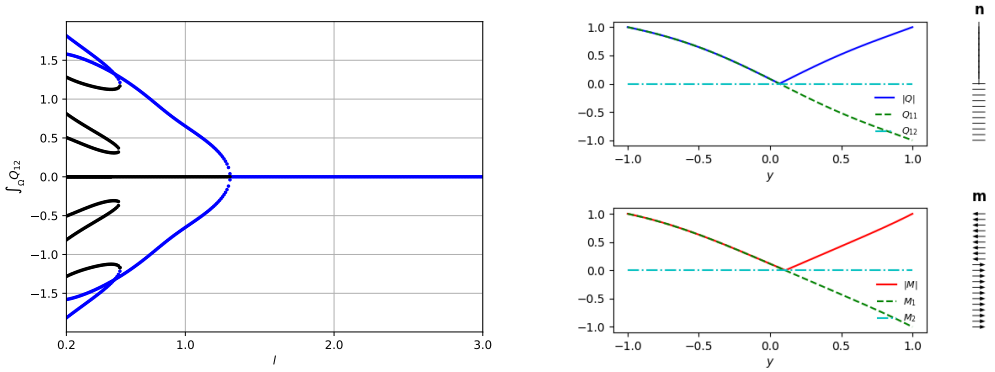

Figure 5.10: Left: the bifurcation diagram of continuing $L^* = l_2 = l \in [0.2, 3.0]$ with fixed $c = \xi = 1$; here, black represents unstable solutions while blue indicates stable solutions. Right: the stable solution for $l = 2$.

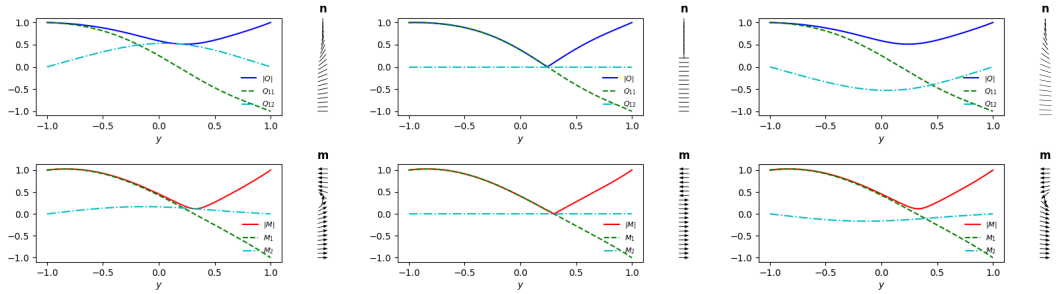

(Solution 1; stable) (Solution 2; unstable) (Solution 3; stable)

Figure 5.11: Three solutions for $l = 1$ in Figure 5.10. Solutions 1 and 3 are global energy minimisers.

cifically, there are four disconnected bifurcations appearing around $l = 0.55$, giving two further stable solutions, which are also local energy minimisers for $l \in [0.2, 0.55]$. Again, they only differ by the sign of Q_{12} and M_2. In Figure 5.12, we plot two examples of newly found stable solution profiles for $l = 0.2$. The stable solutions typically correspond to smooth $\mathbf{n}$-profiles with minimal rotation, while the stable normalised magnetisation profiles $\mathbf{m}$ are also smooth, except near $y = \pm 1$.

We next consider the case of $c = 5$, by numerically computing a bifurcation

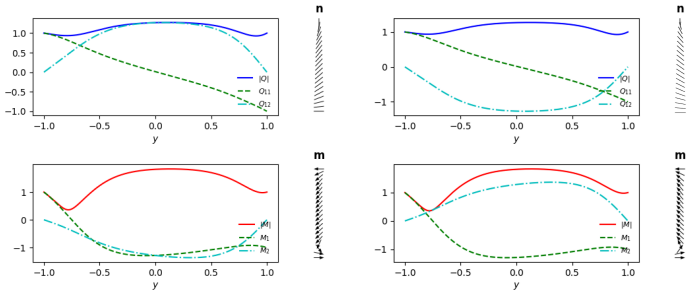

(Solution 1; stable) (Solution 4; stable)

Figure 5.12: Two examples of new stable solutions for $l = 0.2$ in Figure 5.10. They are global energy minimisers.

diagram in Figure 5.13, for the solutions of (5.1.9a)-(5.1.9d), by continuing $l \in [3, 5]$ with a step size of 0.015. The globally stable OR solution is shown in Figure 5.13 and it loses stability at the pitchfork bifurcation point $l \approx 4.44$, leading to two new stable branches (see illustrations in Figure 5.14 for $l = 4.43$). The new stable solutions only differ in the signs of Q_{12} and M_2 and are in fact, energy minimisers for $l \leq 4.34$. Thus, the qualitative features of the bifurcation diagram are unchanged by increasing c, but the OR solution branch loses stability for $l < l^*(c)$, where $l^*(c)$ is an increasing function of c. Hence, as c increases, OR solutions are increasingly difficult to find owing to their shrinking window of stability.

Remark 5.4.1. We comment on the two folds in the bifurcation diagram Figure 5.13. They do not represent the same solution branch at the intersection points. Instead, they are just overlapping points in this plot of $\int_\Omega Q_{12}$ versus l. A different functional may yield a bifurcation diagram without these intersection points.

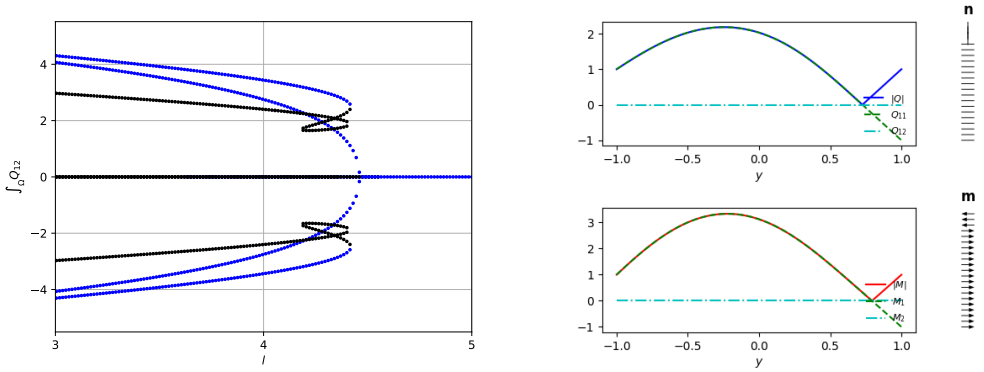

Figure 5.13: Left: the bifurcation diagram with fixed $c = 5$ and $\xi = 1$; here, black labels unstable solutions while blue labels stable solutions. Right: one stable OR solution for $l = 4.45$.

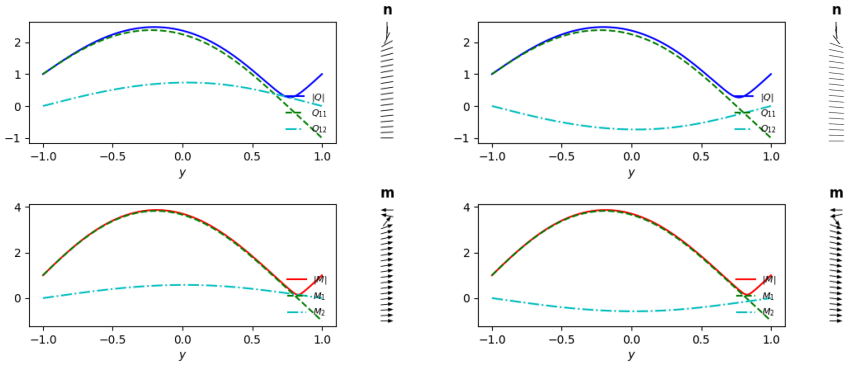

Figure 5.14: Two new stable solutions at $l = 4.43$ in Figure 5.13.

5.5 Summary

We study confined systems with both nematic and magnetic order, inside a channel geometry with Dirichlet boundary conditions. Specifically, we model the stable equilibria as minimisers of an appropriately defined energy on an interval $[-D, D]$, with three contributions: a nematic energy, a magnetic energy and a nemato-magnetic coupling energy. We are interested in two parameters: the scaled elastic parameter l that is inversely proportional to D^2, and the nemato-magnetic coupling parameter c.

We rigorously show that c reduces the effective nematic correlation length ξ_n, for large c, and we have a unique OR solution for $D \ll \frac{c^*}{c}\xi_n$, for some explicitly computable constant c^*, independent of c. The practical implications of this result for experiments is that OR should be observed for sufficiently narrow channels (e.g. for $l = 10$ in Figure 5.4, with $A = -848.5\text{Nm}^{-2}$ and $K = 10^{-11}\text{N}$ [68], $D = 3.43 \times 10^{-8}\text{m}$). For sufficiently small D, the unique OR solution has nematic and magnetic domain walls which coincide in the centre of the channel. As D increases for fixed c, there can be multiple OR solutions, all of which are unstable. Multiple OR solutions for large D, is distinct behaviour when compared to the one-dimensional purely nematic counterpart, for which there is only one OR solution for all domain sizes [64]. The multiplicity of OR solutions in ferronematics will be addressed further in Chapter 6. All ferronematic OR solutions have a single nematic domain wall which migrates to the top of the channel, whilst we can have multiple magnetic domain walls with varying locations, and in general these domain walls need not coincide. The increased complexity of polydomain structures in ferronematics could present interesting possibilities for applications. Our finding of OR solutions for this problem is interesting, as their existence was certainly non-obvious a priori. This work is therefore another example in demonstrating the universality of OR solutions. For large D, we also find multiple stable non-OR solutions that do not have domain walls and are therefore not polydomains, which can be characterised by the rotation profiles of $\mathbf{n}$ and $\mathbf{m}$ between the boundaries. Our choice of boundary conditions necessarily lead to boundary layers, which could have distinct optical signatures, if implemented.

We have also provided analytic characterisations of the limiting profiles for small D (in terms of the unique OR solution) and large D (in terms of limiting maps) accompanied by numerical studies, which beautifully illustrate how we can use

l and c to tune domain walls, boundary layers and multistability, all of which can be exploited for optical and mechanical responses. This work gives informative insight into the complex interplay between geometry, material properties, temperature (captured by l), nemato-magnetic coupling and boundary conditions in the solution landscapes (also see [108] for numerical analysis of this system in two-dimensions). Our methods can be modified to include different types of boundary conditions and nemato-magnetic coupling, which could enhance the stability of OR solutions, and future work would be to develop universal theoretical frameworks for composite materials with multiple order parameters.

Chapter 6

Solution landscapes for ferronematics

6.1 The problem

Once a multistable system is obtained, the next key step in creating a switchable soft device is to understand the switching dynamics when the system transitions between different stable states. One way of doing this is by computing solution landscapes. By this, we mean identifying all the critical points of a given free energy and how they connect to one another on the energy landscape. With the knowledge that ferronematics can support multistability from Chapter 5, and the goal of creating switchable ferronematic devices in mind, we devote this chapter to the study of solution landscapes for ferronematics.

We compute solution landscapes using the numerical algorithm known as the high-index optimisation-based shrinking dimer (HiOSD) method [71]. The HiOSD is a powerful method for finding unstable critical points, their Morse index and system-

atically computing solution landscapes, i.e, pathway maps which illustrate how critical points connect to one another (see Figure 6.1). We explain the algorithm, as well as the notion of stability, pathways and Morse index, in Section 6.1.1. For now, we comment that transition pathways are defined to be pathways connecting stable states (i.e., stable critical points) to unstable states with Morse index-1, and we call such unstable states transition states. These transition states are of particular interest, since they are the most likely to be physically observed in the switching process of liquid crystal devices [109]. That is not to say that critical points with higher Morse index are irrelevant though, because a complete understanding of the solution landscape is vitally important. In general, all unstable solutions matter, because it is these solutions that influence the selection of stable states in multistable systems.

6.1.1 The HiOSD method

The setup of the ferronematic problem is the same as in Chapter 5. We therefore refer the reader to Section 5.1.1 for details.

Remark 6.1.1. As in the previous chapter there are two distinct and important solution types we will encounter. The first type are full solutions of the form $(\mathbf{Q}, \mathbf{M}) = (Q_{11}, Q_{12}, M_1, M_2)$, which exploit all four degrees of freedom. The second, are order reconstruction (OR) solutions of the form $(\mathbf{Q}, \mathbf{M}) = (Q_{11}, 0, M_1, 0)$, which have only two degrees of freedom.

We now make some useful observations that were not (explicitly) made in the previous chapter. Looking at the Euler-Lagrange equations (5.1.9), we can see if $(\tilde{Q}_{11}, \tilde{Q}_{12}, \tilde{M}_1, \tilde{M}_2)$ is a solution, then $(\tilde{Q}_{11}, -\tilde{Q}_{12}, \tilde{M}_1, -\tilde{M}_2)$ must also be a solution. As such, in the numerical results that follow, we expect all full solutions to come in pairs which have the same Q_{11} and M_1 profiles, whilst the Q_{12} and

M_2 profiles are reflections of each other. Moreover, from (5.1.6), we see that the energy of each solution in the pair must be the same.

A critical point $(\mathbf{Q}, \mathbf{M})$ of (5.1.6) is said to be stable if the corresponding Hessian of the free energy $F(\mathbf{Q}, \mathbf{M})$ is positive definite, or equivalently, all its eigenvalues are positive, and is unstable otherwise. Here and hereafter, we will denote a critical point by

$$(\mathbf{Q}, \mathbf{M}) := (Q_{11}, Q_{12}, M_1, M_2), \tag{6.1.1}$$

i.e., a single vector containing information about the $\mathbf{Q}$ and $\mathbf{M}$ profiles, in this order. We find the solutions of (5.1.9a)-(5.1.9d) in two ways:

1. We solve the corresponding gradient flow equations, namely [69]

$$\frac{\partial Q_{11}}{\partial t} = l\frac{\mathrm{d}^2 Q_{11}}{\mathrm{d}y^2} - 4Q_{11}(Q_{11}^2 + Q_{12}^2 - 1) + c\left(M_1^2 - M_2^2\right), \tag{6.1.2a}$$

$$\frac{\partial Q_{12}}{\partial t} = l\frac{\mathrm{d}^2 Q_{12}}{\mathrm{d}y^2} - 4Q_{12}(Q_{11}^2 + Q_{12}^2 - 1) + 2cM_1M_2, \tag{6.1.2b}$$

$$\frac{\partial M_1}{\partial t} = l\frac{\mathrm{d}^2 M_1}{\mathrm{d}y^2} - M_1\left(M_1^2 + M_2^2 - 1\right) + 2cQ_{11}M_1 + 2cQ_{12}M_2, \tag{6.1.2c}$$

$$\frac{\partial M_2}{\partial t} = l\frac{\mathrm{d}^2 M_2}{\mathrm{d}y^2} - M_2\left(M_1^2 + M_2^2 - 1\right) - 2cQ_{11}M_2 + 2cQ_{12}M_1. \tag{6.1.2d}$$

   To solve the gradient flow system, we use finite difference methods in the space direction with a uniform mesh of mesh size $1/20$ partitioning $[-1, 1]$, and use Euler's method in the time direction.

2. Alternatively, we solve the Euler-Lagrange equation (5.1.9) using Newton's method with the same mesh size.

Either method is deemed to have converged when the norm of the gradient of F

(denoted by ∇F) has fallen below 10^{-8}, i.e.,

$$||\nabla F(\mathbf{Q}, \mathbf{M})||_{L^2} < 10^{-8}, \tag{6.1.3}$$

where

$$\nabla F(\mathbf{Q}, \mathbf{M}) = \begin{pmatrix} l\frac{\mathrm{d}^2 Q_{11}}{\mathrm{d}y^2} - 4Q_{11}(Q_{11}^2 + Q_{12}^2 - 1) + c\,(M_1^2 - M_2^2) \\ l\frac{\mathrm{d}^2 Q_{12}}{\mathrm{d}y^2} - 4Q_{12}(Q_{11}^2 + Q_{12}^2 - 1) + 2cM_1M_2 \\ l\frac{\mathrm{d}^2 M_1}{\mathrm{d}y^2} - M_1\,(M_1^2 + M_2^2 - 1) + 2cQ_{11}M_1 + 2cQ_{12}M_2 \\ l\frac{\mathrm{d}^2 M_2}{\mathrm{d}y^2} - M_2\,(M_1^2 + M_2^2 - 1) - 2cQ_{11}M_2 + 2cQ_{12}M_1 \end{pmatrix}. \tag{6.1.4}$$

We require these two approaches for the following reasons. We couple method 1. with the HiOSD dynamics for eigenvectors (explained next) to compute eigenvalues and eigenvectors of stable critical points. This provides us with suitable initial conditions to start searching the solution landscape using the HiOSD method. We use method 2. to find critical points we may have missed using the HiOSD method. By simulating Newton's method many times with random initial conditions we can (in principle) find all critical points for given values of the parameters l and c, but learn no information about their connections on the energy landscape.

The Morse index of any critical point is the number of negative eigenvalues of the Hessian of the free energy [110]. A critical point is stable if all the eigenvalues of its Hessian are positive, and a critical point is unstable if it has Morse index greater or equal to 1 (i.e, it has at least one negative eigenvalue of its Hessian). A saddle point is an unstable critical point which has Morse index-k and hence k negative eigenvalues of the associated Hessian, making it unstable in k-distinguished eigendirections and stable in all other directions. Henceforth, we refer to critical points of a given Morse index as index-k saddles. These index-k saddles are non-energy minimising critical points.

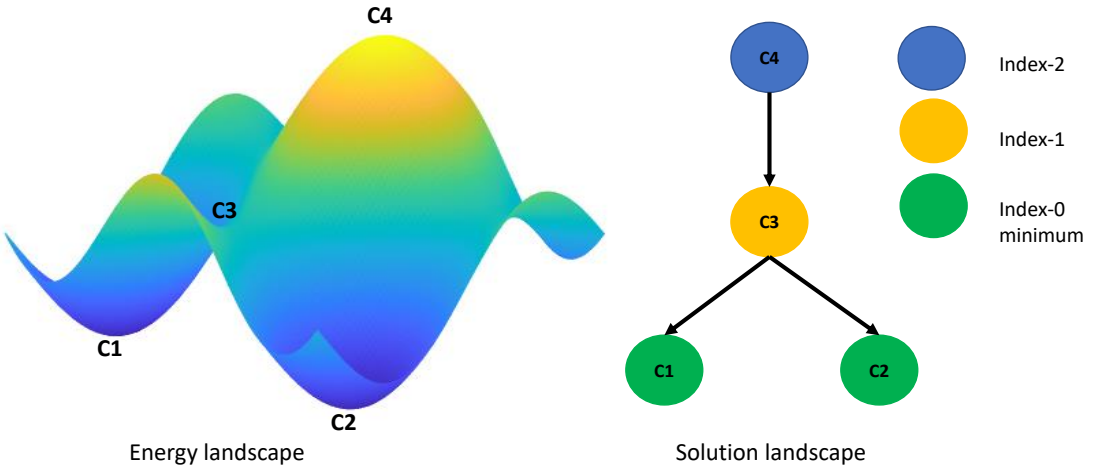

Figure 6.1: A sketch of an energy landscape and its associated solution landscape. The C_i denote critical points of the energy functional.

We now explain and present the HiOSD method in [71], using the notation of our problem. The HiOSD method is a local-search algorithm for the computation of saddle points of arbitrary indices, which can be viewed as a generalisation of the optimisation-based shrinking dimer method for finding index-1 saddle points [111]. It is an efficient tool for constructing the solution landscape searching from high- or low-index saddle points and revealing the connectivity of saddle points and minimisers. We combine the (HiOSD) method [71] with upward/downward search algorithms [80], to compute solution landscapes, or equivalently, pathway maps for this ferronematic problem. We say there exists a pathway between two critical points $(\mathbf{Q}_1, \mathbf{M}_1)$ and $(\mathbf{Q}_2, \mathbf{M}_2)$ if following a stable or unstable eigendirection (of the Hessian) of $(\mathbf{Q}_1, \mathbf{M}_1)$ in the HiOSD method, leads us to find $(\mathbf{Q}_2, \mathbf{M}_2)$ [80]. To make these ideas clear, an example solution landscape and associated energy landscape are presented in Figure 6.1.

For a non-degenerate index-k saddle point $(\hat{\mathbf{Q}}, \hat{\mathbf{M}})$, the Hessian $\mathbb{H}(\mathbf{Q}, \mathbf{M}) = \nabla^2 F(\mathbf{Q}, \mathbf{M})$ at $(\hat{\mathbf{Q}}, \hat{\mathbf{M}})$, has exactly k negative eigenvalues $\hat{\lambda}_1 \leqslant \cdots \leqslant \hat{\lambda}_k$ with

corresponding unit eigenvectors $\hat{\mathbf{v}}_1, \ldots, \hat{\mathbf{v}}_k$, satisfying $\left\langle \hat{\mathbf{v}}_j, \hat{\mathbf{v}}_i \right\rangle = \delta_{ij}$, $1 \leqslant i, j \leqslant k$. We define a k-dimensional subspace $\hat{\mathcal{V}} = \text{span}\left\{\hat{\mathbf{v}}_1, \ldots, \hat{\mathbf{v}}_k\right\}$, then $(\hat{\mathbf{Q}}, \hat{\mathbf{M}})$ is a local maximum on a k-dimensional linear manifold $(\hat{\mathbf{Q}}, \hat{\mathbf{M}}) + \hat{\mathcal{V}}$ and a local minimum on $(\hat{\mathbf{Q}}, \hat{\mathbf{M}}) + \hat{\mathcal{V}}^{\perp}$, where $\hat{\mathcal{V}}^{\perp}$ is the orthogonal complement space of $\hat{\mathcal{V}}$.

The index-k saddle $(\hat{\mathbf{Q}}, \hat{\mathbf{M}})$ can be achieved by a minimax optimisation problem

$$\min_{(\mathbf{Q},\mathbf{M})_{\hat{\mathcal{V}}^{\perp}} \in \hat{\mathcal{V}}^{\perp}} \max_{(\mathbf{Q},\mathbf{M})_{\hat{\mathcal{V}}} \in \hat{\mathcal{V}}} F((\mathbf{Q}, \mathbf{M})_{\hat{\mathcal{V}}^{\perp}} + (\mathbf{Q}, \mathbf{M})_{\hat{\mathcal{V}}}), \tag{6.1.5}$$

where $(\mathbf{Q}, \mathbf{M})_{\hat{\mathcal{V}}} = \mathcal{P}_{\hat{\mathcal{V}}}(\mathbf{Q}, \mathbf{M})$ is the orthogonal projection of $(\mathbf{Q}, \mathbf{M})$ on $\hat{\mathcal{V}}$, and $(\mathbf{Q}, \mathbf{M})_{\hat{\mathcal{V}}^{\perp}} = (\mathbf{Q}, \mathbf{M}) - \mathcal{P}_{\hat{\mathcal{V}}}(\mathbf{Q}, \mathbf{M})$. Here, $(\mathbf{Q}, \mathbf{M})$ is assumed to be sufficiently close to $(\hat{\mathbf{Q}}, \hat{\mathbf{M}})$ so that $\mathbb{H}(\mathbf{Q}, \mathbf{M})$ also has exactly k negative eigenvalues, with corresponding eigenvectors $\mathbf{v}_i$, for $i = 1, \ldots k$. Furthermore, we take $\mathcal{V} = \text{span}\left\{\mathbf{v}_1, \ldots, \mathbf{v}_k\right\}$ to approximate $\hat{\mathcal{V}}$.

For brevity of notation, in what follows $\dot{}$ will denote differentiation with respect to t. To find a solution of the minimax problem (6.1.5), the dynamics of $(\mathbf{Q}, \mathbf{M})$ should satisfy that $\mathcal{P}_{\mathcal{V}}(\dot{\mathbf{Q}}, \dot{\mathbf{M}})$ is an ascent direction on the subspace $\mathcal{V}$ and that $(\dot{\mathbf{Q}}, \dot{\mathbf{M}}) - \mathcal{P}_{\mathcal{V}}(\dot{\mathbf{Q}}, \dot{\mathbf{M}})$ is a descent direction on the subspace $\mathcal{V}^{\perp}$. This ensures $(\mathbf{Q}, \mathbf{M})$ increases to a maximum on $\mathcal{V}$ and decreases to a minimum on $\mathcal{V}^{\perp}$. Therefore, we take $\mathcal{P}_{\mathcal{V}} \nabla F(\mathbf{Q}, \mathbf{M})$ as the direction of $\mathcal{P}_{\mathcal{V}}(\dot{\mathbf{Q}}, \dot{\mathbf{M}})$ and $-\nabla F(\mathbf{Q}, \mathbf{M}) + \mathcal{P}_{\mathcal{V}} \nabla F(\mathbf{Q}, \mathbf{M})$ as the direction of $(\dot{\mathbf{Q}}, \dot{\mathbf{M}}) - \mathcal{P}_{\mathcal{V}}(\dot{\mathbf{Q}}, \dot{\mathbf{M}})$. The following gradient dynamics can then be used to solve (6.1.5)

$$\beta^{-1}(\dot{\mathbf{Q}}, \dot{\mathbf{M}}) = -\nabla F(\mathbf{Q}, \mathbf{M}) + 2\mathcal{P}_{\mathcal{V}} \nabla F(\mathbf{Q}, \mathbf{M}), \tag{6.1.6}$$

where $\beta > 0$ is a relaxation parameter.

The k-dimensional subspace $\mathcal{V}$ is constructed by solving the following constrained

optimization problem

$$\min_{\mathbf{v}_i \in \mathbb{R}^n} \quad \langle \mathbb{H}(\mathbf{Q}, \mathbf{M})\mathbf{v}_i, \mathbf{v}_i \rangle, \qquad \text{s.t.} \quad \langle \mathbf{v}_j, \mathbf{v}_i \rangle = \delta_{ij}, \quad j = 1, 2, \ldots, i. \tag{6.1.7}$$

Using the simultaneous Rayleigh-quotient iterative minimisation method [112] to solve (6.1.7), and noting that under the orthonormal constraint, $\mathcal{P}_{\mathcal{V}}$ is given by $\Sigma_{i=1}^{k} \mathbf{v}_i \mathbf{v}_i^\top$, we obtain a dynamical system of the HiOSD for finding an index-k saddle point,

$$\begin{cases} \beta^{-1}(\dot{\mathbf{Q}}, \dot{\mathbf{M}}) = -\left(\mathbf{I} - 2\sum_{j=1}^{k} \mathbf{v}_j \mathbf{v}_j^\top \right) \nabla F(\mathbf{Q}, \mathbf{M}), \\ \gamma^{-1} \dot{\mathbf{v}}_i = -\left(\mathbf{I} - \mathbf{v}_i \mathbf{v}_i^\top - 2\sum_{j=1}^{i-1} \mathbf{v}_j \mathbf{v}_j^\top \right) \mathbb{H}(\mathbf{Q}, \mathbf{M})\mathbf{v}_i, \ i = 1, \ldots, k, \end{cases} \tag{6.1.8}$$

where the state variable $(\mathbf{Q}, \mathbf{M})$ and k direction variables $\mathbf{v}_i$ are coupled, $\mathbf{I}$ is the identity operator and $\gamma > 0$ is a relaxation parameter.

We implement Algorithm 1 in [71], with the following choices to solve this dynamical system. We take our relaxation parameters $\beta = \gamma = \Delta t$, where Δt is our Euler time step size used to solve the gradient flow equations (6.1.2a)-(6.1.2d). Furthermore, we fix $l^0 = 10^{-6}$ and deem the method to have converged when $||\nabla F(\mathbf{Q}, \mathbf{M})||_{L^2} < 10^{-8}$. An input into this algorithm is a solution of the gradient flow equations (6.1.2a)-(6.1.2d), along with its orthonormal eigenvectors $\mathbf{v}_i$, where $i = 1, \ldots, n$ and $n \in \mathbf{N}$. To find the $\mathbf{v}_i$, we take n random orthonormal vectors as our initial condition and simultaneously iterate the dynamics for $\mathbf{v}_i$ in (6.1.8), as we solve the gradient flow equations. Our initial condition for the method is then a perturbation of the form $(\mathbf{Q}, \mathbf{M}) + \epsilon \mathbf{v}_i$, where we take $\epsilon \in (0, 1]$. In principle, any eigendirection $\mathbf{v}_i$ is possible, but it is typically sufficient to check the first few eigendirections (starting from the eigenvector with the smallest eigenvalue). To find an index-k saddle, we choose $k \in \mathbb{Z}^+$ (such that $k \leq n$) as our final input

to Algorithm 1 in [71]. An index-k saddle found using this initial condition is connected to the state $(\mathbf{Q}, \mathbf{M})$, or equivalently there is a pathway between them. Once an index-k saddle and its eigenvectors have been found, we can use this state to construct new initial conditions and repeat the process just outlined to find higher, or lower index saddles and deduce their connectivity.

6.2 Numerical results

Before discussing results, we introduce our nomenclature for labelling critical points. *Stable* indicates a critical point is stable and therefore index-0. $\pm$ indicates the Q_{12} profile is positive in the interior, whilst M_2 is negative in the interior. Similarly, $\mp$ means Q_{12} is negative in the interior, whilst M_2 is positive in the interior, and $+$ $(-)$ means both Q_{12} and M_2 are positive (negative) in the interior. For unstable saddle points with index greater or equal to 1, we use the following rules. F denotes that we have a full solution which exploits the full four degrees of freedom. Since full solutions come in pairs (remark 6.1.1), we follow F by a number to indicate the pair that we are referring to and finally another number to indicate which solution in the pair we are interested in. For example, $F1.2$ represents solution 2, of full solution pair 1. We denote the unique global minimising OR solution for large l, by OR. This solution branch persists as l decreases, so we continue to denote the solution on this branch by OR. We find more OR solutions as l decreases and to identify them we simply enumerate them as $OR1$, $OR2, \ldots$ etc.

6.2.1 Effects of varying l

We now begin by taking $c = 1$ and varying l, to see the impact l has on the connectivity of the solution landscape. We know that for l sufficiently large

($l > 1.25$ approximately when $c = 1$), we have a unique OR solution which is the global energy minimiser (see Figure 6.2), hence we consider small values of l only.

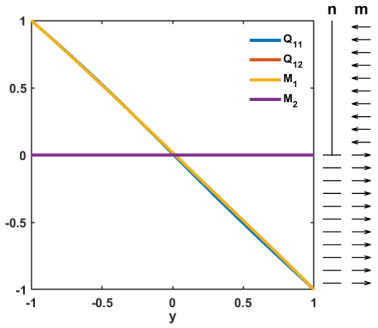

OR

Figure 6.2: The only critical point of (5.1.6) for $l = 10$ and $c = 1$.

$l = 1$ and $c = 1$

We begin with $l = 1$ and $c = 1$, where the solution landscape is simple. From the bifurcation diagram in Figure 5.10, we expect to have two stable solutions and at least one unstable OR solution. We do indeed find two stable solutions which exploit the full four degrees of freedom, and these are presented in Figure 6.3, along with their associated director profiles $\mathbf{n}$ (plotted as lines) and normalised magnetisation vectors $\mathbf{m} = \mathbf{M}/|\mathbf{M}|$ (we include this for all solutions). As expected

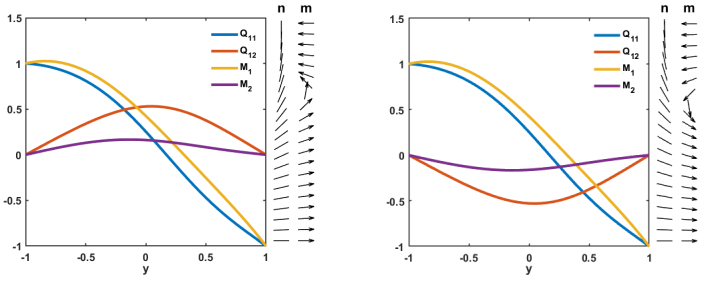

Stable+ *Stable−*

Figure 6.3: The stable critical points of (5.1.6) for $l = 1$ and $c = 1$.

from Remark 6.1.1 and the bifurcation diagram in Figure 5.10, we have a pair of minimisers for which the Q_{11} and M_1 profile are the same, whilst the Q_{12} and M_2 profiles have opposite signs. To be clear, in Figure 6.3, *Stable+* and *Stable−* have the same Q_{11} and M_1 profile, but the Q_{12} and M_2 profiles are reflections of one another in the y-axis. Letting θ denote the director angle for *Stable+*, and γ the director angle for *Stable−*, it follows that $\theta + \gamma = 0$ on Ω. Hence, the director is $\mathbf{n} = (n_1, n_2)$ for *Stable+*, and $\mathbf{n} = (n_1, -n_2)$ for *Stable−*. The $\mathbf{m}$ profiles for each solution vary in their sense of rotation too, since the M_2 profiles have opposite signs. This point is also true for all subsequent full solution pairs we present, we therefore do not comment on this again.

Regarding saddle points, we are only able to find one, an index-1 OR solution (presented in Figure 6.4). In fact, this solution is just the continuation of the unique *OR* state (i.e., it lies on the same solution branch). The absence of any saddle points with four degrees of freedom is consistent with the bifurcation diagram in Figure 5.10, whilst *OR* becoming unstable is consistent with our instability result for OR solutions (Theorem 5.3.4). The connectivity is therefore simple in this case, *Stable+* and *Stable−* are connected via the transition state *OR* only (see Figure 6.4). These parameter values highlight the importance of OR solutions in switching processes, as in this instance, transition pathways are mediated by an OR solution only.

$l = 0.2$ **and** $c = 1$

For $l = 1$ and $c = 1$ we find one OR solution which is a transition state. A natural question then, is what is the effect of the parameter l on the index and multiplicity of OR solutions? To partially answer this, we now take $l = 0.2$ and $c = 1$. We choose this value of l, as we only expect to see qualitatively different

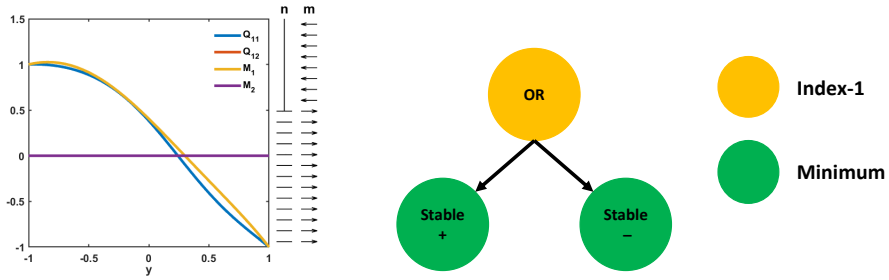

OR - index-1 saddle

Figure 6.4: The only unstable critical point of (5.1.6) for $l = 1$ and $c = 1$ (left) and the solution landscape (right).

features in the solution landscape for $l < 0.55$, or for $l \ll 0.2$. We know this from Figure 5.10 presented in the previous chapter. We keep $c = 1$ so we can make comparisons with the $l = 1$ case above.

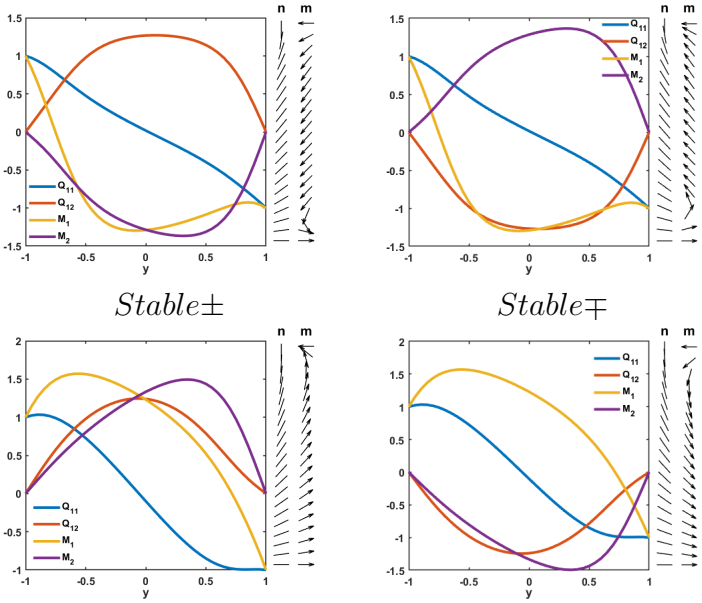

Stable± *Stable*∓

Stable+ *Stable*−

Figure 6.5: The stable critical points of (5.1.6) for $l = 0.2$ and $c = 1$.

When $l = 0.2$ and $c = 1$, the number of stable states of the ferronematic free energy (5.1.6) increases to four. We present these states in Figure 6.5. These four solutions come in two pairs, where once again, the Q_{11} and M_1 profile are the

same in each pair, whilst the Q_{12} and M_2 profiles are different, in that they have opposite signs. The two pairs are $(Stable+, Stable-)$ and $(Stable\pm, Stable\mp)$.

The number of unstable saddle points of the free energy (5.1.6), also increases for $l = 0.2$ and $c = 1$ when compared to the $l = 1$ case. We now have nine saddles and these are presented in Figure 6.6, along with their indices. As with the stable full solutions, we see that the unstable full solutions also come in pairs and the Morse index of both solutions in the pair is the same. Specifically, the pairs of this form are: $F1.1$ and $F1.2$ (both index-1), $F2.1$ and $F2.2$ (both index-1), and $F3.1$ and $F3.2$ (both index-2).

As well as these full solutions, we also observe three OR solutions, these are, OR and $OR1$, which are both index-1 saddles, and $OR2$ which is an index-2 saddle. OR is still the continuation of the unique OR solution branch for large l, while $OR1$ and $OR2$ are new critical points. We notice that all three OR solutions have one nematic and magnetic domain wall, which do not coincide. Therefore, the likely reason as to why $OR2$ has higher index, is because its magnetic domain wall occurs in the centre of the channel. This is consistent with Theorem 5.3.3 and its conclusions. Here we analyse the convergence of OR solutions in the limit $l \to 0$. We compute the transition costs between the points $\mathbf{p}^* = (\rho^*, \sqrt{1 + 2c\rho^*})$ and $\mathbf{p}^{**} = (\rho^*, \sqrt{1 + 2c\rho^*})$, and find that the energy minimiser (amongst OR solutions) is $\mathbf{p}^*$. While $\mathbf{p}^{**}$ has higher energy than $\mathbf{p}^*$, it still has lower energy than any solution with internal transition layers in M_1. Recall that, $(Q_{11}, M_1) = (\rho^*, \pm\sqrt{1 + 2c\rho^*})$ are the OR bulk energy density minimisers, where

$$\rho^* = \left(\frac{c}{8} + \sqrt{\frac{c^2}{64} - \frac{1}{27}\left(1 + \frac{c^2}{2}\right)^3}\right)^{\frac{1}{3}} + \left(\frac{c}{8} - \sqrt{\frac{c^2}{64} - \frac{1}{27}\left(1 + \frac{c^2}{2}\right)^3}\right)^{\frac{1}{3}}. \quad (6.2.1)$$

For $c = 1$, $\rho^* = 1.3008$ and $\sqrt{1 + 2c\rho^*} = 1.8978$. It follows that OR is approximately equal to $\mathbf{p}^*$ in the interior, $OR1$ is approximately equal to $\mathbf{p}^{**}$ in the interior, whilst $OR2$ jumps from $\mathbf{p}^*$ to $\mathbf{p}^{**}$, via a transition layer. So it is very likely that $OR2$ has higher index because it has an internal transition layer (and central magnetic domain wall) which is energetically expensive.

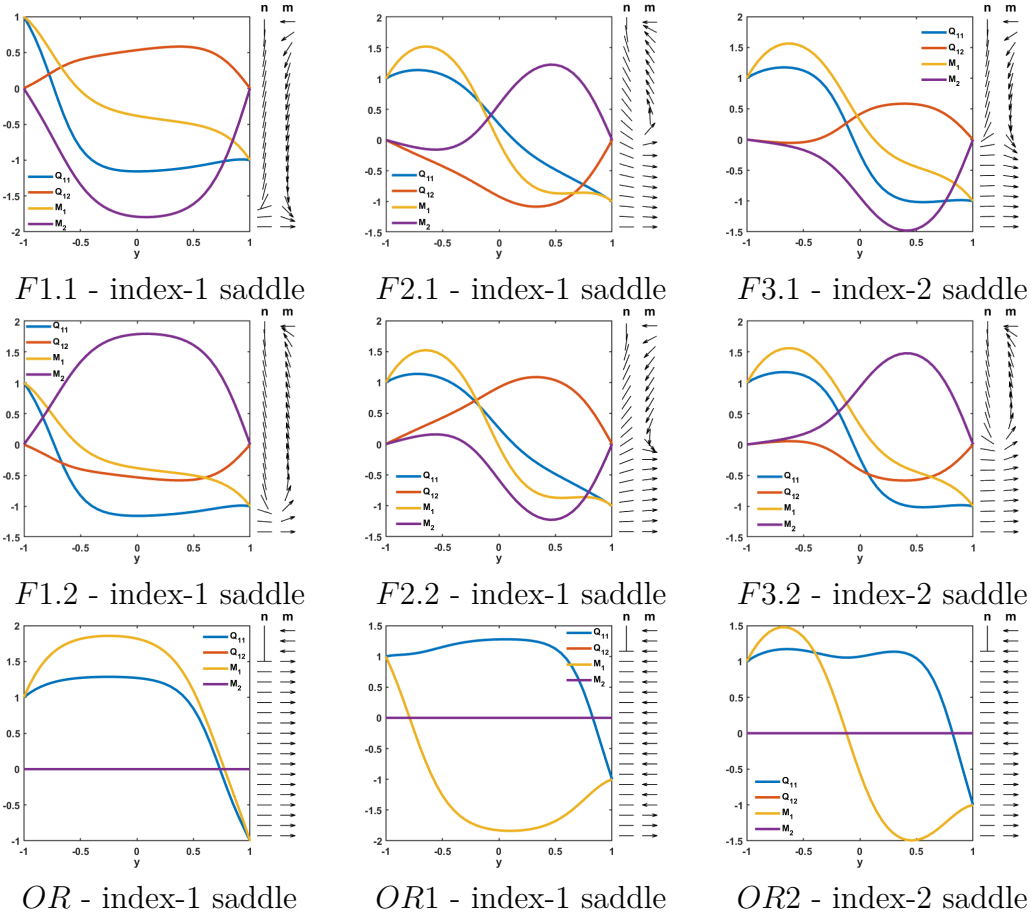

$F1.1$ - index-1 saddle $F2.1$ - index-1 saddle $F3.1$ - index-2 saddle

$F1.2$ - index-1 saddle $F2.2$ - index-1 saddle $F3.2$ - index-2 saddle

OR - index-1 saddle $OR1$ - index-1 saddle $OR2$ - index-2 saddle

Figure 6.6: Unstable saddle points of the energy (5.1.6) for $l = 0.2$ and $c = 1$.

In Figure 6.7, we report on the connectivity of the solution landscape, that is, how the four stable states in Figure 6.5, connect to the unstable saddle points in Figure 6.6. We only include arrows showing how an index-i state connects to any index-$i + 1$ state. That is not to say there do not exist pathways between index-i and index-$i + 2$ (or higher) states. We do not include arrows for these pathways

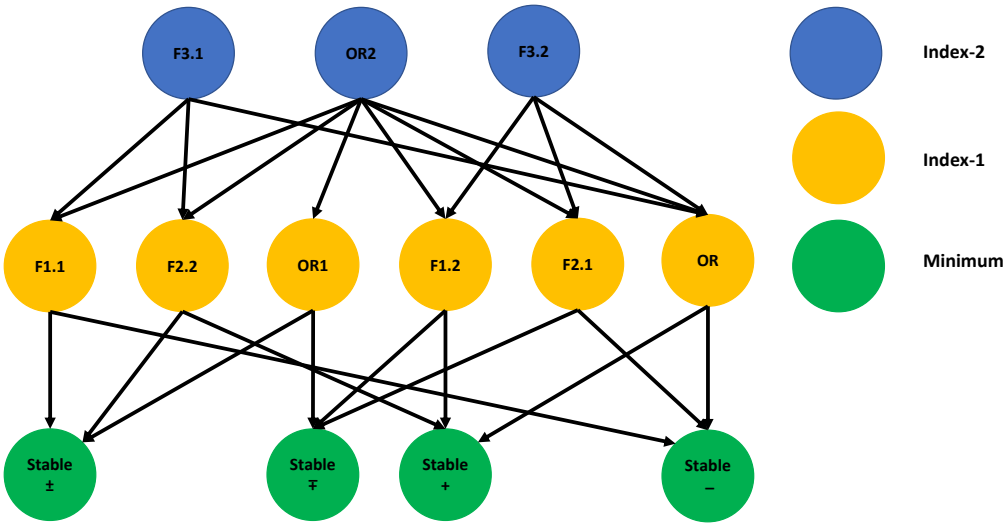

Figure 6.7: Solution landscape for $l = 0.2$ and $c = 1$.

since our diagrams become cluttered and difficult to interpret. These comments apply to all subsequent diagrams depicting solution landscapes.

Of particular interest, are the index-1 saddle points that connect stable states, because as mentioned previously, these are transition states which maybe physically observable in switching processes. Each of the stable states can be connected via one of the index-1 full solutions $F1.1$, $F1.2$, $F2.1$, $F2.2$. However, the OR solutions, OR and $OR1$, are also transition states which can connect $Stable\pm$ to $Stable\mp$, and $Stable+$ to $Stable-$, respectively. This is important, because it demonstrates that even though OR solutions are unstable critical points for small values of l, they may still play a role in switching processes. The importance of OR solutions does not end there though, since $OR2$ is the parent state (the state with highest index, which connects to all solutions with the next highest index, i.e., $OR2$ connects to all index-1 states in Figure 6.7). Since the OR state

is globally stable for large l and becomes unstable for small l, we always expect an OR solution to be the parent state and this is indeed what we observe here, and in Figure 6.4. We also find that we can connect any pair of the stable states via $OR2$. Physically realising the pathways to do this maybe difficult, but not impossible, so this is still a relevant and useful observation.

$l = 0.1$ **and** $c = 1$

We now take $l = 0.1$ and $c = 1$, to continue investigating how the index and multiplicity of OR solutions changes with l. In view of the results in the previous subsection, we also address this same question for full solutions.

Through the use of Newton's method and the HiOSD method, we find a total of thirty-nine critical points, these are: four stable full solutions, fifteen pairs of unstable full solutions (thirty total), and five unstable OR solutions. Due to the large number of critical points, we only present one solution from each pair of unstable full solutions (since the other solution is the same up to a reflection of Q_{12} and M_2 (see Remark 6.1.1)), as well as the OR solutions. We do not present the stable solutions, since they are visually very similar to those shown in Figure 6.5 when $l = 0.2$.

In Figure 6.8, we present the saddle points which are full solutions. We now have full solutions with index-1, 2, 3, 4 and 5, and the index-5 states $F12.1$ and $F12.2$, are the highest index states we have been able to identify. Some of these states are continuations of those we found in Figure 6.6 (i.e., the pairs $F1$, $F2$ and $F3$), for this smaller value of l. As such, their index has not changed and there are only minor changes in appearance since $|\mathbf{Q}|$ tends closer to ρ^*, and $|\mathbf{M}|$ to $\sqrt{1 + 2c\rho^*}$. Looking at the full solutions, it appears as though a higher index is associated with more distorted Q_{11} and M_1 profiles, that is, profiles with internal transition

layers and more of them.

On the other hand, in Figure 6.9, we display the five OR saddle points. We only report two new OR solutions, these are $OR3$, which is index-2, and $OR4$. The three remaining OR solutions are continuations of those found for $l = 0.2$, as such, their index is the same and visually they are very similar with the difference being, Q_{11} tends closer to ρ^*, and M_1 to $\pm\sqrt{1+2c\rho^*}$. Based on our discussion above on what affects the index of OR solutions, we believe $OR4$ must be index-2 or greater, since it has two internal transition layers in M_1.

We now give a partially complete picture of the solution landscape for $l = 0.1$ and $c = 1$. We know the picture is incomplete, because through the use of Newton's method we find the critical points $F5.1$, $F5.2$, $F8.1$, $F8.2$, $F13.1$, $F13.2$ and $OR4$, however, we are unable to find these solutions using the HiOSD method. As such, we are unable to identify their index and how they fit into the solution landscape. It maybe the case that some, or all of these critical points, lie on disconnected solution branches far away from any other solutions.

In Figure 6.10, we present what we have learned about the solution landscape for $l = 0.1$ and $c = 1$. When it comes to the index-1 transition states, the connections to the stable states for the existing critical points OR, $OR1$, $F1.1$, $F1.2$, $F2.1$, and $F2.2$, are unchanged. So again, we can connect $Stable\pm$ to $Stable\mp$ via $OR1$, and $Stable+$ to $Stable-$ via OR. There are two new index-1 states, $F15.1$ and $F15.2$, which connect $Stable\pm$ to $Stable+$, and $Stable\mp$ to $Stable-$, respectively.

Moving on, we have five new index-2 states, the pairs $F4$ and $F14$, and $OR3$. As a consequence, there are a large number of connections from index-2 states to index-1 states. Previously, $OR2$ was the parent state when $l = 0.2$. Since we now have higher index states for $l = 0.1$, this is no longer true, and as such it does

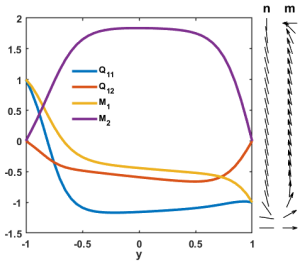

$F1.2$ - index-1 saddle

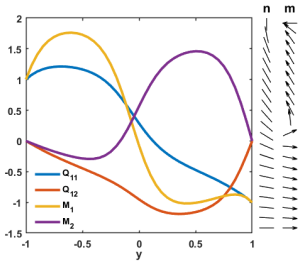

$F2.1$ - index-1 saddle

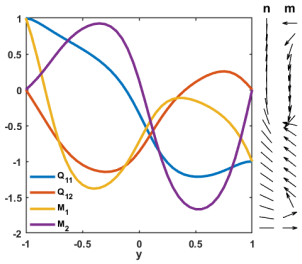

$F15.2$ - index-1 saddle

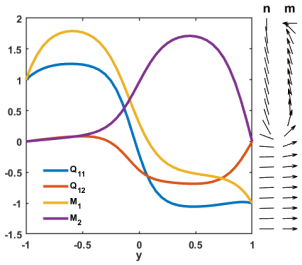

$F3.2$ - index-2 saddle

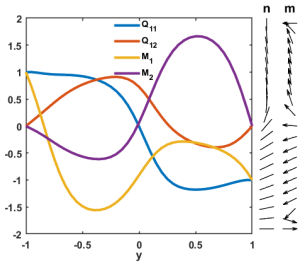

$F4.2$ - index-2 saddle

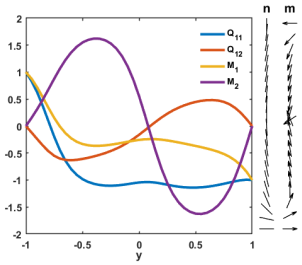

$F14.2$ - index-2 saddle

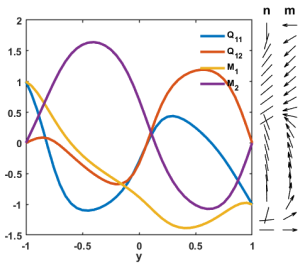

$F6.2$ - index-3 saddle

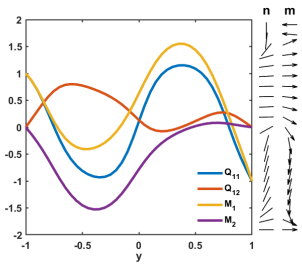

$F7.1$ - index-3 saddle

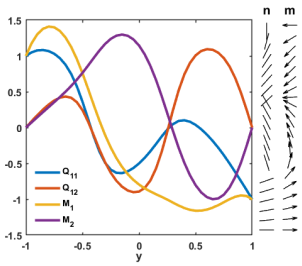

$F10.1$ - index-4 saddle

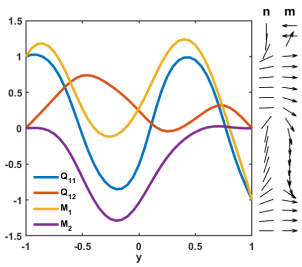

$F11.1$ - index-4 saddle

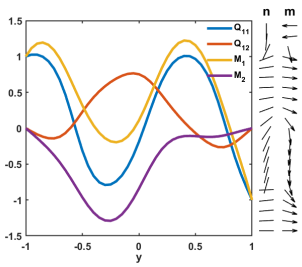

$F9.1$ - index-4 saddle

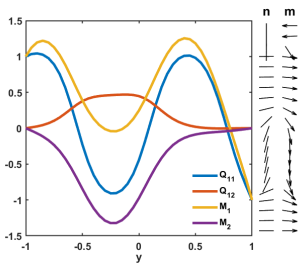

$F12.2$ - index-5 saddle

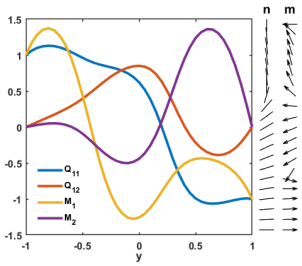

$F8.1$ - index unknown

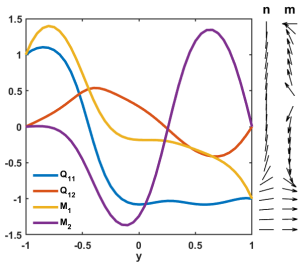

$F5.1$ - index unknown

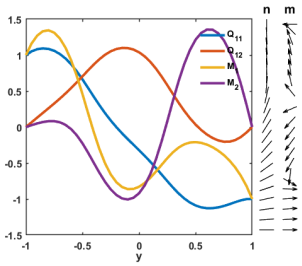

$F13.1$ - index unknown

Figure 6.8: Unstable saddle points of the energy (5.1.6) for $l = 0.1$ and $c = 1$.

not connect to all index-1 states (only the pair $F2$, OR and $OR1$). $OR3$ is a new index-2 state, which connects the two new index-1 states, $F15.1$ and $F15.2$. Like $OR2$, it also connects the two index-1 OR solutions, OR and $OR1$. $F1.1$ and $F1.2$, are the only index-1 states that do not connect to an index-2 OR solution. This highlights the prevalence of pathways mediated by OR solutions and hence there importance to switching mechanisms.

Moving further up the solution landscape, we have four index-3 states (the pairs $F6$ and $F7$), six index-4 states (the pairs $F9$, $F10$, $F11$), and finally, two index-5 states (the pair $F12$). These are all previously unidentified critical points. We do not comment much on the solution landscape at this point, as it is clear the picture is incomplete. We have only one connection from each of the index-4 states to index-3 states, which is unlikely, suggesting we are missing index-3 saddles. We also could not find connections from $F10.1$ and $F10.2$, to an index-5 state. It is clear from this that we have not found the parent state. It is likely one of the seven critical points whose index we could not identify, is the missing parent state.

Observations and conjectures

We now speculate on the index of the critical points we missed above, these are, $F5.1$, $F5.2$, $F8.1$, $F8.2$, $F13.1$, $F13.2$ and $OR4$. Given the lack of index-3 solutions, we believe that (at least) two of these full solution pairs are likely index-3 saddles, and the other pair maybe index-4. As for $OR4$, we speculate that it must be index-5 or greater, making it the missing parent state. In Figure 6.4 and Figure 6.7, the parent state was an OR solution and we expect the same to be true here. In fact, we believe $OR4$ is index-5, so that as in Figure 6.7, we have three solutions with the highest index, a pair of full solutions that connect

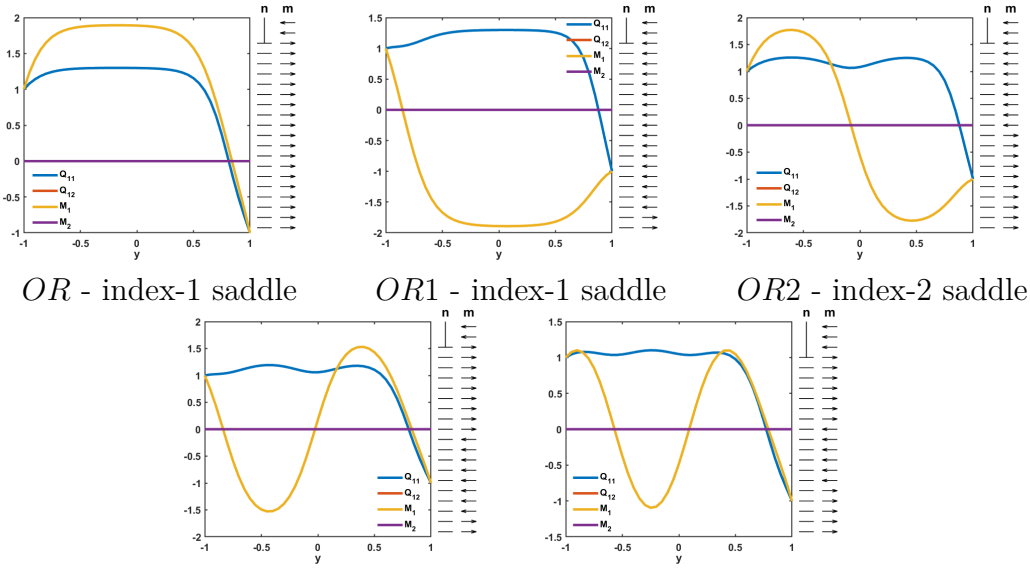

OR - index-1 saddle $OR1$ - index-1 saddle $OR2$ - index-2 saddle

$OR3$ - index-2 saddle $OR4$ - index unknown

Figure 6.9: Unstable OR saddle points of the energy (5.1.6) for $l = 0.1$ and $c = 1$.

to some, but not all of the saddles with index one less, along with an OR solution that is the parent state.

Remark 6.2.1. We now present potential rules for describing the number of critical points, and the index of the parent states at bifurcation points. These rules are just **conjectures** since we have an insufficient number of results to fully support the claims.

We see the total number of critical points increase from $1 \to 3 \to 13 \to 39$, as we decrease l (for $c = 1$ fixed) from $10 \to 1 \to 0.2 \to 0.1$. This can be further broken down into how the number of OR and full solutions change. For OR solutions, the multiplicity goes from $1 \to 1 \to 3 \to 5$ as l decreases from $10 \to 1 \to 0.2 \to 0.1$. Once the state OR became unstable, we see two new OR solutions with each bifurcation. As for full solutions, the multiplicity increases from $0 \to 2 \to 10 \to 34$, as l decreases from $10 \to 1 \to 0.2 \to 0.1$. With this in mind, a **possible** rule for predicting the number of full solutions, is as follows:

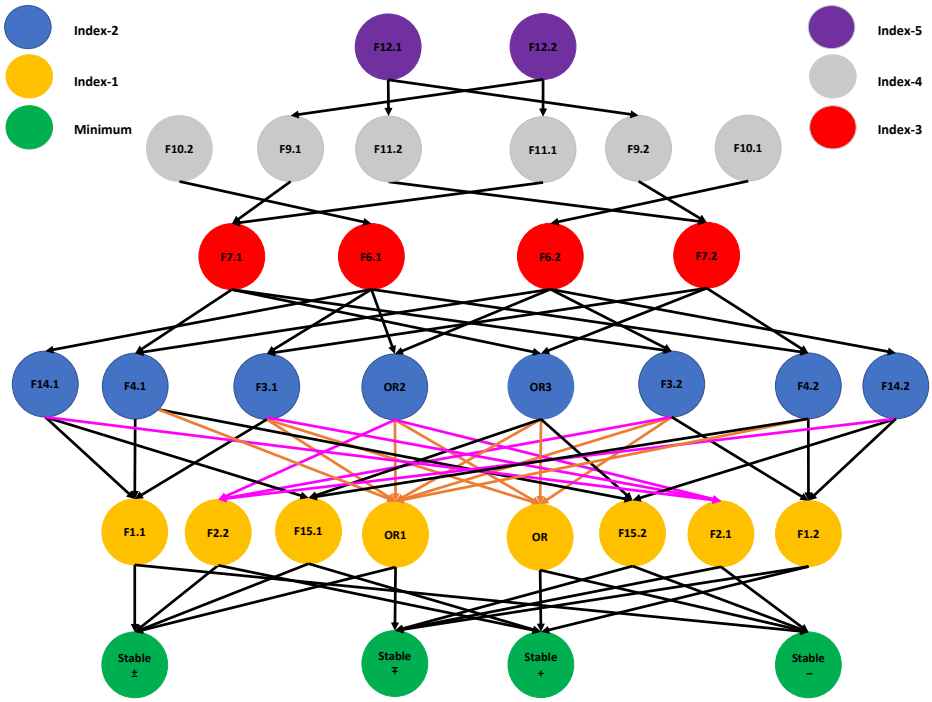

Figure 6.10: Solution landscape for $l = 0.1$ and $c = 1$. We draw the connections from index-2 states to OR and $OR1$ in orange, to make them easier to see and for no other reason. The same comments apply to $F2.1$ and $F2.2$, where we use pink arrows instead.

once full solutions emerge, take the previous number of full solutions, multiply this by 3, and then add 4, to get the number at the next bifurcation point. Using this predicts 106 full solutions at the next bifurcation point. From $l = 0.2 \to 0.1$, the total number of critical points triples, so perhaps if we decrease l enough so that another set of bifurcations occur, the number may triple again to 117. Combining this with our guess of 106 full solutions by this point, means we might expect to have 11 OR solutions to make up this number. What is certain, is that the number of critical points will increase substantially for an $l < 0.1$, such that more bifurcations occur. Therefore, even a partial understanding of the solution

landscape will be difficult to obtain. For this reason we do not decrease l any further.

As well as the number of critical points changing, we also see the index of critical points change. As l decreases (for $c = 1$ fixed) from $10 \to 1 \to 0.2 \to 0.1$, the highest index state increases from $0 \to 1 \to 2 \to 5$. The parent state for $l = 1$ and $l = 0.2$ is an OR solution, and we speculate this is also the case when $l = 0.1$, with $OR4$ in Figure 6.9 being the parent state. After the first bifurcation point ($l \approx 1.25$), the index of the parent state only changes when a bifurcation occurs resulting in the emergence of new solutions, since the index of existing solutions do not change as we decrease l. Assuming $OR4$ is index-5, we suggest that the index of the parent state **may** evolve via the following formula after each bifurcation point:

$$\text{index} = 3j - 1, \text{ for } j = 1, 2, 3, \ldots, \tag{6.2.2}$$

where j is the index of the parent state before the most recent set of bifurcations. For the value of $l < 0.1$ at which the next set of bifurcations occur, we therefore predict the parent state to be index-14, and that it is an OR solution.

To conclude this section, we combine our solution landscapes to create a bifurcation diagram. This can be found in Figure 6.11 (note, we speculate on the index of the pairs $F5$, $F8$ and $F13$, as well as $OR4$). Based on the stability exchange and number of solutions, we can conclude the first bifurcation away from the unique OR solution must be a pitchfork bifurcation (we have one stable solution before the bifurcation, but two stable and one unstable after). Since the stability/index of $Stable+$, $Stable-$ and OR, do not change as l decreases, and in view of the number of critical points, we believe all subsequent solutions emerge via saddle node bifurcations. Moreover, we believe these saddle node bifurcations are

disconnected (indicated by dashed lines connecting solution pairs in Figure 6.11) as in Figure 5.10. For the saddle node bifurcations, we have grouped the solutions together based on the similarity of the Q_{11}, Q_{12}, M_1 and M_2 profiles. For $l = 0.1$, we indicate the full solution pairs that are connected via a saddle node bifurcation, rather than the solutions within each pair, in the interest of space.

6.2.2 Effects of varying c

In Chapter 5, we prove that increasing c decreases the window of stability of OR solutions. That is, the value $l^*(c)$, such that OR is the unique global minimiser for $l > l^*(c)$, is an increasing function of c. As such, increasing c effectively shifts the bifurcation diagram in Figure 5.10, by some amount to the right along the l-axis. Therefore, we hypothesise that solution landscapes with the same qualitative features as those shown in Section 6.2.1, exist for a fixed l and different c. To test this, we begin by fixing $l = 1$ and vary c.

$l = 1$ and $c < 1$

We start by considering $c < 1$, for which we always find two full solutions and no unique OR solution. For $c = 0$, $l \geq 1.316$ is needed to achieve a unique OR solution. Hence, this is an approximate lower bound on the value of $l = \frac{K}{|A|D^2}$ required to achieve a unique OR solution (and unique global minimiser of (5.1.6)), for any value of c. With $K = 10^{-11}$ and $A = -848.5\text{Nm}^{-2}$ [68], this tells us the maximum channel width for which we can observe a unique OR solution is 1.89×10^{-7}m.

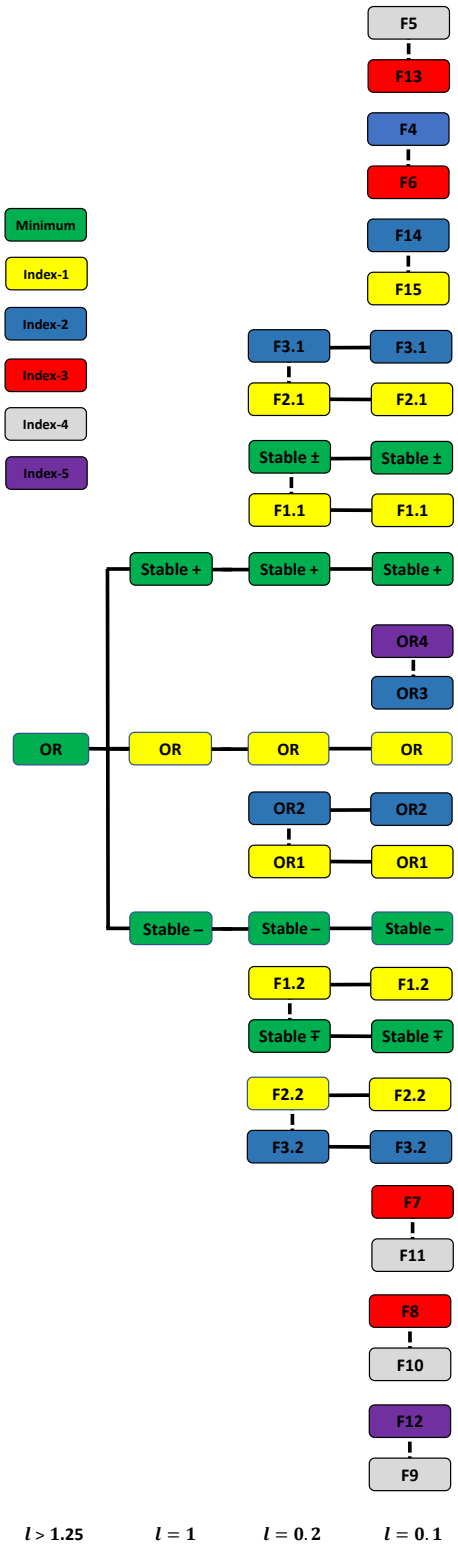

Figure 6.11: Bifurcation diagram for $c = 1$.

$l = 1$ and $c = 3$

We take $c = 3$ to see whether the number of critical points and/or the solution landscape changes. We find four stable critical points, instead of two, as recorded for $l = c = 1$. These can once again be identified as *Stable*$\pm$, *Stable*$\mp$, *Stable*$+$ and *Stable*$-$. The only notable difference here is that $|\mathbf{Q}|$ and $|\mathbf{M}|$ have increased in the interior, which is consistent with the maximum principle and the asymptotic analysis of ρ^* for large c, performed in Chapter 5 (i.e., ρ^* is an increasing function of c). This means the $\mathbf{n}$ and $\mathbf{m}$ plots are almost identical to those in Figure 6.5, with only some minor changes in orientation. As such, we do not present these solutions.

Looking at the unstable saddle points, we now have nine of them, as opposed to one when $l = c = 1$, and they are shown in Figure 6.12. We identify these saddles with the same nomenclature as those in Figure 6.6. Moreover, the saddles in Figure 6.12 are continuations of those in Figure 6.6, since there are clear similarities in appearance. Any differences are due to the larger value of c, which causes $|\mathbf{Q}|$ and $|\mathbf{M}|$ to increase in the interior. The $\mathbf{n}$ and $\mathbf{m}$ plots are almost identical between Figure 6.6 and Figure 6.12 for the full solutions, and for the OR solutions, we spot that the domain walls have moved either up or down slightly. It is unsurprising then that the solution landscape is qualitatively the same to that shown in Figure 6.7. By this, we mean for $l = 1$ and $c = 3$, we have the same number of stable, unstable, full and OR critical points, with the same features, index and connections to one another, as for $l = 0.2$ and $c = 1$ (henceforth this is what mean by a solution landscape being qualitatively the same). Therefore, applying the nomenclature in Figure 6.12, to Figure 6.7, gives the solution landscape for $l = 1$ and $c = 3$. We do not increase c further to see

if we can repeat the solution landscape for $l = 0.1$ and $c = 1$, with $l = 1$. This is because of the significant difficulty incurred in deriving Figure 6.10, which we can expect to encounter again here.

Our results for $l = 1$ and $c = 3$, lead us to believe that the hypothesis at the start of this section is true. For $l = c = 1$ and for $l = 1$ and $c = 3$, we have different solution landscapes, with the latter being equivalent to the solution landscape for $l = 0.2$ and $c = 1$. This demonstrates that increasing c decreases the effective value of l.

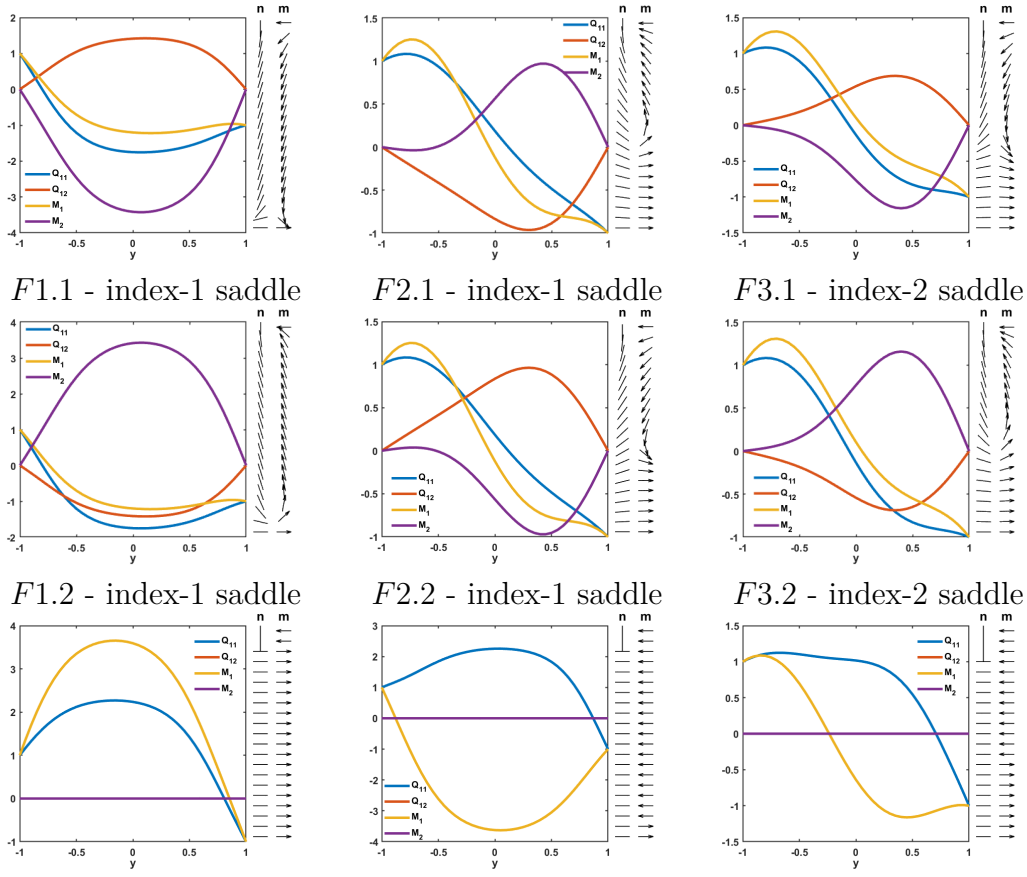

$F1.1$ - index-1 saddle $F2.1$ - index-1 saddle $F3.1$ - index-2 saddle

$F1.2$ - index-1 saddle $F2.2$ - index-1 saddle $F3.2$ - index-2 saddle

OR - index-1 saddle $OR1$ - index-1 saddle $OR2$ - index-2 saddle

Figure 6.12: Unstable saddle points of the energy (5.1.6) for $l = 1$ and $c = 3$.

$c = 5$ for different values of l

So far in this section we have varied c for a fixed l. To conclude this section, we now investigate the solution landscape when $c = 5$, for different values of l. We do this, because in the bifurcation diagram in Figure 5.13, we observe interesting folds where solution branches overlap one another. It seems reasonable then, that we might have different solution landscapes for this, and other large values of c, to what we have seen so far.

For $l > 4.56$, we observe a unique OR solution which we label as OR, and this solution persists for smaller values of l. We then decrease $l = 4.5$ and we immediately observe a new solution landscape. For this value of l, a bifurcation has occurred as we now have three OR solutions (see Figure 6.13), however, no full solutions have emerged. Previously, we have seen a bifurcation away from the unique OR solution by the emergence of a pair of full solutions (see $l = c = 1$ case), and not due to the emergence of new OR solutions. This is interesting, as this means we have identified a parameter regime where we have multiple solutions, all of which are OR solutions. We have two stable OR solutions, OR and $OR1$, which can be connected by, and therefore switched between, via the index-1 state $OR2$ (see Figure 6.14). Regarding the appearance of the OR solutions in Figure 6.13, they essentially vary in the location of nematic and magnetic domain walls, as well as the maximum value of Q_{11} and M_1.

We now decrease l further to $l = 4.45$, which is accompanied by another bifurcation. We now find two new stable states which are a pair of full solutions (see Figure 6.15), and these are the only new solutions which emerge. The three OR solutions reported in Figure 6.13 still exist for $l = 4.45$, moreover, the plots look identical by eye to those in Figure 6.13, so we do not include them. It is worth

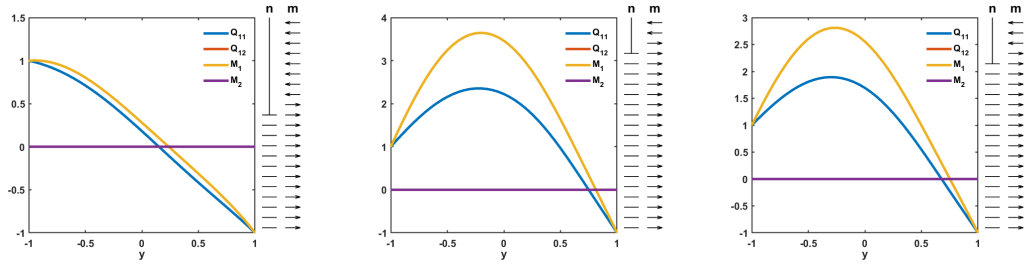

OR - stable $OR1$ - stable $OR2$ - index-1 saddle

Figure 6.13: Critical points of the energy (5.1.6) for $l = 4.5$ and $c = 5$.

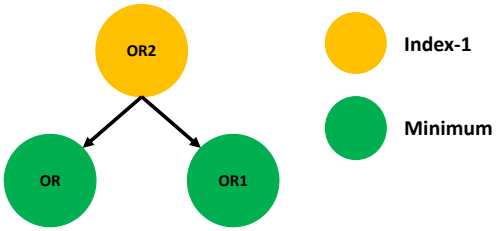

Figure 6.14: Solution landscape for $l = 4.5$ and $c = 5$.

noting that $Stable+$ and $Stable-$ are both close to being an OR solution, since Q_{12} and M_2 are small in the interior, whilst Q_{11} and M_1 are indistinguishable by eye to the same profiles for $OR1$ in Figure 6.13. This is also reflected in the **n** and **m** profiles, which are approximately polydomains. The associated solution landscape is shown in Figure 6.16, where we find OR remains stable, $OR2$ remains index-1, and $OR1$ becomes index-1 too. This is interesting, as we have demonstrated we can have co-stability between OR and full solutions, something not observed in our studies with small l and c. We also find $OR2$ to be the parent state. Hence, we can switch between a stable OR solution and stable full solutions, via an OR transition state, making OR solutions doubly important here, as they can be stable and dictate the dynamics/selection of stable states.

For $l = 4.4$ and $c = 5$, we are unable to compute the full solution landscape.

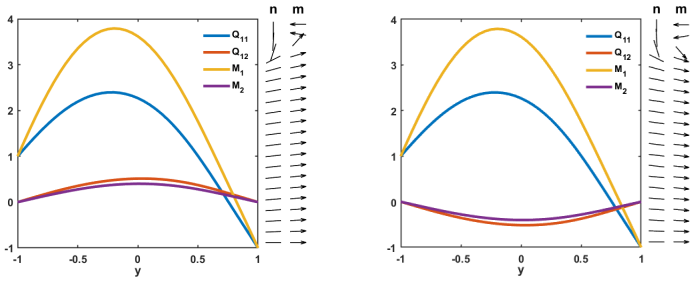

Figure 6.15: The stable critical points of (5.1.6) for $l = 4.45$ and $c = 5$.

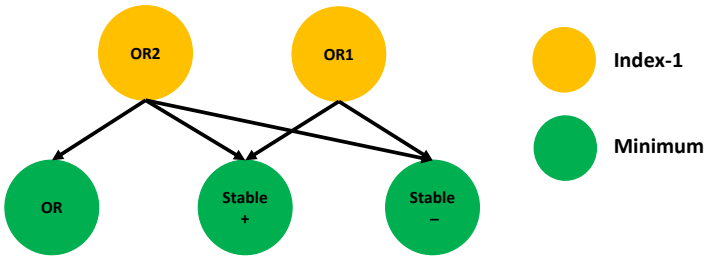

Figure 6.16: Solution landscape for $l = 4.45$ and $c = 5$.

The reason for this, is that we are likely too close to the bifurcation point. At a bifurcation point, one or multiple eigenvalues will move from being positive to negative, hence, the closer we are to this point, the closer these eigenvalues will be to zero and this brings about ill-posedness of $\mathbb{H}$. This ill-posedness means we cannot find the states $F2.1$ and $F2.2$ (see Figure 6.18) using the HiOSD method, which in turn means we cannot identify their index or connections to other critical points. We know these critical points exist, as we can find them using Newton's method. As such, we do not comment in depth on the solution landscape, but do make some quick comments. We now have five stable states, the four familiar stable full solutions (see Figure 6.17), and OR which remains stable (not presented). So we again have co-stability between OR and full solutions. We

find eight other critical points, six of which are new solutions and these are shown in Figure 6.18. The states $OR1$ and $OR2$ persist, and remain index-1 saddles, and as such are not presented.

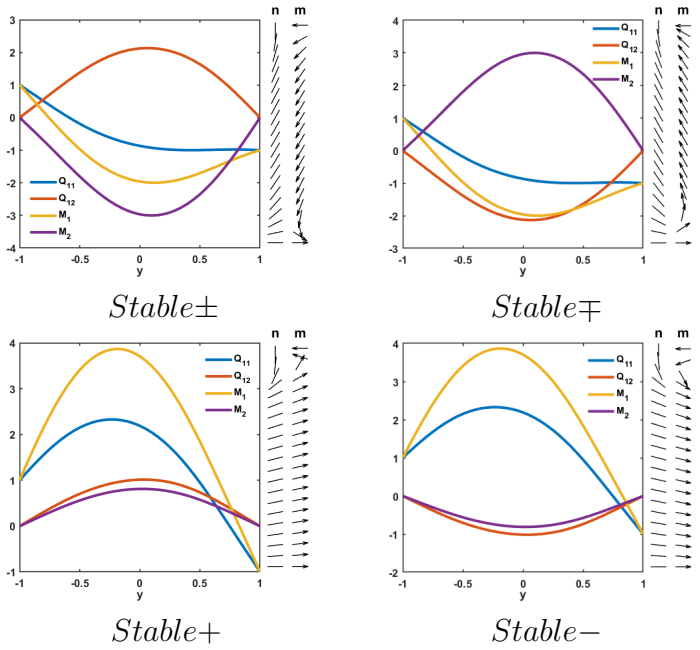

Figure 6.17: The stable critical points of (5.1.6) for $l = 4.4$ and $c = 5$.

Next, we take $l = 4$ and $c = 5$. This value of l is sufficiently far away from any bifurcation points so that we can report a complete solution landscape in Figure 6.19. We see that the solution branches for the full solution pairs $F2$ and $F3$, cease to exist and are replaced by two new OR solutions, $OR3$ (index-1) and $OR4$ (index-2 and the new parent state), which emerge for $l \approx 4.35$. All other solutions persist from $l = 4.4$ and their stability/index is unchanged. We have five OR solutions for these parameter values, making them almost as prevalent as full solutions (there are six), making this another set of parameter values for which OR could likely be observed physically. These OR solutions are presented in Figure 6.20 and we see $OR1$, $OR3$ and $OR4$, are reminiscent of the OR solutions in Figure 6.12. We quickly point out that the stable state OR, can be connected

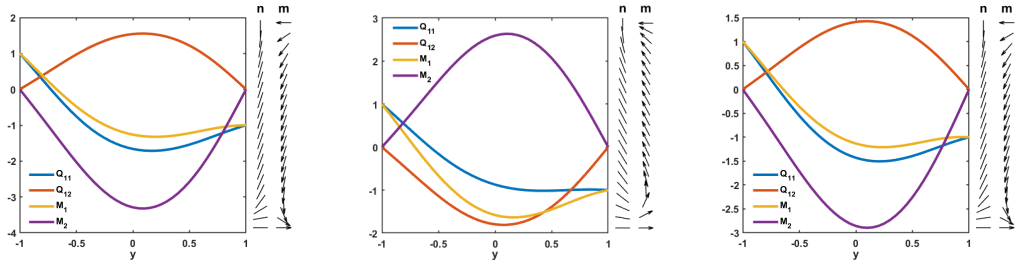

$F1.1$ - index-1 saddle $F2.1$ - index unknown $F3.1$ - index-2 saddle

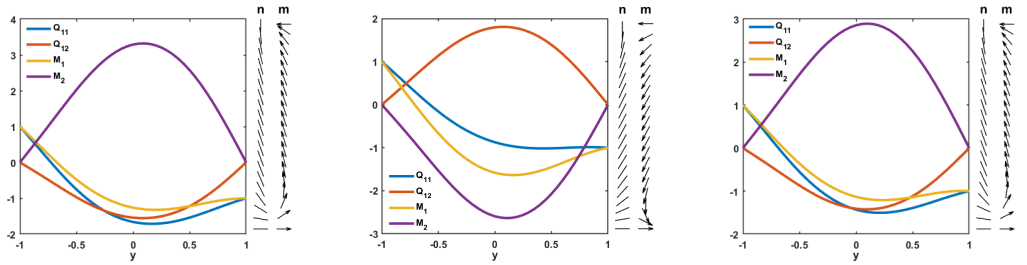

$F1.2$ - index-1 saddle $F2.2$ - index unknown $F3.2$ - index-2 saddle

Figure 6.18: Unstable saddle points of the energy (5.1.6) for $l = 4.4$ and $c = 5$.

to the stable states $Stable\mp$ and $Stable+$ via the OR transition states $OR3$ and $OR2$, respectively.

We conclude this study with $c = 5$ by taking $l = 3$. At this point, the solution branches for OR and $OR2$, cease to exists (they do not exist for $l > 3.6$ approximately). This leaves us with five saddles, the index-1 pair $F1$, $OR1$ and $OR3$ which are both index-1, and the index-2 parent state, $OR4$. Regarding stable solutions, we once again find $Stable\pm$, $Stable\mp$, $Stable+$ and $Stable-$, to be the only ones. All solutions are similar to those seen previously, and are consequently omitted. The solution landscape is presented in Figure 6.21, where the key point is the reduction in OR solutions and hence their importance to the solution landscape. In particular, we no longer have co-stability between OR solutions and full solutions, highlighting that sufficiently large l and c are required for this phenomena to occur.

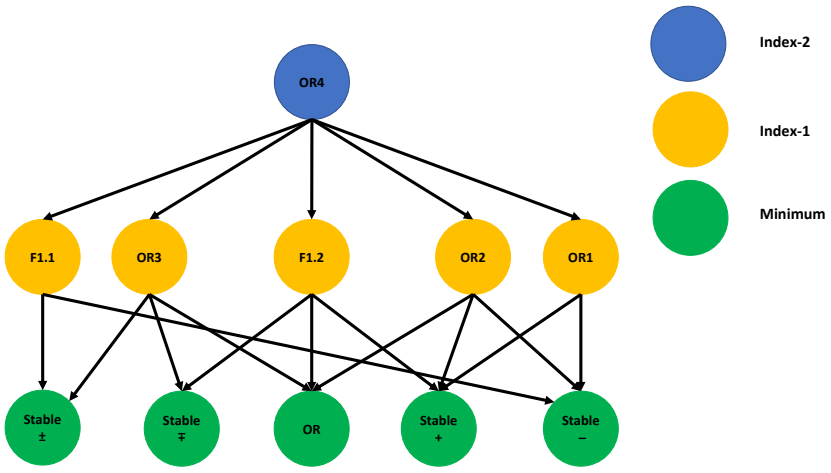

Figure 6.19: Solution landscape for $l = 4$ and $c = 5$.

Observations and conjectures

In Chapter 5, we showed that we could tailor the location of nematic and magnetic domain walls by varying l. For large l, the domain walls coincide at the centre of the channel, then as l decreases, the single nematic domain wall migrates to the top of the channel i.e., $y = 1$, meanwhile the magnetic domain walls are free to move about and could occur at either end of the channel, or in the interior if we have a transition layer.

The example with $c = 5$ shows we can also tailor the location of domain walls through c. For small c ($c \leq 1$) and large l ($l \geq 1.3$) we find one unique OR solution, however, for large c and large l, we can find multiple OR solutions. For these new OR solutions, since l is large, they need not converge to the OR bulk energy minimisers and M_1 can remain positive in the interior as a result. This means, both nematic and magnetic domain walls will occur towards the top of the channel. This suggests, as c increase (so that the maximum principle bounds increase) for a fixed sufficiently large l, both nematic and magnetic domain walls

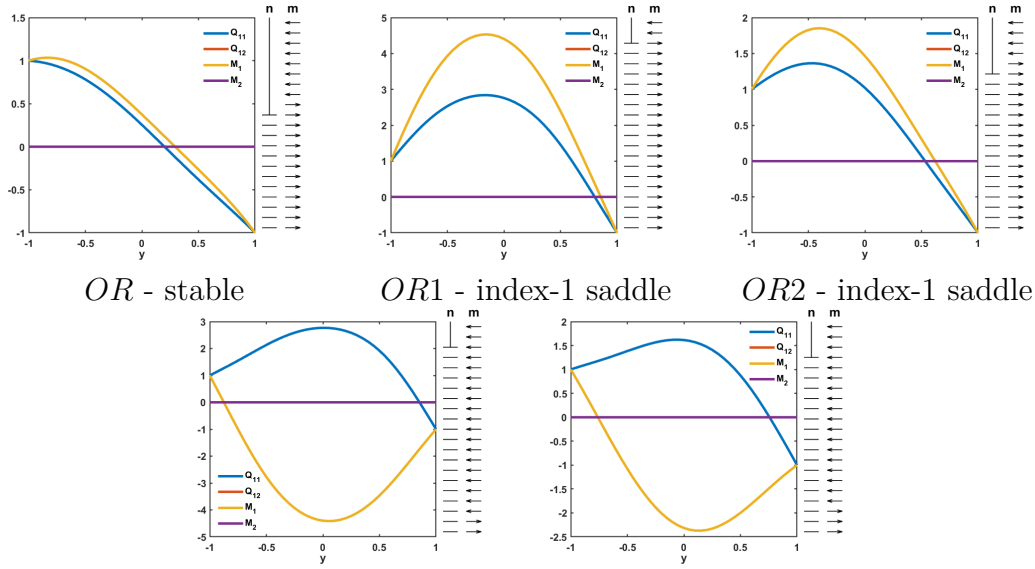

OR - stable $OR1$ - index-1 saddle $OR2$ - index-1 saddle

$OR3$ - index-1 saddle $OR4$ - index-2 saddle

Figure 6.20: OR critical points of the energy (5.1.6) for $l = 4$ and $c = 5$.

move towards the top of the channel at $y = 1$. We can see a numerical illustration of this in Figure 6.13. Looking at $OR1$ and $OR2$, we see $OR1$ has a larger maximum value for both Q_{11} and M_1 than $OR2$ (which is comparable to the affect of increasing c) and its domain walls are closer to the top of the channel.

We conclude this section with a bifurcation diagram for $c = 5$, which can be found in Figure 6.22. Based on the stability exchange and number of critical points, we deduce the first bifurcation is a disconnected saddle node bifurcation amongst OR solutions, resulting in the emergence of $OR1$ and $OR2$. This is then followed by a pitchfork bifurcation of the $OR1$ solution branch, resulting in the emergence of the $Stable+$ and $Stable-$ solutions. We deduce this from the fact $OR1$ loses stability, and that the Q_{11} and M_1 profiles for $Stable+$ and $Stable-$, match the same profiles for $OR1$. Again, looking at the stability and number of critical points, we deduce all subsequent bifurcations are saddle node bifurcations. One pitchfork bifurcation leading to the emergence of $Stable+$ and $Stable-$, and all

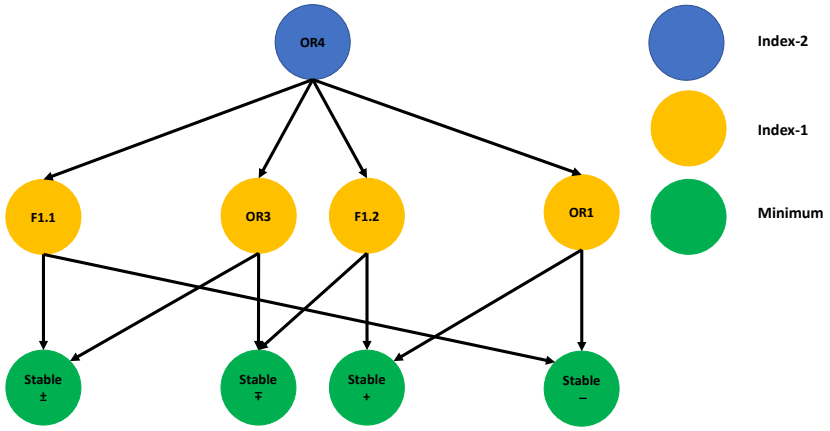

Figure 6.21: Solution landscape for $l = 3$ and $c = 5$.

other bifurcations being saddle node bifurcations, is identical to what we saw in Figure 6.11. We believe all saddle node bifurcations are disconnected here too.

6.2.3 Effects of negative c

In the previous chapter, and thus far in the current chapter, we have considered positive $c > 0$. Positive c encourages the director $\mathbf{n}$ and the magnetisation vector $\mathbf{M}$, to be parallel or anti-parallel to each other, $c = 0$ means the nematic and magnetic parts of our model are decoupled and evolve independently of one another, and finally, negative c encourages $\mathbf{n}$ and $\mathbf{M}$ to be mutually perpendicular. Here, we study negative c and to draw comparisons with the case of positive c, we take $c = -1$ and $l = 0.2$.

Starting with the stable solutions, we again find four of them which are shown in Figure 6.23. In fact, we can make a clear correspondence between the stable solutions in Figure 6.23 and Figure 6.5. We see that reflecting Q_{11} and M_1 in Figure 6.23 in the horizontal-axis of the plot, and then reflecting the result in the

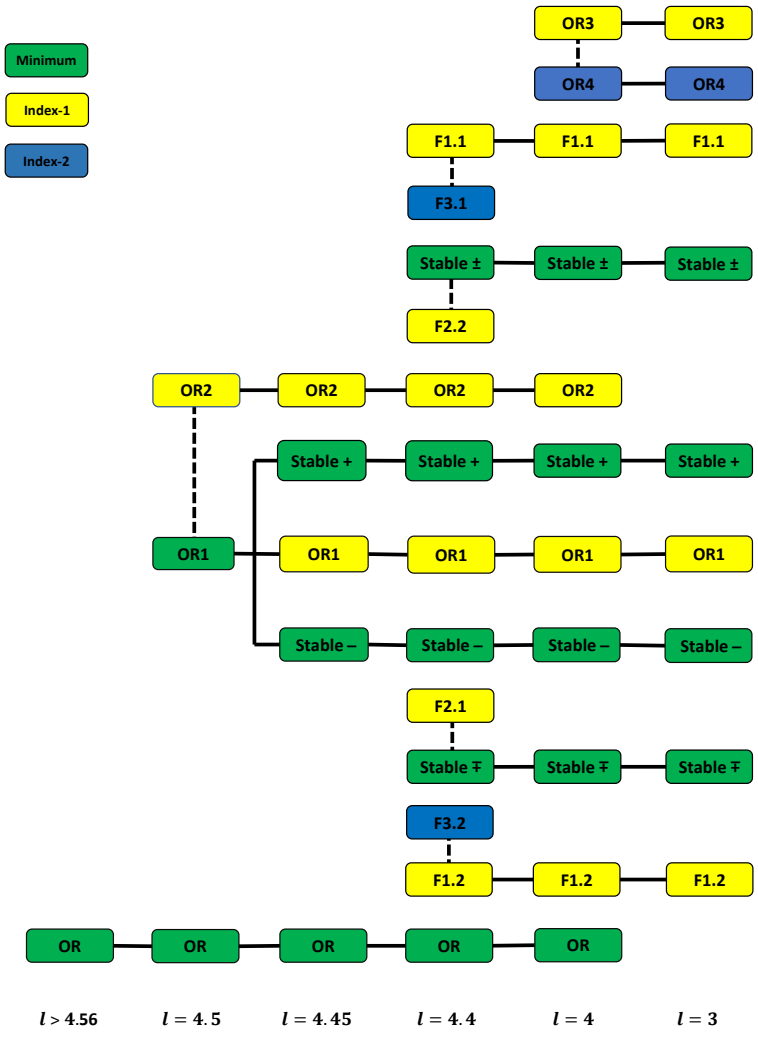

Figure 6.22: Bifurcation diagram for $c = 5$.

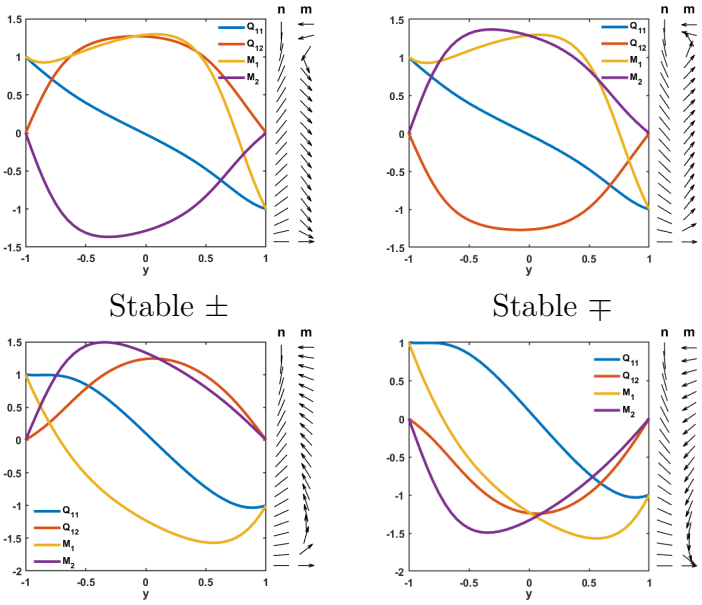

Figure 6.23: The stable critical points of (5.1.6) for $l = 0.2$ and $c = -1$.

vertical-axis of the plot, gives the Q_{11} and M_1 profiles in Figure 6.5. Whilst for Q_{12} and M_2 in Figure 6.23, reflecting these profiles in the vertical-axis of the plot gives the Q_{12} and M_2 profiles in Figure 6.5. This means $\mathbf{n} = (-\cos(\theta(-y)), \sin(\theta(-y)))$ and $\mathbf{m} = (-M_1(-y), M_2(-y))/||\mathbf{M}(-y)||$ for $l = 0.2$ and $c = -1$, where $\theta(y)$ and $M_1(y)$, $M_2(y)$ are the director angle and components of $\mathbf{M}$ respectively, for $l = 0.2$ and $c = 1$.

In Figure 6.24, we show the unstable saddle points when $l = 0.2$ and $c = -1$, along with their index. As in the case of $l = 0.2$ and $c = 1$, we find nine saddle points, three OR solutions and six full solutions. Moreover, the connections we made between the stable solutions for the positive and negative c cases in the previous paragraph, also hold true for the saddle points. As such, we can identify them with the same nomenclature as used in Figure 6.6. There is clearly a connection between all solutions for positive and negative c, which we now make precise.

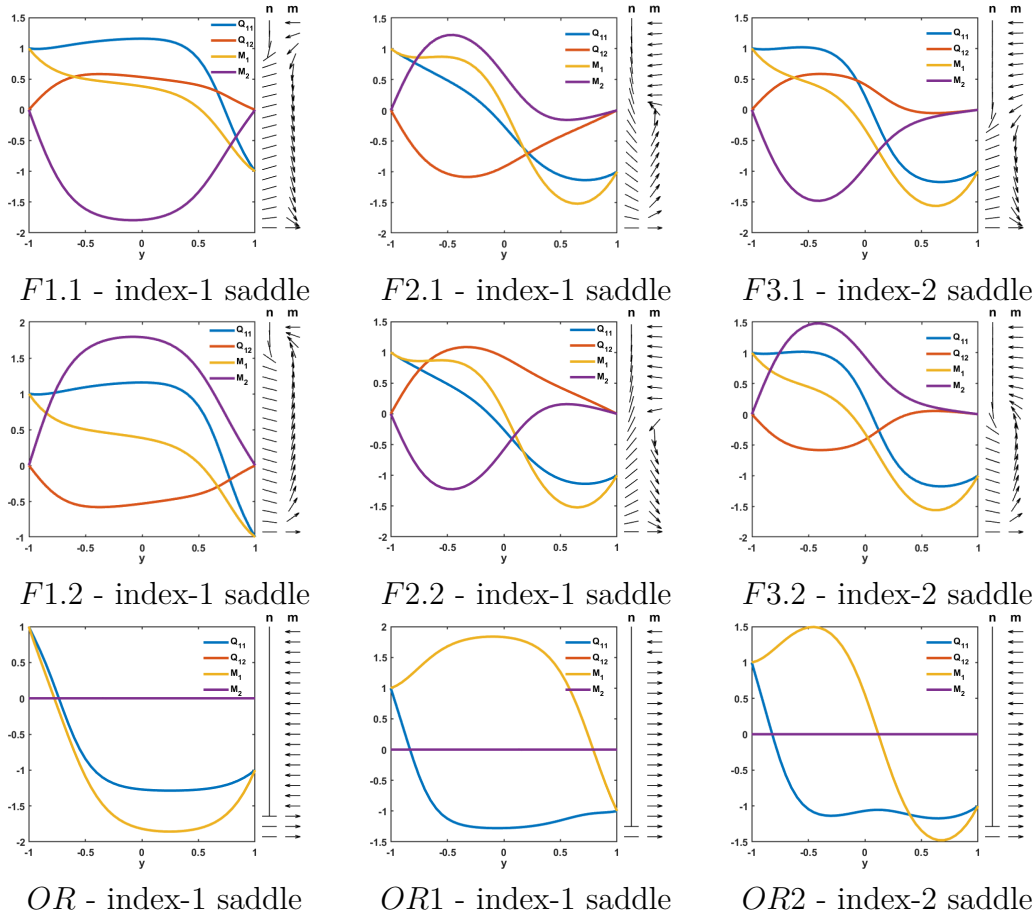

$F1.1$ - index-1 saddle $F2.1$ - index-1 saddle $F3.1$ - index-2 saddle

$F1.2$ - index-1 saddle $F2.2$ - index-1 saddle $F3.2$ - index-2 saddle

OR - index-1 saddle $OR1$ - index-1 saddle $OR2$ - index-2 saddle

Figure 6.24: Unstable saddle points of the energy (5.1.6) for $l = 0.2$ and $c = -1$.

Lemma 6.2.2. *If* $(\tilde{Q}_{11}, \tilde{Q}_{12}, \tilde{M}_1, \tilde{M}_2)(y)$ *is the solution to the Euler-Lagrange equations* (5.1.9a)-(5.1.9d)*, subject to the boundary conditions* (5.1.7)*, for* $c > 0$*, then* $(-\tilde{Q}_{11}, \tilde{Q}_{12}, -\tilde{M}_1, \tilde{M}_2)(-y)$ *is the corresponding solution to* (5.1.9a)-(5.1.9d)*, subject to the boundary conditions* (5.1.7)*, for* $-c < 0$*.*

Proof. Evaluating at $y = \pm 1$, we see the proposed solution for negative c satisfies the boundary conditions,

$$(-\tilde{Q}_{11}, \tilde{Q}_{12}, -\tilde{M}_1, \tilde{M}_2)(-(1)) = (1, 0, 1, 0), \tag{6.2.3}$$

$$(-\tilde{Q}_{11}, \tilde{Q}_{12}, -\tilde{M}_1, \tilde{M}_2)(-(-1)) = (-1, 0, -1, 0). \tag{6.2.4}$$

It therefore remains to see if it satisfies the Euler-Lagrange equations. To see this is a solution for $c < 0$, let $(\tilde{Q}_{11}, \tilde{Q}_{12}, \tilde{M}_1, \tilde{M}_2)$ be the solution for $\tilde{c} > 0$ and now take $c := -\tilde{c}$. The system (5.1.9) then becomes

$$l\frac{\mathrm{d}^2 Q_{11}}{\mathrm{d}y^2} = 4Q_{11}(Q_{11}^2 + Q_{12}^2 - 1) + \tilde{c}\left(M_1^2 - M_2^2\right), \tag{6.2.5a}$$

$$l\frac{\mathrm{d}^2 Q_{12}}{\mathrm{d}y^2} = 4Q_{12}(Q_{11}^2 + Q_{12}^2 - 1) + 2\tilde{c}M_1M_2, \tag{6.2.5b}$$

$$l\frac{\mathrm{d}^2 M_1}{\mathrm{d}y^2} = M_1\left(M_1^2 + M_2^2 - 1\right) + 2\tilde{c}Q_{11}M_1 + 2\tilde{c}Q_{12}M_2, \tag{6.2.5c}$$

$$l\frac{\mathrm{d}^2 M_2}{\mathrm{d}y^2} = M_2\left(M_1^2 + M_2^2 - 1\right) - 2\tilde{c}Q_{11}M_2 + 2\tilde{c}Q_{12}M_1. \tag{6.2.5d}$$

Now take $(Q_{11}, Q_{12}, M_1, M_2) = (-\tilde{Q}_{11}, \tilde{Q}_{12}, -\tilde{M}_1, \tilde{M}_2)(-y)$ as defined above. Substituting this anzats into (6.2.5a), we have

$$l\frac{\mathrm{d}^2(-\tilde{Q}_{11})}{\mathrm{d}y^2}(-y) = \left(4(-\tilde{Q}_{11})((-\tilde{Q}_{11})^2 + \tilde{Q}_{12}^2 - 1) + \tilde{c}\left((-\tilde{M}_1)^2 - \tilde{M}_2^2\right)\right)(-y),$$

which is the original equation satisfied by $(\tilde{Q}_{11}, \tilde{Q}_{12}, \tilde{M}_1, \tilde{M}_2)$ for $\tilde{c} > 0$. The fact that we have $-y$ is not an issue, because $(\tilde{Q}_{11}, \tilde{Q}_{12}, \tilde{M}_1, \tilde{M}_2)$ satisfies the Euler-Lagrange equations for all $y \in [-1, 1]$.

Under our ansatz, (6.2.5b) becomes

$$l\frac{\mathrm{d}^2\tilde{Q}_{12}}{\mathrm{d}y^2}(-y) = \left(4\tilde{Q}_{12}((-\tilde{Q}_{11})^2 + \tilde{Q}_{12}^2 - 1) + 2\tilde{c}(-\tilde{M}_1)\tilde{M}_2\right)(-y),$$

which is again the original equation satisfied by $(\tilde{Q}_{11}, \tilde{Q}_{12}, \tilde{M}_1, \tilde{M}_2)$ when $\tilde{c} > 0$. For the same reasons as before, the $-y$ is not an issue. Repeating identical steps for the remaining two equations, we see $(-\tilde{Q}_{11}, \tilde{Q}_{12}, -\tilde{M}_1, \tilde{M}_2)(-y)$ is the corresponding solution when $c := -\tilde{c} < 0$. □

It is perhaps unsurprising then, that when we map the solution landscape for $l = 0.2$ and $c = -1$, we find it to be qualitatively the same to that when $l = 0.2$

and $c = 1$. We therefore refer the reader to Figure 6.6 once again and the subsequent discussion.

Observations and conjectures

In view of Lemma 6.2.2, and the fact that the solution landscape for $l = 0.2$ and $c = \pm 1$ are the same (in terms of the number of stable, unstable, full and OR critical points, their profiles (up to reflections), and their connections), we believe that the for any given l and c, the solution landscape for l and $-c$, will be the same. A quick check with $l > 1.25$ and $c = -1$ yields a unique OR solution, whilst for $l = 1$ and $c = -1$, we recover the solution landscape in Figure 6.4, giving further support to this claim. Hence, we can refer back to our extensive study on the effects of l and c in Section 6.2.1 and Section 6.2.2, respectively. Differences between the positive and negative c case, should only manifest in the appearance of the actual solutions, and we describe these differences above.

6.3 Summary

In this chapter, we perform an extensive exploration of the solution landscape of one-dimensional ferronematics for different values of l and c, through the implementation of the HiOSD algorithm. This enables us to identify the index of unstable solutions to the Euler-Lagrange equations (5.1.9), and track how critical points are connected to one another for specific choices of l and c, all of which could be useful information for the creation of switchable ferronematic devices. It also yields new information when compared to the numerical results in Chapter 5, and in some situations enables us to find previously unidentified OR critical points.

Our results show that *fixing c and decreasing l*, has the same effect on the solution

landscape as *fixing l and increasing c*, in that both result in more bifurcations and new emergent solutions. Surprisingly, in some cases we find repeating solution landscapes for different values of l and c. For instance, we observe the solution landscape in Figure 6.7 for three choices of (l, c), namely $(0.2, 1)$, $(1, 3)$ and $(0.2, -1)$. As such, we believe there are regions in the (l, c) parameter space where the solution landscapes will be qualitatively the same (i.e., they will have the same number of stable critical points, unstable saddles of a given type and index, along with the same connections between them).

From our results, we also conclude that as l decreases (for c fixed), or c increases (for l fixed), the index of the parent state increases. A heuristic reason as to why we see this behaviour is because, as l decreases, both full and OR solutions tend to the bounds given by the maximum principle. This increases the range of values a solution can take (e.g., when $l = c = 1$ in Figure 6.4, $\min_{\Omega}\{Q_{11}, M_1\} \approx -1$ and $\max_{\Omega}\{Q_{11}, M_1\} \approx 1$, but when $l = 0.1$ and $c = 1$ in Figure 6.9, $\min_{\Omega}\{Q_{11}, M_1\} \approx -1.9$ and $\max_{\Omega}\{Q_{11}, M_1\} \approx 1.9$, amongst all OR solutions) and hence, provides greater freedom in how the solution profile can behave in the interior. This freedom allows new critical points to emerge and in particular, critical points with higher indices, which generally seem to be associated with more local maxima and minima in the components of $\mathbf{Q}$ and $\mathbf{M}$. Similar comments apply to increasing c, where the bounds given by the maximum principle increase, which again gives greater freedom in how a solution can behave. This maybe why we observe multiple solutions for large values of l, when $c = 5$.

In all of our case studies, OR solutions are important to the solution landscape. We either find, or believe, that an OR solution is the parent state for all the solution landscapes considered in this chapter. For those where an OR solution is

the parent state, we find these states can mediate pathways between any of the stable states. Parent states, or states with index greater than one, are perhaps less relevant as it is index-1 saddles that are typically observed in switching processes [109]. However, in certain parameter regimes, these high-index states maybe energetically preferred to lower index-states (as we shall see in Chapter 7). We also find OR solutions to be transition states between the $Stable\pm$ and $Stable\mp$ states, and between the $Stable+$ and $Stable-$ states (see Figures 6.7, 6.10, 6.19, and 6.21). For $c = 5$, we even find co-stability between OR solutions and full solutions, so that OR solutions are both a selectable state and states that dictate selection dynamics. Perhaps our best discovery is for $c = 5$ and $l = 4.5$, where we find two stable OR solutions, which are connected via an index-1 OR solution, and these are the only critical points. This is a useful and unexpected find, as it illustrates there are parameter regimes for which we can have multistable systems dictated by OR solutions only. Further work would be to identify more parameter values where this occurs. In general, OR solutions and pathways mediated by them are prevalent in all the solution landscapes we investigate. The significance of this is that OR solutions and the polydomain structures they represent, should be potentially observable in experiments.

Finally, we look at negative c, which we do not consider in Chapter 5. We find the negative c case is entirely equivalent to the positive c case, up to some reflections of the solution profiles. This is useful information, which almost certainly means the results proven in Chapter 5 are true for negative c after some minor modifications.

We could extend our study in places by looking at more extreme values of l and c. For instance, $l = 0.01$ and $c = 1$, $l = 1$ and $c = 5$, as well as $c > 5$ for various l. However, these cases would likely produce unfriendly and difficult to

interpret solution landscapes, due to either the number of critical points (we see an illustration of this when $l = 0.1$ and $c = 1$), or because of rapid changes in behaviour close to bifurcation points (e.g. when $c = 5$). Furthermore, these cases are examples of extreme values of l and c, and therefore represent less physically meaningful situations. Recall $l = \frac{K}{|A|D^2}$, K being a nematic elasticity constant, A a material and temperature dependent constant, and D is half the physical channel width. From [68], some typical values are $K = 10^{-11}$N, $A = -848.5\text{Nm}^{-2}$ and $2D = 8 \times 10^{-5}$m, which give $l = 7.37 \times 10^{-6}$. Whilst physically realistic, a thorough or useful study of the solution landscape for this value of l, would be difficult. K is always typically of the order 10^{-11}N [65], whilst A can vary for different liquid crystals, and D can certainly vary depending on the size of the geometry, hence l can be tailored. With channels of width $2D = 6 \times 10^{-7}$m, 2×10^{-7}m and 10^{-7}m (and K, A as just given), we find $l = 0.131$, 1.18, and 4.71 respectively, which are close to the values studied in this chapter. These are certainly small, but not unreasonable channel widths since channels on the micron-scale are common. Typical values for the coupling constant c, cannot currently be computed from the literature (to the best of our knowledge), all we can say here is that small values of c represent weak coupling and large values strong coupling. As such, we believe this a sufficient study that illuminates the solutions landscapes of this ferronematic problem, complementing the work in Chapter 5 nicely.

Chapter 7

Uniaxial vs biaxial pathways for one-dimensional cholesteric liquid crystals

This chapter is derived in part from Han, Dalby, Majumdar, Carter and Machon (2022) [3].

7.1 The problem

Cholesterics exhibit a huge variety of metastable states along with complex defect structures (see Section 1.3.2), making them intriguing materials for the creation of soft devices. In an attempt to understand some of this complexity, in this chapter, we perform asymptotic and numerical analysis of the solution landscape for one-dimensional cholesteric liquid crystals in the Landau-de Gennes (LdG) framework. We begin by introducing the relevant free energy, dimensionless parameters, governing equations, and homogeneous Dirichlet boundary conditions

considered. We then conduct asymptotic analysis in various physically relevant limits giving us analytic approximations which yield preliminary insight into the types of behaviour we can expect in different parameter regimes (i.e., uniaxiality or biaxiality). These asymptotic expressions also serve as excellent initial conditions for our numerical scheme.

We then compute the solution landscape for our model cholesteric problem by implementing the high-index optimisation-based shrinking dimmer (HiOSD) method described in Chapter 6. Pathways between different stable states in cholesterics have previously been studied [113, 114]. However, they have been restricted to numerical methods only capable of identifying index-1 critical points, as well as the Oseen-Frank framework which cannot capture biaxiality. The novelty of our work, is its ability to capture greater complexity in the solution landscape where, most importantly, we find an interesting competition between uniaxiality and biaxiality in mediating pathways between different stable states. In particular, our numerical results suggest parameter regimes where biaxiality maybe experimentally observable. We supplement this by also considering conflicting, or inhomogeneous boundary conditions, to demonstrate the generic nature of our conclusions.

7.1.1 Theoretical framework

We study a cholesteric sample confined to a cell of height H, so that our domain is given by $\Omega = \{(x, y, z) \in \mathbb{R}^3 |\ 0 \leq z \leq H\} \subset \mathbb{R}^3$. In order to make this problem tractable, we assume translational symmetry in the x and y directions. The LdG free energy for cholesteric liquid crystals is then given by [115, 116]

$$F(\mathbf{Q}) = \int_0^H \frac{L_2}{4}(\nabla \cdot \mathbf{Q})^2 + \frac{L_4}{4}|\nabla \times \mathbf{Q} + 2q_0\mathbf{Q}|^2 + f_b(\mathbf{Q})\ \mathrm{d}z, \tag{7.1.1}$$

where the bulk energy density is given by

$$f_b(\mathbf{Q}) = \frac{A}{2}\mathrm{tr}\mathbf{Q}^2 - \frac{B}{3}\mathrm{tr}\mathbf{Q}^3 + \frac{C}{4}(\mathrm{tr}\mathbf{Q}^2)^2. \tag{7.1.2}$$

Here L_2 and L_4 are the splay/bend and twist elastic constants respectively. The variable A is a material and temperature dependent constant, while B and $C > 0$ are material dependent constants. We work with low temperatures for which $A < 0$ and the nematic phase is preferred. Finally, $q_0 = 2\pi/p_0$ where p_0 is the pitch of the cholesteric helix i.e., the distance over which a 2π rotation of the director is completed. We note that $q_0 = 0$ for an achiral nematic, since the pitch is effectively infinite in this case. In this chapter, we retain the full five degrees of freedom of the $\mathbf{Q}$-tensor order parameter so that we can capture uniaxiality and biaxiality. Recall, that the full LdG $\mathbf{Q}$-tensor is a symmetric traceless 3×3 matrix, i.e., $\mathbf{Q} \in S_0 := \{\mathbf{Q} \in \mathbb{M}^{3\times 3} : Q_{ij} = Q_{ji}, Q_{ii} = 0\}$, so that $\mathbf{Q}$ is given by

$$\mathbf{Q} = \begin{pmatrix} q_1 & q_2 & q_3 \\ q_2 & q_4 & q_5 \\ q_3 & q_5 & -q_1 - q_4 \end{pmatrix}. \tag{7.1.3}$$

We nondimensionalise the system using the rescaling $z = \bar{z}H$, and multiplying (7.1.1) by the quantity $\frac{H}{L_2}$, we find the dimensionless energy is

$$\bar{F}(\mathbf{Q}) := \frac{HF(\mathbf{Q})}{L_2} = \int_0^1 \left\{ \frac{1}{4}(\nabla \cdot \mathbf{Q})^2 + \frac{\eta}{4}\left|\nabla \times \mathbf{Q} + 2\sigma\mathbf{Q}\right|^2 + \lambda \frac{f_b(\mathbf{Q})}{C} \right\} \mathrm{d}\bar{z}. \tag{7.1.4}$$

Here, $\eta = L_2/L_4$ is the ratio of the twist and splay/bend elastic constants and quantifies the elastic anisotropy (the one-constant approximation corresponds to $\eta = 1$); $\sigma/2\pi = q_0 H/2\pi = H/p_0$ is the number of 2π rotations of the director, in the domain, in the $\bar{z}$-direction ($\sigma = 0$ represents a nematic state); and $\lambda = \frac{H^2 C}{L_2}$ is a measure of domain length. In what follows, we drop bars and assume all

quantities are dimensionless, unless stated otherwise.

Recall, $|\,.\,|$ is the matrix norm, so that

$$|\mathbf{Q}| = \sqrt{\mathrm{tr}\mathbf{Q}^2} = \sqrt{Q_{ij}Q_{ij}}, \tag{7.1.5}$$

and using the Einstein summation convention we have, $(\nabla \cdot \mathbf{Q})_i = \partial_\alpha Q_{i\alpha}$ and $(\nabla \times \mathbf{Q})_{i\beta} = \epsilon_{i,j,k}\partial_j Q_{k\beta}$, where $\epsilon_{i,j,k}$ is the Levi-Civita symbol. In this one-dimensional setting, where quantities depend on z only, the functional (7.1.4) reduces to

$$\begin{aligned} F(q_1, q_2, q_3, q_4, q_5) = \int_0^1 \frac{1}{4}\Bigg[&\left(\frac{\mathrm{d}q_1}{\mathrm{d}z}\right)^2 + \left(\frac{\mathrm{d}q_3}{\mathrm{d}z}\right)^2 + \left(\frac{\mathrm{d}q_4}{\mathrm{d}z}\right)^2 + \left(\frac{\mathrm{d}q_5}{\mathrm{d}z}\right)^2 + 2\frac{\mathrm{d}q_1}{\mathrm{d}z}\frac{\mathrm{d}q_4}{\mathrm{d}z}\Bigg] \\ &+\frac{\eta}{4}\Bigg[\left(8\sigma^2 q_1^2 - 4\sigma q_1\frac{\mathrm{d}q_2}{\mathrm{d}z} + \left(\frac{\mathrm{d}q_2}{\mathrm{d}z}\right)^2\right) + \left(8\sigma^2 q_2^2 - 4\sigma q_2\frac{\mathrm{d}q_4}{\mathrm{d}z} + \left(\frac{\mathrm{d}q_4}{\mathrm{d}z}\right)^2\right) \\ &+ \left(8\sigma^2 q_3^2 - 4\sigma q_3\frac{\mathrm{d}q_5}{\mathrm{d}z} + \left(\frac{\mathrm{d}q_5}{\mathrm{d}z}\right)^2\right) + \left(4\sigma q_2\frac{\mathrm{d}q_1}{\mathrm{d}z} + \left(\frac{\mathrm{d}q_1}{\mathrm{d}z}\right)^2\right) \\ &+ \left(8\sigma^2 q_4^2 + 4\sigma q_4\frac{\mathrm{d}q_2}{\mathrm{d}z} + \left(\frac{\mathrm{d}q_2}{\mathrm{d}z}\right)^2\right) + \left(8\sigma^2 q_5^2 + 4\sigma q_5\frac{\mathrm{d}q_3}{\mathrm{d}z} + \left(\frac{\mathrm{d}q_3}{\mathrm{d}z}\right)^2\right) \\ &+ 8\sigma^2 q_1 q_4\Bigg] + \lambda\frac{f_b(\mathbf{Q})}{C}\,\mathrm{d}z. \end{aligned} \tag{7.1.6}$$

We now compute $f_b(\mathbf{Q})$ in terms of the components of $\mathbf{Q}$. In summation notation

$$f_b(\mathbf{Q}) = \frac{A}{2}\underbrace{Q_{ij}Q_{ji}}_{(1)} - \frac{B}{3}\underbrace{Q_{ik}Q_{kj}Q_{ji}}_{(2)} + \frac{C}{4}\underbrace{(Q_{ij}Q_{ji})^2}_{(3)}.$$

Direct calculations show that

$$\begin{aligned} (1) &= 2(q_1^2 + q_2^2 + q_3^2 + q_4^2 + q_5^2 + q_1 q_4) = |\mathbf{Q}|^2 \\ (2) &= 3(2q_2 q_3 q_5 + q_2^2 q_4 + q_2^2 q_1 - q_3^2 q_4 - q_5^2 q_1 - q_1^2 q_4 - q_4^2 q_1) \\ (3) &= 4(q_1^2 + q_2^2 + q_3^2 + q_4^2 + q_5^2 + q_1 q_4)^2, \end{aligned}$$

so that

$$\begin{aligned} f_b(\mathbf{Q}) &= A(q_1^2+q_2^2+q_3^2+q_4^2+q_5^2+q_1q_4) \\ &\quad - B(2q_2q_3q_5+q_2^2q_4+q_2^2q_1-q_3^2q_4-q_5^2q_1-q_1^2q_4-q_4^2q_1) \\ &\quad + C(q_1^2+q_2^2+q_3^2+q_4^2+q_5^2+q_1q_4)^2. \end{aligned} \tag{7.1.7}$$

The Euler-Lagrange equations of (7.1.6) are therefore given by

$$\begin{aligned} &2\eta\sigma^2(2q_1+q_4)+\lambda\left(\left(\frac{A}{C}+|\mathbf{Q}|^2\right)(2q_1+q_4)-\frac{B}{C}\left(q_2^2-q_5^2-2q_1q_4-q_4^2\right)\right) \\ &=\frac{1+\eta}{2}\frac{\mathrm{d}^2q_1}{\mathrm{d}z^2}+\frac{1}{2}\frac{\mathrm{d}^2q_4}{\mathrm{d}z^2}+2\eta\sigma\frac{\mathrm{d}q_2}{\mathrm{d}z}, \end{aligned} \tag{7.1.8a}$$

$$\begin{aligned} &4\eta\sigma^2q_2+2\lambda\left(\left(\frac{A}{C}+|\mathbf{Q}|^2\right)q_2-\frac{B}{C}(q_3q_5+q_2(q_4+q_1))\right) \\ &=\eta\frac{\mathrm{d}^2q_2}{\mathrm{d}z^2}+2\eta\sigma\left(-\frac{\mathrm{d}q_1}{\mathrm{d}z}+\frac{\mathrm{d}q_4}{\mathrm{d}z}\right), \end{aligned} \tag{7.1.8b}$$

$$4\eta\sigma^2q_3+2\lambda\left(\left(\frac{A}{C}+|\mathbf{Q}|^2\right)q_3-\frac{B}{C}(q_2q_5-q_3q_4)\right)=\frac{1+\eta}{2}\frac{\mathrm{d}^2q_3}{\mathrm{d}z^2}+2\eta\sigma\frac{\mathrm{d}q_5}{\mathrm{d}z}, \tag{7.1.8c}$$

$$\begin{aligned} &2\eta\sigma^2(2q_4+q_1)+\lambda\left(\left(\frac{A}{C}+|\mathbf{Q}|^2\right)(2q_4+q_1)-\frac{B}{C}\left(q_2^2-q_3^2-2q_1q_4-q_1^2\right)\right) \\ &=\frac{1+\eta}{2}\frac{\mathrm{d}^2q_4}{\mathrm{d}z^2}+\frac{1}{2}\frac{\mathrm{d}^2q_1}{\mathrm{d}z^2}-2\eta\sigma\frac{\mathrm{d}q_2}{\mathrm{d}z}, \end{aligned} \tag{7.1.8d}$$

$$4\eta\sigma^2q_5+2\lambda\left(\left(\frac{A}{C}+|\mathbf{Q}|^2\right)q_5-\frac{B}{C}(q_2q_3-q_5q_1)\right)=\frac{1+\eta}{2}\frac{\mathrm{d}^2q_5}{\mathrm{d}z^2}-2\eta\sigma\frac{\mathrm{d}q_3}{\mathrm{d}z}. \tag{7.1.8e}$$

We solve the system (7.1.8) subject to homogeneous Dirichlet boundary conditions imposed on $z=0$ and $z=1$, namely

$$\mathbf{Q}(0)=\mathbf{Q}(1)=s_+\begin{pmatrix}\frac{2}{3} & 0 & 0\\ 0 & -\frac{1}{3} & 0\\ 0 & 0 & -\frac{1}{3}\end{pmatrix}, \tag{7.1.9}$$

which in terms of the components q_i, becomes

$$\begin{aligned} &q_1(0) = q_1(1) = \frac{2}{3}s_+,\ q_4(0) = q_4(1) = -\frac{1}{3}s_+, \\ &q_2(0) = q_2(1) = 0,\ q_3(0) = q_3(1) = 0,\ q_5(0) = q_5(1) = 0. \end{aligned} \tag{7.1.10}$$

Here, $s_+ = \frac{B+\sqrt{B^2-24AC}}{4C}$ is the nematic order of the minimisers of the bulk energy (7.1.2), as shown in [60] (also see Section 2.1.1). These boundary conditions are uniaxial and equivalent to

$$\mathbf{Q}(0) = \mathbf{Q}(1) = s_+\left(\mathbf{n}\otimes\mathbf{n} - \frac{1}{3}\mathbf{I}_3\right),\ \text{where } \mathbf{n} = (1,0,0).$$

Here and hereafter, $\mathbf{n}$ denotes a nematic director. Hence, we have planar boundary conditions for $\mathbf{n}$ on $z = 0, 1$.

Remark 7.1.1. We now make some initial comments about solutions of the Euler-Lagrange equations (7.1.8). First, we see there is always a solution branch with $q_3 = q_5 \equiv 0$, as both (7.1.8c) and (7.1.8e), and the relevant boundary conditions, are satisfied. Expressing $\mathbf{Q}$ in terms of independent basis tensors [77], we have

$$\begin{aligned} \mathbf{Q}(z) =& \frac{1}{2}(q_1(z) - q_4(z))(\mathbf{e}_x\otimes\mathbf{e}_x - \mathbf{e}_y\otimes\mathbf{e}_y) + q_2(z)(\mathbf{e}_x\otimes\mathbf{e}_y + \mathbf{e}_y\otimes\mathbf{e}_x) \\ &+\frac{1}{2}(-q_1(z) - q_4(z))(-\mathbf{e}_x\otimes\mathbf{e}_x - \mathbf{e}_y\otimes\mathbf{e}_y + 2\mathbf{e}_z\otimes\mathbf{e}_z) + q_3(z)(\mathbf{e}_x\otimes\mathbf{e}_z + \mathbf{e}_z\otimes\mathbf{e}_x) \\ &+q_5(z)(\mathbf{e}_y\otimes\mathbf{e}_z + \mathbf{e}_z\otimes\mathbf{e}_y), \end{aligned} \tag{7.1.11}$$

where $\mathbf{e}_x = (1,0,0)$, $\mathbf{e}_y = (0,1,0)$ and $\mathbf{e}_z = (0,0,1)$. If $q_3 = q_5 \equiv 0$, then $\mathbf{e}_z$ is a fixed eigenvector of $\mathbf{Q}$. Since the eigenvectors of $\mathbf{Q}$ are orthonormal, it follows the remaining eigenvectors must lie in the xy-plane for all $z \in [0,1]$. This can also be seen from (7.1.11), since q_3 and q_5 correspond to direction in the xz and yz planes.

Our last observation is that if $(q_1, q_2, q_3, q_4, q_5)$ is a solution to the Euler-Lagrange

equations (7.1.8), then so is $(q_1, q_2, -q_3, q_4, -q_5)$. Looking at (7.1.8a), only q_5^2 appears, hence the equation is invariant under $q_5 \to -q_5$. In (7.1.8b), we have $q_3 q_5$, so changing the sign of both leaves the equation unaffected. For (7.1.8c), substituting $-q_3$ and $-q_5$ we have

$$-4\eta\sigma^2 q_3 - 2\lambda\left(\left(\frac{A}{C} + |\mathbf{Q}|^2\right) q_3 - \frac{B}{C}\left(q_2 q_5 - q_3 q_4\right)\right) = -\frac{1+\eta}{2}\frac{\mathrm{d}^2 q_3}{\mathrm{d}z^2} - 2\eta\sigma\frac{\mathrm{d}q_5}{\mathrm{d}z},$$

which is the original equation (7.1.8c), after multiplying by -1. Analogous comments apply to (7.1.8e). Finally, in (7.1.8d) we have q_3^2 appearing, which is unchanged when replaced by $-q_3$. Since q_3 and q_5 satisfy symmetric zero Dirichlet boundary conditions, $-q_3$ and $-q_5$ also satisfy them.

7.2 Limiting regimes

To gain some useful initial insight into this complex system of Euler-Lagrange equations, we now look at some physically relevant limiting regimes. They are the limits of small and large domains, large elasticity (i.e., large twist L_4, or small splay/bend L_2), and large splay. The limiting profiles obtained provide crucial initial conditions for our numerical solvers.

7.2.1 The thin film limit

We first consider the $H \to 0$ limit, which is a good approximation for cells that are a few nano-meters in height. Taking the $H \to 0$ limit ($\lambda \to 0$ and $\sigma \to 0$ simultaneously in (7.1.4), the energy reduces to

$$F(\mathbf{Q}) = \int_0^1 \frac{1}{4}(\nabla \cdot \mathbf{Q})^2 + \frac{\eta}{4}|\nabla \times \mathbf{Q}|^2 \, \mathrm{d}z. \tag{7.2.1}$$

The associated Euler-Lagrange equations of (7.2.1) are

$$(1+\eta)\frac{\mathrm{d}^2 q_1}{\mathrm{d}z^2} + \frac{\mathrm{d}^2 q_4}{\mathrm{d}z^2} = 0, \tag{7.2.2a}$$

$$(1+\eta)\frac{\mathrm{d}^2 q_4}{\mathrm{d}z^2} + \frac{\mathrm{d}^2 q_1}{\mathrm{d}z^2} = 0, \tag{7.2.2b}$$

$$\frac{\mathrm{d}^2 q_2}{\mathrm{d}z^2} = \frac{\mathrm{d}^2 q_3}{\mathrm{d}z^2} = \frac{\mathrm{d}^2 q_5}{\mathrm{d}z^2} = 0. \tag{7.2.2c}$$

It is straightforward to see that (7.2.2a) and (7.2.2b) reduce to the Laplace equation for q_1 and q_4. Hence, the solutions of this system are constant and given by our boundary conditions,

$$q_1 = \frac{2s_+}{3},\ q_2 = 0,\ q_3 = 0,\ q_4 = -\frac{s_+}{3},\ q_5 = 0. \tag{7.2.3}$$

However, letting $\sigma \to 0$ represents a nematic state, not a cholesteric. We want to preserve the cholesteric nature of the problem, so σ should remain non-zero. Hence, we assume that $p_0 = \mathcal{O}(H)$, so that σ is a finite constant. Therefore, the thin film limit actually corresponds to $\lambda \to 0$, for fixed σ, which yields the energy

$$F(\mathbf{Q}) = \int_0^1 \frac{1}{4}(\nabla \cdot \mathbf{Q})^2 + \frac{\eta}{4}|\nabla \times \mathbf{Q} + 2\sigma\mathbf{Q}|^2 \,\mathrm{d}z, \tag{7.2.4}$$

and the following associated system of Euler-Lagrange equations:

$$2\eta\sigma^2\,(2q_1 + q_4) = \frac{1+\eta}{2}\frac{\mathrm{d}^2 q_1}{\mathrm{d}z^2} + \frac{1}{2}\frac{\mathrm{d}^2 q_4}{\mathrm{d}z^2} + 2\eta\sigma\frac{\mathrm{d}q_2}{\mathrm{d}z}, \tag{7.2.5a}$$

$$4\eta\sigma^2 q_2 = \eta\frac{\mathrm{d}^2 q_2}{\mathrm{d}z^2} + 2\eta\sigma\left(-\frac{\mathrm{d}q_1}{\mathrm{d}z} + \frac{\mathrm{d}q_4}{\mathrm{d}z}\right), \tag{7.2.5b}$$

$$4\eta\sigma^2 q_3 = \frac{1+\eta}{2}\frac{\mathrm{d}^2 q_3}{\mathrm{d}z^2} + 2\eta\sigma\frac{\mathrm{d}q_5}{\mathrm{d}z}, \tag{7.2.5c}$$

$$2\eta\sigma^2\,(2q_4 + q_1) = \frac{1+\eta}{2}\frac{\mathrm{d}^2 q_4}{\mathrm{d}z^2} + \frac{1}{2}\frac{\mathrm{d}^2 q_1}{\mathrm{d}z^2} - 2\eta\sigma\frac{\mathrm{d}q_2}{\mathrm{d}z}, \tag{7.2.5d}$$

$$4\eta\sigma^2 q_5 = \frac{1+\eta}{2}\frac{\mathrm{d}^2 q_5}{\mathrm{d}z^2} - 2\eta\sigma\frac{\mathrm{d}q_3}{\mathrm{d}z}. \tag{7.2.5e}$$

For the system (7.2.5), we can find an exact expression for $q_1 + q_4$. Adding (7.2.5a)

and (7.2.5d), we find

$$6\eta\sigma^2(q_4+q_1)=\left(\frac{2+\eta}{2}\right)\left(\frac{\mathrm{d}^2q_1}{\mathrm{d}z^2}+\frac{\mathrm{d}^2q_4}{\mathrm{d}z^2}\right),$$

and letting $q_1+q_4=:g$, this can be written as

$$\frac{12\eta\sigma^2}{2+\eta}g=\frac{\mathrm{d}^2g}{\mathrm{d}z^2}. \tag{7.2.6}$$

This second order ordinary differential equation can be solved to find

$$g(z):=q_1(z)+q_4(z)=\frac{s_+}{3}\left(\left(1-\frac{1-e^{\gamma}}{e^{-\gamma}-e^{\gamma}}\right)e^{\gamma z}+\left(\frac{1-e^{\gamma}}{e^{-\gamma}-e^{\gamma}}\right)e^{-\gamma z}\right), \tag{7.2.7}$$

where $\gamma=\sqrt{\frac{12\eta\sigma^2}{2+\eta}}$. This relation is independent of q_2, q_3, q_5 and therefore holds for solution branches with both zero and non-zero q_3, q_5.

To check the accuracy of the expression g (7.2.7), we plot the error between g and the numerically computed q_1+q_4 (i.e., q_1+q_4-g), in Figure 7.1 (b), for $\lambda=0$ and $\lambda=0.01$. The agreement is excellent for both values since the error does not exceed 7×10^{-5}, and there is no noticeable error on an interior interval when $\lambda=0$. Details of our numerical solver can be found in Section 7.3.2 and a discussion on parameter values in Section 7.3.1.

7.2.2 The limit of large domains

Next we consider the $H\to\infty$ limit, which is a good approximation for cells that are a few micro-meters in height. Again, we assume $p=\mathcal{O}(H)$, so that this scenario is represented by the $\lambda\to\infty$ limit, with σ fixed. In this limit, bulk effects become dominant hence, we expect minimisers of the energy (7.1.4), to be constrained to the set of bulk energy minimisers. That is, the set of uniaxial $\mathbf{Q}$ tensors, $\mathcal{N}=\{\mathbf{Q}\in S_0:\mathbf{Q}=s_+(\mathbf{n}\otimes\mathbf{n}-\frac{1}{3}\mathbf{I}_3)\}$, where $\mathbf{n}\in\mathbb{S}^2$ is arbitrary [60]. As such, and motivated by the twisted nature of cholesterics, we propose

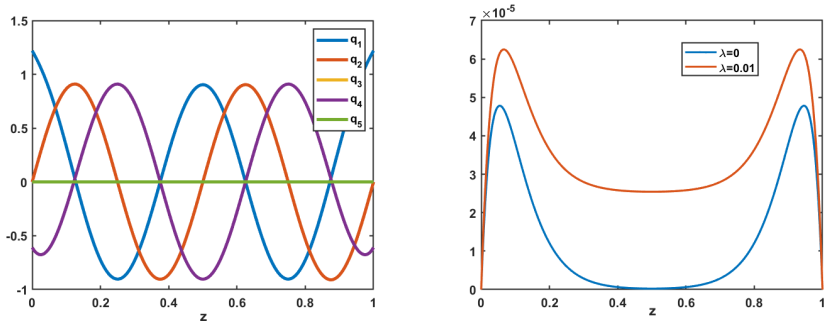

(a) (b)

Figure 7.1: (a) We plot the components of the solution $\mathbf{Q}$ of the Euler–Lagrange equations (7.1.8a)-(7.1.8e), when $\lambda = 0.01$, $\eta = 5$, $\sigma = 2\pi$. (b) For $\eta = 5$, $\sigma = 2\pi$ and λ as stated, we plot the error $q_1 + q_4 - g$, where g is given in (7.2.7), and q_1, q_4 are again the components of the numerical solution. The values of A, B, and C are $A = -B^2/3C$, $B = 0.64 \times 10^4 \mathrm{N/m^2}$ and $C = 0.35 \times 10^4 \mathrm{N/m^2}$ (these are values for the liquid crystal MBBA) [60]. We use the same values of A, B, and C in all subsequent figures.

the following uniaxial state:

$$\begin{aligned}\mathbf{Q}_\omega(z) &= s_+\left(\mathbf{n}\otimes\mathbf{n} - \frac{1}{3}\mathbf{I}_3\right), \quad \mathbf{n}_\omega = (\cos(\omega\pi z), \sin(\omega\pi z), 0),\\ &= s_+\begin{pmatrix} \cos^2(\omega\pi z) - \frac{1}{3} & \cos(\omega\pi z)\sin(\omega\pi z) & 0\\ \cos(\omega\pi z)\sin(\omega\pi z) & \sin^2(\omega\pi z) - \frac{1}{3} & 0\\ 0 & 0 & -\frac{1}{3}\end{pmatrix},\end{aligned} \tag{7.2.8}$$

will be a good approximation to solutions in the $\lambda \to \infty$ limit. Note, (7.2.8) satisfies the boundary conditions (7.1.10), for any $\omega \in \mathbb{Z}$. Here, ω controls the number of π rotations of the director in the z-direction, or equivalently, the number of twists of the director. Substituting $\mathbf{Q}_\omega$ into (7.1.6), the energy is given by

$$F(\mathbf{Q}_\omega) = s_+^2 \int_0^1 \frac{\eta}{2}\left[\frac{4\sigma^2}{3} - 2\sigma\omega\pi + \omega^2\pi^2\right] + \frac{\lambda}{C}\left[\frac{A}{3} - \frac{2Bs_+}{27} + \frac{Cs_+^2}{9}\right] \mathrm{d}z. \tag{7.2.9}$$

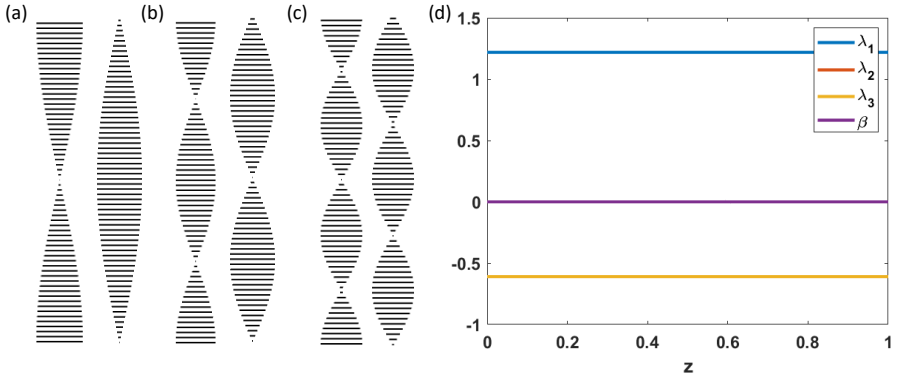

Figure 7.2: (a)-(c) show the eigenvector corresponding to the largest eigenvalue of the solution $\mathbf{Q}$, of the Euler–Lagrange equations (7.1.8a)-(7.1.8e), when $\lambda = 200000$, $\eta = 1$, and $\sigma = 2\pi$. This leading eigenvector of $\mathbf{Q}$, is the director throughout this chapter. We plot the eigenvectors in the xz-plane (first plot in each pair) and yz-plane (second plot in each pair), and the same is true for all subsequent figures depicting eigenvectors. We use three different initial conditions, $\mathbf{Q}_\omega$ given in (7.2.8), with $\omega = 1$, 2 and 3 in (a), (b) and (c) respectively. The eigenvalues of $\mathbf{Q}$, $\lambda_1(z) \geq \lambda_2(z) \geq \lambda_3(z)$, and the biaxiality measure $\beta = 1 - 6\frac{\mathrm{tr}(\mathbf{Q}^3)^2}{\mathrm{tr}(\mathbf{Q}^2)^3}$, are plotted in (d) (note $\lambda_2 = \lambda_3$ as we have uniaxial states). Recall, $\beta(\mathbf{Q}) \in [0, 1]$, $\beta(\mathbf{Q}) = 0$ for an uniaxial $\mathbf{Q}$, and $\beta(\mathbf{Q}) = 1$ for a maximally biaxial $\mathbf{Q}$. The three eigenvalues and β are the same for $\omega = 1, 2, 3$.

From this it is clear the elastic energy density is minimised when $\omega = \frac{\sigma}{\pi}$. Recall $\sigma = \frac{2\pi H}{p_0}$, hence the optimal choice of ω is two times the number of 2π rotations of the director.

In Figure 7.2, we present three numerical solutions of the Euler-Lagrange equations which have one, two and three twists, when $\lambda = 200000$, $\eta = 1$ and $\sigma = 2\pi$ (details about our choice of parameters and interest in one, two and three twist states can be found in Section 7.3.1). Specifically, we plot the director, eigenvalues and

biaxiality parameter of the solutions, which shows they are all uniaxial states. Furthermore, the director has no elevation in the z-axis i.e., it always lies in the xy-plane, and consequently the z-component of the director is zero. In Figure 7.3, we compute the error (i.e., the difference) between the numerical solution with one, two and three twists when $\lambda = 200000$, $\eta = 1$ and $\sigma = 2\pi$, and the limiting profile (7.2.8) with $\omega = 1, 2, 3$ respectively. There is excellent agreement between the numerics and asymptotics (the error does not exceed 4×10^{-5}) indicating (7.2.8) is a good approximation to the actual solution in regimes with large λ.

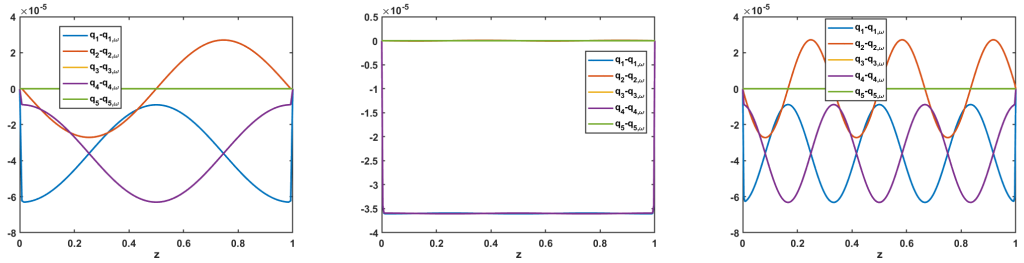

$\omega = 1$ $\omega = 2$ $\omega = 3$

Figure 7.3: Error between the limiting profile (7.2.8) with $\omega = 1$, $\omega = 2$ and $\omega = 3$, and the numerical solution with one, two and three twists respectively, when $\lambda = 200000$, $\eta = 1$ and $\sigma = 2\pi$. The $q_{i,\omega}$ denote the components of $\mathbf{Q}_\omega$.

7.2.3 The large elastic anisotropy limit

Recall, η captures the anisotropy of the problem. Therefore, to model large anisotropy (large twist, or small splay/bend), we study the $\eta \to \infty$ limit in this section. Dividing (7.1.4) by η, and letting $\eta \to \infty$ with fixed λ and σ, yields

$$F[\mathbf{Q}] = \int_0^1 |\nabla \times \mathbf{Q} + 2\sigma \mathbf{Q}|^2 \, \mathrm{d}z. \tag{7.2.10}$$

The Euler-Lagrange equations associated to (7.2.10) are:

$$2\sigma^2 (2q_1 + q_4) = \frac{1}{2} \frac{\mathrm{d}^2 q_1}{\mathrm{d}z^2} + 2\sigma \frac{\mathrm{d}q_2}{\mathrm{d}z}, \tag{7.2.11a}$$

$$4\sigma^2 q_2 = \left(\frac{\mathrm{d}^2 q_2}{\mathrm{d}z^2} + 2\sigma\left(-\frac{\mathrm{d}q_1}{\mathrm{d}z} + \frac{\mathrm{d}q_4}{\mathrm{d}z}\right)\right), \tag{7.2.11b}$$

$$4\sigma^2 q_3 = \frac{1}{2}\frac{\mathrm{d}^2 q_3}{\mathrm{d}z^2} + 2\sigma\frac{\mathrm{d}q_5}{\mathrm{d}z}, \tag{7.2.11c}$$

$$2\sigma^2\left(2q_4 + q_1\right) = \frac{1}{2}\frac{\mathrm{d}^2 q_4}{\mathrm{d}z^2} - 2\sigma\frac{\mathrm{d}q_2}{\mathrm{d}z}, \tag{7.2.11d}$$

$$4\sigma^2 q_5 = \frac{1}{2}\frac{\mathrm{d}^2 q_5}{\mathrm{d}z^2} - 2\sigma\frac{\mathrm{d}q_3}{\mathrm{d}z}. \tag{7.2.11e}$$

In the absence of bulk effects (which prefer an uniaxial $\mathbf{Q}$-tensor), we expect the energy (7.2.10) to be minimised by a biaxial $\mathbf{Q}$-tensor. To this end, we assume the following biaxial ansatz

$$\mathbf{Q} = \lambda_1 \mathbf{n}\otimes\mathbf{n} + \lambda_2 \mathbf{e}_z\otimes\mathbf{e}_z + \lambda_3 \mathbf{m}\otimes\mathbf{m}, \tag{7.2.12}$$

where $\mathbf{n} = (\cos(\sigma z), \sin(\sigma z), 0)$, $\mathbf{m} = (\sin(\sigma z), -\cos(\sigma z), 0)$, and λ_1, λ_2 and λ_3, are the associated eigenvalues. Substituting (7.2.12) into the energy density of (7.2.10), we have

$$\begin{aligned}
|\nabla\times\mathbf{Q} + 2\sigma\mathbf{Q}|^2 = \sigma^2 \Bigg| & \lambda_1 \begin{pmatrix} -\cos(2\sigma z) & -\sin(2\sigma z) & 0 \\ -\sin(2\sigma z) & \cos(2\sigma z) & 0 \\ 0 & 0 & 0 \end{pmatrix} \\
& + \lambda_3 \begin{pmatrix} \cos(2\sigma z) & \sin(2\sigma z) & 0 \\ \sin(2\sigma z) & -\cos(2\sigma z) & 0 \\ 0 & 0 & 0 \end{pmatrix} + \lambda_1 \begin{pmatrix} \cos(2\sigma z)+1 & \sin(2\sigma z) & 0 \\ \sin(2\sigma z) & 1-\cos(2\sigma z) & 0 \\ 0 & 0 & 0 \end{pmatrix} \\
& + 2\lambda_2 \begin{pmatrix} 0 & 0 & 0 \\ 0 & 0 & 0 \\ 0 & 0 & 1 \end{pmatrix} + \lambda_3 \begin{pmatrix} 1-\cos(2\sigma z) & -\sin(2\sigma z) & 0 \\ -\sin(2\sigma z) & \cos(2\sigma z)+1 & 0 \\ 0 & 0 & 0 \end{pmatrix} \Bigg|^2 \\
& = \sigma^2[2(\lambda_1+\lambda_3)^2 + (2\lambda_2)^2].
\end{aligned} \tag{7.2.13}$$

Hence, when $\lambda_1 + \lambda_3 = 0$ and $\lambda_2 = 0$, so that the associated $\mathbf{Q}$ is maximally biaxial (i.e., $\beta = 1$), the energy density of (7.2.10) obtains its minimum, i.e., $|\nabla \times \mathbf{Q} + 2\sigma\mathbf{Q}|^2 = 0$. Therefore, when $\sigma \neq 0$, the following maximally biaxial state

$$\begin{aligned}\mathbf{Q}_B(z) &= \lambda_1 \left(\mathbf{n} \otimes \mathbf{n} - \mathbf{m} \otimes \mathbf{m}\right) \\ &= \lambda_1 \begin{pmatrix} \cos(2\sigma z) & \sin(2\sigma z) & 0 \\ \sin(2\sigma z) & -\cos(2\sigma z) & 0 \\ 0 & 0 & 0 \end{pmatrix}, \end{aligned} \tag{7.2.14}$$

is the energy minimiser of (7.2.10) in the absence of boundary conditions. Therefore, we expect (7.2.14), to describe the limiting profile of the energy minimiser of (7.1.4) for large η, away from the boundaries (since $\mathbf{Q}_B$ does not satisfy the boundary conditions (7.1.10)).

To verify our prediction of biaxiality for large η, in Figure 7.4 we compute a numerical solution of the Euler-Lagrange equations (7.1.8a)-(7.1.8e) with 2π twisting, when $\lambda = 1$, $\eta = 1000$ and $\sigma = 2\pi$. Away from the boundaries, the solution is maximally biaxial since $\lambda_1 = -\lambda_3$ and $\lambda_2 = 0$ in the interior, consistent with (7.2.14). Moreover, we plot the error (i.e, the difference) between $\mathbf{Q}_B$ and the numerical solution when $\lambda = 1$, $\eta = 1000$ and $\sigma = 2\pi$ in Figure 7.5, and this confirms we have good agreement away from the boundaries as the error does not exceed 8×10^{-4}. These conclusions persist for $\lambda = 1$, $\eta = 5$ and $\sigma = 2\pi$, where the error does not exceed 5×10^{-3} (see Figure 7.6).

7.2.4 The large splay elasticity limit

The large splay limit corresponds to taking $L_2 \to \infty$ in (7.1.4), which is equivalent to letting $\eta \to 0$ and $\lambda \to 0$ simultaneously. Taking these limits, we have a

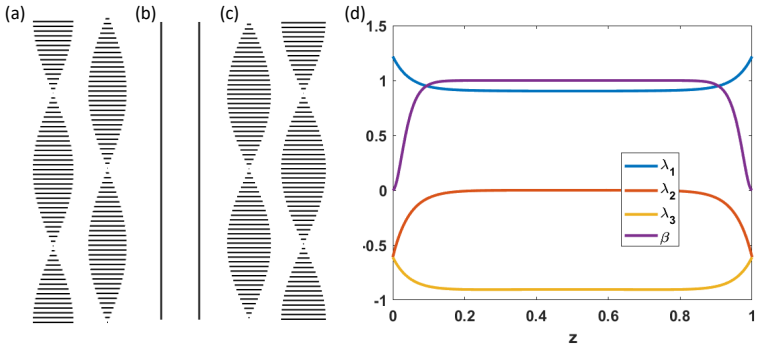

Figure 7.4: (a)-(c) show the three eigenvectors of $\mathbf{Q}$ (the solution of (7.1.8a)-(7.1.8e) with $\lambda = 1$, $\eta = 1000$, $\sigma = 2\pi$), corresponding to the eigenvalues $\lambda_1(z) \geq \lambda_2(z) \geq \lambda_3(z)$ in (d). We also plot the biaxiality measure β, in (d).

significantly reduced model where (7.1.4) becomes

$$F(\mathbf{Q}) = \int_0^1 |\nabla \cdot \mathbf{Q}|^2 \, \mathrm{d}z = \int_0^1 \left(\frac{\mathrm{d}q_3}{\mathrm{d}z}\right)^2 + \left(\frac{\mathrm{d}q_5}{\mathrm{d}z}\right)^2 + \left(\frac{\mathrm{d}(q_1+q_4)}{\mathrm{d}z}\right)^2 \, \mathrm{d}z. \quad (7.2.15)$$

Clearly we cannot determine q_2 from this model. The associated Euler-Lagrange equations of (7.2.15) have the following solutions,

$$q_3 = q_5 = 0, \text{ and } q_1 + q_4 = \frac{s_+}{3}, \text{ for all } z \in [0,1]. \quad (7.2.16)$$

Hence, we expect solutions of (7.1.8a)-(7.1.8e) which satisfy (7.2.16), to be minimisers of (7.1.4) in the limit of large splay. Moreover, we label solutions which satisfy (7.2.16) as splay free. That is to say, the director always lies in the xy-plane (see Remark 7.1.1).

Considering $\eta \to 0$ and $\lambda \to 0$ yields the constraint (7.2.16), but (7.2.16) also holds for any value of η and λ if the solution is splay free. To this end, we now study the energy and Euler-Lagrange equations for the class of splay free solutions.

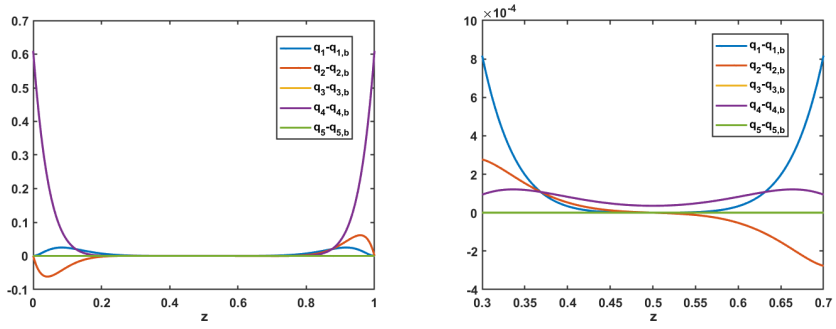

(a) (b)

Figure 7.5: Error between the limiting profile for large η (7.2.14) and the numerical solution when $\lambda = 1$, $\eta = 1000$ and $\sigma = 2\pi$. In (a) we present the error over the whole domain, and in (b) we plot the error at interior points only. The $q_{i,b}$ denote the components of $\mathbf{Q}_B$.

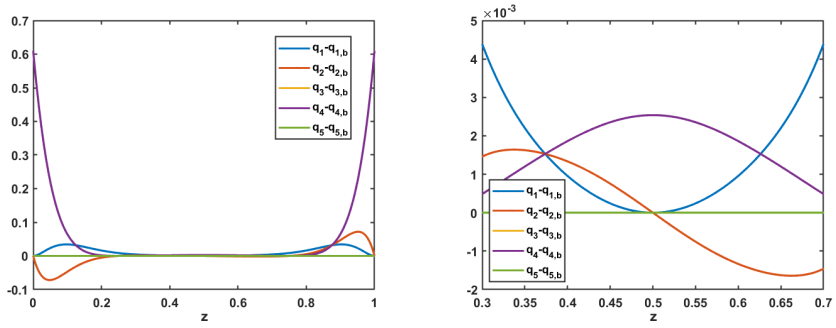

(a) (b)

Figure 7.6: Error between the limiting profile for large η (7.2.14) and the numerical solution when $\lambda = 1$, $\eta = 5$ and $\sigma = 2\pi$.

With the constraints in (7.2.16), the energy functional in (7.1.6) reduces to

$$\begin{aligned} F(\mathbf{Q}) = \int_0^1 \frac{\eta}{2} \left(\left(\frac{\mathrm{d}q_2}{\mathrm{d}z} \right)^2 + \left(\frac{\mathrm{d}(q_1 - q_4)/2}{\mathrm{d}z} \right)^2 \right) \\ + 2\sigma\eta \left(q_2 \left(\frac{\mathrm{d}(q_1 - q_4)/2}{\mathrm{d}z} \right) - \frac{\mathrm{d}q_2}{\mathrm{d}z} \left(\frac{q_1 - q_4}{2} \right) \right) + \frac{\sigma^2 \eta s_+}{6} \\ + 2\sigma^2\eta \left(q_2^2 + \left(\frac{q_1 - q_4}{2} \right)^2 \right) + \frac{\lambda}{C} f_b(\mathbf{Q}) \, \mathrm{d}z. \end{aligned}$$

The bulk potential can be simplified as follows

$$\begin{aligned} f_b(\mathbf{Q}) &= A\left(\frac{s_+^2}{9} - q_1q_4 + q_2^2\right) - B\left(\frac{s_+q_2^2}{3} - \frac{s_+q_1q_4}{3}\right) + C\left(\frac{s_+^2}{9} - q_1q_4 + q_2^2\right)^2 \\ &= A\left(\frac{s_+^2}{12} + \left(\frac{q_1-q_4}{2}\right)^2 + q_2^2\right) - \frac{s_+B}{3}\left(q_2^2 + \left(\frac{q_1-q_4}{2}\right)^2 - \frac{s_+^2}{36}\right) \\ &\quad + C\left(\frac{s_+^2}{12} + \left(\frac{q_1-q_4}{2}\right)^2 + q_2^2\right)^2. \end{aligned}$$

Here, we have used the fact that $q_1q_4 = \left(\frac{q_1+q_4}{2}\right)^2 - \left(\frac{q_1-q_4}{2}\right)^2 = \frac{s_+^2}{36} - \left(\frac{q_1-q_4}{2}\right)^2$. The energy can therefore be written as,

$$F(\mathbf{q}) = \int_0^1 \left\{\frac{\eta}{2}|\nabla\mathbf{q}|^2 + 2\sigma\eta(\mathbf{q}\cdot\nabla\times\mathbf{q}) + \frac{\lambda}{C}f_b(s_+,|\mathbf{q}|^2) + 2\sigma^2\eta|\mathbf{q}|^2 + \frac{\sigma^2\eta s_+}{6}\right\}\,\mathrm{d}z, \tag{7.2.17}$$

where $\mathbf{q} = \left(\frac{q_1-q_4}{2}, q_2\right)$ are the only degrees of freedom. The Euler-Lagrange equations of this functional are

$$\begin{aligned} &\eta\frac{\mathrm{d}^2q_2}{\mathrm{d}z^2} - 4\sigma\eta\frac{\mathrm{d}(q_1-q_4)/2}{\mathrm{d}z} = \\ &\qquad 2q_2\left(2\eta\sigma^2 + \frac{\lambda}{C}\left(A - \frac{B}{3}s_+ + 2C\left(\frac{s_+^2}{12} + \left(\frac{q_1-q_4}{2}\right)^2 + q_2^2\right)\right)\right), \end{aligned} \tag{7.2.18a}$$

$$\begin{aligned} &\eta\frac{\mathrm{d}^2(q_1-q_4)/2}{\mathrm{d}z^2} + 4\sigma\eta\frac{\mathrm{d}q_2}{\mathrm{d}z} = \\ &\qquad 2\left(\frac{q_1-q_4}{2}\right)\left(2\eta\sigma^2 + \frac{\lambda}{C}\left(A - \frac{B}{3}s_+ + 2C\left(\frac{s_+^2}{12} + \left(\frac{q_1-q_4}{2}\right)^2 + q_2^2\right)\right)\right), \end{aligned} \tag{7.2.18b}$$

which can be solved subject to the boundary conditions

$$q_2(0) = q_2(1) = 0, \text{ and } \left(\frac{q_1-q_4}{2}\right)(0) = \left(\frac{q_1-q_4}{2}\right)(1) = \frac{s_+}{2}. \tag{7.2.19}$$

The energy (7.2.17), Euler–Lagrange equations (7.2.18), and boundary conditions (7.2.19), give us the tools to study the splay free solution landscape only, if needed. This description is useful in the proof of Theorem 7.3.2 in the next section.

7.3 Solution landscapes for one-dimensional cholesteric liquid crystals

We now study solution landscapes for our one-dimensional cholesteric liquid crystal system. By this, we mean identifying the stable and unstable critical points of the energy (7.1.4), and how they connect to one another (we recap the notion of stability in due course). Critical points and the pathways connecting them, are found using the HiOSD method (as seen in Chapter 6). Recall that, we say there exists a pathway between two critical points $\mathbf{Q}_1$ and $\mathbf{Q}_2$, if following a stable or unstable eigendirection (of the Hessian) of $\mathbf{Q}_1$ in the HiOSD method, leads us to find $\mathbf{Q}_2$. The focus here, is on observing qualitatively distinct pathways between different stable states. Some motivation and details of our numerical study our now presented and for clarity, the HiOSD algorithm is explained in the context of this cholesteric system.

The numerical results for homogeneous Dirichlet boundary conditions (7.1.10) in Section 7.3.3, were first produced by Dr. Yucen Han [3] and then reproduced and added to by the author.

7.3.1 Motivation for our numerical study

A note on topology

The discussion in this section is based on the arguments in [3]. We want to study pathways between critical points $\mathbf{Q}$, of the energy (7.1.4), which have different twist numbers ω, for the nematic director. This is because the ground state in a cholesteric phase will be twisted [45]. In Section 7.2.2, we saw that the states $\mathbf{Q}_\omega$, are good approximations to such ω-twist states for sufficiently large λ. In

general, we expect the cholesteric free energy to be minimised by a quasi-uniaxial $\mathbf{Q}$-tensor (i.e., a $\mathbf{Q}$ which is nowhere maximally biaxial) close to $\mathbf{Q}_\omega$. As such, we work with the states $\mathbf{Q}_\omega$ in the discussion that follows, since they are tractable. We expect the same results to hold for solutions of the Euler-Lagrange equations which have ω-twists.

We want to study pathways between states of the form $\mathbf{Q}_{\omega=2n}$ and $\mathbf{Q}_{\omega=2m}$ (with $n \neq m$), and $\mathbf{Q}_{\omega=2n+1}$ and $\mathbf{Q}_{\omega=2m}$, for any $n, m \in \mathbb{Z}$, i.e., states where the twist number changes by an odd or even number. There is a qualitative difference between pathways connecting states where the twist number varies by an odd or even amount, which we now explain. The limiting tensors $\mathbf{Q}_\omega$ are uniaxial and belong to the space $W^{1,2}([0,1])$, hence by Theorem 9 in [13], $\mathbf{Q}_\omega$ is orientable for any ω. Therefore, we can orientate the director $\mathbf{n}$, so that it is a vector not a line field. Orientating the $\omega = 2n+1$ state, the director $\mathbf{n}$ points in opposite directions on the two boundaries. While orientating the $\omega = 2m$ state, the director points in the same direction on each boundary. Therefore, the boundary conditions for $\mathbf{n}$ are conflicting between the $\omega = 2n+1$ and $\omega = 2m$ states. Hence, they are topologically distinct states and cannot be continuously deformed into each other along a pathway $\mathbf{n}(t, z)$. Consequently, at least one defect in the form of an isotropic point, a discontinuity in the director, or a point of maximal biaxiality (i.e., a change in the number of distinct eigenvalues), is needed to mediate the pathway between $\omega = 2n+1 \to \omega = 2n+2$. For $\omega = 2n+1 \to \omega = 2n+3$, the boundary conditions for $\mathbf{n}$ (orientated) are the same at $z = 0$ and $z = 1$, so that the corresponding directors are topologically equivalent and a quasi-uniaxial (a pathway that is nowhere maximally biaxial) defect free pathway is possible.

We now state two results about pathways between different $\mathbf{Q}_\omega$ twist states, proven

in [3]. First, for quasi-uniaxial pathways, arguments from contact topology give us additional insight into the behaviour of $\mathbf{n}$ along such pathways.

Theorem 7.3.1. *The director field* $\mathbf{n}$*, along any quasi-uniaxial pathway between* $\mathbf{Q}_{w_1}$ *and* $\mathbf{Q}_{w_2}$*, for* $w_1 \neq w_2$ *must untwist, that is,* $\mathbf{n} \cdot (\nabla \times \mathbf{n})$ *must vanish at some point in space and time along the pathway [3].*

Theorem 7.3.2. *Any smooth zero-splay and bend pathway (*$\nabla \cdot \mathbf{Q} = \mathbf{0}$ *for all* t*) between* $\mathbf{Q}_{w_1}$ *and* $\mathbf{Q}_{w_2}$*, for* $w_1 \neq w_2$*, must contain points of maximal biaxiality [3].*

We do not comment on the proof of Theorem 7.3.1 (see [3] for a proof), but do outline the proof of Theorem 7.3.2, which utilises the reduced splay free description in Section 7.2.4. Recall that any splay free $\mathbf{Q}$-tensor can be described by a vector $\mathbf{q} = ((q_1 - q_4)/2, q_2)$, and satisfies the boundary conditions (7.2.19). The helical states $\mathbf{Q}_\omega$ (7.2.8) satisfy the constraints in (7.2.16) and are therefore splay free, meaning they can written as

$$\mathbf{q}(z) = \frac{s_+}{2}(\cos(2\omega\pi z), \sin(2\omega\pi z)). \tag{7.3.1}$$

This vector defines a closed curve in the $((q_1 - q_4)/2, q_2)$ plane, of radius $\frac{s_+}{2}$, which winds around the origin ω times, making ω the winding number or winding index. Any splay free pathway between $\mathbf{q}_{\omega_1}$ and $\mathbf{q}_{\omega_2}$ can also be described by a two-dimensional vector $\tilde{\mathbf{q}}(t, z) = ((\tilde{q}_1 - \tilde{q}_4)/2, \tilde{q}_2)\,(t, z)$, such that $\tilde{\mathbf{q}}(0, z) = \mathbf{q}_{\omega_1}(z)$, $\tilde{\mathbf{q}}(1, z) = \mathbf{q}_{\omega_2}(z)$, and $\tilde{\mathbf{q}}(t, 0) = \tilde{\mathbf{q}}(t, 1) = (s_+/2, 0)$ for all $t, z \in [0, 1]$. Now, since $\mathbf{q}_{\omega_1}$ and $\mathbf{q}_{\omega_2}$ have different winding numbers, and the winding number must always be an integer, any pathway must pass through the origin to change the winding number, so that $\tilde{\mathbf{q}}$ vanishes at at least one point (z^*, t^*).

A $\mathbf{Q}$-tensor is maximally biaxial when one of its eigenvalues is zero, which implies its determinant is zero too. Setting the determinant of a splay free $\mathbf{Q}$ equal to zero,

a quick calculation shows $|\mathbf{q}| = \frac{s_+}{6}$. From the previous paragraph, any pathway must start and finish on the circle radius $\frac{s_+}{2}$ and pass through the origin at least once, hence, it must also cross the circle of radius $\frac{s_+}{6}$ at least twice introducing two points of maximal biaxiality.

Remark 7.3.3. We now discuss the implications of the above theorems. From Theorem 7.3.1, since $\mathbf{n} \cdot (\nabla \times \mathbf{n})$ corresponds to the twist term in the Oseen-Frank energy density (7.3.2), if this term is zero somewhere, it means the cholesteric must untwist at this point. Since a quasi-uniaxial pathway cannot be maximally biaxial anywhere, Theorem 7.3.2 implies such a pathway must also have non-zero splay/bend. It is therefore splay that mediates the untwisting of $\mathbf{n}$. (7.2.16) will not hold everywhere along a quasi-uniaxial pathway, and consequently $\mathbf{e}_z$ will not be a fixed eigenvector along the pathway. As such, eigenvectors can lie in the xz- and yz-planes.

In summary, any pathway that changes the twist number can proceed via untwisting and splay, the introduction of maximal biaxiality, or both. Combined with the discussion at the beginning of this section, we make the following conjectures: (i) when ω changes by an even number, we can have a defect free quasi-uniaxial pathway which proceeds by untwisting and splay, as well as a pathway containing maximal biaxiality, (ii) when the twist number changes by an odd amount, a defect must be introduced and any pathway must therefore contain maximal biaxiality. To investigate this, we consider the simplest case of pathways between states with one, two and three twists in Section 7.3.3.

Typical values

In order to look at physically meaningful material values in our model, we now connect the LdG and Oseen-Frank theories. For a chiral nematic, the general

Oseen-Frank elastic energy density can be written as [17]:

$$f_{OF}(\mathbf{n}) = K_{11}(\nabla \cdot \mathbf{n})^2 + K_{22}(\mathbf{n} \cdot \nabla \times \mathbf{n})^2 + K_{33}(\mathbf{n} \times (\nabla \times \mathbf{n}))^2 + (K_{22} + K_{24})\nabla \cdot [(\mathbf{n} \cdot \nabla)\mathbf{n} - (\nabla \cdot \mathbf{n}))\mathbf{n}] + q_0 K_{22}(\mathbf{n} \cdot \nabla \times \mathbf{n}). \quad (7.3.2)$$

As in Section 1.4.2, K_{11}, K_{22}, K_{33} and K_{24} are the Frank elastic constants. Since this is a one-dimensional problem, the saddle splay term (the term with coefficient $K_{22}+K_{24}$) is identically zero. It is then clear we have three Frank elastic constants K_{11}, K_{22} and K_{33}, but only two elastic constants in our LdG free energy, L_2 and L_4. To account for this degeneracy, it is convention to take $K_{11} = K_{33}$ i.e., splay equals bend [117]. The elastic energy density of (7.1.1) can be written as

$$\frac{L_2 - L_4}{4}(\nabla \cdot \mathbf{Q})^2 + \frac{L_4}{4}|\nabla \mathbf{Q}|^2 + L_4 q_0 \epsilon_{lik} Q_{lj} \frac{\partial Q_{ij}}{\partial x_k}. \quad (7.3.3)$$

Using the relation in [11], we can relate the constants in (7.3.2) and (7.3.3) to find

$$L_2 = \frac{1}{s_0^2}(2K_{11} - K_{22}) \text{ and } L_4 = \frac{K_{22}}{s_0^2}. \quad (7.3.4)$$

Here, s_0 is the experimental observation of the order parameter and may not equal s_+. Therefore,

$$\eta = \frac{K_{22}}{2K_{11} - K_{22}} \text{ and } \lambda = \frac{H^2 C s_0^2}{2K_{11} - K_{22}}. \quad (7.3.5)$$

Although s_+ may not be equal to s_0, we take $s_+ = s_0$, so that we can use the expression for λ in (7.3.5).

Using typical values of the Frank elastic constants for 5CB, namely $K_{11} = 4.5$pN and $K_{22} = 3$pN [113], implies $\eta = \frac{1}{2}$ using (7.3.5). To study the transition between one and three twist states, it is most appropriate to fix $\sigma = 2\pi$ (which represents one 2π rotation of the director) in all of our numerical results. A

typical value of q_0 is also given in [113] to be $q_0 = 10000\text{m}^{-1}$, which with $\sigma = 2\pi$, gives a corresponding cell height of 6.28×10^{-4}m. Moreover, using values for the material and temperature dependent bulk constant $A = -0.171 \times 10^6\text{N/m}^2$, $B = 2.12 \times 10^6\text{N/m}^2$, $C = 1.73 \times 10^6\text{N/m}^2$ for 5CB given in [118], we then find $\lambda = 7.256 \times 10^{10}$. Alternatively, for a cell on the nano-scale of height 5nm, we have $\lambda = 4.595$. Ultimately, the values of η and λ can be tailored by the material and the geometry. See Table 7.1 for a summary of these parameter values.

Using the values of A, B and C in Figure 7.1, with $2K_{11} - K_{22} = 2\text{pN}$, we calculate that our choice of $\lambda = 200000$ corresponds to a cell of height 5.85μm, which is very reasonable for most large physically relevant cells on the micron-scale. In [113] and [118] for instance, they consider cells of height 5μm and 2μm respectively. With the same choices for A, B, C and $2K_{11} - K_{22}$, we find that $\lambda = 0.01$ and $\lambda = 1$ (Figure 7.1 and Figure 7.4), correspond to cells of height 1.31nm and 13.1nm respectively, which are still physically relevant for cells on the nano-scale. Finally, elastic constants are typically of the same order of magnitude, so our choices of $\eta = 5$ in Figure 7.1 and Figure 7.6, and $\eta = 1$ in Figure 7.2 and Figure 7.3, are valid choices. In view of this discussion on typical parameter values, our choice of $\lambda = 3500$ (so that $H = 0.773\mu$m with A, B, C as in Figure 7.1 and $2K_{11} - K_{22} = 2\text{pN}$) and $\eta = 4.5$, for the exploration of the solution landscape that follows, are reasonable. See Table 7.2 for a summary of these parameter values.

Parameter values	λ
$q_0 = 10000\mathrm{m}^{-1}$, $H = 6.28 \times 10^{-4}\mathrm{m}$	7.256×10^{10}
$q_0 = 1.07 \times 10^{6}\mathrm{m}^{-1}$, $H = 5 \times 10^{-9}\mathrm{m}$	4.595

Table 7.1: Values of λ for different choices of the model parameters H and q_0, with $A = -0.171 \times 10^{6}\mathrm{N/m}^2$, $B = 2.12 \times 10^{6}\mathrm{N/m}^2$, $C = 1.73 \times 10^{6}\mathrm{N/m}^2$, $K_{11} = 4.5 \times 10^{-12}\mathrm{N}$ and $K_{12} = 3 \times 10^{-12}\mathrm{N}$. Note, $\sigma = 2\pi$ is fixed.

Parameter values	λ
$q_0 = 4.79 \times 10^{-9}\mathrm{m}^{-1}$, $H = 1.31 \times 10^{-9}\mathrm{m}$	0.01
$q_0 = 4.79 \times 10^{-8}\mathrm{m}^{-1}$, $H = 1.31 \times 10^{-8}\mathrm{m}$	1
$q_0 = 8.13 \times 10^{6}\mathrm{m}^{-1}$, $H = 7.73 \times 10^{-7}\mathrm{m}$	3500
$q_0 = 1 \times 10^{4}\mathrm{m}^{-1}$, $H = 5.85 \times 10^{-6}\mathrm{m}$	2×10^{5}

Table 7.2: Values of λ for different choices of the model parameters H and q_0, with $A = -0.39 \times 10^{4}\mathrm{N/m}^2$, $B = 0.64 \times 10^{4}\mathrm{N/m}^2$, $C = 0.35 \times 10^{4}\mathrm{N/m}^2$ and $2K_{11} - K_{22} = 2 \times 10^{-12}\mathrm{N}$. Note, $\sigma = 2\pi$ is fixed.

7.3.2 Numerical method

Solver details

We solve the system of Euler-Lagrange equations (7.1.8) in two ways: (i) we solve the corresponding gradient flow equations

$$\frac{\partial q_i}{\partial t} = \frac{\partial}{\partial z}\left(\frac{\partial F}{\partial\left(\frac{dq_i}{dz}\right)}\right) - \frac{\partial F}{\partial q_i}, \text{ for } i = 1,2,3,4,5, \tag{7.3.6}$$

(where F is as in (7.1.6)) using finite difference methods along with Euler's method; or (ii) we use the HiOSD method (explained in the next subsection). We focus on method (i) here, which we use to produce the numerical results in the preceding sections of this chapter. We use a uniform mesh of mesh size $1/124$ to partition $[0,1]$, and deem the solution to have converged when $||\nabla F(\mathbf{Q})||_{L^2} < 10^{-6}$, where

$$(\nabla F(\mathbf{Q}))_i = \frac{\partial}{\partial z}\left(\frac{\partial F}{\partial\left(\frac{dq_i}{dz}\right)}\right) - \frac{\partial F}{\partial q_i}, \text{ for } i = 1,2,3,4,5. \tag{7.3.7}$$

Solutions depend strongly on the initial condition and to obtain solutions with ω twists for large λ, we simply use $\mathbf{Q}_\omega$ in (7.2.8) as the initial condition to obtain the numerical solution $\mathbf{Q}_{s\omega}$ (see Figure 7.2), of the Euler-Lagrange equations (7.1.8a)-(7.1.8e). From Section 7.2.2, it is clear the elastic energy density is minimised when $\omega = \frac{\sigma}{\pi}$. Hence, for $\sigma = 2\pi$ and large λ, the solution $\mathbf{Q}_{s2}$ is always the global minimiser of (7.1.4) ($|\nabla \times \mathbf{Q}_\omega + 2\sigma\mathbf{Q}_\omega|^2$ is minimised by $\omega = 2$) and therefore stable, whilst $\mathbf{Q}_{s3}$ and $\mathbf{Q}_{s1}$, are critical points. We say a state $\tilde{\mathbf{Q}}$ is stable if the Hessian of the free energy $F(\tilde{\mathbf{Q}})$ is positive definite, or equivalently, all of its eigenvalues are positive, and unstable otherwise. We find the stability of $\mathbf{Q}_{s\omega}$ with $\omega = 1,3$, depends on the parameter η. When η is small ($\eta < 5$) and $\lambda = 3500$, the solutions $\mathbf{Q}_{s3}$ and $\mathbf{Q}_{s1}$ are stable. When $\eta > 5$ and $\lambda = 3500$, the solutions $\mathbf{Q}_{s1}$ and $\mathbf{Q}_{s3}$ are unstable. This is likely because biaxiality is preferred for large η (see

Section 7.2.3). Hence, we fix $\eta = 4.5$ in our exploration of the solution landscape so that the one, two and three twist states are stable.

For large η, we take the constant tensor

$$\mathbf{Q}(z) \equiv s_+ \begin{pmatrix} \frac{2}{3} & 0 & 0 \\ 0 & -\frac{1}{3} & 0 \\ 0 & 0 & -\frac{1}{3} \end{pmatrix}, \tag{7.3.8}$$

as our initial condition. We then find biaxial solutions of the Euler-Lagrange equations (7.1.8a)-(7.1.8e) for large η, as predicted in Section 7.2.3 (see Figure 7.4).

HiOSD method

Recall that for any critical point, the Morse index is the number of negative eigenvalues of the corresponding Hessian $\mathbb{H}(\mathbf{Q})$, of the free energy [110]. Stable critical points are such that all the eigenvalues of its Hessian are positive, while critical points with index greater or equal to one are unstable, and labelled as index-k saddle points. We use the simultaneous Rayleigh-quotient iterative minimisation method to calculate the smallest k eigenvalues of the Hessian [112].

Using the HiOSD method [71], we can find critical points of the free energy with arbitrary Morse index. The HiOSD dynamics for an index-k critical point are given as follows:

$$\begin{cases} \beta^{-1}\dot{\mathbf{Q}} &= -\left(\mathbf{I} - 2\sum_{j=1}^{k} \mathbf{v}_j \mathbf{v}_j^\top\right)(\nabla F(\mathbf{Q})), \\ \gamma^{-1}\dot{\mathbf{v}}_i &= -\left(\mathbf{I} - \mathbf{v}_i\mathbf{v}_i^\top - 2\sum_{j=1}^{i-1} \mathbf{v}_j \mathbf{v}_j^\top\right)\mathbb{H}(\mathbf{Q})\mathbf{v}_i, \ i = 1, \cdots, k, \end{cases} \tag{7.3.9}$$

where the state variable $\mathbf{Q}$ and k direction variables $\mathbf{v}_i$ are coupled, $\mathbf{I}$ is the identity operator, and $\beta, \gamma > 0$ are relaxation parameters ($\dot{\cdot}$ denotes differentiation with

respect to t). The first equation in (7.3.9) describes a transformed gradient flow, which allows $\mathbf{Q}$ to move along an ascent direction on the unstable subspace, and a descent direction on the stable subspace. The second equation in (7.3.9), is used to search for an orthonormal basis of k eigenvectors, corresponding to the k smallest eigenvalues for the index-k saddle point.

We again implement Algorithm 1 in [71], with the following choices to solve this dynamical system. We take our relaxation parameters $\beta = \gamma = \Delta t$, where Δt is a fixed time step, and fix $l^0 = 10^{-6}$. We again use a uniform mesh of mesh size $1/124$ to partition $[0, 1]$, and deem the method to have converged when $||\nabla F(\mathbf{Q})||_{L^2} < 10^{-6}$. The remaining inputs to this algorithm to find an index-k saddle are, a suitable initial condition, an orthonormal set of vectors, and a choice of $k \in \mathbb{Z}^+$. Once an index-k critical point $\mathbf{Q}$ is found, our initial condition for the methods is a perturbation of the form $\mathbf{Q} + \epsilon \mathbf{v}_i$, where we take $\epsilon \in (0, 1]$. We can then search up (down) to find higher (lower) index critical points. Any new critical points found using this initial condition are connected to $\mathbf{Q}$, or equivalently, there is a pathway between them. This process can be repeated to keep finding new critical points and deduce their connectivity.

As explained in Section 7.3.1, we expect there to be a pathway containing maximal biaxiality connecting the one and three twist states. To find this pathway, we start by numerically computing the highest index biaxial state. We do this with

the following initial condition in the HiOSD algorithm

$$\mathbf{Q}(z) = \begin{cases} s_+ \begin{pmatrix} \cos^2(2\pi z) - \frac{1}{3} & \cos(2\pi z)\sin(2\pi z) & 0 \\ \cos(2\pi z)\sin(2\pi z) & \sin^2(2\pi z) - \frac{1}{3} & 0 \\ 0 & 0 & -\frac{1}{3} \end{pmatrix}, \\ \quad \text{for } 0 \le z \le 0.25 \text{ and } 0.75 \le z \le 1, \\ s_+ \begin{pmatrix} \cos^2\left(2\pi z + \frac{\pi}{2}\right) - \frac{1}{3} & \cos\left(2\pi z + \frac{\pi}{2}\right)\sin\left(2\pi z + \frac{\pi}{2}\right) & 0 \\ \cos\left(2\pi z + \frac{\pi}{2}\right)\sin\left(2\pi z + \frac{\pi}{2}\right) & \sin^2\left(2\pi z + \frac{\pi}{2}\right) - \frac{1}{3} & 0 \\ 0 & 0 & -\frac{1}{3} \end{pmatrix}, \\ \quad \text{for } 0.25 < z < 0.75. \end{cases} \tag{7.3.10}$$

This initial condition has a 2π rotation of the director $\mathbf{n}$. $\mathbf{n}$ also has two discontinuous points at $z = 0.25$ and 0.75. Using this initial condition we are able to find what we call the *Biaxial* state (described in Section 7.3.3).

7.3.3 Results: homogeneous boundary conditions

We now construct the solution landscape, that is, we find the critical points of the energy (7.1.4) and the pathways between them. We do this by combining the HiOSD method with downwards and upwards search algorithms [80]. Regarding nomenclature, 'B' indicates that the state has biaxial regions, 'Z' indicates that q_3 is non-zero (and q_5 although we do not plot this) so that $\mathbf{Q}$ has splay and consequently, the director lies in the xz- and yz-planes somewhere (for splay free solutions, we find (7.2.16) always holds, but again only plot q_3), and the number at the end indicates the approximate number of periods of q_2. For example, $BBZ2$ has two biaxial regions, splay, and q_2 completes two approximate periods. Some

states have the same labels following this nomenclature. In these cases, we simply follow the label with an underscore and a number to enumerate them. The states with one, two or three twists are uniaxial stable states and labeled as One, Two and $Three$, respectively (see Figure 7.9 for these solutions).

Simulating the dynamics (7.3.9) with (7.3.10) as our initial condition, we find what we call the $Biaxial(BB2)$ state, to be index-4 and searching up we find no higher index state. Hence, $Biaxial(BB2)$ is the parent state (the critical point with highest Morse Index). The solution landscape starting from the $Biaxial(BB2)$ state, is shown in Figure 7.11.

We now analyse the discovered saddle points. We find ten saddle points connecting the stable One, Two and $Three$ states, four index-1 saddle points ($Uniaxial(Z2)$, $Uniaxial\_2(Z2)$, $BZ2$ and $BZ2\_2$) which we label as transition states (shown in Figure 7.8), five index-2 saddle points ($B1.5$, $BBZ2$, $BBZ2\_2$, $B2.5$ and $B2.5\_2$) and an index-4 saddle point $Biaxial(BB2)$ (shown in Figure 7.7). We see that our observation in Remark 7.1.1 is correct, with all solutions containing splay coming in pairs of the form $(q_1, q_2, q_3, q_4, q_5)$ and $(q_1, q_2, -q_3, q_4, -q_5)$. These pairs also differ in their director profile, which is reflected in the z-axis between pairs (we do not repeat these comments which also hold true in the inhomogeneous case presented in Section 7.3.4). $Biaxial(BB2)$ has a pair of negative degenerate eigenvalues away from the regions of biaxiality, i.e., $\lambda_2 = \lambda_3 < 0$, and two pairs of points where the eigenvalue λ_2 is zero, which gives us four points of maximal biaxiality. In the centre of the two biaxial regions, we have a point where λ_1 and λ_2 are almost equal and consequently, we have an almost uniaxial part. We call these two points of maximal biaxiality encompassing a point of almost uniaxiality, a biaxial torus [119]. Analogous comments apply to the eigenvalues of all other

biaxial critical points. Hence, the biaxial torus is a repeating defect motif. Of the remaining biaxial critical points, three of them have no splay ($B1.5$, $B2.5$, and $B2.5\_2$) and differ in the location of their single biaxial torus, as well as the period of q_2. Finally, we have two pairs of biaxial critical points with splay, a pair with two biaxial tori ($BBZ2$, $BBZ2\_2$) and a pair with one biaxial torus ($BZ2$, $BZ2\_2$). We note that all biaxial critical points have constant twist away from their biaxial tori. Furthermore, those which are splay free, have zero splay away from their biaxial regions and the boundaries, while those with splay, have increasing splay as they approach their biaxial regions. To illustrate this, we plot the splay measure $|\nabla \cdot \mathbf{Q}|$, and twist measure $\mathbf{n} \cdot (\nabla \times \mathbf{n})$, for $Biaxial(BB2)$ and $BZ2$ in Figure 7.10 (we omit the twist measure in the biaxial regions as it is large). In general, for a state with b biaxial tori, we numerically see the index is equal to

$$b \times (ns + 1), \tag{7.3.11}$$

where $ns = 1$ for a state with no splay, and $ns = 0$ for a state with splay. $Uniaxial(Z2)$ and $Uniaxial\_2(Z2)$ are the only non-biaxial, and hence defect free saddle points, since they both have a pair of degenerate eigenvalues ($\lambda_1 \approx \lambda_2$) throughout the domain. They both also have splay patterns and in particular, we can see the director untwists at two points in the interior of the cell i.e., $\mathbf{n} \cdot (\nabla \times \mathbf{n}) = 0$ (see Figure 7.10).

We now explain the solution landscape in Figure 7.11. As in Chapter 6, we only include arrows showing how an index-i state connects to any index-$i+1$ state. We find that our conjecture regarding the possibility of both a defect free (quasi-)uniaxial pathway and biaxial pathway (containing maximal biaxiality), between the *One* and *Three* twist states (explained in Section 7.3.1), holds. Both the index-1 $Uniaxial(Z2)$ and $Uniaxial\_2(Z2)$ transition states facilitate a uniaxial

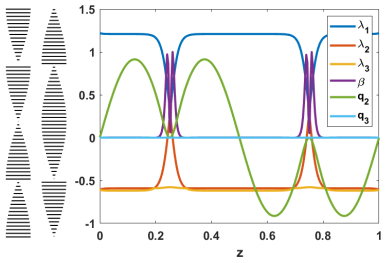

Biaxial($BB2$) - index-4 saddle

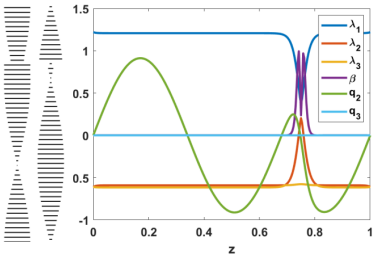

$B1.5$ - index-2 saddle

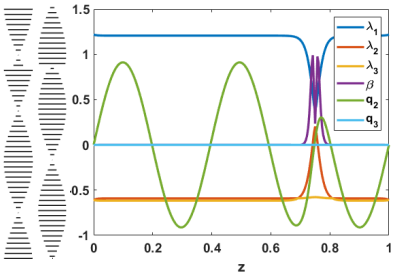

$B2.5$ - index-2 saddle

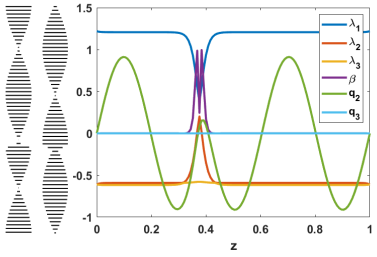

$B2.5\_2$ - index-2 saddle

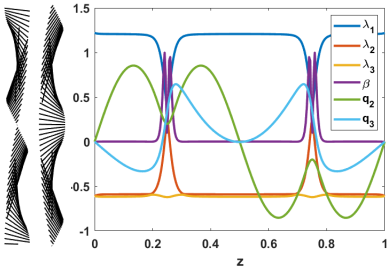

$BBZ2$ - index-2 saddle

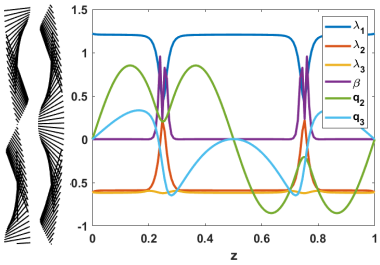

$BBZ2\_2$ - index-2 saddle

Figure 7.7: Saddle points for $\lambda = 3500$, $\eta = 4.5$ and $\sigma = 2\pi$, with homogeneous boundary conditions. We plot the three eigenvalues of the $\mathbf{Q}$-tensor $\lambda_1(z) \geq \lambda_2(z) \geq \lambda_3(z)$, the components q_2 and q_3 of $\mathbf{Q}$, and the biaxiality parameter β. On the left hand side we plot the director. The same quantities are plotted in all subsequent solutions.

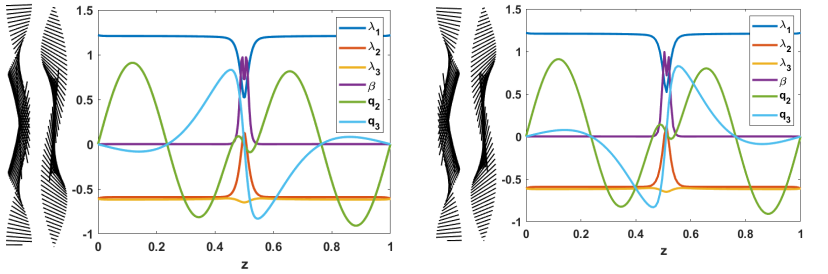

$BZ2$ - index-1 saddle

$BZ2\_2$ - index-1 saddle

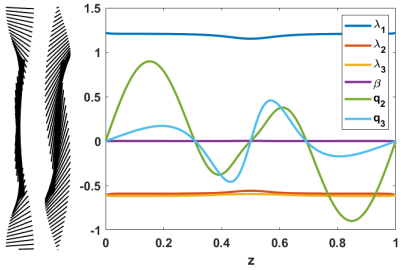

$Uniaxial(Z2)$ - index-1 saddle

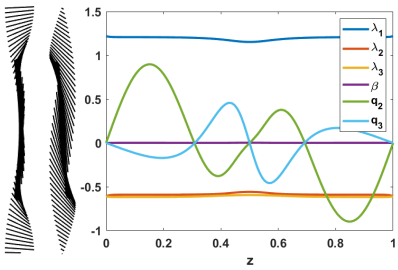

$Uniaxial\_2(Z2)$ - index-1 saddle

Figure 7.8: Saddle points for $\lambda = 3500$, $\eta = 4.5$ and $\sigma = 2\pi$, with homogeneous boundary conditions.

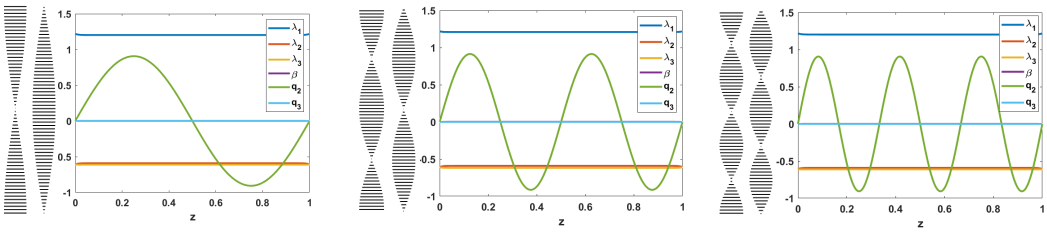

One *Two* *Three*

Figure 7.9: Stable twist states for $\lambda = 3500$, $\eta = 4.5$ and $\sigma = 2\pi$, with homogeneous boundary conditions.

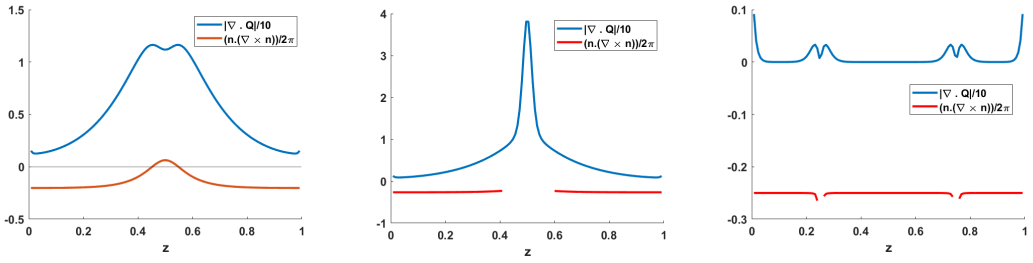

$Uniaxial(Z2)$ $BZ2$ $Biaxial(BB2)$

Figure 7.10: Plot of the twist and splay measures $\mathbf{n} \cdot (\nabla \times \mathbf{n})$ and $|\nabla \cdot \mathbf{Q}|$ respectively, for $Uniaxial(Z2)$, $BZ2$ and $Biaxial(BB2)$.

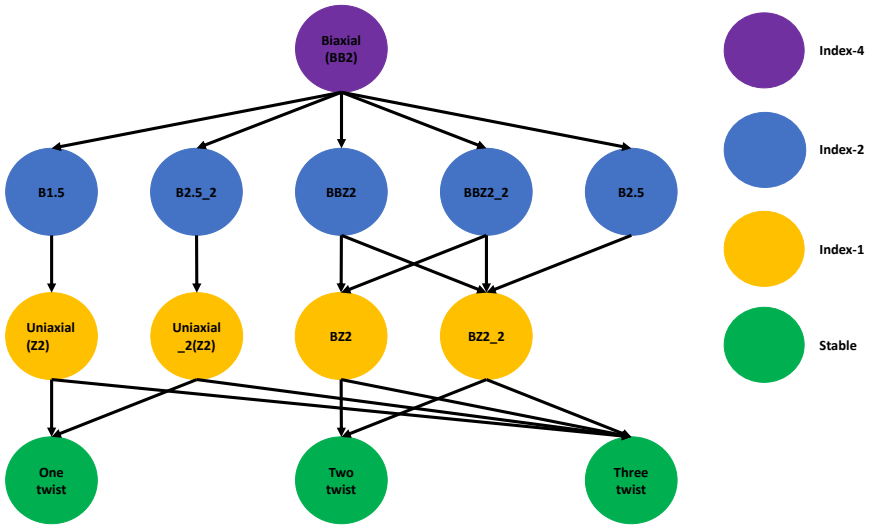

Figure 7.11: The solution landscape for $\lambda = 3500$, $\eta = 4.5$ and $\sigma = 2\pi$, with homogeneous boundary conditions.

pathway, whilst the index-4 $Biaxial(BB2)$ state enables us to have a biaxial pathway. In Figure 7.12 (Figure 7.13), we display some of the transient states (explained in the next paragraph) along the uniaxial (biaxial) pathway between One and $Three$, going via $Uniaxial(Z2)$ ($Biaxial(BB2)$). Along the uniaxial pathway, we find all states to contain splay and be uniaxial, consistent with Theorem 7.3.1 and Theorem 7.3.2. Along the biaxial pathway, which necessarily contains points of maximal biaxiality due to $Biaxial(BB2)$, we find all states to be splay free indicating the entire pathway is splay free, consistent with Theorem 7.3.2. Hence, our uniaxial pathway with untwisting is mediated by the presence of splay (non-zero q_3), whilst the biaxial pathway is splay free. Finally, our belief that any pathway connecting states where the twist number changes by an odd amount, must proceed via maximal biaxiality, also holds, since any pathway between One and Two, or Two and $Three$, must be mediated via a critical point with maximal biaxiality in Figure 7.11.

So far we have presented the critical points of the free energy (7.1.4). We now

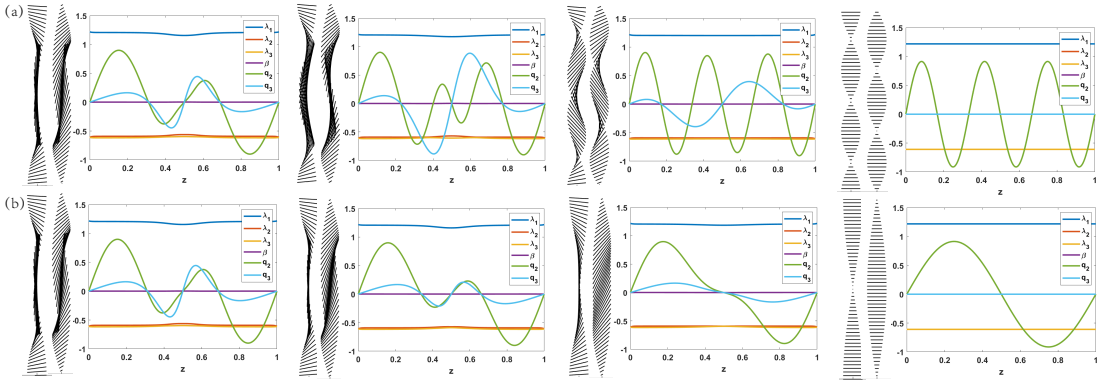

Figure 7.12: The pathway between the stable states *Three* and *One* via index-1 $Uniaxial(Z2)$, when $\lambda = 3500$, $\eta = 4.5$, $\sigma = 2\pi$. (a) The pathway from $Uniaxial(Z2)$ to *Three*. (b) The pathway from $Uniaxial(Z2)$ to *One*.

provide snapshots of how critical points evolve between one another via the HiOSD dynamics. Using gradient flow, along the positive or negative eigendirections, we plot the transient states on the uniaxial pathway (i.e., we pause our numerical solver and plot the state at that point) between the transition state $Uniaxial(Z2)$, and the stable states *Three* and *One*, in Figure 7.12 (a) and (b) respectively. Similarly, using gradient flow, with a small perturbation along the positive or negative eigendirections, we obtain the pathway between *Three* and *One* via the index-4 $Biaixial(BB2)$ state. The transient states on the biaxial pathway are plotted in Figure 7.13 (a) and (b).

Large splay regime

The preceding arguments suggest that the key to observing an uniaxial pathway which untwists, is splay. Recall, in Section 7.2.4 we analysed the large splay limit represented by $L_2 \to \infty$, where we found the energy (7.1.4) essentially reduces to $\int_0^1 |\nabla \cdot \mathbf{Q}|^2 \, \mathrm{d}y$, so that splay free configurations satisfying (7.2.16) would be minimisers. Therefore, we might expect that in regimes where splay is energetically

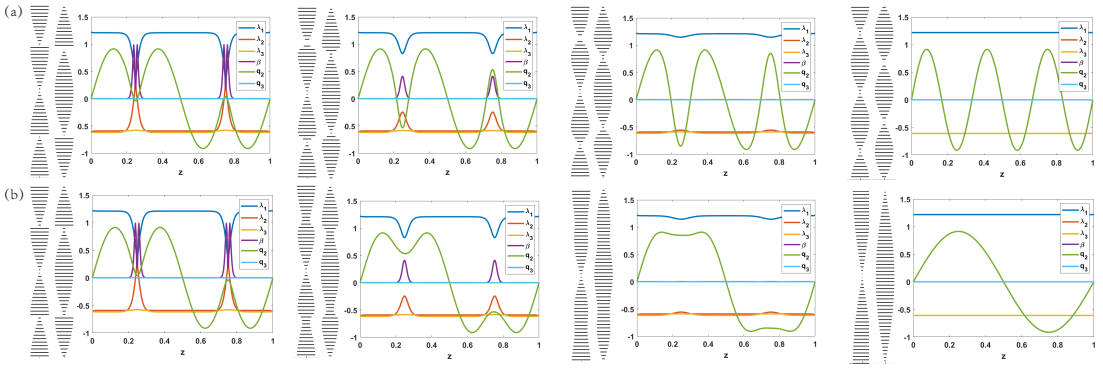

Figure 7.13: The pathway between the stable states *Three* and *One* via index-4 $Biaxial(BB2)$, when $\lambda = 3500$, $\eta = 4.5$, $\sigma = 2\pi$. (a) The pathway from $Biaxial(BB2)$ to *Three*. (b) The pathway from $Biaxial(BB2)$ to *One*.

expensive (i.e., large L_2), that the splay free biaxial pathway between the one and three twist states, is preferred to the uniaxial pathway. We now investigate the impact of large splay to answer this. This is practically implemented by fixing $H = 0.773\mu$m, $C = 3500$Nm^{-2}, $L_4 = 1$pN, $\sigma = 2\pi$, and then increasing L_2 in varying step sizes starting from $L_2 = 0.598$pN, up to $L_2 = 36.45$pN.

We find for $L_2 = 2.98$pN, that the index of $Biaxial(BB2)$ falls from 4 to 2, and this remains true until $L_2 = 36.45$pN (at least). As we increase L_2, the visual appearance of $Biaxial(BB2)$ is qualitatively the same to what is presented in Figure 7.7 (i.e., when $L_2 = 0.598$pN), in that it has two biaxial tori and remains splay free. As such we omit plots of these solutions. Moving onto $Uniaxial(Z2)$, it remains an index-1 saddle point until $L_2 = 36.45$pN, at which point we can no longer find it. As such, we conclude $Uniaxial(Z2)$ no longer exists as a critical point for $L_2 \geq 36.45$pN (approximately). Again, we omit plots of $Uniaxial(Z2)$ for large L_2 as the qualitative features are unchanged.

To determine which pathway, uniaxial or biaxial, is preferred between the one and three twist states, we now compute the associated energy barriers. We define

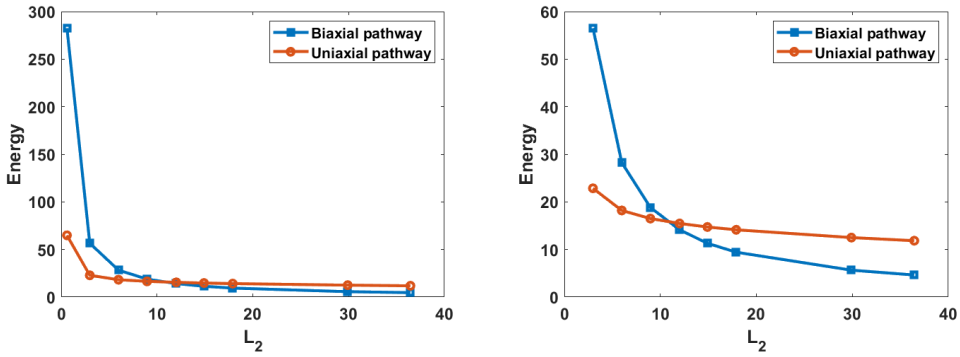

(a) (b)

Figure 7.14: (a) Plot of the (dimensionless) energy barrier between *One*, and $Uniaxial(Z2)$ and $Biaxial(BB2)$, as the splay elastic constant L_2 is varied (L_2 is in pN). (b) The same plot with the first data point omitted.

the energy barrier to be the energy difference between either $Uniaxial(Z2)$, or $Biaxial(BB2)$, and the *One* or *Three* twist state. By energy, we mean the value of (7.1.4) at that critical point. We plot the energy barrier between *One* and both $Uniaxial(Z2)$ and $Biaxial(BB2)$, in Figure 7.14. We omit the same plot for the three twist state, since the energy barrier values are nearly identical to the one twist case. As L_2 increases, the energy barrier of both the uniaxial and biaxial pathway decrease, however, the energy barrier of the biaxial pathway decreases quicker so that for $L_2 \geq 11$pN (approximately), the biaxial pathway is always preferred. In fact, for $L_2 \geq 36.45$pN (approximately), when $Uniaxial(Z2)$ no longer exists, the pathway can only be mediated by $Biaxial(BB2)$.

7.3.4 Results: inhomogeneous boundary conditions

We now extend our study of solution landscapes for one-dimensional cholesteric liquid crystals, by considering conflicting Dirichlet boundary conditions. The

boundary conditions are as follows:

$$\begin{aligned} &q_1(0) = \frac{2}{3}s_+,\ q_1(1) = -\frac{1}{3}s_+, \\ &q_2(0) = q_2(1) = q_3(0) = q_3(1) = q_5(0) = q_5(1) = 0, \\ &q_4(0) = -\frac{1}{3}s_+,\ q_4(1) = \frac{2}{3}s_+. \end{aligned} \tag{7.3.12}$$

These are again uniaxial boundary conditions which can be expressed equivalently as

$$\mathbf{Q}(0) = s_+\left(\mathbf{n}\otimes\mathbf{n} - \frac{1}{3}\mathbf{I}_3\right),\ \text{with } \mathbf{n} = (1,0,0),$$
$$\text{and } \mathbf{Q}(1) = s_+\left(\mathbf{n}\otimes\mathbf{n} - \frac{1}{3}\mathbf{I}_3\right),\ \text{with } \mathbf{n} = (0,1,0).$$

This means we have planar boundary conditions for $\mathbf{n}$ at $z = 0$, and normal/homeotropic boundary conditions at $z = 1$, ensuring the director rotates by some odd multiple of $\frac{\pi}{2}$ between the bounding plates. As such, we expect the following modification to the limiting profile (7.2.8)

$$\begin{aligned} \mathbf{Q}_\omega(z) &= s_+\left(\mathbf{n}\otimes\mathbf{n} - \frac{1}{3}\mathbf{I}_3\right) \quad \mathbf{n}_{\omega/2} = \left(\cos\left(\frac{\omega\pi z}{2}\right), \sin\left(\frac{\omega\pi z}{2}\right), 0\right), \\ &= s_+\begin{pmatrix} \cos^2\left(\frac{\omega\pi z}{2}\right) - \frac{1}{3} & \cos\left(\frac{\omega\pi z}{2}\right)\sin\left(\frac{\omega\pi z}{2}\right) & 0 \\ \cos(\frac{\omega\pi z}{2})\sin(\frac{\omega\pi z}{2}) & \sin^2\left(\frac{\omega\pi z}{2}\right) - \frac{1}{3} & 0 \\ 0 & 0 & -\frac{1}{3} \end{pmatrix}, \end{aligned} \tag{7.3.13}$$

where $\omega = 2n+1$ for $n \in \mathbb{Z}$, to be a good approximation to states with $\frac{\omega}{2}$ twists. This is indeed a good approximation to such states, as well as an excellent initial condition for for finding them.

The goal of this section is to confirm that the predictions of Section 7.3.1 relating to pathway types, still hold true under different boundary conditions. That is, (i)

we have a defect free quasi-uniaxial pathway and a pathway containing maximal biaxiality, between the 0.5 and 2.5 twist states, since the twist number changes by two, but (ii) only a pathway containing maximal biaxiality between the 0.5 and 1.5, or 1.5 and 2.5 twist states, as the twist number changes by one. Hence, supporting the claim that these pathway types are a bulk effect, independent of the boundary conditions. In this study, we again take $\lambda = 3500$, $\eta = 4.5$ and $\sigma = 2\pi$, so we can draw comparisons with the homogeneous case. We use the same nomenclature as in the homogeneous case and label the stable solution as 0.5 *twist*, 1.5 *twist* and 2.5 *twist* (see Figure 7.17 for these solutions).

We begin by finding the parent state. To do this, we take an initial condition that linearly interpolates between the conflicting boundary conditions for q_1 and q_4, along with constant initial conditions for q_2, q_3 and q_4, i.e.,

$$q_1(z) = s_+\left(-z + \frac{2}{3}\right),\ q_4(z) = s_+\left(z - \frac{1}{3}\right), \tag{7.3.14a}$$

$$q_2(z) = q_3(z) = q_5(z) = 0. \tag{7.3.14b}$$

Using them, we find an index-4 parent state which we label as $Biaxial(BB2.5)$, since it is splay free and has two biaxial tori (see Figure 7.15). The biaxial tori in this case are closer to the boundary of our domain when compared to the homogeneous counterpart (the same comments as in the homogeneous case apply to the eigenvalues of all the biaxial critical points in the current study). The q_2 profile is also substantially different and has a period of two and a half.

With the parent state identified we now discuss the solution landscape. For the inhomogeneous case, we find nine saddle points, four index-1 saddles ($Uniaxial(Z1.5)$, $Uniaxial\_2(Z1.5)$, index-1 $BZ2.5$, and index-1 $BZ2.5\_2$), four index-2 saddles ($B1.5$, $B1.5\_2$, index-2 $BZ2.5$, and index-2 $BZ2.5\_2$), and the index-4 parent

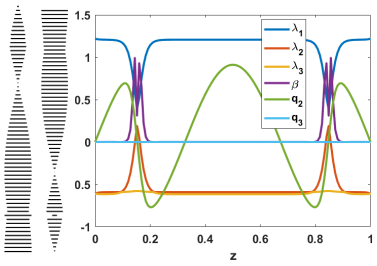

$Biaxial(BB2.5)$ - index-4 saddle

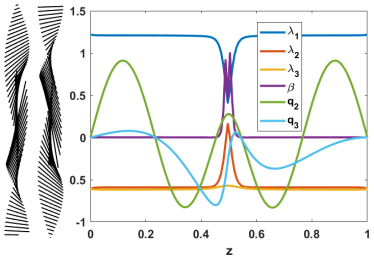

$BZ2.5$ - index-2 saddle

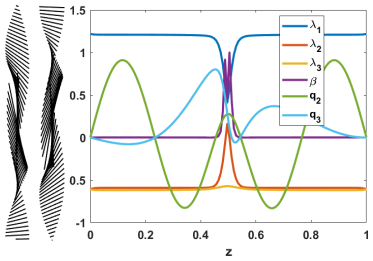

$BZ2.5\_2$ - index-2 saddle

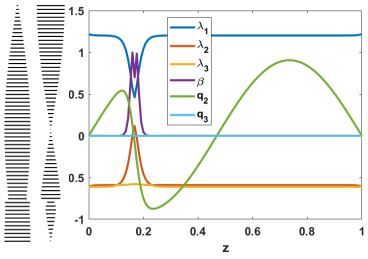

$B1.5$ - index-2 saddle

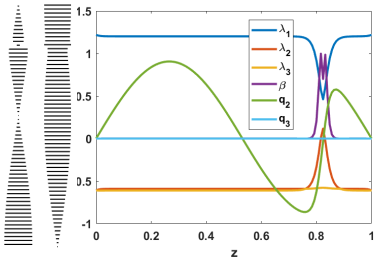

$B1.5\_2$ - index-2 saddle

Figure 7.15: Saddle points for $\lambda = 3500$, $\eta = 4.5$ and $\sigma = 2\pi$, with inhomogeneous boundary conditions.

state $Biaxial(BB2.5)$. Unlike the homogeneous, case we do not find any index-2 states with two biaxial tori, instead, they all have one biaxial torus. We find two index-2 states with splay, $BZ2.5$ and $BZ2.5\_2$ (Figure 7.15), which have a biaxial torus at the centre of the domain and vary in the sign of q_3 and q_5. The index-1 states $BZ2.5$ and $BZ2.5\_2$ (Figure 7.16) have the same features, hence we use the same nomenclature. $B1.5$ and $B1.5\_2$ (Figure 7.15), are splay free index-2 states that differ in the location of their biaxial tori, which can be found at either end of the domain. Finally, we have a pair of index-1 uniaxial saddle points which we label as $Uniaxial(Z1.5)$ and $Uniaxial\_2(Z1.5)$ (see Figure 7.15) and they differ in the sign of q_3 and q_5. These uniaxial critical points are analogous to those in our homogeneous study. We plot the splay and twist measures for $Uniaxial(Z1.5)$, index-1 $BZ2.5$, and $Biaxial(BB2.5)$, in Figure 7.18, where the same comments from the homogeneous case apply. Finally, we note that the rule for the index of critical points outlined in (7.3.11), does not hold for the inhomogeneous case.

The solution landscape for $\lambda = 3500$, $\eta = 4.5$ and $\sigma = 2\pi$, with the boundary conditions (7.3.12), is shown in Figure 7.19. We find an uniaxial pathway connecting the 0.5 and 2.5 twist states, which can be mediated via either of the index-1 states $Uniaxial(Z1.5)$ and $Uniaxial\_2(Z1.5)$, while we have a splay free biaxial pathway (containing maximal biaxiality) between the same states mediated by the parent $Biaxial(BB2.5)$ state. Some transient states along the splay mediated uniaxial pathway, and splay free biaxial pathway, are shown in Figure 7.20 and Figure 7.21, respectively. We only have biaxial pathways (containing maximal biaxiality) between either 0.5 and 1.5, or 1.5 and 2.5 twist states, since there are no uniaxial critical points connecting these pairs. These results are analogous to our homogeneous study and again consistent with Theorem 7.3.1 and Theorem 7.3.2.

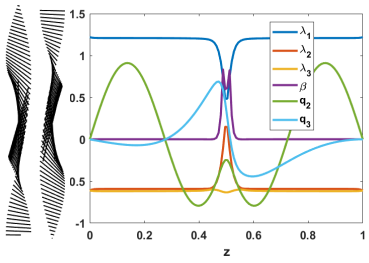

$BZ2.5$ - index-1 saddle

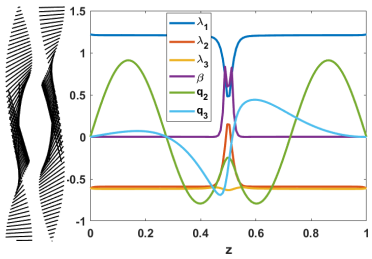

$BZ2.5\_2$ - index-1 saddle

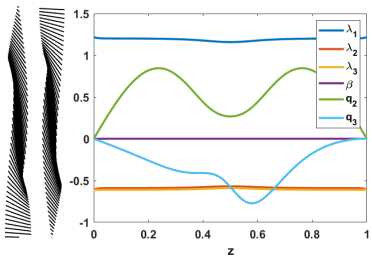

$Uniaxial(Z1.5)$ - index-1 saddle

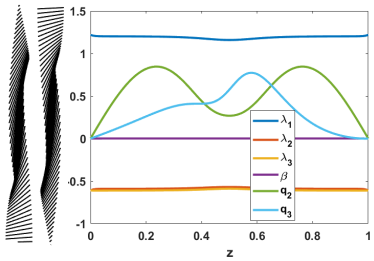

$Uniaxial\_2(Z1.5)$ - index-1 saddle

Figure 7.16: Saddle points for $\lambda = 3500$, $\eta = 4.5$ and $\sigma = 2\pi$, with inhomogeneous boundary conditions.

This supports the claim that these uniaxial and biaxial pathways are independent of boundary effects.

Large splay regime

We now complete a study of large splay for the inhomogeneous problem. The process and conclusions are analogous to the homogeneous case. $Biaxial(BB2.5)$

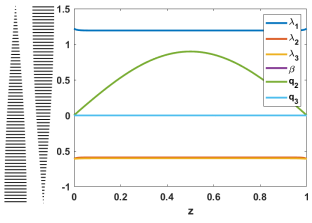

0.5 *twist*

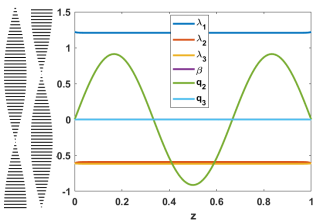

1.5 *twist*

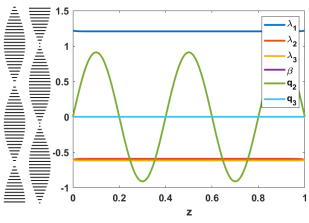

2.5 *twist*

Figure 7.17: Stable twist states for $\lambda = 3500$, $\eta = 4.5$ and $\sigma = 2\pi$, with inhomogeneous boundary conditions.

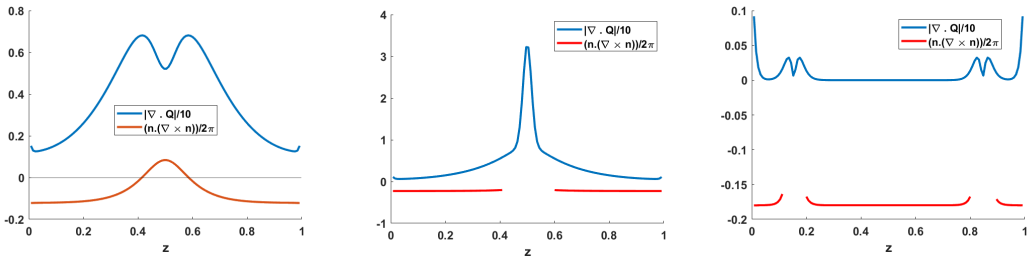

$Uniaxial(Z1.5)$ index-1 $BZ2.5$ $Biaxial(BB2.5)$

Figure 7.18: Plot of the twist and splay measures $\mathbf{n}\cdot(\nabla\times\mathbf{n})$ and $|\nabla\cdot\mathbf{Q}|$ respectively, for $Uniaxial(Z1.5)$, $BZ2.5$ and $Biaxial(BB2.5)$.

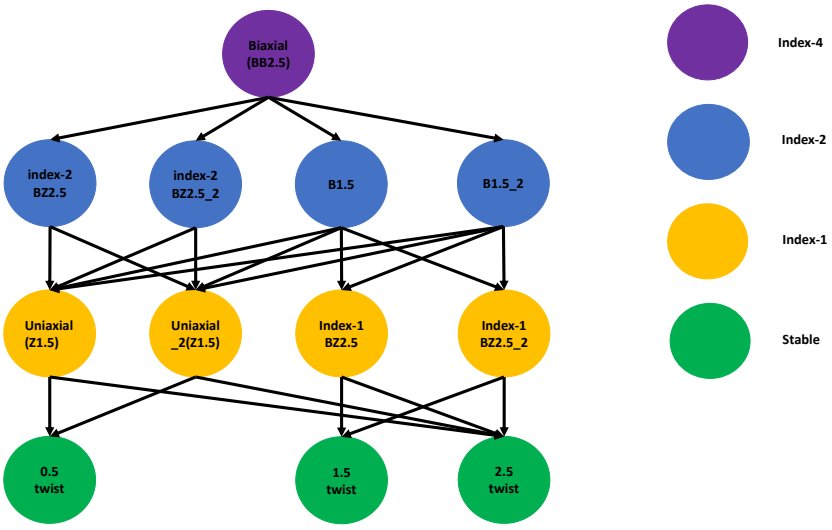

Figure 7.19: The solution landscape for $\lambda = 3500$, $\eta = 4.5$ and $\sigma = 2\pi$, with inhomogeneous boundary conditions.

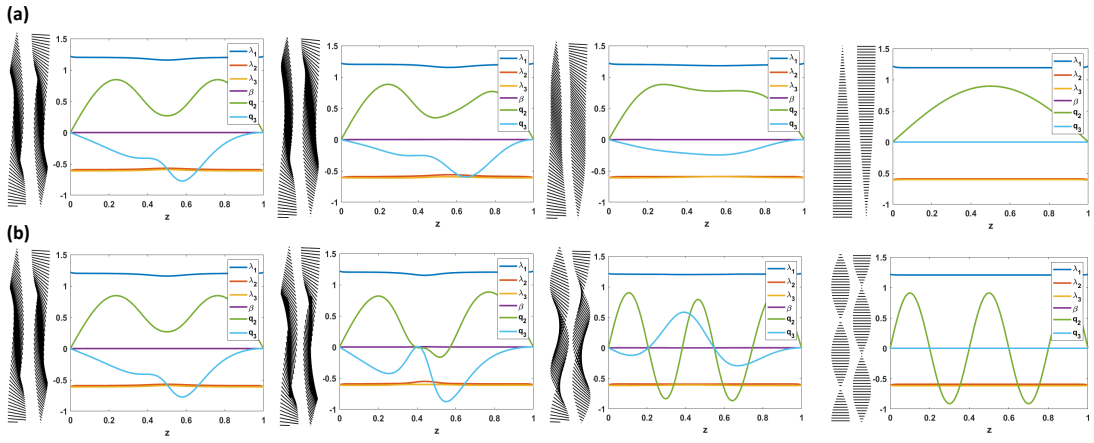

Figure 7.20: The pathway between the stable states 0.5 *twist* and 2.5 *twist* via index-1 $Uniaxial(Z1.5)$, when $\lambda = 3500$, $\eta = 4.5$, $\sigma = 2\pi$. (a) The pathway from $Uniaxial(Z1.5)$ to 0.5 *twist*. (b) The pathway from $Uniaxial(Z1.5)$ to 2.5 *twist*.

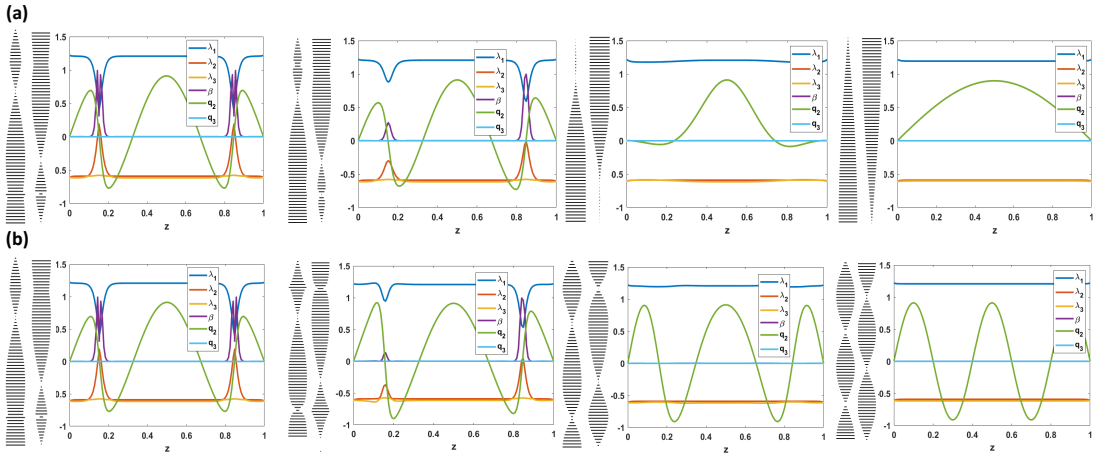

Figure 7.21: The pathway between the stable states 0.5 *twist* and 2.5 *twist* via index-4 $Biaxial(BB2.5)$, when $\lambda = 3500$, $\eta = 4.5$, $\sigma = 2\pi$. (a) The pathway from $Biaxial(BB2.5)$ to 0.5 *twist*. (b) The pathway from $Biaxial(BB2.5)$ to 2.5 *twist*.

is an index-2 saddle point for $L_2 \geq 2.98$pN and remains index-2 until $L_2 = 57.36$pN (at least). $Uniaxial(Z1.5)$ is an index-1 saddle point for $L_2 \leq 54.97$pN, but for larger values of L_2, we no longer find this solution and therefore conclude it is not a critical point for $L_2 > 54.97$pN (approximately). We omit the plots of both $Biaxial(BB2.5)$ and $Uniaxial(Z1.5)$ for large values of splay, as they remain qualitatively the same to the plots already presented. The energy barriers between the 0.5 *twist* and 2.5 *twist* states, and both $Uniaxial(Z1.5)$ and $Biaxial(BB2.5)$, can be found in Figure 7.22. For $L_2 \geq 13$pN (approximately), the biaxial pathway between 0.5 *twist* and 2.5 *twist* mediated by $Biaxial(BB2.5)$, is energetically preferred to the uniaxial pathway mediated by $Uniaxial(Z1.5)$.

Remark 7.3.4. We conclude by commenting on related previous works. In [113, 114], the authors consider unwinding transitions for cholesteric liquid crystals in the presence of an applied electric field, and with a Rapini-Papoular surface energy. Along such unwinding pathways, they find an uniaxial saddle point with out of plane deformation (splay), and this is visually similar to half of our uniaxial pathway. However, in contrast to our results, they find unwinding to be driven by deformation at the boundary. Finally, we note that these related works utilise an Oseen-Frank model, which unlike the LdG model, fails to capture biaxiality. This is why no splay free biaxial pathways, or biaxial critical points, have been reported and is why our work is needed.

7.4 Summary

In this chapter, we perform asymptotic analysis in four physically relevant limits: the limit of small domain heights, the limit of large domain heights, large anisotropy, and large splay. These limits give good preliminary insights into the types of behaviour we can expect e.g. uniaxiality for large domains and biaxiality for

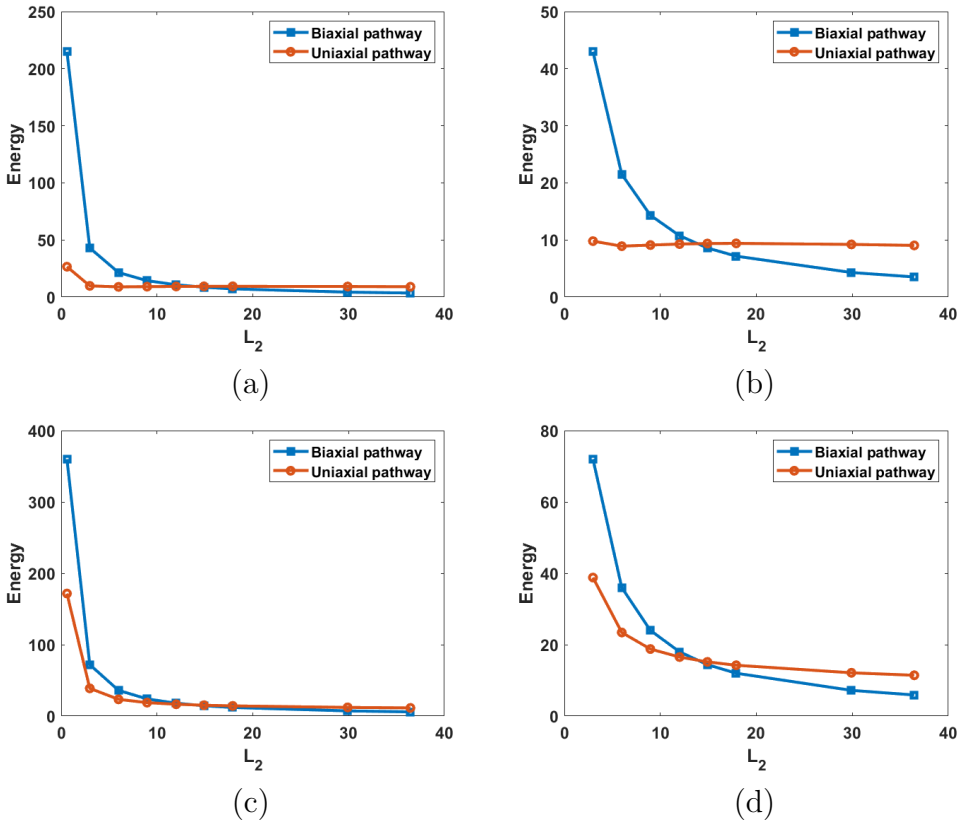

Figure 7.22: (a) Plot of the (dimensionless) energy barrier between 0.5 *twist*, and $Uniaxial(Z1.5)$ and $Biaxial(BB2.5)$, as the splay elastic constant L_2 is varied (L_2 is in pN). (b) The same plot with the first data point omitted. (c) and (d), are analogous to (a) and (b), but for the 2.5 *twist* state.

large anisotropy. Importantly, we find a characterisation for splay free solutions in Section 7.2.4, which proves useful in the proof of Theorem 7.3.2. Our asymptotic expressions also serve as good initial conditions for our numerical simulations and solution landscape exploration.

Motivated by topological results, we investigate the solution landscape for one-dimensional cholesteric liquid crystals, to gain an understanding of how such systems behave. These topological insights have been combined with classic variational methods, as well as the powerful HiOSD algorithm, and these different approaches agree beautifully. We have identified a clear choice between an uniaxial pathway permitted by splay mediated untwisting, and a splay free biaxial pathway (containing maximal biaxiality), when the change in twist number is even between the target states. Furthermore, in regimes where the splay constant L_2 is sufficiently large, we find the biaxial pathway is energetically preferred to the uniaxial pathway. This observation suggests a potential way to experimentally observe biaxiality, that is, by switching between different stable twisted states in regimes where splay is energetically expensive, biaxiality could be observed during the switching process. These results are seemingly independent of the imposed boundary conditions. This work is also a first step in establishing a dictionary of critical points that appear in cholesteric liquid crystals. Such critical points could potentially be exploited in the switching processes of soft devices.

Future work would include:

1. Investigating the solution landscape for different values of our dimensionless parameters. In particular, a thorough study of the solution landscape for large splay (small λ and η) would be illuminating.

2. A study with an imposed surface energy instead of Dirichlet boundary conditions, to further support the claim that these pathway types are a consequence of bulk effects in the cholesteric, not boundary effects.

Chapter 8

Conclusions

In this thesis, we study a variety of liquid crystalline systems in the Landau-de Gennes framework, namely, nematic liquid crystals, passive and active nematodynamics, ferronematics, and cholesteric liquid crystals. In all of these settings, we consider one-dimensional problems which can be relevant for microfludics, where the liquid crystal material is confined to thin/shallow channels or cells. As such, we consider coupled systems of ordinary differential equations with varying degrees of complexity, in every chapter of this thesis.

An overarching and key theme throughout this thesis has been that of order reconstruction (OR) and OR-type solutions. That is, solutions which describe polydomain structures possessing domain walls that separate potentially distinct sub-domains. OR solutions have distinct constant director profiles in each sub-domain, while OR-type solutions can have non-constant director profiles but still possess domain walls. OR solutions are well known for nematics, but in this thesis we have now identified OR solutions for ferronematics and passive nematodynamics with constant flow and pressure; as well as OR-type solutions

for passive and active nematodynamics without the requirement of constant flow and pressure. Our description of OR and OR-type solutions in nematodynamics is particularly powerful, given the resemblance of these solutions to experimental results (see the discussion in Section 2.3). In the one-dimensional nematic setting, we have built upon the work in [64] by investigating the effect of the imposed Dirichlet boundary conditions on the nematic director. In the **Q**-formulation, we have shown OR solutions are only compatible with orthogonal boundary conditions on the channel walls, while in the (s, θ)-formulation, when OR solutions are disallowed, we always have a unique solution to the governing equations.

Another key focus of this thesis is solution landscapes for the physical systems we investigate, i.e., trying to identify all the critical points of an energy functional and how they connect to one another. We are interested in solution landscapes as they give insight into how a multistable system may behave when switching between different stable states. In particular, the unstable critical points connecting them dictate selection dynamics and maybe observed during the switching process. In Chapter 6 and Chapter 7, we numerically study solution landscapes for ferronematics and cholesterics respectively via the high-index optimisation-based shrinking dimer method. For ferronematics, this approach yields additional information in the form of new OR solutions not identified in the numerical results of Chapter 5, and illustrates the importance of OR solutions in the solution landscape. Our study of solution landscapes for cholesterics is noteworthy as we identify both a biaxial and uniaxial pathway between certain stable states. Moreover, for physical regimes where the splay elastic constant (in the Landau-de Gennes framework) is large, we find the biaxial pathway is energetically cheaper than the uniaxial pathway. This suggests a possible approach for experimentally observing biaxiality, a problem of much contemporary interest.

Where appropriate, we indicate specific directions for future work for the problems in this thesis. Some overarching questions that deserve further investigation are as follows:

1. OR and OR-type solutions are seemingly a result of a Dirichlet elastic energy density and suitable asymmetric boundary conditions, which allow the order parameter to vanish. With this in mind, can we find universal principles that can be applied to any system with this structure, hence providing a language to describe what we call OR solutions in different physical settings?

2. As discussed in Section 2.3, there are experimental observations of textures that can be well described by OR and OR-type solutions in nematodynamics. However, there have been no experimental observations of OR solutions in ferronematics, or for the two- and three- dimensional analogues of OR solutions in nematics. This lack of experimental observation raises the question that OR solutions may just be a consequence of the mathematical models we consider. It may also be the case that the right experimental systems have not yet been designed to observe OR, or perhaps OR solutions are just approximations of the textures that would be observed. This is speculation and the physical status of OR solutions is unclear in these situations. A first step in addressing these points would be to employ molecular models where additional physics can be incorporated and see if our OR solutions survive. The connection between continuum and molecular models is an open question of huge importance. If we observe OR solutions in molecular models and identify reasons as to why, perhaps, we can gain insight on how to connect these two models.

Appendix A

Elliptic regularity

We now reproduce some arguments in elliptic regularity for completeness. We do this using (2.1.13) and the associated Euler-Lagrange equations (2.1.20), as an example.

Theorem A.0.1. *Let $f(p,z,x) : \mathbb{R}\times\mathbb{R}\times\Omega\to\mathbb{R}$ be a C^2 function. Assume $u\in C^2(\Omega)$, is a minimiser of*

$$inf\Big\{I(u)=\int_\Omega f(p,z,x)\ \mathrm{d}\Omega : u\in W^{1,2}(\Omega),\ u=u_b\ on\ \partial\Omega\Big\}, \tag{A.0.1}$$

then u satisfies the Euler-Lagrange equations associated with I for every $x\in\Omega$ [120].

Henceforth, we consider $\Omega\subset\mathbb{R}^2$ to be an open bounded set with Lipschitz boundary. We first note that the minimiser $\mathbf{Q}\in W^{1,2}(\Omega;S_0)$ (established by the direct method in the calculus of variations in Section 2.1.3) is a solution of the

weak form of the Euler-Lagrange equations i.e.,

$$-\int_\Omega \nabla Q_{ij}\cdot\nabla\phi \,\mathrm{d}\Omega = \int_\Omega \left(AQ_{ij} - B\left(Q_{ip}Q_{pj} - \frac{1}{3}\mathrm{tr}\mathbf{Q}^2\delta_{ij}\right) + C(\mathrm{tr}\mathbf{Q}^2)Q_{ij}\right)\phi \,\mathrm{d}\Omega, \tag{A.0.2}$$

for all $\phi \in W_0^{1,2}(\Omega)$ and $i,j = 1,2,3$. Here, $W_0^{1,2}(\Omega)$ is the space of functions in $W^{1,2}(\Omega)$ that vanish on $\partial\Omega$.

Applying the following theorems, we show $\mathbf{Q} \in C^2(\Omega)$ and therefore a classical solution of the Euler-Lagrange equations.

Theorem A.0.2. *(Elliptic Regularity Theorem) Let Ω be an open bounded set, and suppose $u \in W^{1,2}(\Omega)$ is such that*

$$\int_\Omega \nabla u\cdot\nabla\phi \,\mathrm{d}\Omega = \int_\Omega g\phi \,\mathrm{d}\Omega, \tag{A.0.3}$$

for all $\phi \in W_0^{1,2}(\Omega)$ and $g \in W^{k,2}(\Omega)$. Then $u \in W^{k+2,2}(\Omega)$ [74].

Theorem A.0.3. *(Sobolev Embedding Theorem) Let Ω be a bounded open set with Lipschitz boundary, then $W^{k,p}(\Omega) \subseteq W^{l,q}(\Omega)$ provided $k - \frac{2}{p} > l - \frac{2}{q}$. Furthermore, $W^{k,p}(\Omega) \subset C^r(\Omega)$ provided $k - \frac{2}{p} > r$ [121].*

We first show $g = AQ_{ij} - B\left(Q_{ip}Q_{pj} - \frac{1}{3}\mathrm{tr}\mathbf{Q}^2\delta_{ij}\right) + C(\mathrm{tr}\mathbf{Q}^2)Q_{ij} \in W^{0,2}(\Omega) = L^2(\Omega)$. From now on, we suppress the dependence of function spaces on Ω. Since $\mathbf{Q} \in W^{1,2}$, it is clear $\mathbf{Q} \in L^2$. From the Sobolev Embedding Theorem, $W^{1,2} \subseteq W^{0,q} = L^q$ for $2 \leq q < \infty$. Therefore, $\mathbf{Q} \in L^6$ i.e.,

$$\left(\int_\Omega |\mathbf{Q}|^6 \,\mathrm{d}\Omega\right)^{\frac{1}{6}} < \infty,$$

and $\mathbf{Q}^3 \in L^2$ as a result. Similarly, $\mathbf{Q} \in L^4$ so that $\mathbf{Q}^2 \in L^2$. Hence, $g \in W^{0,2}$ and $\mathbf{Q} \in W^{2,2}$ by the Elliptic Regularity Theorem.

We next show $g \in W^{1,2}$, which requires $\mathbf{Q}^2, \mathbf{Q}^3 \in W^{1,2}$. We know $\mathbf{Q}^3 \in L^2$, so we

only need $\mathbf{Q}^2 \frac{\partial \mathbf{Q}}{\partial x_k} \in L^2$ $(k = 1, 2)$. Applying the Cauchy-Schwarz inequality,

$$\left| \int_\Omega \mathbf{Q}^2 \frac{\partial \mathbf{Q}}{\partial x_k} \, \mathrm{d}\Omega \right|^2 \leq \int_\Omega |\mathbf{Q}^2|^2 \, \mathrm{d}\Omega \int_\Omega \left| \frac{\partial \mathbf{Q}}{\partial x_k} \right|^2 \, \mathrm{d}\Omega < \infty$$

implying $\mathbf{Q}^2 \frac{\partial \mathbf{Q}}{\partial x_k} \in L^2$. Analogous arguments show $\mathbf{Q}^2 \in W^{1,2}$. Consequently, $g \in W^{1,2}$ and the Elliptic Regularity Theorem yields $\mathbf{Q} \in W^{3,2}$.

Repeating the same steps shows $\mathbf{Q} \in W^{4,2}$. Applying the second part of the Sobolev Embedding Theorem, $W^{4,2} \subset C^2$ so that $\mathbf{Q} \in C^2$, as required. Since $\mathbf{Q} \in C^2$ and solves (A.0.1), it is a classical solution of the Euler-Lagrange equation (2.1.20) in Ω. In fact, continuing this bootstrapping process shows $\mathbf{Q} \in C^\infty$. An application of Theorem 1 in [122], then implies the solution $\mathbf{Q}$ of (2.1.20) is (real) analytic in Ω.

Bibliography

[1] J. Dalby, Y. Han, A. Majumdar and L. Mrad, 'A multi-faceted study of nematic order reconstruction in microfluidic channels,' *arXiv:2204.07808 [math.AP]*, 2022.

[2] J. Dalby, P. Farrell, A. Majumdar and J. Xia, 'One-Dimensional Ferronematics in a Channel: Order Reconstruction, Bifurcations and Multistability,' *SIAM Journal on Applied Mathematics*, vol. 82, no. 2, pp. 694–719, 2022.

[3] Y. Han, J. Dalby, A. Majumdar, B. M. G. D. Carter and T. Machon, 'Uniaxial versus biaxial pathways in one-dimensional cholesteric liquid crystals,' *Physical Review Research*, vol. 4, no. 3, p. L032018, 2022.

[4] E. van den Pol, D. M. E. Thies–Weesie, A. V. Petukhov, D. V. Byelov and G. J. Vroege, 'Uniaxial and biaxial liquid crystal phases in colloidal dispersions of board-like particles,' *Liquid Crystals*, vol. 37, no. 6-7, pp. 641–651, 2010.

[5] X. Ma and E. Tjhung, 'Banana- and pizza-slice-shaped mesogens give a new constrained O(n) ferromagnet universality class,' *Physical Review E*, vol. 100, no. 1, p. 012 701, 2019.

[6] F. Reinitzer, 'Beiträge zur kenntniss des cholesterins,' *Monatshefte für Chemie*, vol. 9, pp. 421–441, 1888.

[7] D. Dunmur and T. Sluckin, *Soap, science, and flat-screen TVs: a history of liquid crystals*. Oxford: Oxford University Press, 2011.

[8] H. Kelker, 'History of liquid crystals,' *Molecular Crystals and Liquid Crystals*, vol. 21, no. 1-2, pp. 1–48, 1973.

[9] G. Friedel, 'Les états mésomorphes de la matière,' *Annales de Physique*, vol. 18, pp. 273–474, 1922.

[10] M. J. Stephen and J. P. Straley, 'Physics of liquid crystals,' *Reviews of Modern Physics*, vol. 46, no. 4, p. 617, 1974.

[11] N. J. Mottram and C. J. Newton, 'Introduction to Q-tensor theory,' *arXiv:1409.3542 [cond-mat.soft]*, 2014.

[12] I. W. Stewart, *The Static and Dynamic Continuum Theory of Liquid Crystals: A Mathematical Introduction*. London and New York: Taylor & Francis, 2004.

[13] J. M. Ball, E. Feireisl and F. Otto, *Mathematical Thermodynamics of Complex Fluids: Cetraro, Italy 2015*, 1st edition. Cham: Springer International Publishing, 2017.

[14] P. G. de Gennes. and J. Prost, *The Physics of Liquid Crystals*, 2nd edition. Oxford: Clarendon Press, 1993.

[15] F. P. da Costa, M. Grinfeld, N. J. Mottram, J. T. Pinto and K. Xayxanadasy, 'Steady state solutions in a model of a cholesteric liquid crystal sample,' *Afrika mathematica*, vol. 32, no. 3-4, pp. 645–672, 2020.

[16] P. J. W. E. Priestley and P. Sheng, *Introduction to Liquid Crystals*. New York and London: Plenum Press, 1975.

[17] E. G. Virga, *Variational theories for liquid crystals*. London: Chapman & Hall, 1994.

[18] H. Agha and C. Bahr, 'Nematic line defects in microfluidic channels: Wedge, twist and zigzag disclinations,' *Soft Matter*, vol. 14, no. 4, pp. 653–664, 2018.

[19] J. P. F. Lagerwall and G. Scalia, 'A new era for liquid crystal research: Applications of liquid crystals in soft matter nano-, bio- and microtechnology,' *Current Applied Physics*, vol. 12, no. 6, pp. 1387–1412, 2012.

[20] J. C. Jones, 'The fiftieth anniversary of the liquid crystal display,' *Liquid Crystals Today*, vol. 27, no. 3, pp. 44–70, 2018.

[21] J. C. Jones and S. Beldon, 'High Image-Content Zenithal Bistable Devices,' *SID International Symposium Digest of technical papers*, vol. 35, no. 1, pp. 140–143, 2004.

[22] C. Tsakonas, A. J. Davidson, C. V. Brown and N. J. Mottram, 'Multistable alignment states in nematic liquid crystal filled wells,' *Applied physics letters*, vol. 90, no. 11, p. 111 913, 2007.

[23] J. Bailey, P. Morgan, H. Gleeson and J. C. Jones, 'Switchable Liquid Crystal Contact Lenses for the Correction of Presbyopia,' *Crystals*, vol. 8, no. 1, p. 29, 2018.

[24] J. E. Lydon, 'The DNA double helix-the untold story,' *Liquid Crystals Today*, vol. 12, no. 2, pp. 1–9, 2003.

[25] S. Sivakumar, K. L. Wark, J. K. Gupta, N. L. Abbott and F. Caruso, 'Liquid Crystal Emulsions as the Basis of Biological Sensors for the

Optical Detection of Bacteria and Viruses,' *Advanced functional materials*, vol. 19, no. 14, pp. 2260–2265, 2009.

[26] A. Yaghmur and O. Glatter, 'Characterization and potential applications of nanostructured aqueous dispersions,' *Advances in colloid and interface science*, vol. 147, no. C, pp. 333–342, 2009.

[27] Y. Geng, J. Noh, I. Drevensek-Olenik, R. Rupp, G. Lenzini and J. P. F. Lagerwall, 'High-fidelity spherical cholesteric liquid crystal Bragg reflectors generating unclonable patterns for secure authentication,' *Scientific Reports*, vol. 6, no. 26840, 2016.

[28] M. Schwartz, G. Lenzini, Y. Geng, P. B. Rønne, P. Y. A. Ryan and J. P. F. Lagerwall, 'Cholesteric Liquid Crystal Shells as Enabling Material for Information-Rich Design and Architecture,' *Advanced materials*, vol. 30, no. 30, p. 1 707 382, 2018.

[29] Y. Geng, R. Kizhakidathazhath and J. P. F. Lagerwall, 'Encoding Hidden Information onto Surfaces Using Polymerized Cholesteric Spherical Reflectors,' *Advanced functional materials*, vol. 31, no. 21, p. 2 100 399, 2021.

[30] M. Schwartz, Y. Geng, H. Agha, R. Kizhakidathazhath, D. Liu, G. Lenzini and J. P. F. Lagerwall, 'Linking physical objects to their digital twins via fiducial markers designed for invisibility to humans,' *Multifunctional Materials*, vol. 4, no. 2, p. 22 002, 2021.

[31] F. Brochard and P. G. de Gennes, 'Theory of magnetic suspensions in liquid crystals,' *Journal de Physique*, vol. 31, no. 7, pp. 691–708, 1970.

[32] J. Rault, P. E. Cladis and J. P. Burger, 'Ferronematics,' *Physics Letters A*, vol. 32, no. 3, pp. 199–200, 1970.

[33] S. V. Burylov and Y. L. Raikher, 'Macroscopic Properties of Ferronematics Caused by Orientational Interactions on the Particle Surfaces. I. Extended Continuum Model,' *Molecular Crystals and Liquid Crystals*, vol. 258, no. 1, pp. 107–122, 1995.

[34] M. C. Calderer, A. DeSimone, D. Golovaty and A. Panchenko, 'An Effective Model for Nematic Liquid Crystal Composites with Ferromagnetic Inclusions,' *SIAM Journal on Applied Mathematics*, vol. 74, no. 2, pp. 237–262, 2014.

[35] A. Mertelj, D. Lisjak, M. Drofenik and M. Čopič, 'Ferromagnetism in suspensions of magnetic platelets in liquid crystals,' *Nature*, vol. 504, no. 7479, pp. 237–241, 2013.

[36] Q. Liu, P. J. Ackerman, T. C. Lubensky and I. I. Smalyukh, 'Biaxial ferromagnetic liquid crystal colloids,' *Proceedings of the National Academy of Sciences*, vol. 113, no. 38, pp. 10 479–10 484, 2016.

[37] S. Mondal, I. M. Griffiths, F. Charlet and A. Majumdar, 'Flow and nematic director profiles in a microfluidic channel: The interplay of nematic material constants and backflow,' *Fluids*, vol. 3, no. 2, p. 39, 2018.

[38] J. G. Cuennet, A. E. Vasdekis and D. Psaltis, 'Optofluidic-tunable color filters and spectroscopy based on liquid-crystal microflows,' *Lab on a Chip*, vol. 13, no. 14, pp. 2721–2726, 2013.

[39] A. Sengupta, C. Bahr and S. Herminghaus, 'Topological microfluidics for flexible micro-cargo concepts,' *Soft Matter*, vol. 9, no. 30, pp. 7251–7260, 2013.

[40] S. Ramaswamy, 'The Mechanics and Statistics of Active Matter,' *Annual Review of Condensed Matter Physics*, vol. 1, pp. 323–345, 2010.

[41] M. C. Marchetti, J. F. Joanny, S. Ramaswamy, T. B. Liverpool, J. Prost, M. Rao and R. A. Simha, 'Hydrodynamics of soft active matter,' *Reviews of Modern Physics*, vol. 85, no. 3, p. 1143, 2013.

[42] S. Shankar., S. Ramaswamy., M. C. Marchetti. and M. J. Bowick, 'Defect Unbinding in Active Nematics,' *Physical Review Letters*, vol. 121, no. 10, p. 108 002, 2018.

[43] G. Salbreux., J. Prost. and J. F. Joanny, 'Hydrodynamics of Cellular Cortical Flows and the Formation of Contractile Rings,' *Physical Review Letters*, vol. 103, no. 5, p. 058 102, 2009.

[44] L. Giomi, M. J. Bowick, P. Mishra, R. Sknepnek and M. C. Marchetti, 'Defect dynamics in active nematics,' *Philosophical Transactions of the Royal Society A*, vol. 372, no. 2029, p. 20 130 365, 2014.

[45] J. Eun, J. Pollard, S.-J. Kim, T. Machon and J. Jeong, 'Layering Transitions and Metastable Structures of Cholesteric Liquid Crystals in Cylindrical Confinement,' *Proceedings of the National Academy of Sciences*, vol. 118, no. 33, p. 1, 2021.

[46] I. M. Tambovtsev, A. O. Leonov, I. S. Lobanov, A. D. Kiselev and V. M. Uzdin, 'Topological structures in chiral media: Effects of confined geometry,' *Physical Review E*, vol. 105, no. 3, p. 034 701, 2022.

[47] T. Machon and G. P. Alexander, 'Knots and nonorientable surfaces in chiral nematics,' *Proceedings of the National Academy of Sciences*, vol. 110, no. 35, pp. 14 174–14 179, 2013.

[48] P. J. Ackerman and I. I. Smalyukh, 'Diversity of Knot Solitons in Liquid Crystals Manifested by Linking of Preimages in Torons and Hopfions,' *Physical Review X*, vol. 7, no. 1, p. 011 006, 2017.

[49] G. Posnjak, S. Čopar and I. Muševič, 'Hidden topological constellations and polyvalent charges in chiral nematic droplets,' *Nature Communications*, vol. 8, no. 1, p. 14 594, 2017.

[50] J.-I. Fukuda and S. Žumer, 'Quasi-two-dimensional Skyrmion lattices in a chiral nematic liquid crystal,' *Nature Communications*, vol. 2, no. 1, p. 246, 2011.

[51] A. Darmon, M. Benzaquen, S. Čopar, O. Dauchota and T. Lopez-Leon, 'Topological defects in cholesteric liquid crystal shells,' *Soft Matter*, vol. 12, no. 1, pp. 9280–9288, 2016.

[52] D. B. Emersona, P. E. Farrell, J. H. Adlera, S. P. MacLachlan and T. J. Atherton, 'Computing equilibrium states of cholesteric liquid crystals in elliptical channels with deflation algorithms,' *Liquid Crystals*, vol. 45, no. 3, pp. 341–350, 2018.

[53] A. R. Fialho, N. R. Bernardino, N. M. Silvestre and M. M. T. da Gama, 'Effect of curvature on cholesteric liquid crystals in toroidal geometries,' *Physical Review E*, vol. 95, no. 1, p. 012 702, 2017.

[54] I. I. Smalyukh and O. D. Lavrentovich, 'Three-dimensional director structures of defects in Grandjean-Cano wedges of cholesteric liquid crystals studied by fluorescence confocal polarizing microscopy,' *Physical Review E*, vol. 66, no. 5, p. 051 703, 2002.

[55] V. S. R. Jampani, R. H. Volpe, K. R. de Sousa, J. F. Machado, C. M. Yakacki and J. P. F. Lagerwall, 'Liquid crystal elastomer shell

actuators with negative order parameter,' *Science Advances*, vol. 5, no. 4, eaaw2476, 2019.

[56] C. Oseen, 'The theory of liquid crystals,' *Transactions of the Faraday Society*, vol. 29, no. 140, pp. 883–899, 1933.

[57] F. C. Frank, 'I. Liquid crystals. On the theory of liquid crystals,' *Discussions of the Faraday Society*, vol. 25, pp. 19–28, 1958.

[58] J. L. Ericksen, 'Liquid crystals with variable degree of orientation,' *Archive for Rational Mechanics and Analysis*, vol. 113, pp. 97–120, 1991.

[59] J. M. Ball, 'Mathematics and liquid crystals,' *Molecular Crystals and Liquid Crystals*, vol. 647, no. 1, pp. 1–27, 2017.

[60] A. Majumdar, 'Equilibrium order parameters of nematic liquid crystals in the Landau-de Gennes theory,' *European Journal of Applied Mathematics*, vol. 21, no. 2, pp. 181–203, 2010.

[61] N. Schopohl and T. J. Sluckin, 'Defect Core Structure in Nematic Liquid Crystals,' *Physical Review Letters*, vol. 59, no. 22, pp. 2582–2584, 1987.

[62] H. Mori, E. C. Gartland Jr, J. R. Kelly and P. J. Bos, 'Multidimensional Director Modeling Using the Q Tensor Representation in a Liquid Crystal Cell and Its Application to the π Cell with Patterned Electrodes,' *Japanese Journal of Applied Physics*, vol. 38, pp. 135–146, 1999.

[63] Y. Han, J. Harris, A. Majumdar and L. Zhang, 'Elastic anisotropy in the reduced Landau-de Gennes model,' *Proceedings of the Royal Society A: Mathematical, Physical and Engineering Sciences*, vol. 478, no. 2261, p. 20 210 966, 2022.

[64] X. Lamy, 'Bifurcation analysis in a frustrated nematic cell,' *Journal of Nonlinear Science*, vol. 24, no. 6, pp. 1197–1230, 2014.

[65] A. Majumdar and A. Zarnescu, 'Landau-de Gennes theory of nematic liquid crystals: The Oseen–Frank limit and beyond,' *Archive for Rational Mechanics and Analysis*, vol. 196, no. 1, pp. 227–280, 2010.

[66] G. Canevari, A. Majumdar and A. Spicer, 'Order reconstruction for nematics on squares and hexagons: a Landau-de Gennes study,' *SIAM Journal on Applied Mathematics*, vol. 77, no. 1, pp. 267–293, 2017.

[67] M. Nobili and G. Durand, 'Disorientation-induced disordering at a nematic liquid-crystal solid interface,' *Physical Review A*, vol. 46, no. 10, p. R6174–R6177, 1992.

[68] C. Luo, A. Majumdar and R. Erban, 'Multistability in planar liquid crystal wells,' *Physical Review E*, vol. 85, no. 6, p. 061 702, 2012.

[69] K. Bisht, V. Banerjee, P. Milewski and A. Majumdar, 'Magnetic nanoparticles in a nematic channel: A one-dimensional study,' *Physical Review E*, vol. 100, no. 1, p. 012 703, 2019.

[70] K. Bisht, Y. Wang, V. Banerjee and A. Majumdar, 'Tailored morphologies in two-dimensional ferronematic wells,' *Physical Review E*, vol. 101, no. 2, p. 022 706, 2020.

[71] J. Yin, L. Zhang and P. Zhang, 'High-index optimization-based shrinking dimer method for finding high-index saddle points,' *SIAM Journal on Scientific Computing*, vol. 41, no. 6, A3576–A3595, 2019.

[72] S. Kralj, E. G. Virga and S. Žumer, 'Biaxial torus around nematic point defects,' *Physical Review E*, vol. 60, no. 2, pp. 1858–1866, 1999.

[73] S. Kralj and A. Majumdar, 'Order reconstruction patterns in nematic liquid crystal wells,' *Proceedings of the Royal Society A: Mathematical, Physical and Engineering Sciences*, vol. 470, no. 2169, p. 20 140 276, 2014.

[74] L. C. Evans, *Partial Differential Equations*, 2nd edition. Providence, RI: American Mathematical Society, 2010.

[75] A. H. Lewis, I. Garlea, J. Alvarado, O. J. Dammone, P. D. Howell, A. Majumdar, B. M. Mulder, M. Lettinga, G. H. Koenderink and D. G. Aarts, 'Colloidal liquid crystals in rectangular confinement: Theory and experiment,' *Soft Matter*, vol. 10, no. 39, pp. 7865–7873, 2014.

[76] D. Golovaty, J. A. Montero and P. Sternberg, 'Dimension Reduction for the Landau-de Gennes Model in Planar Nematic Thin Films,' *Journal of Nonlinear Science*, vol. 25, no. 6, pp. 1431–1451, 2015.

[77] Y. Wang, G. Canevari and A. Majumdar, 'Order reconstruction for nematics on squares with isotropic inclusions: a Landau-de Gennes study,' *SIAM Journal on Applied Mathematics*, vol. 79, no. 4, pp. 1314–1340, 2019.

[78] F. Bethuel, H. Brezis and F. Hélein, 'Asymptotics for the minimization of a Ginzburg–Landau functional,' *Calculus of Variations and Partial Differential Equations.*, vol. 1, no. 2, pp. 123–148, 1993.

[79] H. Yucen, A. Majumdar and L. Zhang, 'A Reduced Study for Nematic Equilibria on Two-Dimensional Polygons,' *SIAM Journal on Applied Mathematics*, vol. 80, no. 4, pp. 1678–1703, 2020.

[80] J. Yin, Y. Wang, J. Z. Y. Chen, P. Zhang and L. Zhang, 'Construction of a Pathway Map on a Complicated Energy Landscape,' *Physical Review Letters*, vol. 124, no. 9, p. 090 601, 2020.

[81] A. Braides, 'A Handbook of Γ-Convergence,' in *Handbook of Differential Equations: Stationary Partial Differential Equations*, vol. 3, North-Holland, Amsterdam: Elsevier, 2006, pp. 101–213.

[82] S. Čopar, Ž. Kos, T. Emeršič and U. Tkalec, 'Microfluidic control over topological states in channel-confined nematic flows,' *Nature communications*, vol. 11, no. 1, pp. 1–10, 2020.

[83] T. P. Rieker, N. A. Clark, G. S. Smith, D. S. Parmar, E. B. Sirota and C. R. Safinya, '"Chevron"local layer structure in surface-stabilized ferroelectric smectic-C cells,' *Physical Review Letters*, vol. 59, no. 23, pp. 2658–2661, 1987.

[84] J. E. Maclennan, M. A. Handschy and N. A. Clark, 'Director reorientation dynamics in chevron ferroelectric liquid crystal cells,' *Liquid Crystals*, vol. 7, no. 6, pp. 787–796, 1990.

[85] L. Mrad and D. Phillips, 'Dynamic analysis of chevron structures in liquid crystal cells,' *Molecular Crystals and Liquid Crystals*, vol. 647, no. 1, pp. 66–91, 2017.

[86] P. Guillamat, J. Ignés-Mullol and F. Sagués, 'Control of active liquid crystals with a magnetic field,' *Proceedings of the National Academy of Sciences*, vol. 113, no. 20, pp. 5498–5502, 2016.

[87] G. Canevari, J. Harris, A. Majumdar and Y. Wang, 'The well order reconstruction solution for three-dimensional wells, in the Landau-de Gennes theory,' *International journal of non-linear mechanics*, vol. 119, p. 103 342, 2020.

[88] P. Palffy-muhoray, E. C. Gartland Jr and J. R. Kelly, 'A new configurational transition in inhomogeneous nematics,' *Liquid Crystals*, vol. 16, no. 4, pp. 713–718, 1994.

[89] L. Fang, A. Majumdar and L. Zhang, 'Surface, Size and Topological Effects for some Nematic Equilibria on Rectangular Domains,' *Mathematics and Mechanics of Solids*, vol. 25, no. 5, pp. 1101–1123, 2020.

[90] MathWorks, *MATLAB*, version 9.10.0.1710957 (R2021a), 2021.

[91] A. N. Beris and B. J. Edwards, *Thermodynamics of Flowing Systems: With Internal Microstructure*. Oxford, UK: Oxford University Press, 1994.

[92] M. C. Calderer and B. Mukherjee, 'Chevron patterns in liquid crystal flows,' *Physica D: Nonlinear Phenomena*, vol. 98, no. 1, pp. 201–224, 1996.

[93] L. Giomi, L. Mahadevan, B. Chakraborty and M. F. Hagan, 'Banding, excitability and chaos in active nematic suspensions,' *Nonlinearity*, vol. 25, no. 8, pp. 2245–2269, 2012.

[94] L. Giomi, M. J. Bowick, X. Ma and M. C. Marchetti, 'Defect annihilation and proliferation in active nematics,' *Physical Review Letters*, vol. 110, no. 22, p. 228 101, 2013.

[95] A. Doostmohammadi, J. Ignés-Mullol, J. M. Yeomans and F. Sagués, 'Active nematics,' *Nature communications*, vol. 9, no. 1, p. 3246, 2018.

[96] S. A. Edwards and J. M. Yeomans, 'Spontaneous flow states in active nematics: A unified picture,' *Europhysics letters*, vol. 85, no. 1, p. 18 008, 2005.

[97] L. Giomi, T. B. Liverpool and M. Marchetti, 'Sheared active fluids: Thickening, thinning, and vanishing viscosity,' *Phys. Rev. E*, vol. 81, no. 5, p. 051 908, 2010.

[98] G.-Q. Chen, A. Majumdar, D. Wang and R. Zhang, 'Global existence and regularity of solutions for active liquid crystals,' *Journal of Differential Equations*, vol. 263, no. 1, pp. 202–239, 2017.

[99] A. Logg, K.-A. Mardal and G. Wells, *Automated solution of differential equations by the finite element method: The FEniCS book*. Springer Science & Business Media, 2012, vol. 84.

[100] H. Yucen, J. Yin, P. Zhang, A. Majumdar and L. Zhang, 'Solution landscape of a reduced Landau-de Gennes model on a hexagon,' *Nonlinearity*, vol. 34, no. 4, pp. 2048–2069, 2021.

[101] P. Sternberg, 'The effect of a singular perturbation on nonconvex variational problems,' *Archive for Rational Mechanics and Analysis*, vol. 101, no. 3, pp. 209–260, 1988.

[102] J. Xia, 'Computational and Analytical Aspects of Energy Minimisation Problems in Cholesteric, Ferronematic and Smectic Liquid Crystals,' Ph.D. thesis, Keble College - University of Oxford, 2021.

[103] P. R. Brune, M. G. Knepley, B. F. Smith and X. Tu, 'Composing scalable nonlinear algebraic solvers,' *SIAM Review*, vol. 57, no. 4, pp. 535–565, 2015.

[104] P. R. Amestoy, I. Duff and J.-Y. L'Excellent, 'Multifrontal parallel distributed symmetric and unsymmetric solvers,' *Computer Methods in Applied Mechanics and Engineering*, vol. 184, no. 2–4, pp. 501–520, 2000.

[105] F. Rathgeber, D. A. Ham, L. Mitchell, M. Lange, F. Luporini, A. T. T. McRae, G. T. Bercea, G. R. Markall and P. H. J. Kelly, 'Firedrake: automating the finite element method by composing

abstractions,' *ACM Transactions on Mathematical Software*, vol. 43, no. 3, pp. 1–27, 2017.

[106] S. Balay *et al.*, 'PETSc users manual,' Argonne National Laboratory, Tech. Rep. ANL-95/11 - Revision 3.9, 2018.

[107] P. E. Farrell, Á. Birkisson and S. W. Funke, 'Deflation techniques for finding distinct solutions of nonlinear partial differential equations,' *SIAM Journal on Scientific Computing*, vol. 37, no. 4, A2026–A2045, 2015.

[108] R. R. Maity, A. Majumdar and N. Nataraj, 'Parameter dependent finite element analysis for ferronematics solutions,' *Computers & mathematics with applications*, vol. 103, pp. 127–155, 2021.

[109] H. Kusumaatmaja and A. Majumdar, 'Free energy pathways of a multistable liquid crystal device,' *Soft matter*, vol. 11, no. 24, pp. 4809–4817, 2015.

[110] J. Milnor, *Morse Theory*, 1st edition. Princeton, NJ: Princeton University Press, 1963.

[111] L. Zhang, Q. Du and Z. Zheng, 'Optimization-based shrinking dimer method for finding transition states,' *SIAM Journal on Scientific Computing*, vol. 38, no. 1, A528–A544, 2016.

[112] D. E. Longsine and S. F. McCormick, 'Simultaneous rayleigh-quotient minimization methods for $Ax = \lambda Bx$,' *Linear Algebra and its Applications*, vol. 34, pp. 195–234, 1980.

[113] S. S. Tenishchev, A. D. Kiselev, A. V. Ivanov and V. M. Uzdin, 'Multiple minimum-energy paths and scenarios of unwinding transitions in chiral nematic liquid crystals,' *Physical Review E*, vol. 100, no. 6, p. 062 704, 2019.

[114] S. S. Tenishchev, I. M. Tambovtcev, A. D. Kiselev and V. M. Uzdin, 'Hysteresis and Fréedericksz thresholds for twisted states in chiral nematic liquid crystals: Minimum-energy path approach,' *Journal of Molecular Liquids*, vol. 325, p. 115 242, 2021.

[115] J. Fukuda and S. Žumer, 'Cholesteric blue phases: Effect of strong confinement,' *Liquid Crystals*, vol. 37, no. 6-7, pp. 875–882, 2010.

[116] Y. Tong, Y. Wang and P. Zhang, 'Defects Around a Spherical Particle in Cholesteric Liquid Crystals,' *Numerical Mathematics: Theory, Methods & Applications*, vol. 10, no. 2, pp. 205–221, 2017.

[117] G. P. Alexander and J. M. Yeomans, 'Stabilizing the blue phases,' *Physical Review E*, vol. 74, no. 6, p. 061 706, 2006.

[118] M. Ravnik and S. Žumer, 'Landau–de gennes modelling of nematic liquid crystal colloids,' *Liquid Crystals*, vol. 36, no. 10-11, pp. 1201–1214, 2009.

[119] D. Henao, A. Majumdar and A. Pisante, 'Uniaxial versus biaxial character of nematic equilibria in three dimensions,' *Calculus of variations and partial differential equations*, vol. 56, no. 2, p. 55, 2017.

[120] B. Dacorogna, *Direct methods in the calculus of variations*, 2nd edition. New York: Springer, 2008.

[121] R. A. Adams and J. J. F. Fournier, *Sobolev Spaces*, 2nd edition. San Diego: Elsevier Science and Technology, 2003.

[122] A. Friedman, 'On the regularity of the solutions of nonlinear elliptic and parabolic systems of partial differential equations,' *Journal of Mathematics and Mechanics*, vol. 7, no. 1, pp. 43–59, 1958.